University of Hertfordshire

Thesis

# Investigation of the physical and physiochemical relationships in Nanoparticles and their attributions to antimicrobial activities

Submitted to the University of Hertfordshire in partial fulfilment of the requirement of the degree of PhD

Xiuyi Yang
15068775

Supervisor: Guogang Ren
Yuen-Ki Cheong
Jacqueline Stair

School of Physics, Engineering and Computer Sciences
May 2021

**ABSTRACT**

Antibiotic resistance is one of the greatest threats to global health, as bacteria are becoming increasingly resistant to antibiotics leading to failure of treatments. This PhD project investigated the physical, chemical and physiochemical properties of a total of eleven potential antimicrobial nanomaterials. Some of which were engineered with antiviral function using Tesima$^{TM}$ thermal plasma technology, others were commercially available. The aims of this project are to select 2-3 nanomaterial candidates with the best physiochemical and antimicrobial performances and to exploit them into a single antimicrobial formulation, which would generically deactivate a wide spectrum of pathogens and suitable to be applied as a coating/impregnating agent for the applications in biomedical instrument.

In order to understand how nanoparticles such as Tungsten (W), Copper (Cu), Silver (Ag), Zinc (Zn) and their derivatives lead to the inactivation of Gram-negative bacteria (*P. aeruginosa*) and Gram-positive bacteria (*S. aureus*), different instrumentation analyses were used to examine these nanoparticles in powder and aqueous suspension forms. These analyses were then used to reflect on the associated antimicrobial testing results. SEM was used to reveal the shapes and approximate sizes of the nanoparticle powder. Powder X-ray diffraction identified the exact crystal phases in the raw nanopowders. FTIR and Raman spectroscopy were used to trace the presence of organic impurities. ICP-OES was used to quantify the elemental compositions in nanoparticles and the amount of metallic ions saturated in the aqueous media. Nanoparticle tracking analysis (NTA) was used to not measure the concentration and size distribution of nanoparticles in the aqueous media, but also reveal the difference between nanoparticle suspensions and their powder forms. Zetasizer was used to measure their surface charge, which affects their stability. The physiochemical study provided details of the hydrodynamic particle sizes, distributions and stabilities of the selected materials, which had direct reflection on their exposure and static interactions to different microbial cells. Different dispersing methods were investigated, in order to optimize the processing parameters to obtain uniform and stable nanoparticle suspensions, of which are the basic requirements for enhancing fabrication compatibility and antimicrobial efficacy with hybridizable substrates for biomedical devices.

In general, different shapes of nanoparticles were found in both commercial and engineered samples, nevertheless, they all met the physical criteria as nanoparticles. Engineered nanoparticles, especially the Ag nanoparticles, appeared to be less pure when comparing to the commercial ones, however it was found to be the most effective materials against *P. aeruginosa*. The ion release as the main antimicrobial mechanism performed differently

depending on types of nanoparticle forms, pH levels and salt effect in the aqueous media. In this study, the pH values of all samples in water were basically neutral, and the zeta potential values were mostly negative. Overall, the best way to obtain stable nanoparticle suspension is to disperse raw nanoparticle in aqueous medium using high frequency liquid processor (sonicator) for 2 minutes in the present of surface treatment. NTA detected that most of the tested metallic nanoparticles and formulations prepared with using this method showed to exhibit good dispersion, while excessive sonication can cause overheating, particle collisions and contamination. Besides, a processing method based on microwave reactor was developed for poorly dispersed Cu nanoparticle, which enhanced dispersion with increasing the heating temperature. The level of antimicrobial efficacy appeared to be highly dependent on their hydrodynamic sizes and stability. A 30-minute dispersant measurement using NTA showed good antimicrobial nanoparticle agents (Ag, CuAg and AMNP2 suspensions) remained relatively high concentrations and small sizes in the end. The combination of multi-elements played a stronger role in killing bacteria. Therefore, alloy nanoparticles, such as CuAg and CuZn showed the most promising physiochemical and antimicrobial characteristics. Their formulas were calculated ($CuAg_{42}$ and $Cu_{2.3}Zn_1$) based on the atomic ratio of elements from elemental analysis.

**ACKNOWLEDGEMENTS**

First and foremost, I would like to express my sincere gratitude to my wonderful supervisors Dr. Guogang Ren, Dr. Yuen-Ki Cheong and Dr. Jacqueline Stair, for their continuous instruction and generous support throughout the course of my PhD programme.

I am also grateful with many other members of the University, this include the technical members Jesus Calvo-Castro, James Stanley, Malcolm Meeson from the School of life and medical sciences; Arthur Collyer and Sufyan Akram from the School of Physics, Engineering and Computer Sciences. Without their help, this work would not be achieved.

I would also like to thank Dr. Claire Bankier, Dr. Lena Ciric (Department of Civil, Environmental and Geomatics Engineering, University College London), Prof. Mohan Edirisinghe (Department of Mechanical Engineering, University College London) and Elaine Cloutman-Green (Department of Microbiology, Virology, and Infection Prevention Control, Great Ormond Street Hospital), for their expert advice and extending my knowledge in clinical and microbiological sciences.

Finally, I will express the most heartfelt gratitude to my beloved parents for their love and supporting me financially.

# CONTENT PAGE

## LIST OF FIGURES

## LIST OF TABLES

## LIST OF ABBREVIATIONS

| Symbol | Description |
|---|---|
| *A. niger* | *Aspergillus niger* |
| AFM | Atomic force microscope |
| Ag | Silver |
| $AgNO_2$ | Silver nitrite |
| $AgNO_3$ | Silver nitrate |
| AMNP | Antimicrobial nanoparticles |
| ATR | Attenuated Total Reflectance |
| Au | Gold |
| *B. megaterium* | *Bacillus megaterium* |
| *C. albicans* | Candida albicans |
| CCD | Charge-coupled device |
| CFU | Counting colony forming units |
| CMOS | Complementary metal–oxide–semiconductor |
| CNTs | Carbon nanotubes |
| Cu | Copper |
| $Cu(OH)_2$ | Copper(II) hydroxide |
| $CuNO_3$ | Copper nitrate |
| CVD | Chemical vapour deposition |
| DLS | Dynamic light scattering |
| DNA | Deoxyribonucleic acid |
| DTI | Department of Trade and Industry |
| DWCNTs | Double-walled carbon nanotubes |
| *E. coli* | *Escherichia coli* |
| EMRSA | Epidemic methicillin-resistant *Staphylococcus aureus* |
| FTIR | Fourier-transform infrared spectroscopy |
| GO | Graphene oxide |
| $HNO_3$ | Nitric acid |
| ICP-AES | Inductively coupled plasma-atomic emission spectroscopy |
| ICP-OES | Inductively coupled plasma-optical emission spectrometry |
| *K. pneumoniae* | *Klebsiella pneumoniae* |
| KBr | Potassium bromide |
| LOD | Limit of detection |
| LOQ | Limit of quantification |

| | |
|---|---|
| MBC | Minimum bactericidal concentration |
| MIC | Minimum inhibitory concentration |
| MRSA | Methicillin-resistant *Staphylococcus aureus* |
| MWCNTs | Multi-walled carbon nanotubes |
| NTA | Nanoparticles tracking analysis |
| ORR | Oxygen reduction reaction |
| *P. aeruginosa* | *Pseudomonas aeruginosa* |
| ppm | Parts per million |
| qPCR | Quantitative polymerase chain reaction |
| ROS | Reactive oxygen species |
| *S. aureus* | *Staphylococcus aureus* |
| *S. choleraesuis* | *Salmonella choleraesuis* |
| *S. epidermidis* | *Staphylococcus epidermidis* |
| *S. paratyphi* | *Salmonella paratyphi* |
| *S. typhi* | *Salmonella typhi* |
| SARS | Severe acute respiratory syndrome |
| SEEDA | Southeast England Development Agency |
| SEM | Scanning electron microscope |
| SWCNTs | Single-walled carbon nanotubes |
| TEM | Transmission electron microscope |
| *V. cholerae* | *Vibrio cholerae* |
| W | Tungsten |
| Zn | Zinc |

# CHAPTER 1 INTRODUCTION

## 1.1 Background

Antibacterial refers to the general term for inhibition of microbial growth and sterilization of instruments. Since many known bacteria are undesired to human beings and are the cause of many severe diseases, Nanomaterials that function similarly to those of antibiotics have been developed with proven antimicrobial efficacy. Although antibiotics are efficient in destroying bacteria at the first instance, a subset of them often survives after exposure to antibiotics and is able to rapidly develop resistance to antibiotics [1]. Thus, it is predictable that more superbugs will arise in a very short time. As an example, methicillin-resistant *Staphylococcus aureus* (MRSA) is currently known as serious pathogens to resist to many of the antibiotics used to treat ordinary staph infections, such as penicillin, vancomycin, and oxacillin [2]. The patients have to bear a higher and wider expense to be cured. In addition, the US Centre for Disease Control and Prevention reports that antibiotic-resistant infections are still a major problem in the United States, with more than 2.8 million infections and more than 35,000 deaths in 2019 [3]. Although decline in the prevalence of hospital-onset MRSA infections has slowed since 2012 due to the implementation of preventative measures, the outbreak of MRSA is still a potential concern primarily due to the overuse and improper use of antibiotics [1].

## 1.2 Objectives of the thesis

The current priority is to reduce antibiotic usage and to explore alternative approaches to prevent infectious diseases transmission. With the recent developments in materials science, nanomaterials were found to have enhanced antimicrobial activities as compared with traditional bulk materials. Good examples are the antimicrobial properties of Ag and Cu nanoparticle in comparison to their bulk materials. Recently, novel antimicrobial nanoparticles (AMNP) derivatives mainly containing Cu, Ag, and WC have been found to counteract a range of bacteria with high inhibitory rates [4]. Although these AMNP derivatives are efficient in inhibiting a wide spectrum of pathogens, their chemistry and physical properties are not fully understood. To understand how these AMNPs and other metallic nanomaterial derivatives attribute the observed antimicrobial effects, their physical and chemical properties were studied using various analytical instruments (e.g., SEM, XRD, FTIR/Raman, ICP-OES, NTA.) [5]. The subsequent analytical investigation was then used to identify the relationships between the nanoparticles and the antimicrobial results obtained from literature (or provided by UCL collaborative partners). The ultimate aim of this research

is to process and develop metallic nanoparticles with novel antimicrobial function which target a wide spectrum of pathogenic microorganisms. The objectives in this project are:

(1) Characterisation and validation of the physical and chemical properties of engineered and commercial nanoparticles using a range of analytical techniques, e.g., SEM, XRD, FTIR/Raman and ICP-OES.

(2) Preparation and investigation of the physiochemical properties of nanoparticle in aqueous suspensions. The physiochemical investigations of different nanoparticle candidates included particle concentration, size distribution, ion leaching, pH and surface potential.

(3) Providing evidence and structural-activity relationships between the nanoparticles and two affected pathogens (*P. aeruginosa* and *S. aureus*) which may lead to interactions of the microbes. This can give a better understanding of mechanisms involved in the antimicrobial process.

(4) Developing method(s) that can describe the behaviour of a nanoparticle suspension. This provides a more detailed understanding of suspension stability.

(5) Developing optimal process parameters for nanoparticle suspension preparation or exploring other processing methods of improving nanoparticle dispersibility to figure out if it can improve the antimicrobial effects.

The research project plan is illustrated in **Figure 1.1** as a flow chart for the overall strategy.

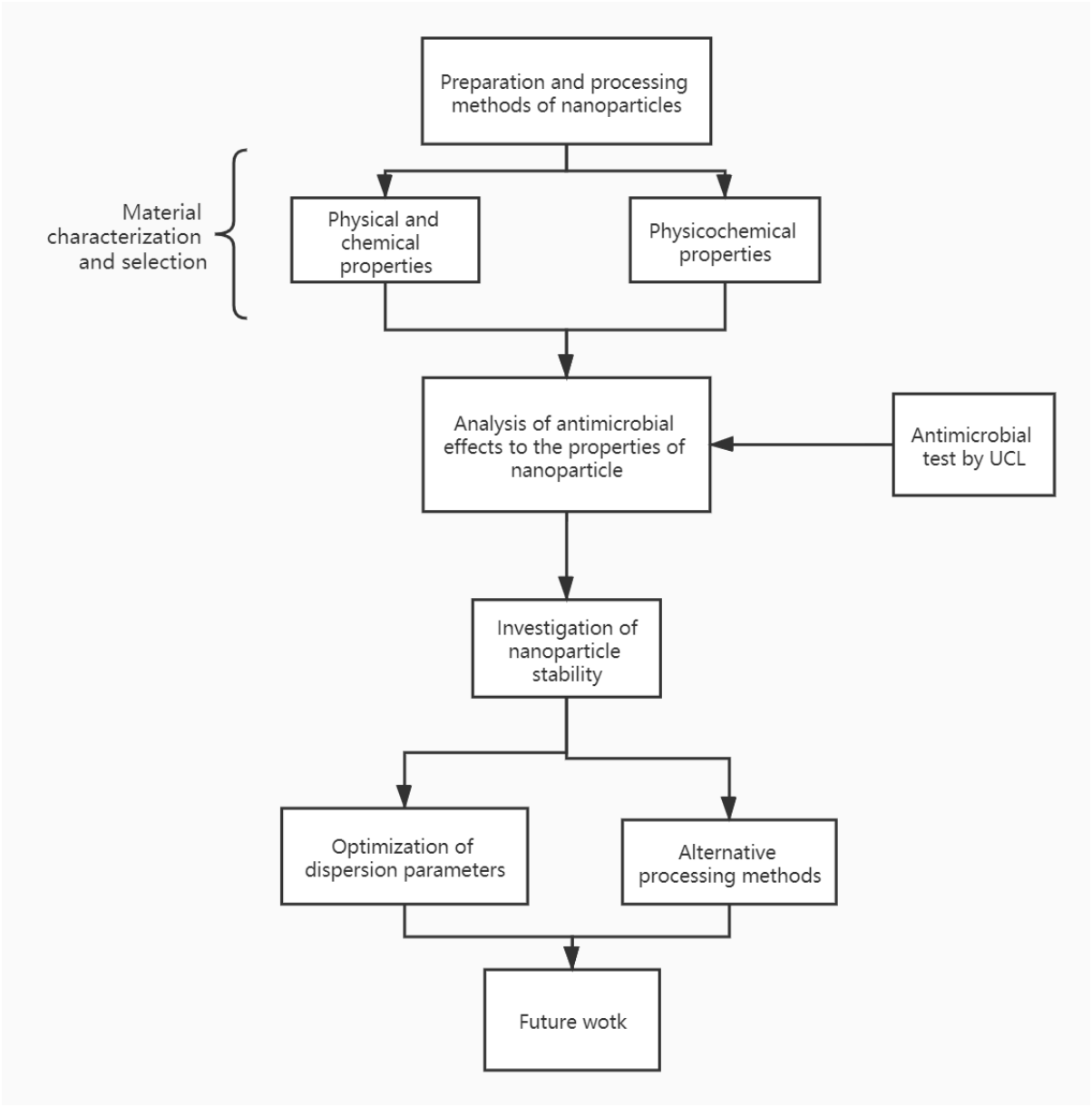


**Figure 1.1** The flow chart of the overall strategy of the thesis from Chapter 3 to Chapter 8.

## 1.3 Thesis structure

This thesis is divided into 8 chapters. In addition to Chapter 1 introduction and Chapter 2 literature review, each chapter individually describes used nanomaterials, instrumentation/methodology and experimental work. The content of each chapter is briefly introduced as follows:

**Chapter 1**: The introduction describes the motivation and objectives of the research, as well as the overview of the thesis. **Chapter 2** covers the literature reviews of nanomaterial synthesis and characterization techniques. Common antimicrobial nanomaterials and the background knowledge of nanofluids also have been considered for the literature review.

**Chapter 3** contains the results and discussion of characterization analysis regarding physical and chemical properties of engineered and commercial nanomaterials using various techniques. **Chapter 4** investigates physiochemical properties of these nanoparticle suspensions including NTA study, pH and zeta potential measurements. **Chapter 5** presents antimicrobial activities of nanoparticles results and links the antimicrobial effects to the properties of nanoparticles we investigated throughout this research. The antimicrobial properties of these nanoparticles were assessed by our University College London collaborators towards Gram-positive and Gram-negative pathogens. **Chapter 6** analyses the supernatant and dispersant measurement of nanoparticle trying to explain the chance of nanoparticles exposure to the microbes during their treatment of which has direct effect on their antimicrobial abilities. **Chapter 7** contains two different studies: (1) the effect of sonication duration on nanoparticle dispersions at different concentrations as well as pH and zeta potential changes and (2) an alternative method that uses microwave on nanoparticle dispersions and its feasible application. **Chapter 8** summaries the overall outcomes and benefits in this thesis. Future works and recommendations have also been discussed as well.

## CHAPTER 2 LITERATURE REVIEW

### 2.0 Nanomaterials

Nanoparticles can be defined as particulate dispersions with size in the range of 1 - 100 nm [6]. The existence of natural nanomaterials began after the big bang, which includes seashells, skeletons*, etc*. [7] Unconsciously, human has been producing and employing nanomaterials since ancient times. For instance, studies from Jaina Island found that the Maya blue paint was made of needle-shaped crystals [7]. The pigment appeared as the blue colour because of the presence of a superlattice structure in nanoscales.

However, the scientific application of nanomaterials began much later – the concept of nanotechnology was first introduced in 1959 stated by Richard Feynman [8]. One of the earliest nanotechnology applications was reported by Michael Faraday in 1857, where he was fascinated by the ruby colour of colloidal gold [9]. By the early 1940's, commercial $SiO_2$ nanoparticles were already used for rubber reinforcement in USA and Germany [8]. After two decades, metallic nanoparticles were developed for recording tapes and later nanocrystals were produced by gas evaporation techniques for the first time [10]. Today, the development of nanotechnology is rapidly growing and nanomaterials have immense applications in almost all the fields from the fields of engineering to health sciences [7].

### 2.1 Applications and intrinsic properties of nanomaterials

Nanomaterials has been intensively used in several applications because of their ability to produce various unique properties in comparison to traditional bulk materials [8]. Ag NPs can be used for solar cells, such as Shen *et. al.* (2013) enhanced 15.11% of power conversion efficiency of polymer solar cells when they added Ag–$SiO_2$ core–shell nanoparticles in the active layer [11]. In another study, Ghiaci *et. al.* (2016) synthesized Ag NP compounds as new electrochemical sensors for glucose detection [12]. The author claimed that Ag NPs improved the performance of the electrodes that used to determine glucose concentration in biological samples. Therefore, the detection limit of this Ag-based electrochemical sensors had almost two orders of magnitude lower than other electrochemical sensors. Cu NPs used as the fuel additive for diesel engine was reported [13]. The Cu NPs in the range of 40 - 50 nm were prepared and added in order to reduce nitrogen oxide emissions and improve engine performance. ZnO NPs have been found to possess catalytic activity for prepare organic chemical such as Benzenes and coumarins [14, 15]. All three nanomaterials

described above also exhibited highly effective in antimicrobial properties, together with other antimicrobial agents will be discussed later in Section 2.4.

In addition, many studies demonstrated intermetallic nanoparticles synthesized from two or more metals showed more enhanced properties than monometallic nanoparticles [16]. For instance, Ag–Au nanoclusters combined with biomolecules were prepared to be used as label probe because this alloy do not only displayed better fluorescence property than each of them individually but also exhibited good dispersibility and stability in aqueous solution as well as favourable biocompatibility [17]. In another field, An *et. al.* (2011) synthesized Ag–Pd NPs as catalysis of chlorinated organic solvents and chlorinated aromatic compounds [18]. The result showed that Ag–Pd nanoparticles exhibited better electrocatalytic activity for benzyl chloride and better long-term performance than Ag NPs. In this study, CuAg and CuZn NPs will be investigated for their characteristics (Please see Chapter 3 and 4).

Two primary factors including surface effect and quantum confinement effect can explain that why nanomaterials have such unique properties [19]. Nanomaterials have a much greater surface area to volume ratio than their conventional forms. Compared to bulk materials, a large portion of the atoms reside on the surface than those in the core of the particle and they are also found to be less stable (hence more reactive), due to lower coordination and the presence of unsatisfied bonds in their atomic structures [15]. In particular, where edge and corner atoms are often associated to the minimum energy interactions and binding with foreign atoms [14]. With regards to quantum confinement effect, of which is associated by the discrete energy levels presence in the atomic structure. In other words, when the particle sizes is reduced to nanometres, the confining dimension is decreased, thus resulting in the discrete energy levels and widening the energy band gaps [19, 20]. These factors affect the chemical reactivity of materials as well as leading to novel optical, electrical and magnetic behaviours. For example, 3.5 nm average-sized Ag NPs have a melting temperature approximately 112 ℃, which is much lower than that of bulk Ag (960 ℃) to be employed [21]. Similarly, a wide melting point range of Cu was determined as a function of its particle size varied from 47 to 2319 nm [22]. The melting temperature of the smallest size of Cu NP (47 nm) was 670 ℃ which was lower than that of bulk Cu. The thermal conductivity of Cu NP showed the same growth trend as its melting temperature, which was still lower than that of bulk Cu.

## 2.2 Nanoparticle synthesis and processing methods

Depending upon the method of synthesis, nanoparticles can traditionally be either assembled atoms together or dis-assembled (break or dissociate) bulk solids into extremely tiny size that constituted of only a few atoms, which refers the 'bottom up' or the 'top down' approaches [7].

### 2.2.1 Sol-gel method

Sol-gel process is a widely used approach for synthesizing nanoparticles (also known as chemical solution deposition) which is also the most primary bottom-up method due to its simplicity and universality. As shown in **Figure 2.1**, metal oxides and chlorides are the typically common precursors in sol-gel process which undergoes a series of hydrolysis and polycondensation reaction to form a colloidal suspension or a solution. The transition of a system from a liquid "sol" into a solid "gel" phase occurs by dehydration reactions. The method of drying the gel will then determine whether to form an aerogel or a xerogel. An aerogel is obtained when the liquid phase of a gel is replaced by a gas, while a Xerogel is obtained when the liquid phase of a gel is removed by evaporation. The final product is produced when the gel is calcinated. In addition, powder or film coating can also be obtained when the sol is calcinated. The advantages of the sol-gel process are economical, low processing temperature and well-controlled even for small production [23]. Many research groups reported the synthesis of $Al_2O_3$ nanomaterials using the sol-gel method [24-26]. One of the methods involved completely dissolving the precursor powder $AlCl_3$ in an ethanol solution. A 28% $NH_3$ solution was then added to form the gel and allowed to maturate at room temperature and finally dried for 24 hours. The resulting gel was finally calcined at 1000℃ for 2 hours. In another experiment, Alwan *et. al.* (2015) also synthesized ZnO NPs *via* sol-gel method [27]. Zinc acetate was used as a precursor, which was blended into double distilled water and heated to 50 ℃. Then an absolute ethanol and 47% $H_2O_2$ were added to the solution, incubated for 24 hours and dried at 80 ℃ to obtain ZnO NPs. Complex nanoparticles can also be synthesized by sol-gel technique as well. Ramesh (2013) fully blend the reagent and citric acid solution and then dried them to obtain nanoparticles that composed of Ag, Al, Ti and O elements [28]. The characterization results showed that the average size was between 17 and 48 nm, depending on the ratio of $Ti^{3+}$ and $Al^{3+}$ ions with different ion radii. Lastly, the formation of Ag-$TiO_2$ NPs was determined to be used for degradation of methylene blue under UV light irradiation [29].

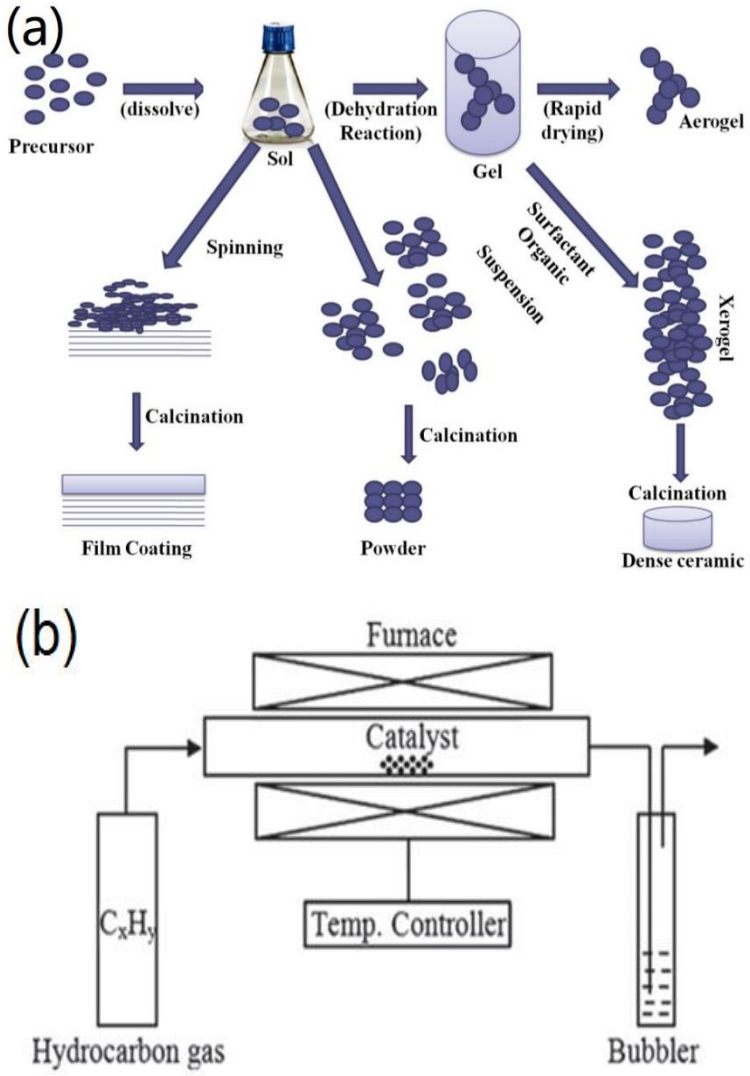


**Figure 2.1** A schematic diagram of (a) sol-gel method [30]. The precursors form a solution by hydrolysis and polycondensation, which will then be transformed into a gel, and finally, a dry gel is obtained. (b) A schematic diagram of preparing CNTs using CVD method, where hydrocarbon vapour are injected into a high-temperature furnace containing catalysts and deposited on the surface of catalyst to obtain CNTs [31].

### 2.2.2 Chemical vapour deposition (CVD)

Chemical vapour deposition (CVD) is a bottom-up method for synthesizing nanoparticles that involves depositing a thin film of volatile precursors onto a substrate. A thin film of product is generated on the material surface when the chamber is heated to a temperature that combines with the precursor gas [32]. The benefits of CVD are that it can produce high quality homogeneous hard nanoparticles. However, the challenges of CVD are the requirement of

high temperature conditions and specialized equipment [33]. Taking carbon nanotubes (CNTs) as an example, the process involves injecting a hydrocarbon vapour through a furnace at high temperature (600 – 1200 ℃) where there are catalyst materials such as Fe, Co and Ni. CNTs are deposited on the surface of catalyst in the reactor, and they are finally collected after cooling the system to room temperature [31]. The schematic diagram is shown above at **Figure 2.1**. Other dimensional carbon nanomaterials such as fullerenes (0D) and graphene (2D) can also be synthesized. For instance, the production of fullerenes *via* hot-filament CVD method was completed with a vertical W filament and a stainless-steel film under a pressure less than 1 bar, where the wire provided a high current that heats temperature to 2200 °C and the film was used for deposition [34].

### 2.2.3 Spray pyrolysis

The use of spray pyrolysis is the most common situation of top-down synthesis of nanoparticles in the industry [35]. It begins from burning a precursor, fed into the furnace through a hole or opening, becoming liquid and/or vapour under high pressure. Some of the furnaces use laser and plasma instead of flame to deliver the necessary energy to cause the evaporation of small micrometre size particles [36]. After this, the aerosol is fully sprayed and then deposited onto the heated surface obtaining the particles. The difference between the spray pyrolysis method and the CVD method is that the aerosol of the spray pyrolysis method may contain a solvent and undergo a chemical change, while the CVD precursor is completely vaporized during the deposition process without any change. The advantages of spray pyrolysis are simple, effective, cost-effective, continuous process and high yield. Ren and his co-workers reported the nanoparticles (e.g., CuO, Cu and Ag) for antimicrobial applications prepared using thermal plasma (Tesima$^{TM}$) technology by Intrinsiq Materials Ltd., as displayed in **Figure 2.2**. This method used a sufficiently high temperature to evaporate metals and then generate ultrafine nanoparticle rapidly. The CuO NPs were determined in the size range of 20 - 95 nm and the calculated atomic compositions of Cu and O were, respectively, 54.18% and 45.26%. Thus the compound formula was determined as $Cu_{1.2}O$ or $CuO_{0.84}$ [37]. Moreover, the time–kill experiments suggested that a number of bacterial pathogens were inhibited by CuO NPs. In another study, the precursors zinc acetate solution was employed to prepared ZnO NPs *via* spray pyrolysis at different conditions [38]. By changing pressure of atomizer that generates droplets, the crystallite size of ZnO NPs was in the range between 10 to 25 nm. As a result, these ZnO NPs can absorb $H_2S$ from mud six times faster than bulk ZnO.

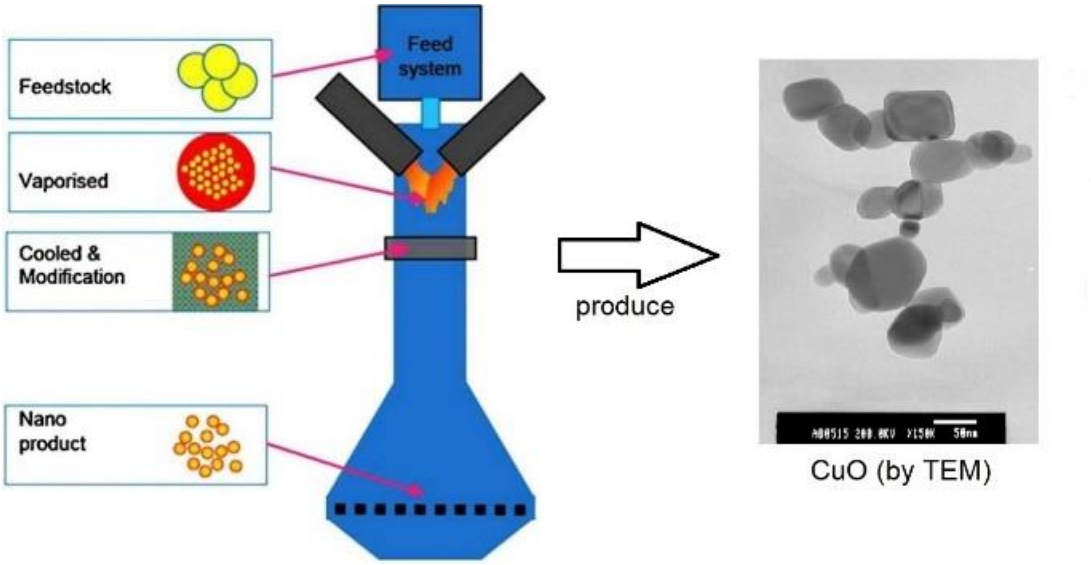


**Figure 2.2** Tesima™ plasma process to generate CuO NPs [37]. This process allows continuous gas phase production of nano-sized nanoparticles.

### 2.2.4 Sonication technique

Sonication technique is one of effective processing top-down technology to break apart compounds or cells in liquid for further dispersion examination [39]. A signal generated from ultrasonic electric generator powers piezoelectric transducer, which converts an electrical signal into physical vibration. After amplification of mechanical movement, the probe then sonicates the solution by creating many microscopic bubbles that constantly form and collapse generating localized shockwaves, to deagglomerate and disperse the particles eventually.

As shown in **Figure 2.3**, sonication disperses suspensions either directly (probe sonication) or indirectly (ultrasonic bath). The probe in direct sonication contacts directly the suspension medium, thereby generating high effective energy output into the suspension; while the ultrasonic probe in indirect sonication is separated from the suspension to re-suspend or avoid damage the sonication [40]. In general, many previous studies have proved direct sonication can obtained the most uniform sized particle dispersion [41, 42]. One of them was Pradhan who dispersed Cu NPs in ultrapure water by manual shaking, vortexing, bath sonication and probe sonication, followed by evaluated their size distributions using DLS (dynamic light scattering) [42]. There were very few Cu particles observed using manual shaking and vortexing method. The particle size of Cu suspension using bath sonication was 1688 ± 64 nm, while the Cu NPs in the solution treated with probe sonication had the smallest

particle size (down to 230 ± 28 nm), and longer remaining time. In this study, the calorimetric method was applied for calculation of energy density. The method and details are described in Section 7.3.2.

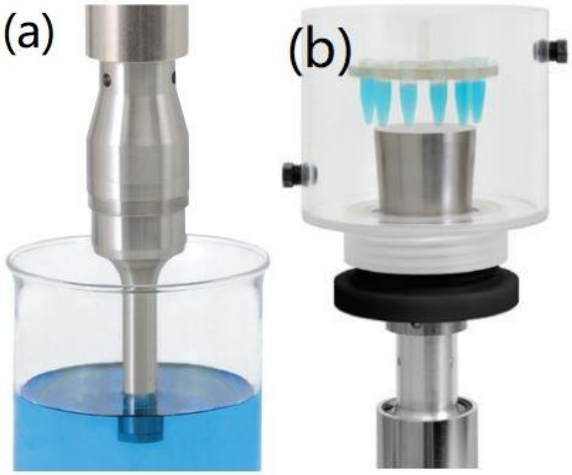


**Figure 2.3** (a) Direct sonication is believed to generate the most homogenously sized particle dispersions, and (b) indirect sonication is to re-suspend or avoid damage of suspensions.

In addition, changes in the surface properties of nanoparticles and complex physicochemical interactions vary with parameters on particle characteristics and selected sonication parameters. For instance, excessive sonication may accelerate aggregation, dissolve and/or form complexes with surrounding medium components [43], but insufficient sonication cannot disperse the nanoparticles well. Therefore, an optimal condition for nanoparticle dispersion must be determined to meet certain requirements such as nanotoxicology. The following parameters had been taken into considerations during the nanoparticle preparation process in this study.

(1) Temperature: a large amount of overheating can take place in container during the ultrasonic treatment process as time passes, leading to changes of volume or components. Immersing the container in a cooling bath and/or selecting a high thermal conductivity container are recommended to address this issue.

(2) Sample and concentration: the amount of energy transferred to a suspension per unit volume is expressed as energy density, an overtime probe sonication may result in evaporate of the liquid and increased the concentration of suspension, both of which

can further bring particle collision frequency and disruptive effect. Besides, a local over-collision can also cause the formation of agglomerate or aggregate. Thus, the physiochemical properties of the suspension and the delivered energy into the suspension both affect the effect of suspension concentration [40].

(3) Medium: the property of medium including viscosity, density, acoustic wave speed and chemical composition can influence the effect of delivered acoustic energy. For example, the difference among saline solutions can attribute to salt concentration - saline with a higher viscosity will greater attenuate acoustic energy relative to pure water.

Along with those mentioned above, there are other considerations including the operations of the instrument [40]. For example, the immersion depth of the probe in the suspension should be 2 to 5 cm and at least 1 cm away from the bottom of the container. In addition, the geometry of the container heavily influences the effect of dispersion as well. A cylindrical vessel with the smallest diameter and flat bottom without touching probe is recommended, because using such vessel increase the suspension height and maximizes the volume of liquid exposed to the acoustic waves. Note that the container should be incompatible with the suspension components so aluminium, stainless steel, glass and plastic container materials are more recommended.

### 2.2.5 Mechanical mill method

Mechanical milling for preparing nanomaterials has been found to have great acceptability, especially in industrial environments due to its simplicity, versatility, scalability of the process and the economic cost. During the grinding process, the metal ball is used as grinding medium to fall from near the top of the rotating hollow cylindrical shell to generate shear force nanoparticles in the cylindrical shell are then decomposed from micrometre to nanometre under strong mechanical shearing force, and are post-annealed in an inert atmosphere [44]. The two main problems of this top-down method are the contamination of the nanomaterials by milling media and/or atmosphere as well as powder consolidation, especially for the highly energetic mills. For instance, continuous grinding for high-energy shaker mills can cause more than 10 at.% Fe contamination from steel balls and containers [44]. In addition to the milling media, if milling is carried out in air, $N_2$ and $O_2$ will be easily reacted with reactive metals such as Al, Ti and Zr [44, 45]. These are main reasons why this method is slowly getting dismissed.

### 2.2.6 Biosynthesis

Recent years, it has been found an eco-friendly and non-toxic approach for the synthesis of nanoparticles – biosynthesis. This bottom-up method uses microorganisms or plant extracts to react with the precursors to produce nanoparticle, and the nanoparticles do not need to use conventional toxic chemicals for bio-reduction and capping [46]. In 2006, Chandran *et. al.* synthesised triangular Au NPs and spherical Ag NPs using aloe vera leaf extract as the reducing agent [47]. According to the amount of aloe extract used, the size of Au NPs was in range of 50 - 350 nm, and the formation of spherical Ag NPs was approximately 15.2 nm. Moreover, Lin *et. al.* (2010) reported a simple production of Ag nanowires by reduction of silver nitrate ($AgNO_3$) with sundried leaf extract at room temperature [48]. It was found that these reducing components did not only play a reducing role, but also played a role of capping and stabilizing agent.

### 2.2.7 Microwave irradiation

Currently, microwaves are intensively applied in chemical industry to accelerate chemical reactions, because microwave reactor generate effective internal heating to exactly deliver electromagnetic energy to the place where it is needed [49, 50]. Other advantages of using controlled microwave include eco-friendly, energy saving and reduction in reaction times.

Microwave heating as a bottom-up method is based on the electromagnetic energy conversion where the electric field, magnetic field and wave propagation are mutually perpendicular to each other [50, 51]. Moreover, the energy of the wave stored in the electric and magnetic fields is considered to be small enough (negligible to X-rays) so that it cannot produce ionization, radiation damage or any breakdown phenomena.

Comparing with conventional heating techniques, microwave reactor can both accelerate the synthesis time and obtain a smaller size of the nanoparticles. For instance, Professor Yu S-H. and co-workers (2008) synthesized Ag NPs environment-friendly using microwave reactor [52]. $AgNO_3$ was heated in water at 150 ℃, followed by adding reducing and protecting agents. After 10 seconds, uniform and monodispersed Ag NPs were produced. TEM detected that their average sizes using with L-lysine and L-arginine were 26.3 and 26.7 nm in diameter, respectively. In **Figure 2.4**, the authors also compared this method with conventional heating which required longer heating times and produced larger sizes.

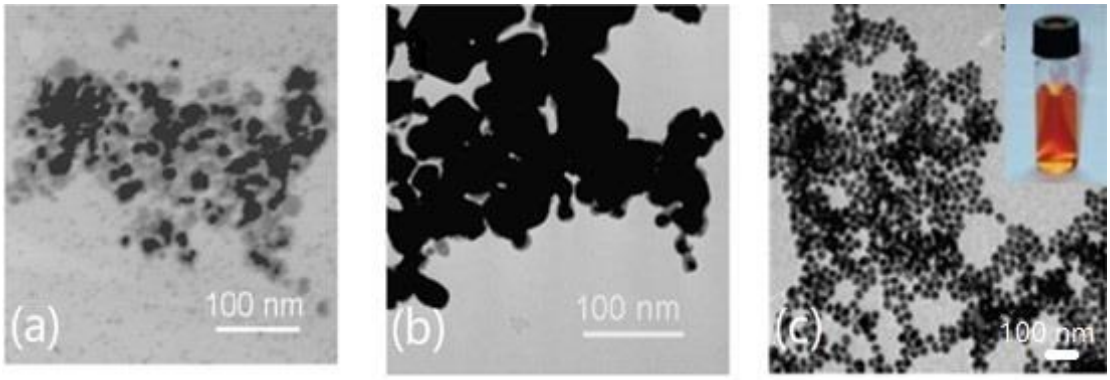


**Figure 2.4** A study on the synthesis of Ag NPs prepared using L-lysine at a temperature of 150 ℃ for (a) 1 hour conventional heating; (b) 2 hours conventional heating, and (c) 10 seconds microwave heating which produced smaller particle size of Ag NPs with shorter reaction time [52].

In another study, Cu NPs were produced using microwave heating and they were improved by adding ascorbic acid (reducing agent) and chelating polymer [53]. In the temperature range of 60 to 170 °C, the synthetic sample showed the smallest particle size (about 90 nm) at 100 °C, because there was a dynamic equilibrium between nucleation and growth at this temperature. Fast heating ramps also contributed on generating smaller nanoparticles - Cu NPs with very high purity were produced even at the lowest synthesis temperature (60 °C), while larger and heterogeneous Cu particles were generated at slow heating ramps.

## 2.3 Nanoparticle characterizations techniques

### 2.3.1 Scanning electron microscopy (SEM)

Scanning electron microscope (SEM) enables to detect the sample information and crystalline structure using a high-energy electron beam. In contrast to optical microscopes with 10 to 1,000 times magnification, SEM has the ability to magnify up to 1 - 2 million times more detailed information on surface morphology and electrical behavior of materials [54]. Moreover, further advantages of using SEM involve fast preparation procedures of specimen and deeper field imaging ability (3D image of surface) over optical microscopes. In 2007, Puchalski *et. al.* presented the study of Ag NPs using SEM and other instruments [55]. The authors dissolved Ag NPs in an organic solvent, dried the supernatant colloid solution and deposited on Au surface to be examined with SEM. The SEM images showed a smaller size of sample with a narrow particle size distribution was achieved. Suleiman *et. al.* (2013) have prepared CuO NPs and studied the effect of reaction time on morphology by SEM [56]. The needle-like shape of CuO NPs can be seen from the beginning, and a more platelet-like structure was obtained in up to 90 hours, displayed in **Figure 2.5a** and **2.5b**. Suresh *et. al.*

(2014) described the production of Cu NPs from different copper salts and plant extract stabilizer [57]. The SEM images of Cu NPs showed they had a spherical shape with an average particle size around 20 nm and the distribution was almost uniform. Medjo (2013) described SEM observations of carbon nanotubes (CNTs) with different orientations [58]. Highly oriented film CNTs were aligned perpendicularly on a flat substrate that is very suitable for electronic devices, while poorly oriented CNTs were disordered and had more defects, given in **Figure 2.5c** and **2.5d**.

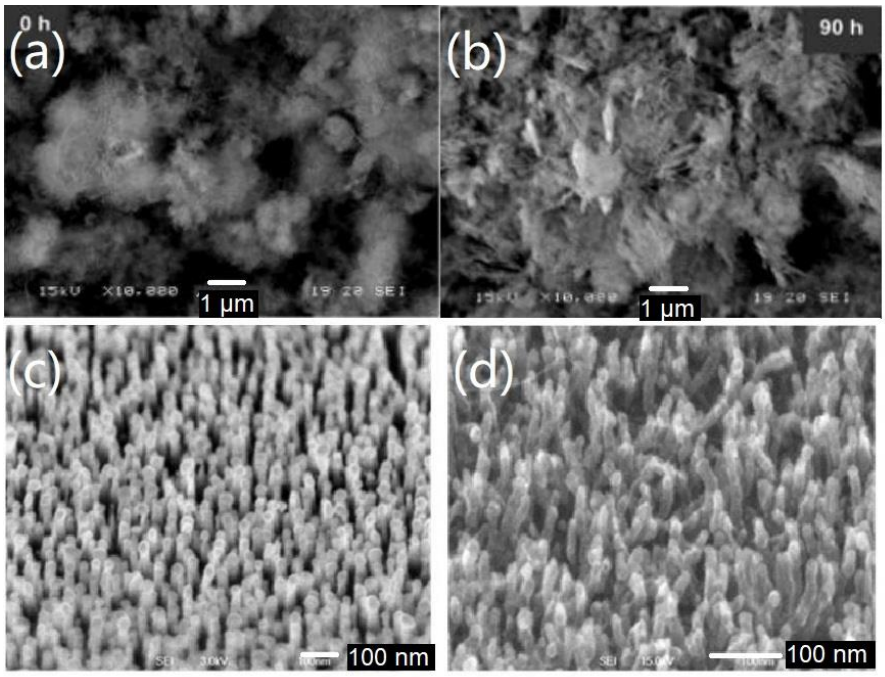


**Figure 2.5** A SEM study on CuO nanostructures changing from (a) needle-like to (b) fiber-like with increasing the reaction time from 0 to 90 hours [56]; Another study using SEM observed that (c) highly oriented CNTs were aligned perpendicularly on a flat substrate and (d) poorly oriented CNTs were disordered and had more defects [58].

In other cases, the specimen is required to further process varies depending on the specimen. A common powder sample preparation used for SEM imaging is to sputter coat a layer of Au, which provides an electrically conductive thin film to enhance imaging resolution. Alwan and co-workers (2015) synthesized ZnO NPs *via* sol-gel method and characterized them using SEM, FTIR, *etc.* [27]. Before sampling, ZnO NPs were dispersed in absolute ethanol under ultrasonic stirring and droplets of the solution were evaporated onto a glass slide to be coated with a thin Au layer in vacuum. Finally, the SEM images was taken at 25,000 times magnification showing that the diameter of the spherical ZnO particles ranged from 100 to 200 nm. In addition, they compared ZnO NPs with fresh samples by the same method to prove that the ZnO NPs can grow even at room temperature after synthesis.

Not only nanometals but also living microorganisms can be visualized under SEM. Similarly, bacteria are supposed to be dried or frozen to avoid releasing any volatile substances before imaging. However, as living microorganisms, bacteria contain proteins and a high proportion of water in their cells, thus a fixation method was initially applied to maintain their structure. In 1984, Allan-Wojtas and Kaláb described a SEM method for some bacteria in soft foods (such as yogurt and cheese) [59]. The encapsulated specimens were washed with buffer and then dehydrated in ethanol. The new flat surface of fractures was produced by freeze-fracturing under liquid $N_2$. After melting and drying, the fragments were eventually ready to be examined by SEM. This method can also be used to study some other similar food.

Alternatively, the filter can capture live or fixed form of bacteria. In other words, if a filter is used, there is no need to fix bacteria. Recently, Golding *et. al.* (2016) employed a conducting filter substrate and ionic liquid to perform SEM imaging of fully hydrated and unfixed microbes [60]. Specifically, a metal-coated filters with appropriate pore size can collect bacteria and viruses in ionic liquid samples which were conductive and had a negligible vapour pressure. The samples were observed by SEM, and then compared with the image of Au-coated samples (observed by SEM) and negative-stained samples (observed by TEM). They concluded that the size of bacteria and viruses infiltrated by the ionic liquid were the most accurate in comparison of the dehydrated sputter-coated SEM preparations and the TEM negative-stained images, as shown in **Figure 2.6**.

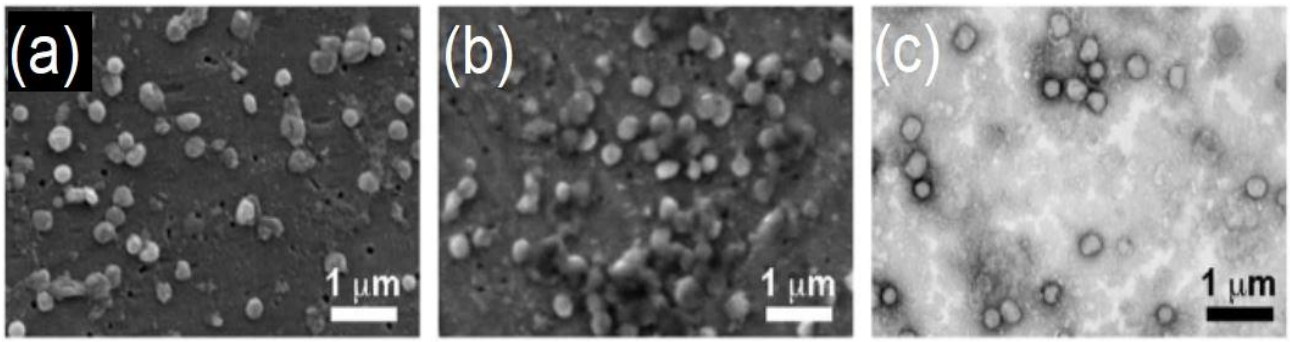


**Figure 2.6** Golding *et. al.* observed Vaccinia virus using (a) sputter coat under SEM, (b) ionic liquid under SEM and (c) TEM [60].
The ionic liquid method was the most accurate in comparison of the other two method.

### 2.3.2 Transmission electron microscopy (TEM)

Transmission electron microscopy (TEM) projects 2D images of inner structure when a beam of electrons hits the specimen, and the interaction to the specimen is occurred. As a result, TEM has an advantage over SEM in that the inner structures of the specimen (such as crystal structure, morphology and stress state information) can be viewed at even higher magnifications which is typically more than 50 million times [61]. Besides, TEM is capable of obtaining an optimal spatial resolution less than 50 picometers (1000 pm = 1 nm) in comparison of 0.5 nm of that of SEM.

Subha and co-workers (2016) biosynthesized Ag NPs from a plant extract [62]. SEM only found that the size and shape of Ag NPs were, respectively, spherical and nanoscale, while TEM further observed a more detailed average particle size of 25 nm. In a study of comparison of experimental methods among atomic force microscopy (AFM) and DLS, SEM and TEM were used to measure the size of nanoparticles in both powder and/or suspension forms. The authors concluded that SEM was the least appropriate method to measure nanoparticles sizes, as an error of up to 14 nm was introduced by metal coating during samples preparation [63]. This point was in agreement with previous experience that SEM was far from characterizing particle diameters frequently below 6 nm [64]. Additionally, TEM has the highest speed for collecting images containing an adequate number of nanoparticles with high quality, because their deposition and imaging conditions are simple and common, while SEM requires several tests before optimal conditions were found [63].

### 2.3.3 Fourier transform Infrared (FTIR) and Raman spectroscopy

Fourier transform infrared spectroscopy (FTIR) and Raman spectroscopy are both non-destructive tools based on the vibrational spectroscopies for identification and characterization of major functional groups that are presence in materials [65].

FTIR is a technology based on the absorbance, transmittance or reflectance of infrared light to measure a wide variety of solid and liquid samples without requiring complex preparations [65]. The core of FTIR spectrometers is the Michelson Interferometer including a beam splitter, a fixed mirror and a moving mirror. The beam splitter transmits half of the beam light striking it to the fixed mirror and reflects the other half to the moving mirror. With the change of the moving mirror, the reflected beams vary the optical path and differentiate the fixed mirror. After that, the two beams are recombined at the beam splitter (causing interference) and pass to the detector [66].

An attenuated total reflection (ATR) technique is developed in order to enhance the surface sensitivity. It requires the sample to be tightly held in place against the ATR crystal where the fraction of beam extends only a few microns beyond the surface of the crystal into the sample and returns to the crystal [67].The main benefit of this mode is strongly avoiding the attenuation of the infrared signal in some unfavourable situations due to the short path length [68]. In addition, ATR-FTIR can analyse solid samples either in powder form or dispersing them in a matrix. One of matrix dispersion methods is to make the ground sample and potassium bromide (KBr) into thin disc pellets. Salam *et. al.* (2012) prepared multi-walled carbon nanotubes (MWCNTs) with side wall functionalization with organic compounds [69]. FTIR analysis was performed to provide the evidence of the functional organic groups on MWCNTs surface. It turned out that the band at around 3,500 $cm^{-1}$ corresponded to the O-H stretching, and the C-H stretching vibrations were observed between 2,850 and 3,000 $cm^{-1}$. A peak at 1,730 $cm^{-1}$ corresponding to C=O and a peak at 1,100 $cm^{-1}$ corresponding to the C–O stretching vibration were also observed. In another study, Betancourt-Galindo (2014) synthesized Cu NPs in KBr pellets with the aid of phenyl ether and oleic acid controlling the growth of Cu NPs [70]. FTIR spectra of Cu NPs confirmed that there were functional organic groups on the surface of Cu NPs. These bands included that two broad bands at 2,901 and 2,838 $cm^{-1}$ correspond to -$CH_2$- and −$CH_3$ groups, asymmetric stretching COO− bands at 1,623 and 1,450 $cm^{-1}$, and symmetric stretching of COO− bands at 1,123 and 847 $cm^{-1}$. However, the fundamental vibrational frequencies of metal-metal bonds is generally out of the measuring range of conventional FTIR spectrometers, thus metals usually cannot be detected by infrared light [71]. The summary of FTIR spectra is listed in **Table 2.1**.

**Table 2.1** The tabulated summary of above-mentioned FTIR stretching [69-71].

| Functional group representation | O-H stretching | C-H stretching | C=O stretching | C–O stretching |
|---|---|---|---|---|
| Wavenumber ($cm^{-1}$) | 3500 | 2850 - 3000 | 1730 | 1100 |
| Functional group representation | -$CH_2$- stretching | -$CH_3$ stretching | Asymmetric COO- stretching | Symmetric COO- stretching |
| Wavenumber ($cm^{-1}$) | 2901 | 2838 | 1450 and 1623 | 847 and 1123 |

Raman spectroscopy is based on the Raman effect. When an incident light hits a sample, the photon of the incident light is absorbed and then reemitted by the sample. Normally, the reemitted photon is at the same frequency as the incident photon, this does not offer helpful information and is known as Rayleigh or elastic scattering. However, a small fraction of the

re-emitted photon gain or lose energy and the frequency of these reemitted photon is higher or lower than the incident photon. This is called anti-Stokes (higher frequency) or Stokes scattering (lower frequency). Since Anti-Stokes-Raman scattering is mostly weaker than Stokes-Raman scattering, Stokes‑scattering is mainly measured in Raman spectroscopy [72].

It is common to combine FTIR technique with complementary Raman spectroscopy, because the nature of the molecular transitions between the two techniques are different – Raman spectra resulting from an inelastic Raman scattering process that occurs when light interacts with molecules whereas IR spectra result from light absorption by vibrating molecules [73].Moreover, Raman spectroscopy requires the changes in the polarizability of functional groups, whereas the change of the intrinsic dipole moment can be detected by FTIR spectroscopy. Therefore, bands that are strong either in FTIR or Raman measurement tend to be weak in the other measurement. As an example, oxygen as a symmetrical molecule cannot be observed in FTIR spectroscopy, but it can be observed a strong dipole moment in Raman spectroscopy. As far as the excitation wavelength concerned, Raman spectroscopy measures relative frequencies of scattered radiation, whereas FTIR spectroscopy measures absolute frequencies of absorbed radiation [74]. Thus, the combination of FTIR and Raman techniques is able to further characterize components of the sample [75].

Costa *et. al.* (2008) characterized single-walled, double-walled and multi-walled carbon nanotubes (SWCNTs, DWCNTs, MWCNTs, respectively) using Raman spectroscopy [76]. The three types of CNTs showed D and G bands around 1,350 and 1,600 $cm^{-1}$. The ratio of D to G bonds indicates a measure of the quality with nanotubes, in which SWCNTs and DWCNTs both showed a higher ratio of intensities of D and G bands, while MWCNTs had the lowest values due to multiple graphite layers resulting in greater number of structural defects. This agreed with Richter who published an article in 1981 indicating that the increase in the agglomeration state of nanoparticles can vary on red-shifts and a broadening of the Raman modes [77]. Rashad *et. al.* (2013) prepared CuO NPs from $Cu(NO_3)_2$ and distilled water using microwave irradiation showing three Raman peaks of CuO were observed at 282, 330, and 616 $cm^{-1}$ [78]. In another study using surface-enhanced Raman spectroscopy, Cu NPs were immersed in crystal violet solution and rinsed with deionized water after the synthesis of Cu NPs and the results showed the signal of crystal violet on the Cu NPs, of which the aromatic C–C stretching modes are corresponding to 1,619, 1,585, 1,535 and 1,444 $cm^{-1}$. Aromatic C–H bending modes were observed at 1,171, 915 and 809 $cm^{-1}$ as well. Similarly, the summary of Raman stretching is listed in **Table 2.2**.

**Table 2.2** The tabulated summary of above-mentioned Raman stretching [76-78].

| Functional group representation | D band | G band | Cu-O | Aromatic C–C stretching | Aromatic C–H bending |
|---|---|---|---|---|---|
| Wavenumber ($cm^{-1}$) | 1350 | 1600 | 282, 330, and 616 | 1619, 1585, 1535 and 1444 | 1171, 915 and 809 |

2.3.4 X-ray diffraction (XRD)

X-ray diffraction (XRD) is another powerful and non-destructive technique for both organic and inorganic phase identification. In the XRD experiment, the monochromatic X-rays beam interacts with the sample to produce constructive interference and the diffracted X-rays (peaks) are detected when conditions satisfy Bragg's Law [79]:

$$n\lambda = 2d \cdot sin\theta$$

Where *d* is the spacing between diffracting planes, *θ* is the incident angle, *n* is an integer, and *λ* is the beam wavelength. As the equation indicated, this law reflects the relationship of the wavelength of electromagnetic radiation with the diffraction angle and the lattice spacing in a crystalline sample. By scanning the sample within the selected 2θ angles range, all possible peaks in the X-ray signal should be recorded and then these peaks are used to calculate lattice parameters and identify the sample. For instance, Rivero and Ruud (2008) used XRD technology to analyse steel bearing balls [79]. The amount of retained austenite and martensite phases - that are directly related to the phase transitions - were accurately measured by the residual stresses of metals. In fact, XRD has been used for a long time. In addition to the use of computerization, modern XRD instruments are close to early models in the late 1940s [80]. In this study, unknown substances will be identified from our nanoparticles as well.

It is worth mentioning that XRD technique has been utilized widely for the identification of unknown crystalline materials since it can rapidly determine minerals with minimal sample preparation in most cases, a database is required for identification of unknown substances [80, 81]. In addition, XRD technique can not only reveal the particle size and components of the materials, but also detect quantitative phase identification, crystal structure determination, and residual stresses, *etc* [81, 82]. The Scherrer equation describes the broadening of a

peak at a particular diffraction angle ($\theta$), as it relates the crystalline domain size to the width of the peak at half of its height ($\beta$) [82]:

$$\gamma = \frac{K\lambda}{\beta \cdot cos\theta}$$

Where $\gamma$ is the crystallite size in the direction perpendicular to the lattice planes, $K$ is a shape factor constant, $\lambda$ is the wavelength of the X-rays, $\beta$ is the line broadening at half the maximum intensity and $\theta$ is the Bragg angle. Theivasanthi and Alagar (2010) prepared Cu NPs *via* electrolytic cathode deposition method at room temperature [83]. They observed the three peaks at 2θ values of 43.64°, 50.80°, and 74.42° corresponding to (111), (200), and (220) planes. In addition to this, they confirmed the resultant particles were face-centered cubic and smaller than 30 nm.

When characterizing composite materials, XRD technology also has been found to play an important role in determining their various properties and composite materials. Zawrah *et. al.* (2013) milled metal-matrix composites composed of Cu and 20 wt.% $Al_2O_3$ to investigate the relationship between the milling time and the properties of obtained powders [84]. The X-ray diffraction results of the composite material implied that the main diffraction peaks of Cu were observed at around 2θ = 50°, 74°, 90°, while that of $Al_2O_3$ were observed at around 2θ = 35° and 43°. When increasing milling time, the XRD intensities of Cu and $Al_2O_3$ was decreased, and their diffraction peaks were broader. Consequently, it was concluded that as the grinding time increased, the average crystal size decreased.

In the same year, Abbas *et. al.* (2013) synthesized the CNTs-CuO composite by a simple chemical method [85]. They identified the monoclinic CuO NPs by characterizing the diffraction peaks around 2θ = 35° and 38°, while the broad peak at 2θ = 25° corresponded to the hexagonal graphite structure (CNTs), which confirmed CNTs has been successfully introduced in the composite. The average crystallite size of the composite was therefore calculated to be 36 nm. In the same study mentioned earlier, Subha *et. al.* (2016) used XRD to identify biosynthetic Ag NPs [62]. The strong peaks at 38° and 43.9° (2θ) was identified as face-centered and cubic Ag NPs, and their particle size was also estimated to be 12 nm.

### 2.3.5 Inductively coupled plasma - optical emission spectrometry (ICP-OES)

Inductively coupled plasma optical emission spectrometry (ICP-OES), also referred to as inductively coupled plasma atomic emission spectroscopy (ICP-AES), becomes a versatile

and classic analytical tool for the determination and quantification of trace elements. The technique involves electrons being excited to release photons, and then capturing their measurement of wavelength to identify the chemical species and measure the intensity for inorganic analysis [86]. The main advantage of ICP-OES technique is that the use of high electromagnetic field can generate high temperatures up to 7,000 K, which is much higher than flames or furnace (3,300 K), thus refractory elements can be excited. More importantly, simultaneous determination of multiple elements can be proceeded with no contamination from electrodeless source. Furthermore, ICP-OES is not only a cost-effective analysis, but it also has favourable detection limit and a wide linear dynamic range [87].

In addition to ICP-OES, inductively coupled plasma mass spectrometry (ICP-MS) combines ICP with a mass spectrometer (MS) system to obtain the mass-to-charge ratio of ions, which provides extra information on isotopic and mass. In a determination study of trace metals in electrolytic Cu sample, Santos *et. al.* (2005) reported ICP-MS had higher sensitivity and accuracy than ICP-OES, regardless of whether the Cu element was being separated from the analytes [88]. Besides, it can be used to determine the analytes whose concentration was even lower than the limit value. However, the setup and operation cost of ICP-MS are much greater than that of ICP-OES system.

In the antimicrobial application, Du *et. al.* (2017) synthesized $Cu_2O$ NPs for antimicrobial agents [89]. The $Cu_2O$ NPs exhibited highly bactericidal efficiency against *Escherichia coli* (*E. coli*) and the Cu content was found to be approximately 10.5% by ICP-OES analysis. Lin *et. al.* (2011) characterized the antibacterial properties of Ag-$TiO_2$ NPs with core-shell structure [90]. Before performing the ICP-OES measurement for ion release study, the sample was dispersed in distilled water, allowed to stand for 10 days and then centrifuged. It was found that in the first two days, the sample released a large amount of Ag ions, and then the ion release rate decreased. Specifically, on the first, second, fifth, and tenth days, it was found the concentrations of released Ag ions were 0.023, 0.046, 0.062 and 0.069 ppm (part per million), respectively. It was concluded that the porous $TiO_2$ shells can prevent Ag corrosion as well as control the amount of Ag ion release to extend the release time of Ag ions. As a result, the Ag/$TiO_2$ NPs with core/shell structure performed excellent inhibitions against *E. coli*.

In this project, ICP-OES will be used to study elemental analysis to quantify their chemical compositions and for leaching study to measure the release of Ag, Cu, and Zn ions from nanoparticles that affects antibacterial effects. Please refer to Section 3.3.4 for ICP details,

Section 3.3.5 for preparation of elemental analysis and Section 4.3.5 for preparation of leaching study.

2.3.6 Nanoparticles tracking analysis (NTA) and dynamic light scattering (DLS) analysis.

Nanoparticles tracking analysis (NTA) is a nanoparticle-tracking device that measures the size, concentration and distribution of nanoparticles in the range of 10 to 1,000 nm in a liquid suspension. Based on a high intensity laser-illuminated microscopical technique and low-background optical configuration, NTA technique uses a high-sensitivity scientific complementary metal–oxide–semiconductor (CMOS) camera to analyse the light scattering and Brownian motion characteristics of nanoparticles in liquid at real-time. All particles can be displayed individually visualized, and their size distribution are analysed by a program related to image. This is different from conventional particle sizing methods (e.g., DLS or photon correlation spectroscopy) which use the intensity-weighted average size of particle aggregates to estimate hydrodynamic particle sizes and distributions together. Thus, NTA has the ability to measure multi-particle mixtures and directly track the concentration of nanoparticles. It is recommended that the required sample concentration is between $10^7$ to $10^9$ particles/ml [91].

Currently, due to the better properties of nanoparticles that improve the efficacy of existing drugs, they are increasingly used in drugs in various multifunctional structures. NTA has the ability to detect small changes in hydrodynamic diameter and quantify aggregates [92]. Wei *et. al.* (2012) explored cancer treatment methods based on nanomedicine to reduce non-specific cytotoxicity and extend lifetime of storage [93]. During the experiment, NTA and DLS were employed to characterize the size and polydispersity of nanoparticles. They stated that compared with most DLS detection systems, NTA provided higher accuracy and multimodal distribution, while the size analysis of DLS is essentially unimodal. In addition, the size distribution detected by NTA is almost Gaussian because it avoids interference from strong scattering or aggregation [93]. This statement was also proved by Bhise *et. al.* (2011) who characterized nanoparticles in their study and quantify the number of plasmids within polymeric nanoparticles [94]. They equipped NTA with a 405 nm laser source to distinguish between plasmids and polymer nanoparticles, and determined the plasmid value of each nanoparticle, while DLS cannot measure plasmids that are biased toward larger particles.

In other fields of studies, nanoparticles and protein aggregates were assessed using both NTA and the DLS techniques by Filipe *et. al.* (2010), as shown in **Figure 2.7** [91]. In the NTA measurement, these samples were measured using a 640-nm laser in triplicate, and the DLS

measurement used a 633-nm He-Ne laser to detect 15 runs of 10 seconds in triplicate, both of which were all performed at a stable room temperature. The Authors confirmed that compared to the DLS method, NTA provided more accurate sizing measurement in both monodisperse and polydisperse samples. Although NTA technology requires relatively time-consuming and operational adjustment experience, other advantages of NTA over DLS include (1) visualizing samples on a monitor to provide kinetic and size information; (2) output of individual particle size and intensity and (3) approximate particle concentration and number distribution. It was also found that NTA obtained a better resolution of peaks because it was less affected by the presence of a small number of large particles (up to1000 nm) and by the mixture of different population ratio, which affect size accuracy and sizing distribution, respectively [91].

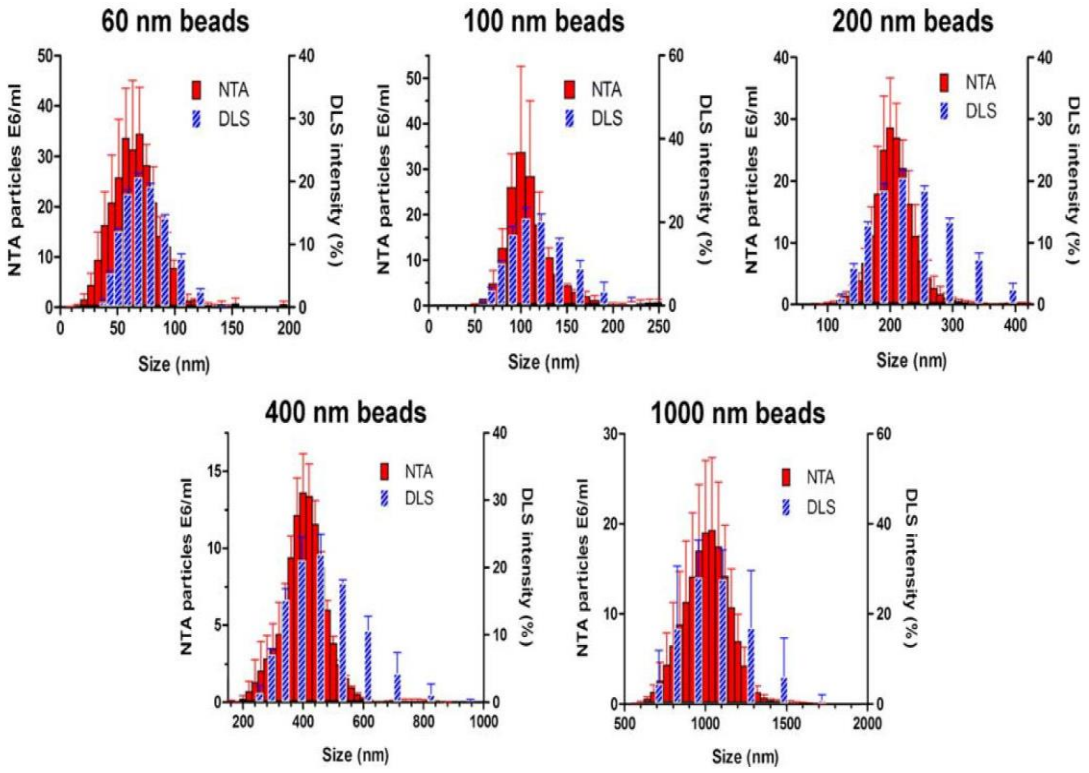


**Figure 2.7** Size distributions from NTA and DLS measurements of monodisperse polystyrene beads by Filipe *et. al*. [91].
NTA provided more accurate size measurement and a better resolution of peaks than DLS in both monodisperse and polydisperse samples.

Overall, NTA is a relatively new technique that can complement DLS as it allows that individual nanoparticles are tracked and analyses on the basis and that the resolution of polydisperse and/or heterogeneous sample types are much improved [95]. Through the visualization of the sample, user can also benefit from a rich profile of nanoparticle properties.

In this project, NTA will be used to study a wide variety of nanoparticles in suspension to reveal the difference between them and their powder forms and the chance of nanoparticles exposure to the microbes in an aqueous medium.

In addition to size measurement, DLS can be used to measure zeta potential which can be explained by DLVO theory [96]. This theory assumes that the total energy ($V_T$) depends on the combination of the effect of electrostatic repulsion ($V_R$) and van der Waals attraction ($V_A$). The electrostatic repulsion becomes increasing when the particles are forced together. At the same time, the interference between their electrical double layers increases as well, which requires some energy to overcome. On the other hand, the van der Waals interaction becomes more and more attractive as similar particles approach, which is caused by the interaction of the rotating or fluctuating dipoles of atoms and molecules. Taking metal nanoparticles as an example, the van der Waals force is much stronger than the repulsive force, so the van der Waals force dominates the interaction and leads to rapid agglomeration and sedimentation [42].

Eventually, the smaller value of net potential energy is subtracted from the larger value to get the total interaction. At very small distance, there is a deep attractive well overpowering the repulsive forces, which is referred to the minimum value. As the distance increases, the energy profile will pass through a maximum energy barrier, in which the repulsion is in turn greater than attraction. At this point, unless the particles have enough thermal energy to overcome this obstacle, they will remain dispersed. The height of this potential energy barrier can be indicated by the magnitude of the zeta potential which is the potential difference between the mobile dispersion medium and the stationary layer of the dispersion medium attached to the dispersed particle [97].

## 2.4 Nanomaterials with antimicrobial activity

Bulk and powder metals with antimicrobial activities such as Ag, Cu, CuO and ZnO have been known to inhibit microorganisms at low concentrations since ancient times [98]. For example, ancient Persian used vessels made of Cu and Ag for water disinfection and food preservation [5]. Although the Greek, Romans and Egyptians subsequently continued to contact and used this method for a long time, the effect was not entirely desirable.

Until recent years, artificial nanoparticles have been engineered, which in turn increased their functionalities and with enhanced properties compared to traditional bulk materials [8]. Generally, smaller size nanoparticles are expected to have a stronger antibacterial effect,

which is mainly due to their large area of exposure to volume ratio. For instance, recent antimicrobial nanoparticle (AMNP) formulations were developed by Ren *et. al.* It was claimed that this formulations contained Cu, Ag, and WC NPs and showed stable inhibitions (99.99%) against various deadly pathogens, such as *S. aureus* and *P. aeruginosa* [99].

### 2.4.1 Assessment of nanoparticles with antimicrobial activities

Currently, as pathogens become multi-drug resistant and antibiotics are often found to be inactive against certain superbugs, there is an increasing demand on disinfection and decontamination processes for healthcare. In particular, metallic nanoparticles were found to perform strong antimicrobial effects without harming mammalian cell [99, 100]. In this project, 11 different nanomaterials and formulations were tested against Gram-positive *Staphylococcus aureus* (*S. aureus*) and Gram-negative *Pseudomonas aeruginosa* (*P. aeruginosa*) bacteria, please refer to Chapter 5 for the corresponding results. This antimicrobial assessment was performed by collaborative partners at UCL using the following methods:

(1) Plate count method is one of the most common method. Viable bacterial cell concentrations are estimated by counting colony forming units (CFUs) before and after exposure to nanoparticles. This is prepared by dilution a culture of bacteria and spreading it on an agar plate, then incubating the plate at 37°C for 24 hours and calculating the CFU [99]. This method is economical and simple to operate but time-consuming and labour intensive.

(2) Flow cytometry is one method that uses fluorescent marker where bacteria cells are stained and their membranes are penetrated [101]. After incubation, the populations of live and/or dead bacteria are distinguished by different fluorescent channels. Although this method can rapidly distinguish bacterial viability, the challenges of flow cytometry are relatively large investment, complicated training and unavailable for determining species of bacteria.

(3) Quantitative polymerase chain reaction (qPCR) is one of molecular methods that are also commonly used. This method does not require the culturing of bacteria because it can offer specific target genomic material present within a sample [102]. A viability polymerase chain reaction assay is used to differentiate between live and dead cells by eliminating free DNA.

The research, published by UCL, determined that flow cytometry could be one of the best methods to evaluate antimicrobial efficacies of heterogenous metallic nanoparticles in suspension, as it can reliably quantify live and dead cells without being disturbed by the presence of nanoparticles [99]

### 2.4.2 Silver nanoparticles

Silver has been long known to have antibacterial properties and silver nanoparticles (Ag NPs) have also been widely applied in the various fields such as dental cares, pharmaceutical and biomedical industries due to their low toxicity and high efficiency [103]. The average diameter of 5 nm Ag NPs with a concentration greater than 75 μg/mL performed a growth inhibition effect on many Gram-negative bacteria species including *E. coli*, *Vibrio cholerae* (*V. cholerae*), *Salmonella typhi* (*S. typhi*), and *P. aeruginosa* at approximately $5 \times 10^7$ CFU/mL [104]. The authors hypothesised several mechanisms of Ag NPs that may lead to the antimicrobial effect. First of all, Ag NPs can destroy the metabolic activity of cells and cause membrane damage to bacterial cells, which both trigger the generation of reactive oxygen species (ROS) and DNA damage [105], as displayed in **Figure 2.8**. According to literature [106], Ag NPs can also induce pits and gaps on the bacterial membrane which further accumulate more Ag NPs and format free radicals causing cell death. Finally, the release of Ag ions is also considered as the main bactericidal mechanism which interact with $-S_2$ or -SH groups of enzymes, leading to disrupt cellular metabolic processes [107, 108].

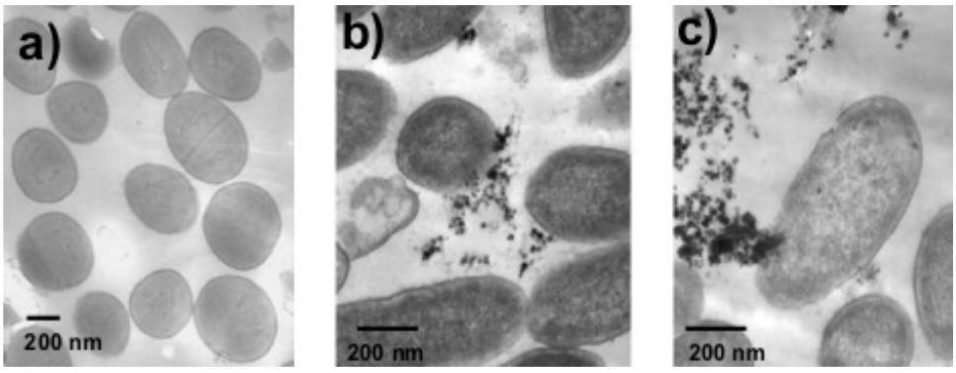


**Figure 2.8** TEM images of *P. aeruginosa* bacteria at different magnifications. (a) Control sample without Ag NPs; (b) and (c) samples that were previously treated with Ag NPs [104].In microbiology, the minimum inhibitory concentration (MIC) is the lowest concentration of antimicrobial agents (nanoparticles) that inhibit the growth of a microorganism. In a determination study using Ag NPs to reducing bacteria growth, approximately $10^5$ CFU of *E. coli* were cultured on agar plates. The Ag NP solutions with a diameter of 12.4 nm and a concentration of 10 μg/mL inhibited bacterial growth by 70%, while the Ag NP solutions at a

concentration of 50 - 60 µg/mL completely inhibited the growth of *E. coli* [106]. A study of Ag NP suspensions showed that they directly inhibited the surface of bacteria in *vitro* investigation [109]. It was found that the MIC for *E. coli* was approximately 3.3 nM, while the MIC for *S. aureus* was more than 10 times of the former. In a separate experiment, Pal *et. al.* (2007) investigated the antibacterial activities related to the shape of Ag NPs [110]. They suggested that compared with spherical and rod-shaped Ag NPs, triangular nanoparticles showed the strongest bactericidal activities in reducing the viability of *E. coli* due to their high-atom-density surfaces, and with Ag ions in form of $AgNO_3$. The colony was almost completely inhibited by 1 µg of triangular Ag NPs, and more than 12.5 µg and 50 µg of spherical nanoparticles can, respectively, significantly and totally inhibited the growth of bacteria. Even 100 µg of rod-shaped Ag NPs and $AgNO_3$ were unable to achieve the same effect.

Another study concerned the size- and shape-dependent antimicrobial activities proved that the smaller size of Ag NPs had better antimicrobial performance against Gram-positive including *Staphylococcus epidermidis* (*S. epidermidis*) and *Bacillus megaterium* (*B. megaterium)*, Gram-negative bacteria (*P. aeruginosa*) and fungal strains including *Candida albicans* (*C. albicans*) and *Aspergillus niger* (*A. niger*) [111]. The authors concluded that Ag NPs were potentially applied in clinical wound dressing, bio-adhesives, biofilms and the coating of biomedical materials.

### 2.4.3 Copper and copper oxide nanoparticles

Although copper (Cu) is an essential trace element in most organisms, excessive concentrations of exogenous Cu can be toxic as well [112]. In addition, Cu NPs have lower economical cost and wider inhibition range than Ag [113, 114]. Currently, three widely recognized antimicrobial mechanisms of Cu have been proposed amongst other minor mechanisms. First, Cu (as well as Fe and Zn) ions have the catalytic activity for ROS production by the Fenton and Haber-Weiss Reaction:

$$Cu^{+} + H_2O_2 + O_2^{-} \rightarrow O_2 + Cu^{2+} + OH^{-} + OH^{*} \text{ (Haber-Weiss reaction)}$$

$$Cu^{+} + H_2O_2 \rightarrow Cu^{2+} + OH^{-} + OH^{*} \text{ (Fenton reaction)}$$

In the production of such ROS, hydroxyl radicals are formed to damage a range of cellular molecules, such as causing mutations in DNA [115].

$Cu^{+}$ or $Cu^{2+}$ ions are also easily to combine with S-, N- or O-containing functional groups to form organic complexes, resulting in defects in the conformational structure of nucleic acids

and proteins [113]. Alternatively, $Cu^{+}$ or $Cu^{2+}$ ions may inactivate essential cellular functions by forming complexes or replace non-Cu metal ions, leading to reduced cellular functions [112]. Taking the inhibition of *E. coli* as an example, excess Cu cause the decomposition of Fe-S clusters, which essentially exist in a family of dehydratase enzymes of *E. coli*, and eventually the dehydratases are unable to biosynthesize amino acid [116].

Another research demonstrated 100 nm of Cu NP suspensions with concentrations of 33.4 and 28.2 μg/mL can, respectively, reduce the populations of *E. coli* and *B. subtilis* by 90%, while complete inhibitions of both bacteria were more than 60 μg/mL [117]. The MIC of Cu NPs was determined using broth microdilution. The MIC of Cu NPs for *E. coli* and *S. aureus* were both 40 nM [118]. In another study, Usman *et. al.* (2013) stated Cu-chitosan NPs with a particle size of 2 to 350 nm can inhibit microorganisms including *S. aureus, B. subtilis, P. aeruginosa, Salmonella choleraesuis* (*S. choleraesuis*)*, and C. albicans* [119].

Although Cu NPs are easily oxidized into copper oxide nanoparticles (CuO NPs), they are still effectively against *Klebsiella pneumoniae* (*K. pneumoniae), P. aeruginosa, Salmonella paratyphi (S. paratyphi)* and *Shigella strains* in a similar way as Cu NPs [119]. For instance, Mahapatra *et. al.* (2008) stated CuO NPs can pass through the bacterial cell membrane and then damage the vital enzymes of bacteria to inhibit cells [120].

Similar to Cu NPs, higher concentrations of CuO NPs than Ag NPs are required and the antimicrobial effect increases with higher doses [114]. One evidence was from Ren *et. al.* (2008)*,* who prepared CuO NPs by thermal plasma (Tesima™) technology and then applied them along with Cu and Ag NPs against various bacteria for minimum bactericidal concentration (MBC) determination [37]. Approximately $5 \times 10^{7}$ CFU/mL of bacterial pathogens were added to the nanoparticle suspensions. The MBC of CuO for *S. aureus* (Golden) was 2,500 μg/mL, and the MBC of *E. coli* and *P. aeruginosa* were, respectively, 250 and 5,000 μg/mL. In contrast, all MBC values of Ag NPs against above bacteria were all 100 μg/mL.

With regards to MIC, Ahamed *et. al.* (2014) used a broth microdilution method with 96-well microtiter plate technique to determine the antimicrobial activities of 23 nm CuO NPs against various bacterial cells [121]. They indicated that the lowest MIC of CuO NPs (31.25 μg/mL) was for *E. coli* and *E. faecalis*, while the highest MIC (250 μg/mL) was for *K. pneumonia*. In another similar research, Azam *et. al.* (2012) confirmed that the inhibitory effect of CuO NPs was related to particle size, stability, and concentration after CuO NPs were prepared and

annealed at different temperatures [122]. They also synthesized CuO NPs with a minimum size of 20 nm to achieve an MIC value of 20 ± 3 μg/mL for *E. coli*, which was lower than the previous result of 23 nm CuO NPs.

### 2.4.4 Zinc oxide nanoparticles

Although zinc oxide nanoparticles (ZnO NPs) are nontoxic and compatible with human skin, they are highly toxic to a wide range of bacteria pathogens including *E.coli* and *S .aureus* [123, 124]. For example, Azam *et. al.* (2012) stated ZnO NPs achieved the most effective bactericidal activities among CuO and $Fe_2O_3$ against Gram-negative (*E. coli and P. aeruginosa*) and Gram-positive (*S. aureus* and *B. subtilis*) bacteria [125]. Yet, the detailed mechanisms of ZnO NPs are not fully understood. The possible mechanisms of ZnO are assumed as ion release, the generation of ROS, and accumulation of the particles on the bacteria surface, which need further investigation [126, 127]. For more explanation of ion release and ROS generation to kill bacteria, please refer to Section 5.4.3.

Typically, ZnO NPs are found to be more effective than micron-size ZnO particles. In a study, both sizes of ZnO particles with a fixed concentration of 20 μg/mL were carried out to inhibit *B. subtilis*, *E. coli*, and *P. fluorescens* [128]. It turned out that the nano-sized ZnO particles can totally inhibit all kinds of tested bacteria, while the micro-sized ZnO particles can only inhibit 50 to 100% of all tested bacteria species. Furthermore, in another antimicrobial study that ZnO NPs in direct contact with *E. coli*, Padmavathy *et. al.* (2008) prepared ZnO NPs with three different sizes (12, 45 and 2 μm). The ZnO suspension with 12 nm particles exhibited higher efficacy than the ZnO suspensions with other particle sizes under the same concentration [129]. The authors explained the greater the amount of nanopore particles, the higher the generation of active oxygen species and thus they kill bacteria more effectively. They also proposed both the abrasiveness and the surface oxygen species of ZnO NPs can enhance the antimicrobial effect.

### 2.4.5 Intermetallic compounds and composites

Although very limited antimicrobial studies have been performed using intermetallic compounds, Ag–Au alloy nanoparticles combined with penicillin G and piperacillin had been claimed to intensify antimicrobial effect against *S. aureus* [130]. The authors suggested that Ag–Au alloy nanoparticles can be potentially used as an adjuvant in combination therapy of antibiotics. A group from China (2016) demonstrated the Ti–Ni–Cu shape memory alloys simultaneously possessed excellent shape memory effects, cytocompatibility and antibacterial properties after adding Cu element [131]. Future application of this compound

included biomedical implants and devices that do not cause bacterial infections. A more recent work showed that the Pt-Ag nanoparticles remarkably enhanced multiple enzyme-mimic activities related to oxygen reduction reaction and exerted favourable antibacterial effects on *E. coli* and *S. aureus* [132]. The forthcoming work was related the controllable synthesis of high-quality nanoalloys to their novel catalytic properties for a variety of promising applications, including catalysts, biosensors, and biomedicine.

Regarding the mixture of metallic nanoparticle composites, one of major advantages is that they produce higher antimicrobial effect then single elemental nanoparticles. Miguel *et. al.* (2012) investigated the antimicrobial activities of six metal and metal oxide nanoparticles and their two composites [133]. Specifically, the mean value of MIC100 of ZnO and of Ag-ZnO composites were, respectively, 437.5 and less than 362.5 µg/ml; that of CuO and of Ag-CuO composites were, respectively, 312.5 and less than 237.5 µg/ml. Moreover, the used of these composites decreased the amount of individual element, which also reduced the cost of materials and diminished the potential of bacterial resistance.

In another study, Ag, Ag-Zn and Ag-Cu ionic mediums were incorporated into glasses in order to determine their ion release as well as antimicrobial activity, which were prepared from powder of nitrate salts [134]. The result of Ag ion release from single Ag showed an upward trend in the first three days and then the release rate tended to slow down until it remained constant. All dual-elemental incorporation samples with different ratios greatly reduced the amount of Ag ion release from the sample, while Cu and Zn elements in the corresponding samples were unchanged due the formation of oxide phases. In addition to this, pH variations of all solutions which the glass matrix was immersed in were stable. The antimicrobial results revealed that all glasses only containing Ag ions showed stronger efficacy than dual-elemental imparted samples against *E. coli*, *S. aureus* and *C. albicans* cells. However, the release of Ag ions beyond the safety limit may potentially be toxic to human cells and environment (see Section 2.4.9 for details), while the dual-elemental samples having both low ion release effect can not only avoid toxic side effect but also extend the duration of antimicrobial activity. This experiment further suggested that pH values were less relevant than ion release regarding antimicrobial efficacy.

### 2.4.6 Carbon-based nanomaterials

Carbon-based nanomaterials have been found to show the antimicrobial activity [135]. Literature showed that the size and surface area of carbon nanomaterials relate to the inactivation of the microorganisms. More precisely, smaller size or larger surface area of

carbon nanomaterials are more toxic to bacteria [136]. The major antimicrobial mechanism of carbon-based nanomaterials was presumed to damage bacteria membrane due to an oxidative stress. However, recent studies indicated the physical interaction with cell membrane are the primary reason [135].

Akhavan and Ghaderi (2010) investigated graphene and graphene oxide (GO) against *E. coli* and *S. aureus* bacteria as Gram-negative and Gram-positive models, respectively [137]. They claimed that the extremely sharp edges of the nano-walls directly contacted the cell membrane of the bacteria resulting in the effective bacterial inactivation. Moreover, the Gram-positive *S. aureus* was more vulnerable to the cell membrane damage caused by the nano-walls than the Gram-negative *E. coli* due to lacking the outer membrane.

Carbon nanotubes (CNTs) are allotropes of carbon with a cylindrical nanostructure which can directly contact with bacteria that affects their cellular membrane integrity, metabolic processes and morphology [136]. In addition, there are some studies indicated SWCNTs were more effective to inhibit bacteria than MWCNTs due to the size of carbon nanotubes, as displayed in **Figure 2.9**. Kang *et. al.* (2008) reported that SWCNTs could more efficiently penetrate the cell wall than MWCNTs due to a larger surface area of SWCNTs interaction better with the cell surface [136]. Arias and Yang (2009) prepared SWCNTs and MWCNTs with different surface groups against Gram-negative and Gram-positive bacteria [138]. The authors claimed that SWCNTs with surface groups of -OH and -COOH improved the antimicrobial activity while that of MWCNTs did not show significant improvement.

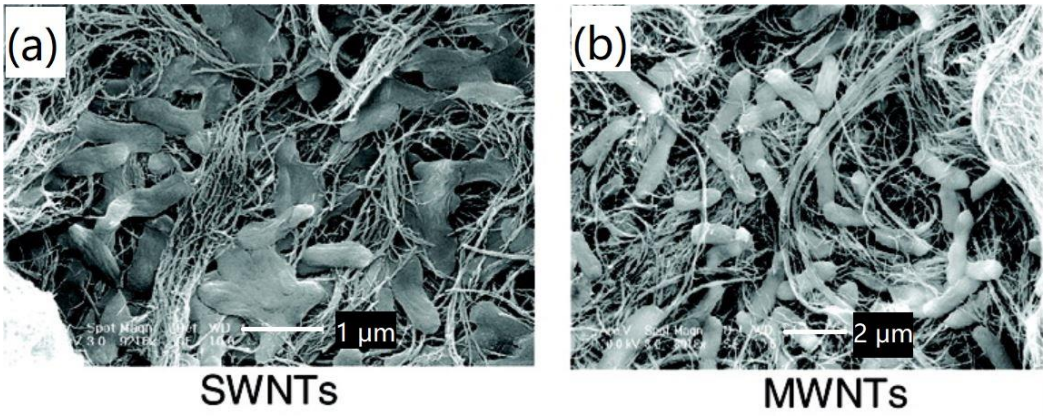


**Figure 2.9** SEM images of *E. coli* cells exposed to CNTs.
(a) Cells incubated with MWCNTs for 60 minutes. (b) Cells incubated with SWCNTs for 60 minutes. [136]. SWCNTs were more effective to inhibit bacteria than MWCNTs due to smaller size.

Carbon/metal nanocomposites also have been studying against both Gram-negative and Gram-positive bacteria. Yun *et. al.* (2013) investigated the antimicrobial activity of CNTs-Ag and GO-Ag nanocomposites [139]. According to Yun *et. al.*, CNTs-Ag nanocomposites had better antibacterial activity comparing to GO-Ag nanocomposites. The reason of this was that Ag NPs were expected to have a better dispersion into the CNTs.

2.4.7 Antimicrobial mechanisms of actions

**Table 2.3** Summary of nanoparticles that have been tested for antimicrobial activity.

| Monometallic / metal oxide nanoparticles | Mean size (shape) | Bacteria/fungi tested | Reference |
|---|---|---|---|
| **Silver (Ag)** | 21 nm (cuboctahedron icosahedron and decahedron) | *E. coli*<br>*V. cholerae*<br>*S. Typhi*<br>*P. aeruginosa* | [104] |
| | 12.4 nm | *E. coli* | [106] |
| | 13.5 nm (spherical) | *Yeast*<br>*E. coli*<br>*S. aureus* | [109] |
| | 39 nm (spherical); 16 nm (rod) | *E. coli* | [110] |
| | 1.5-10 nm (spherical, triangular and polyhedron) | *S. epidermidis*<br>*B. megaterium*<br>*P. aeruginosa*<br>*E. coli*<br>*C. albicans*<br>*A. niger* | [111] |
| **Copper (Cu)** | 100 nm (spherical) | *E. coli*<br>*B. subtilis* | [117] |
| | 9 nm (quasi-sphere) | *E. coli*<br>*S. aureus* | [140] |
| | 2-350 nm | *S. aureus*<br>*B. subtilis*<br>*P. aeruginosa*<br>*S. choleraesuis*<br>*C. albicans* | [119] |
| **Copper (Cu)** | 80-160 nm | *K. pneumoniae*<br>*P. aeruginosa*<br>*S. paratyphi*<br>*Shigella* | [120] |
| **Copper oxide (CuO)** | 20–95 nm (rod and rectangle) | EMRSA<br>MRSA<br>*S. aureus*<br>*S. sepidermidis*<br>*E. coli*<br>*Proteus spp.*<br>*P. aeruginosa* | [37] |
| | 23 nm | *E. coli*<br>*E. faecalis*<br>*K. pneumonia* | [121] |
| | 20-28.9 nm | *E. coli*<br>*P. aeruginosa*<br>*B. subtilis*<br>*S. aureus* | [122] |

| | | | |
|---|---|---|---|
| **Zinc oxide (ZnO)** | 20 nm | *E. coli*<br>*P. aeruginosa*<br>*S. aureus*<br>*B. subtilis* | [125] |
| | 20 nm | *B. subtilis*<br>*E. coli*<br>*P. fluorescens* | [128] |
| | 20-40 nm | *E. coli* | [129] |
| **Intermetallic nanoparticles** | **Mean size (nm)** | **Bacteria/fungi tested** | **Reference** |
| **Silver-Gold alloy (Ag-Au)** | < 200 nm (spherical) | *S. aureus* | [130] |
| **Titanium-Nickel-Copper alloy (Ti-Ni-Cu)** | N/A | *S. aureus*<br>*E. coli* | [131] |
| **Platinum-Silver alloy (Pt-Ag)** | N/A | *E. coli*<br>*S. aureus* | [132] |

The antimicrobial properties of different nanomaterials that mentioned earlier are summarized in **Table 2.3**. Although nanomaterials in different forms (particles, ions, salt, *etc*.) have been used as antimicrobial agents, the exact mechanisms of antibacterial activities of metal/metal oxide are still to be investigated. In general, four proposed pathways were considered to trigger the bactericidal deactivations and a schematic diagram of these mechanisms is shown in **Figure 2.15**. The four mechanisms are as follow:

(1) Reactive oxygen species (ROS): typically, the redox-active essential metals in biomolecules act as catalytic cofactors when ROS are either generated or catalysed by cell enzymes. The presence of external metals intensifies the reactions and produce an excess of ROS which triggers oxidative stress and subsequently leads to cellular programmed death [141]. For certain metals such as Cu and Zn, an occurrence of Haber-Weiss reaction and Fenton reactions both increases the formation of ROS and stimulates the electron transport chain to eventually promote bacteria death through the catabolism of the carbon source and the generation of nicotinamide adenine dinucleotide [142].

(2) Dissolved metal ions: external metal ions are absorbed through the cell membrane and inhibit cellular function or enzyme activity by interacting with the functional groups of proteins and nucleic acids, eventually affecting the normal physiological processes [143].

(3) Physical interaction: Gram-positive and Gram-negative bacteria have different cell wall structures: Gram-negative bacteria are covered by a layer of thin peptidoglycan with an additional outer membrane including lipopolysaccharide and periplasm, while

Gram-positive bacteria only possess a thicker layer of peptidoglycan. Generally, Gram-negative bacteria are more vulnerable to the mechanism of action of nanoparticles since their wall structure may help the ions released from the nanoparticles enter the cell [144]. In addition, although both bacteria cell walls are dominated by negative charges, Gram-negative bacteria have a higher affinity for the positive ions due to electrostatic attraction. Please refer to Section 5.4.2 for more details.

(4) Internalization into cell: very tiny nanoparticles are likely to enter the cells *via* endocytosis [145]. Subsequently, the released nanoparticle ions are then up-taken in intracellular high concentrations, which can cause harmful oxidative stress.

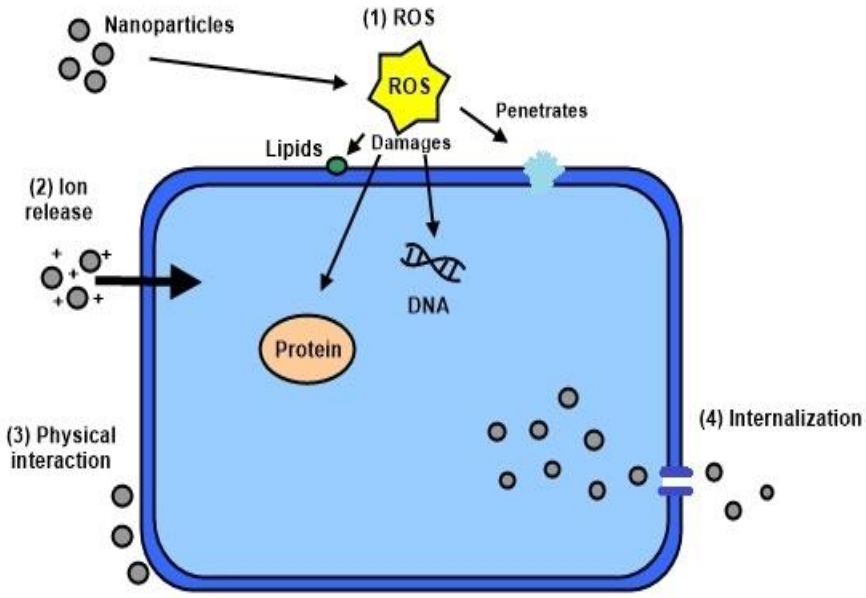


**Figure 2.10** Various antimicrobial activities of metal nanoparticles including: (1) reactive oxygen species (ROS) triggers oxidative stress; (2) dissolved metal ions interacts with the functional groups of proteins and nucleic acids; (3) physical interaction destroys cell walls; (4) internalization into cell *via* endocytosis [103].

### 2.4.8 Utilizations of metallic nanoparticles and their pathways to antimicrobial actions

At present, metallic nanoparticles have been extensively applied in consumer, health-related and industrial products [146]. **Table 2.4** summarizes the proposed mechanism and influencing factors of these metal nanoparticles. As one of the mostly investigated and

explored antimicrobial agents, Ag NPs can be prepared and used in the Ag nanocomposite fibers of textile fabrics. The fiber can have high antibacterial activities against *E. coli* and *K. pneumoniae*. A study from Yeo *et. al.* (2003) suggested that two spun fibers of the seven types of fibers which contained Ag NPs in the sheath-part with a concentration of 0.3 and 1.5 wt%, respectively, both inhibiting 99.9% of *E. coli* and *K. pneumoniae* [147]. In another study, Farkas *et. al.* (2011) assessed the wastewater from a commercially available Ag nano-washing machine using ICP-MS, TEM and NTA [148]. The washing machine was installed an exchangeable Ag NP generating part to enhance the enrichment of the washing water with Ag in the solution supply device. The presence of Ag NPs was confirmed by ICP-MS and the size of nanoparticles was measured by TEM and NTA. The authors concluded that the wastewater showed a strong bactericidal effect on the natural bacterial community. More recently, Illangakoon *et. al.* (2017) polymer fibres embedded with hybrid nanoparticles (including Cu, Ag and W) using pressurised gyration, as displayed in **Figure 2.17** [149]. The antimicrobial study against *P. aeruginosa* showed the fibres loaded with the nanoparticles inhibited over 70% of bacteria, while pure fibres showed 35%. For other applications, $TiO_2$ NPs were used in cosmetics, which had strong antibacterial properties and removed odors, and ZnO NPs can be used in food systems or creams, lotions and ointments [146].

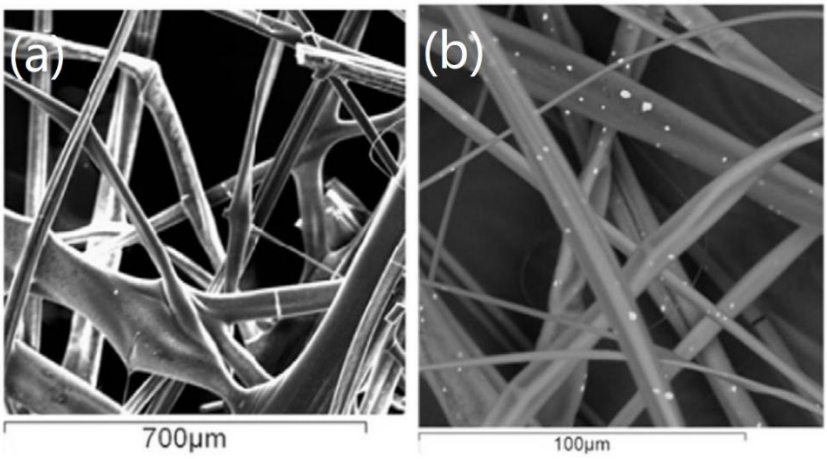


**Figure 2.11** SEM images of (a) PMMA fibre alone and (b) antimicrobial NPs embedded PMMA fibre mats [149].

**Table 2.4** Summary of Ag, Cu, CuO, ZnO and carbon-based nanomaterials as antimicrobial agents.

| Nano-materials | Proposed mechanism of antimicrobial activity | Influencing factors | Reference |
|---|---|---|---|
| Ag | Disruption of cellular metabolic activity; induction of pits and gaps in the bacterial membrane; ion release. | Particle size and shape of particles. | [106-110] |
| Cu | Catalyst for hydroxyl radicals, forming organic complexes, binding in protein. | Particle size. | [114, 115, 117] |
| CuO | Crossing through the bacterial cell membrane and damaging the vital enzymes of bacteria. | Particle size and concentration. | [122] |
| ZnO | Ion release; the generation of $H_2O_2$ and ROS, and accumulation of the particles on the bacteria surface. | Particle size and concentration. | [128, 129] |
| Carbon-based | ROS and physical interaction | Material size and structure. | [137] |

2.4.9 Toxicity of nanoparticles

Despite nanotechnology has brought an enthusiastic and promising revolution in several fields. However, as a side effect, the emerging field of nanotechnology may also pose a number of harmful threats to human life and the possible adverse health effects appears to be a concern.

Due to the smaller size of nanoparticles, they may enter the human body more easily and eventually damage organs [150]. Inhalation of nanoparticles is considered to be one of the most common routes of human exposure. Nanoparticles smaller than 10 nm act like gas and can enter the human nose, mouth and throat, while ultrafine particles can even reach the bronchial tree and then transfer to other different organs [151, 152]. Even exposure to low-toxic substances can still cause chronic inflammatory processes [153]. Additionally, permeation into the skin and ingestion through the digestive tract are other common routes of entry into the body. In a clinical report, an acute burn patient has been found liver malfunction because of treating nano-Ag coated medication [154]. Orally ingestion of Cu NPs in experimental mice had toxic effects on liver and kidneys [155].

In general, the toxicity of nanoparticles is influenced by size, shape, chemical composition and stability, *etc.* [153]. Due to the surface to volume ratio, particle size is inversely proportional to toxic effects. As can be seen above, the smaller the particles, the higher the toxicity. De Jong *et. al.* (2007) performed a kinetic study to determine the influence of particle size on the in *vivo* tissue distribution in the rat [156]. After intravenous injection of Au nanoparticles *in vivo*, the 10 nm nanoparticles were more widely found in different organs than larger nanoparticles. The shape also determined the toxic effects of nanoparticles. Similarly, it was found the needle-shaped and short rod-like nanoparticles are more effective than spherical and long-rod-like ones, which was consistent with the antibacterial properties [157]. Besides, it is noteworthy to point out that metallic can move more rapidly into the blood circulatory system in comparison to non-metallic species, thus they appear to be more toxic [152, 158].

Ultimately, much attention should be paid to balance the relationship between the properties of nanoparticles and toxicity, because nowadays daily supplies such as shampoo, toothpaste and cosmetics are increasingly produced based on nanotechnology, and therefore humans are more frequently exposed to nanoparticles.

## CHAPTER 3 CHARACTERISATION OF ENGINEERED AND COMMERCIAL NANOPARTICLES

### 3.1 Introduction

In order to select the nanomaterials with optimal antimicrobial effects, it is necessary to perform sophisticated characterisations of each nanoparticle to reveal their powder information, as the relevant physical and chemical properties of these ultra-small particles allow us to understand how each nanoparticle may attribute to the interactions and/or deactivations of specific microbes. A total of eleven commercial and engineered nanomaterials focusing on W, Ag, Cu and Zn were fully or partially investigated by SEM, XRD, FTIR, Raman spectroscopy and element analysis using ICP-IES, as summarized in **Table 3.1**. The details of nanomaterials are described in next section.

**Table 3.1** Investigation of physical and chemical properties of nanoparticles by different techniques.

The row in the white indicates commercial nanoparticles: “SA” stands for nanomaterials from Sigma-Aldrich; and “NF” stands for nanomaterials from Suzhou Canfuo Nano Technology. The row in grey show engineering nanoparticle: “QNA” stands for nanomaterials from Intrinsiq Materials® (formally Qinetiq Nanomaterials).

| Sample | SEM | XRD | FTIR | Raman | Elemental analysis |
|---|---|---|---|---|---|
| 1.SA WC | ● | | ● | ● | |
| 2.QNA WC | ● | | ● | ● | |
| 3.QNA Ag | ● | ● | ● | ● | ● |
| 4.NF Cu10 | ● | | ● | ● | ● |
| 5.QNA Cu | ● | | ● | ● | ● |
| 6.NF CuO | ● | ● | ● | ● | ● |
| 7.QNA CuO | ● | | ● | ● | ● |
| 8.CuAg | ● | ● | ● | ● | ● |
| 9.CuZn | ● | ● | ● | ● | ● |
| 10.AMNP2 | | | | | ● |
| 11.AMNP3 | | | | | ● |

Scanning electron microscope (SEM) was used to study surface morphology and dispersity, as well as to estimate sizes of each nano powder samples, because the size and shape of

powder nanoparticles influence their antimicrobial effects [110, 159, 160]. The nanoparticles are hoped to have a high surface area without agglomeration. X-ray powder diffraction (XRD) methods were used to investigate crystalline structure and reveal chemical composition information, which also helped us discover whether some samples contain additional compounds. Fourier-transform infrared spectroscopy (FTIR) and Raman spectroscopy were used to analyse metal/metal oxides bonds and/or other functional groups (e.g., -OH and -COOH), as well as to identify the present of any unexpected organic impurities.

For elemental metal trace analysis using inductively coupled plasma optical emission spectroscopy (ICP-OES), each nanomaterial was fully digested using microwave in concentrated nitric acid ($HNO_3$) and then diluted to the appropriate levels prior performing analysis in order to determine their purity. Fully quantitative method was used to measure the exact Ag, Cu and Zn ion concentrations present in each sample, while the presence of other unexpected trace metallic impurities was detected using semi-quantitative approach. (Please refer to Section 3.4.4 for more details).

## 3.2 Nanomaterials

### 3.2.0 General

All engineered and commercial nanoparticles were used as received and stored in a dark and well-ventilated cupboard. Manufacturing and engineering details of each nanomaterial and their composites are described in this section, whereas the corresponding SEM images can be found in Section 3.4.1. For ICP-OES analysis, the 2 v/v% $HNO_3$ was prepared using 70 v/v% $HNO_3$ (Sigma-Aldrich, Merck, UK) diluted in pure particle-free water (Acros, Belgium). Different ICP analytical standards (Ag, Cu and Zn) were purchased from (Sigma-Aldrich, Merck, UK) and were diluted into serial concentrations for calibration purpose (see Section 3.3.4 for more details).

### 3.2.1 Tungsten carbide

A nano-scale hexagonal tungsten carbide SA WC with a particle size of 150 - 200 nm and purity of more than 99% was purchased from Sigma-Aldrich (US). The tungsten carbide sample appeared as dark grey powder.

QNA WC was engineered by Intrinsiq Materials® (formally Qinetiq Nanomaterials) using the Tesima™ thermal plasma technology [161]. The elemental ratio of QNA WC were identified by using a combination of analytical techniques including Raman spectroscopy, XRD, 13C-NMR and XPS [162]. XRD confirmed QNA WC contained over 99.8% single phase of WC, the antiviral functions of QNA WC was firstly reported and patented in 2010 [163].

### 3.2.2 Silver

QNA Ag was engineered *via* the Tesima™ thermal plasma technology [161] provided by Intrinsiq Materials® (formally Qinetiq Nanomaterials). It appeared as golden-orange colour and had rod and needle-like particles with approximately 100 nm.

### 3.2.3 Copper and copper oxide

Two Cu NPs (QNA Cu and NF Cu10) with various particle shapes and sizes from different manufacturers were used in this study. QNA Cu was engineered by Intrinsiq Materials® (formally Qinetiq Nanomaterials) using patented technology called Tesima™ thermal plasma technology [161]. Commercial powder NF Cu10 was purchased from Suzhou Canfuo Nano Technology, it was claimed to have 10 - 30 nm particle size range and a spherical shape. Please refer to **Table 3.2** for the detailed specifications.

QNA CuO was engineered by Intrinsiq Materials® (formally Qinetiq Nanomaterials) using patented technology called Tesima™ thermal plasma technology [161], it was with a density of 6.3 - 6.49 g/cm$^3$ and size of 20 - 70 nm [164]. Commercial powder NF CuO rods was purchased from Suzhou Canfuo Nano Technology, it was claimed to have 40 - 60 nm particle size range and porous long-rod shape. Please refer to **Table 3.2** for the detailed specifications. Both CuO are deep brown or black powder.

**Table 3.2** Specifications of NF Cu and NF CuO NPs.

| Model | Purity (%) | Diameter (nm) | Average particle size (nm) | Shape | Specific surface area ($m^2/g$) | Density ($g/cm^3$) |
|---|---|---|---|---|---|---|
| NF Cu | 99.9+ | 10-30 | 20 | Spherical | 10-35 | 0.1-0.3 |
| Model | Purity (%) | Diameter (nm) | Length (μm) | Shape | Specific surface area ($m^2/g$) | Density ($g/cm^3$) |
| NF CuO | 99.9+ | 40-60 | 1-2 | Porous nanorods | 20-60 | 0.1-0.5 |

### 3.2.4 CuAg and CuZn alloys

The commercial alloy nanoparticles CuAg and CuZn were purchased from Sigma-Aldrich (Dorset, UK). The CuAg nanoparticle was less than 100 nm in particle size range and containing 96% - 98% of Ag. The CuZn nanoparticle appeared as a dark brown powder with less than 150 nm particle size range containing 56% - 60% of Cu and 37% - 41% of Zn. These alloy nanoparticles were further analysed using SEM, XRD, FTIT, Raman.

### 3.2.5 Antimicrobial nanoparticle formulations (AMNPs)

AMNP2 was previously engineered by the Antiviral Consortium found by the UK Department of Trade and Industry (DTI) and Southeast England Development Agency (SEEDA). AMNP2 nanoparticles were produced by Intrinsiq Materials® (formally Qinetiq Nanomaterials) using patented method, the Tesima™ thermal plasma technology [161]. A previous report concluded that the atomic ratio of AMNP2 was 77.7% C, 5.5% O, 6.7% W, 4.7% Ag and 5.4% Cu [165].

AMNP3 consists of 55:45 ratio of NF CuO rods and CuZn which was developed through the UH-UCL collaborative project[1]. This formulation was developed based on the analytical results obtained from the study in this chapter. Although data remain unpublished, AMNP3 was found to be the most effective formulation against both *P. aeruginosa* and *S. aureus*.

[1] EPSRC project (EP/N034368/1) 'Antimicrobial filters for hospital air and water systems'

3.3 Instrumentation and methodology.

3.2.1 Scanning electron microscope (SEM)

Each nanoparticle (2 mg) was secured onto a carbon-based adhesive substrate and positioned on a specimen stage, all samples were sputter-coated with 20 nm of Au under low pressure argon using an Emitech SC7620 (Quorum Technologies, Ltd., East Sussex, UK). All SEM analyses were acquired using a JEOL JCM-5700 (JEOL Ltd., Welwyn Garden City, UK) instrument and images were collected using the built-in software with an accelerating voltage of 20 kV. Adobe® Lightroom CC was used to improve contrast and quality of images.

3.2.2 X-ray diffraction (XRD)

XRD analyses were performed using a Panalytical X'Pert Pro diffractometer (Panalytical, Almelo, Netherlands). This instrument was equipped with a X'Celerator solid state detector where Cu Kα was used as the radiation source with 0.25° divergence slits. The samples were mounted on zero background silicon single crystal substrates. Data were collected from 5 to 120° 2θ in steps of 0.033° and a counting time of 200 seconds equivalent was used at each point. All data sets were analysed using the HighScore program (Panalytical B.V.2012 version 3.0.5) and all visible XRD patterns were supported by matching ICDD (previously called JCPDS) references.

3.2.3 Fourier transform Infrared and Raman spectroscopy

Infrared spectra of nanoparticles were acquired using a PerkinElmer Frontier FT-IR/FIR spectrometer equipped with an Attenuated Total Reflectance (ATR) accessory. Powder samples were loaded directly onto the diamond crystal stage and secured by a compressor rod. Blanks were performed prior to each sample submission; all data were acquired at a resolution of 64 $cm^{-1}$ using built-in software 'IRWinLab' and 256 scans were collected.

Raman spectra of nanoparticles were obtained utilising a Renishaw InVia Raman microscope and associated WiRE 3.4 software. All measurements were performed by means of the 785 nm excitation wavelength and a 2-mW power laser. Powder samples were presented on a microscope slide with an approximate examined area of 20 x 20 $\mu m^2$ and each measurement was taken after an average of 20 scans. Data were further analysed using BioRed® program and all visible Raman shifts were studied against references supported by the database within the program.

3.3.4 Inductively coupled plasma optical emission spectrometry (ICP-OES)

The amount of dissolved metals in solution ($Cu^{+}$ or $Cu^{2+}$, $Ag^{+}$ or $Ag^{2+}$ and $Zn^{2+}$ ions) were detected and quantified using inductively coupled plasma optical emission spectrometry Varian 710 (Germany) fitted with a Seaspray nebuliser. 1.2 kW power, 15 L/min plasma flow, 1.5 L/min auxiliary flow and 180 kPa nebulizer pressure were set to this study. Calibration standards for each element were purchased from Sigma-Aldrich (Switzerland). The standards at concentration of 10,000 ppm of Cu, Ag and Zn were prepared at the following concentrations: 10, 5, 1, 0.5, 0.1 and 0.05 ppm. Three different emission wavelengths of each element were selected for detection: Cu(213.598 nm), Cu(324.754 nm), Cu(327,395 nm), Ag(241.318 nm), Ag(328,068 nm), Ag(338.289 nm), Zn(202.548 nm), Zn(206.200 nm) and Zn(213.857 nm). The limit of detection (LOD) and quantification (LOQ) were calculated for each wavelength by analysis of a 2 v/v% $HNO_3$ blank. All labware was acid washed overnight with 4M $HNO_3$ prepared from 70% $HNO_3$ (Fisher Scientific®, UK) and rinsed thoroughly with deionized water before use.

3.3.5 ICP-OES sample preparations: Elemental analysis

In order to determine elemental compositions and validate the qualities of different nanomaterials used in this study, each sample was fully digested in harsh condition prior to ICP-OES analysis. 50 mg of each nanoparticle (QNA Ag, NF Cu10, QNA Cu, NF CuO rods, QNA CuO, CuAg, CuZn, AMNP2 and AMNP3) was mixed in 5 mL of pure $HNO_3$ (99.999% purity, Sigma-Aldrich, UK) in a Teflon vessel. Each mixture was pre-digested by swirling tube for 20 - 30 minutes to ensure release of any gas or volatiles. After this, it was diluted into 50 mL. All caps were then well-secured in carousel jackets before placing rack of samples in a CEM microwave digester (1600 W, Mars 240/50 CEM™, USA). All samples were digested using the program illustrated in **Table 3.3** and then cooled to room temperature on completion.

**Table 3.3** Program of microwave digestion for elemental analysis.
Before digestion, each nanoparticle was mixed in pure $HNO_3$ and swirled in a tube for 20 - 30 min, followed by dilution.

| Stage | Energy (W) | Percent (%) | Ramp rate (℃/min) | Temperature (℃) | Hold time (min) |
|---|---|---|---|---|---|
| 1 | 400 | 100 | 5 | 100 | 5 |
| 2 | 400 | 100 | 5 | 110 | 10 |
| 3 | 400 | 100 | 10 | 150 | 25 |

0.5 mL of digested samples were further diluted using 45 mL of 2 v/v% $HNO_3$, all samples were filtered using 0.1 µm syringe filter (Millipore) prior subjected to ICP-OES analysis. Fully quantitative approach (*via* external calibration) was used to quantify the presence of Ag, Cu and Zn ions in each nanomaterial samples, whereas semi-quantitative method (*via* external calibration) was used to estimate approximate concentrations of trace metals present as impurities (see **Table 3.4** for results). Both approaches were measured in triplicates.

## 3.4 Results and discussion

### 3.4.1 Morphological and physical properties of the nanomaterials

The surface morphology of each nano samples was studied using scanning electron microscopy (SEM), this technique was used to study the shapes and to estimate sizes of these particles.

**Figure 3.1a** and **3.1b** show the SEM images of commercial SA WC and engineered QNA WC nanoparticles. They were both hexagonal, quite uniformly distributed and are both agglomerated, because the high surface energy causes these smaller nanoparticles more likely to aggregate. The size of nanoparticle is one of main factors influencing the antibacterial activity [136, 159]. Generally, smaller particles have a larger antimicrobial effect due to larger specific surface areas, the bacterial cell membrane is thus more likely to contact with nanoparticles [159].

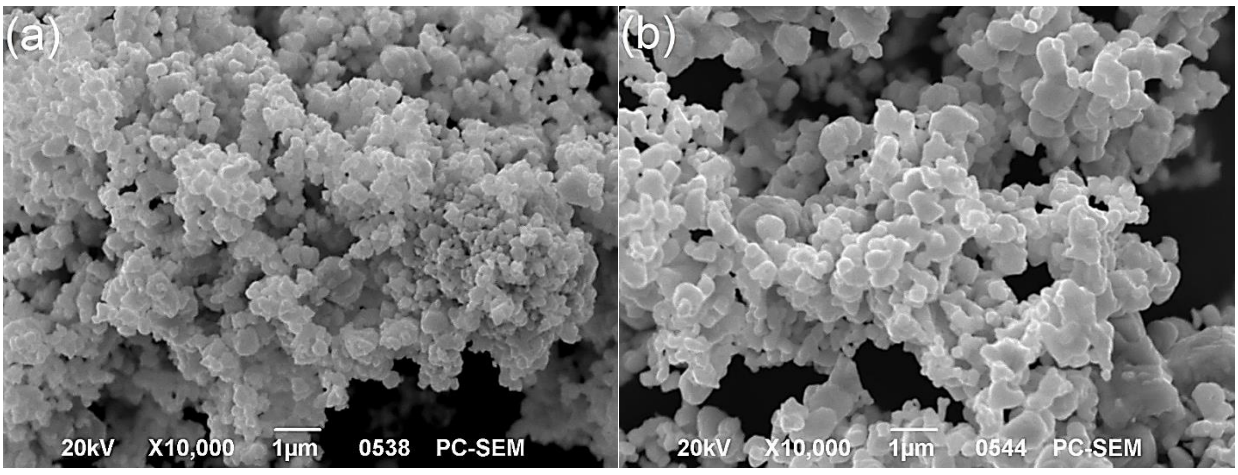


**Figure 3.1** SEM images of (a) commercial SA WC and (b) engineered QNA WC. Both engineered and commercial samples were hexagonal, quite uniformly distributed but agglomerated.

In **Figure 3.2**, a mixture of particle sizes can be seen in SEM images of the engineered QNA Ag, an approximate 100 nm sizes in irregular shapes such as needle-like and spherical shapes can be observed, which may contribute to antimicrobial activity. Many studies indicated that shape is another important factor in causing antimicrobial activity. In particular, nanoparticles with more tips or corners are “sharper” to kill bacteria in comparison of spherical and long-rod-like ones, this is not only because they are able to penetrate the cell member but also affect the specific surface area and reactivity [110, 160].

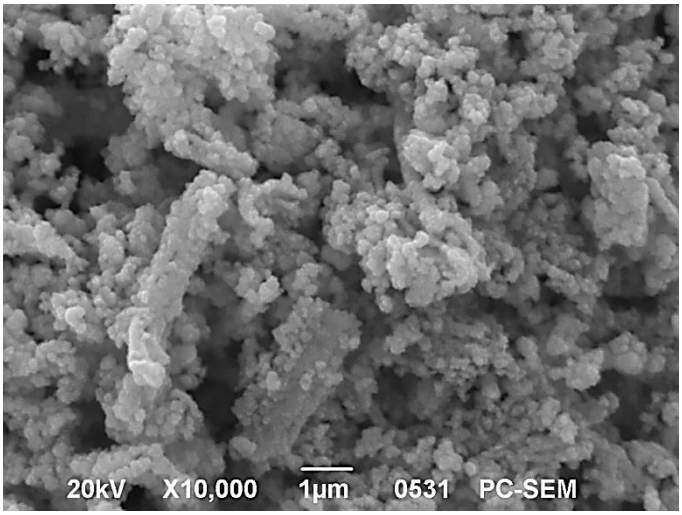


**Figure 3.2** SEM image of engineered QNA Ag.
It had a size of 100 nm and different shapes such as needle-like and spherical.

The SEM images of two different Cu nanomaterials, commercial NF Cu10 and engineered QNA Cu samples are presented in **Figure 3.3**. The image of NF Cu10 (**Figure 3.3a**) showed a mix shape of rod and rectangular. The majority of QNA Cu (**Figure 3.3b**) appeared to have cubical shapes within the nano-scale range, however large spherical micron-sized particles were observed as contaminant.

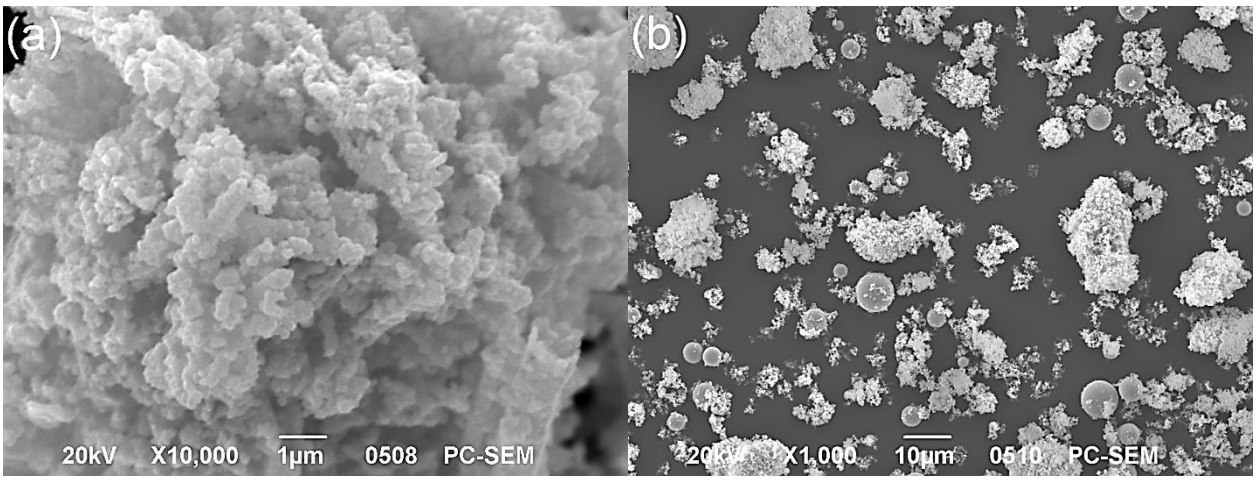


**Figure 3.3** SEM images of (a) commercial NF Cu10 and (b) engineered QNA Cu.
NF Cu10 had a mix shape of rod and rectangular, and QNA Cu NPs were mainly cubic in shape with a small amount of micron-sized spherical particles.

As shown in **Figure 3.4a**, the SEM image of CuO NPs indicated the commercial NF CuO rods NP had long-rod crystalline with approximately 40 - 50 nm diameter in one dimension, while the engineered QNA CuO displayed in **Figure 3.3b** was fluff-like and appeared as the finest nano spheres (approximately 10 nm) of all NPs in this study.

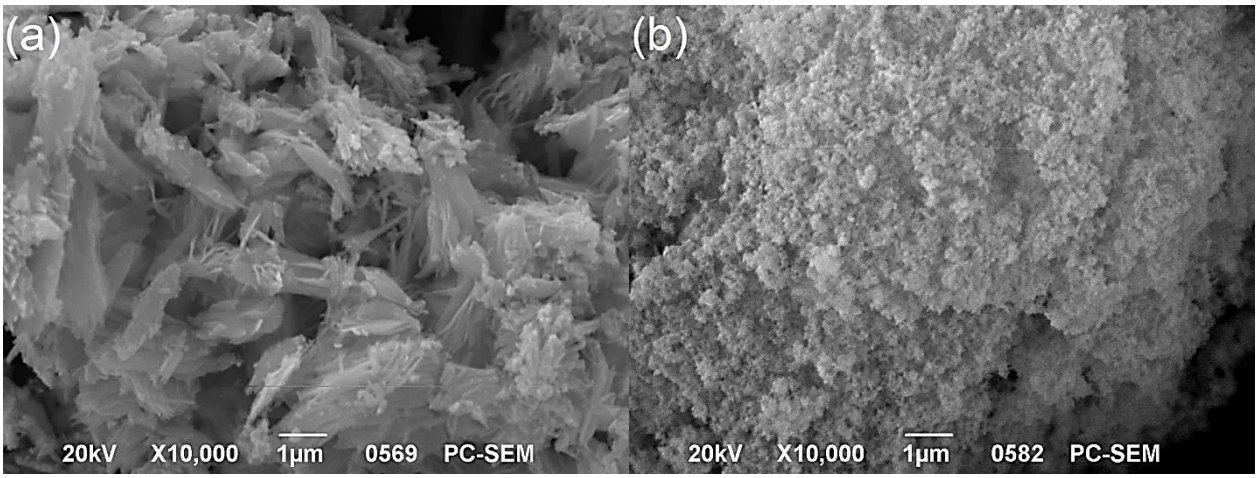


**Figure 3.4** SEM images of (a) commercial NF CuO rods and (b) engineered QNA CuO.
NF CuO had rod shape and a size of 40 - 50 nm, while QNA Cu was fluff-like and appeared as fine nano spheres with 10 nm in diameter.

SEM images of CuAg and CuZn alloys are, respectively, shown in **Figure 3.5a** and **3.5b**. These micrographs showed both alloys were spherical and aggregated, the particle size of

CuAg was ranging from 90 to 95 nm, which was smaller than that of CuZn (135 - 150 nm). It was also found that the morphology of CuAg was more uniform than that of CuZn.

In conclusion, various degrees of aggregations were visualized in this study due to the large surface area ratio to volume of nanoparticles. Heavy aggregations were observed in small sizes particles such as QNA CuO, CuAg and CuZn powders, suggesting that reduced reactive surface area may result in antimicrobial effect [166]. Most of our samples seem to be spherical or rod shapes. Further morphological observations (i.e., TEM) may help to examine in depth morphology of industrial particles.

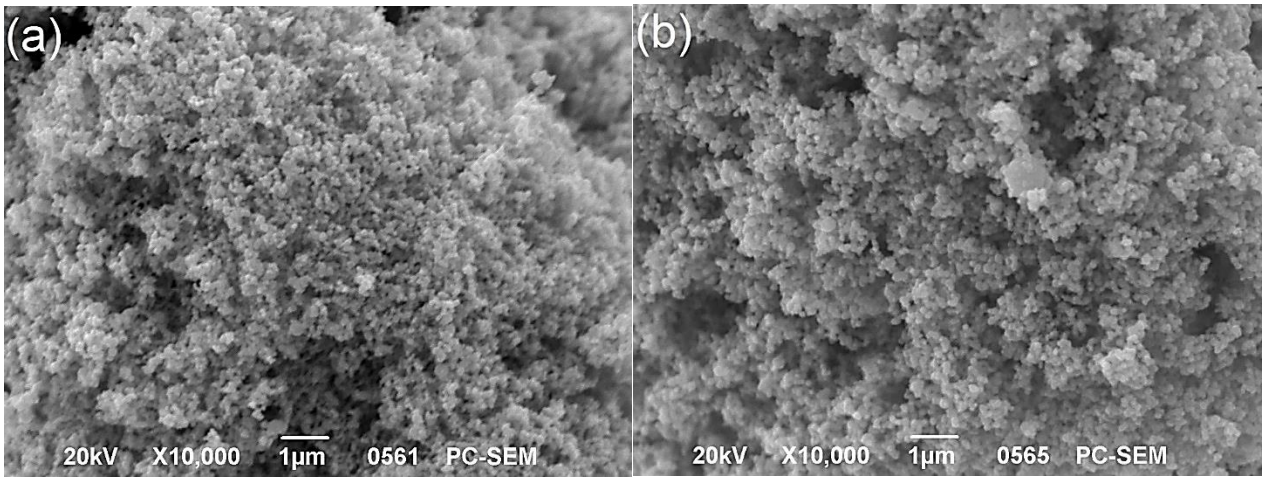


**Figure 3.5** SEM images of commercial (a) CuAg and (b) CuZn alloy NPs. Both of them were spherical and aggregated. CuAg had particle size ranging from 90 to 95 nm, while CuZn had particle size ranging from 135 to 150 nm.

### 3.4.2 XRD analyses

X-ray diffractometry is a rapid and powerful analytical technique primarily used for characterizing crystalline materials, which is based on Bragg's law [167]. According to the last section, four powders were further studied since QNA Ag had mixed particle sizes and QNA CuO, CuAg and CuZn were heavy aggregated. The XRD pattern of QNA Ag presents in **Figure 3.6.** The major XRD peaks of QNA Ag powder at 2θ of 37.71, 43.83, 63.71 and 76.47° correspond to (111), (200), (220) and (311) planes and further analysis comparing JCPDS (file no: 89-3722) indicated that QNA Ag contained not only elemental Ag but also $AgNO_2$ and $AgNO_3$, which were often the precursor used for synthesizing Ag NP from bottom-up method as previous discussed in Section 2.2.6 and 2.2.7. Ag was face-centred cubic crystalline and $AgNO_2$ and $AgNO_3$ were orthorhombic crystal structure [167].

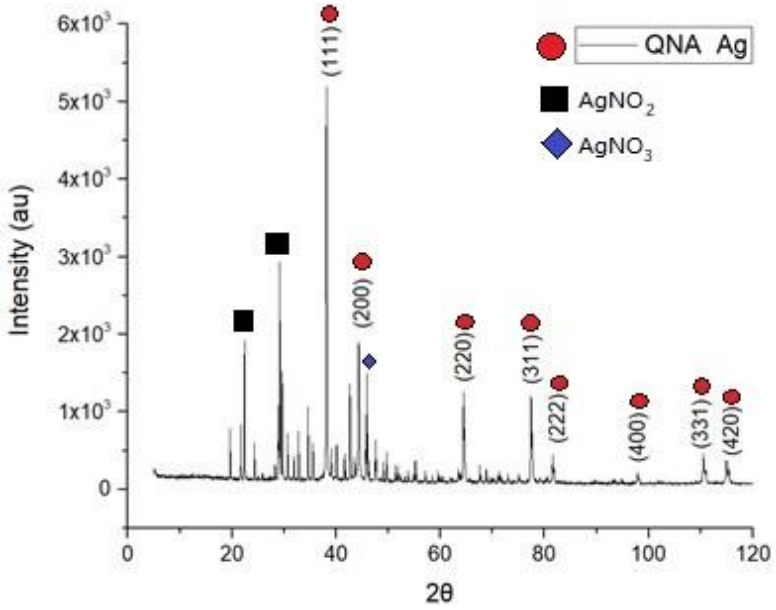


**Figure 3.6** XRD graph of engineered QNA Ag NPs.

The major XRD peaks at 2θ of 37.71, 43.83, 63.71 and 76.47° correspond to (111), (200), (220) and (311) planes, which indicated face-centred cubic structure of elemental Ag as well as orthorhombic structure of $AgNO_2$ and $AgNO_3$.

**Figure 3.7** shows two intense peaks of QNA CuO powder at 2θ values of 35.60 and 38.87° and a single unidentified peak at about 12.8°. The XRD has determined that the corresponding crystal system was monoclinic and CuO (Tenorite) was the only visible compound found in this engineered sample (JCPDS card no 45-0937).

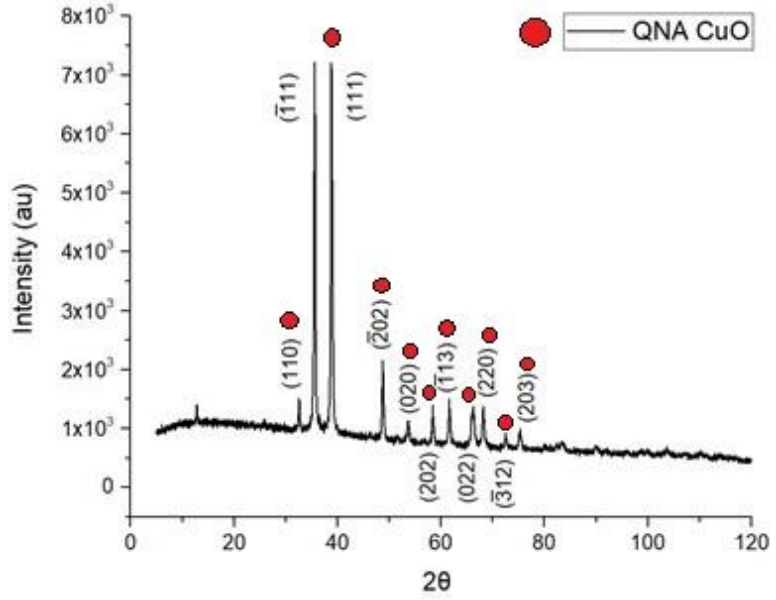


**Figure 3.7** XRD graph of engineered QNA CuO NPs with monoclinic structure. The peaks were located at 2θ values of 35.60 and 38.87° and a single unidentified peak at about 12.8°.

As shown in **Figure 3.8**, major peaks at 2θ = 38.1, 44.2, 64.4 and 77.8°was observed in the commercial CuAg powder, which were associated to elemental Ag. Another two tiny peaks positioned at 28.51 and 29.78° were corresponding to $Cu(OH)_2$ and $Cu_2O$, respectively. $Cu(OH)_2$ was found to have an orthorhombic crystal structure and the other two had cubic crystal structure.

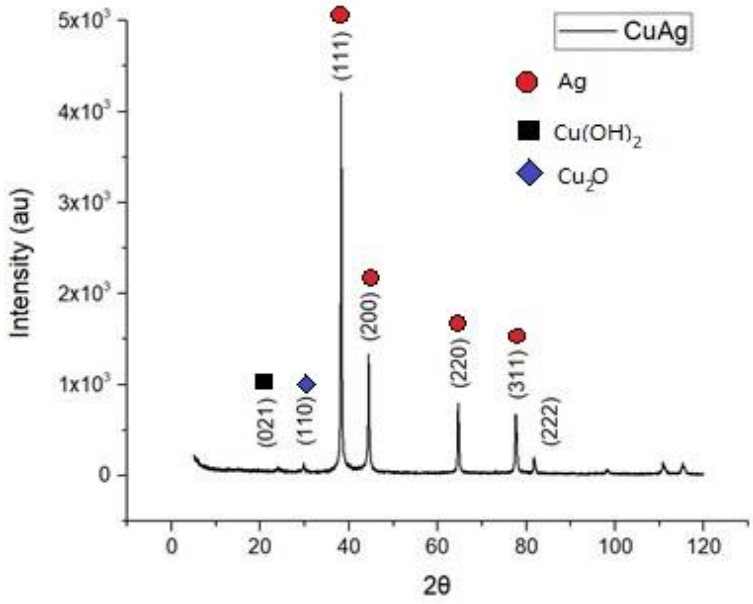


**Figure 3.8** XRD graph of commercial CuAg NPs containing cubic structure of elemental Ag and $Cu_2O$ as well as orthorhombic structure of $Cu(OH)_2$.
The peaks were located at 2θ values of 38.1, 44.2, 64.4 and 77.8° corresponding to elemental Ag.

In **Figure 3.9**, X-ray diffraction of commercial CuZn NP identified the presence of ZnO as well as intermetallic compounds $Cu_2Zn$ and CuZn. The diffraction peaks were located at 31.72, 34.53, 36.40, 47.40, 56.69, 63.27 and 67.58° corresponding to $(10\bar{1}0)$, (0002), $(10\bar{1}1)$, $(10\bar{1}2)$, $(11\bar{2}0)$, $(10\bar{1}3)$, and $(11\bar{2}2)$ reflection planes of hexagonal structure of ZnO. Moreover, the apparent ZnO found in this analysed sample may have been attributed by the oxidation of $Cu_2Zn$/ CuZn due to the large surface area ratio to volume of nanoparticles.

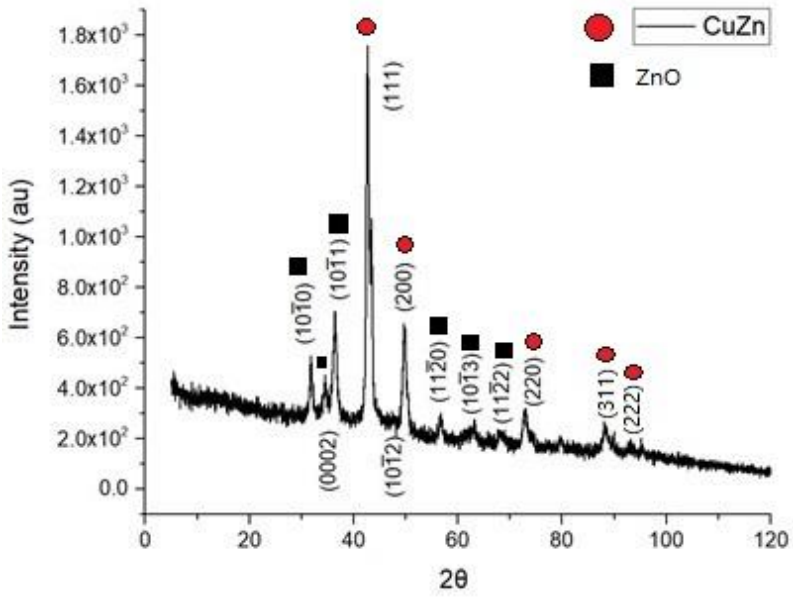


**Figure 3.9** XRD graph of commercial CuZn NPs.
It contained hexagonal structure of ZnO as well as body-centred cubic structure of $Cu_2Zn$ and CuZn.

In conclusion, engineered QNA Ag, QNA CuO, commercial CuAg and CuZn were investigated using XRD. The results demonstrated three of them consisted of unexpected components. QNA Ag contained possible un-reacted staring materials $AgNO_2$ and $AgNO_3$, CuAg alloy contained $Cu(OH)_2$ and $Cu_2O$, and intermetallic CuZn contained $Cu_2Zn$ and ZnO. QNA CuO by far showed to be the purest nanoparticle of all.

### 3.4.3 FTIR and Raman spectra of nanomaterials

FTIR and Raman spectroscopy are complementary techniques that are expected to identify various organic/inorganic components. Although all substances vibrate at temperatures above absolute zero, not all molecular vibrations will cause observable absorption. Recall that FTIR spectroscopy uses low energy radiation causing vibrational and rotational excitation of groups of atoms to absorb infrared energy. As a rule, a vibration must cause a change in dipole moment within a molecule to absorb infrared light [74]. Furthermore, the spectral region of infrared radiation from 4,000 to 1,500 $cm^{-1}$ is the functional group region, where the stretching vibration of a functional group usually exists. Absorption bands in 1,500 and 600 $cm^{-1}$ is often called the fingerprint region [168]. This region contains a very complicated series of absorptions so that it is difficult to identify individual bonds. Our samples are mostly composed of metallic bonds which are described as the sharing of free electrons among a lattice of positively charged ions by the electrostatic attractive force. Unlike organic compounds, the presence of metallic bonds with heavy atoms requires higher frequency source to produce molecular vibration/absorption, thus a majority of vibrational absorptions are expected to observe below 1,500 $cm^{-1}$ and this technique used in this study was to trace the presence of organic impurities.

In contrast to FTIR spectroscopy, Raman spectroscopy uses high energy to excite molecules to a higher energy state through the absorption of photon [74]. The energy must be equal to the energy difference between the two vibrational states. A change in polarizability during molecular vibration is an essential requirement to obtain Raman spectra of samples. The metallic bonding mostly does not always provide polarizability change and hence Raman in our case was used to trace the presence of impurities and oxidized components.

In this study, FTIR (red) and Raman (blue) spectra of commercial SA WC and engineered QNA WC samples are displayed in **Figure 3.10.** The results of FTIR analysis showed that there were peaks of the two WC NPs between 2260 and 2100 $cm^{-1}$, which may be related to -C=C- [169]. From Raman spectra, it was observed the O−W−O stretching mode, the W−O stretching mode, and the O−W−O bending mode were located at approximately 800, 710, and 270 $cm^{-1}$, respectively, which suggested the presence of monoclinic $WO_3$ structures in both samples [170].

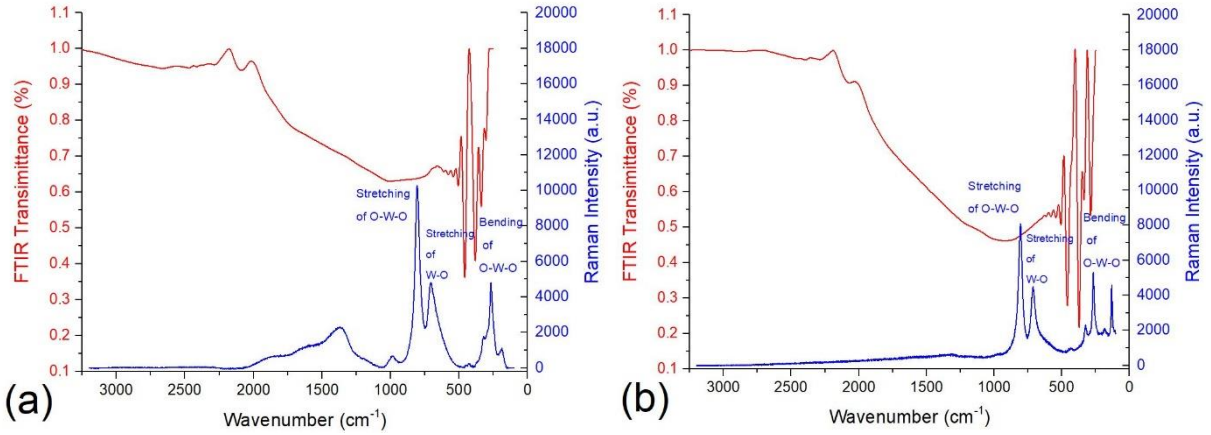


**Figure 3.10** FTIR and Raman spectra of (a) SA WC and (b) QNA WC.
Raman peaks showed the stretching of O−W−O, the stretching of W−O, and the bending of O−W−O, respectively, which confirmed the presence of monoclinic $WO_3$ structures.

FTIR and Raman spectra of engineered QNA Ag shown in **Figure 3.11**, normally FTIR vibration frequency of Ag–O is expected to appear at approximately 500 $cm^{-1}$ [171]. In this study, the QNA Ag sample only observed a weak intensity, which suggested the sample was well-preserved. Besides, according to previous literatures, functional organic groups (e.g., C-H) are normally observed more than 1,100 $cm^{-1}$ in FTIR spectra, which were not found in this case [70, 71]. Regarding Raman spectroscopy, a strong vibrational stretch observed slightly more than 1,000 $cm^{-1}$ was unidentified.

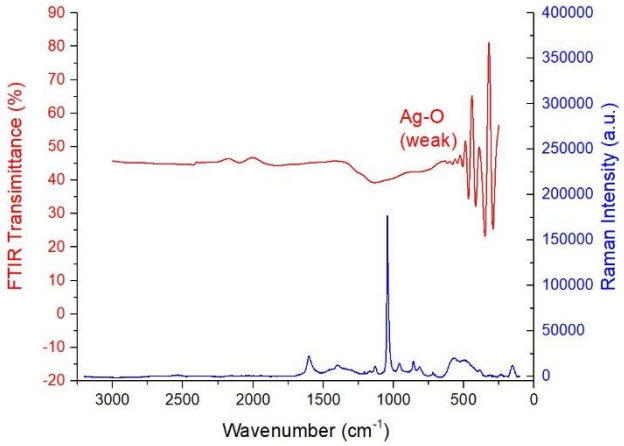


**Figure 3.11** FTIR and Raman spectra of QNA Ag.
For FTIR spectra, there was a weak vibration frequency of Ag–O at approximately 500 $cm^{-1}$, indicating well-preserved.

In **Figure 3.12**, FTIR spectra of commercial NF Cu10 and engineered QNA Cu NPs, vibrational mode of Cu-O displayed between 500 to 700 $cm^{-1}$ was not found in neither of the sample, which indicated good quality of both samples [171, 172]. For Raman spectra in **Figure 3.12b**, a strong vibrational stretch observed between 2,240 to 2,650 $cm^{-1}$ for QNA Cu indicated the presence of intermolecular hydrogen bonding indicating the sample was relatively damp.

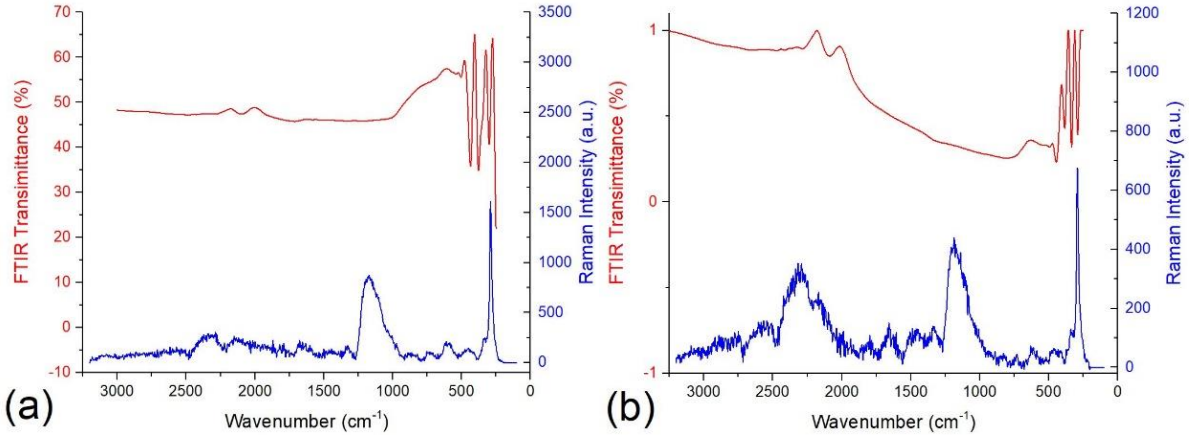


**Figure 3.12** FTIR and Raman spectra of (a) NF Cu10 and (b) QNA Cu.
For FTIR spectra, the vibration mode of Cu-O between 500 and 700 $cm^{-1}$ was not found in both samples, indicating good quality of both samples. Raman spectra found hydrogen bonding between 2,240 to 2,650 $cm^{-1}$ in engineered QNA Cu.

The FTIR and Raman spectra of commercial NF CuO rods and engineered QNA CuO NPs were acquired and shown in **Figure 3.13**. The FTIR analysis showed peaks for both CuO at approximately 480, 530, and 590 $cm^{-1}$ implied the vibrations of Cu-O [172]. For Raman spectra, both CuO samples also matched well with spectral profile signals resonated at approximately 260, 329.9, and 610.8 $cm^{-1}$ [173]. A heavily damp between 2,200 to 2,600 $cm^{-1}$ for QNA CuO can be observed as well in **Figure 3.13b**.

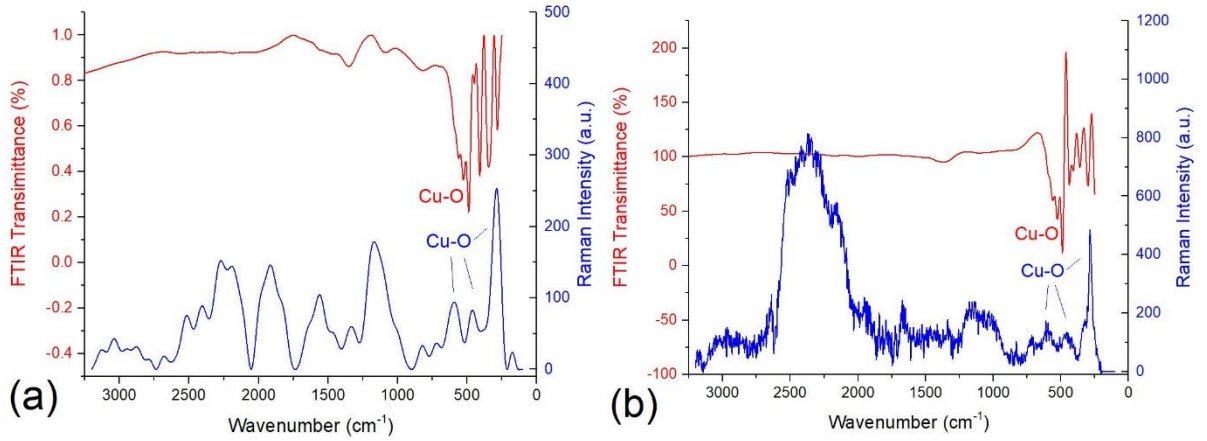


**Figure 3.13** FTIR and Raman spectra of (a) NF CuO rods and (b) QNA CuO.

The FTIR peaks for both CuO at approximately 480, 530, and 590 $cm^{-1}$ associated to the vibrations of Cu-O. For Raman spectra, both CuO samples also matched Cu-O peaks and QNA CuO had a damp signal between 2,200 to 2,600 $cm^{-1}$.

**Figure 3.14** shows both FTIR and Raman spectra of alloy nanoparticles CuAg and CuZn. For CuAg sample, there were two overlapping board Raman bands at 1,351.1 and 1,567.4 $cm^{-1}$. It is believed to be caused by the lack of spatial order in a solid-state lattice, as known as broadening effect [174]. Regarding CuZn, one sharp shift at 567.8 $cm^{-1}$ was observed in Figure **3.15b**. However, there is no discussion about CuZn or CuAg NP before, so this is the first reported absorption spectra.

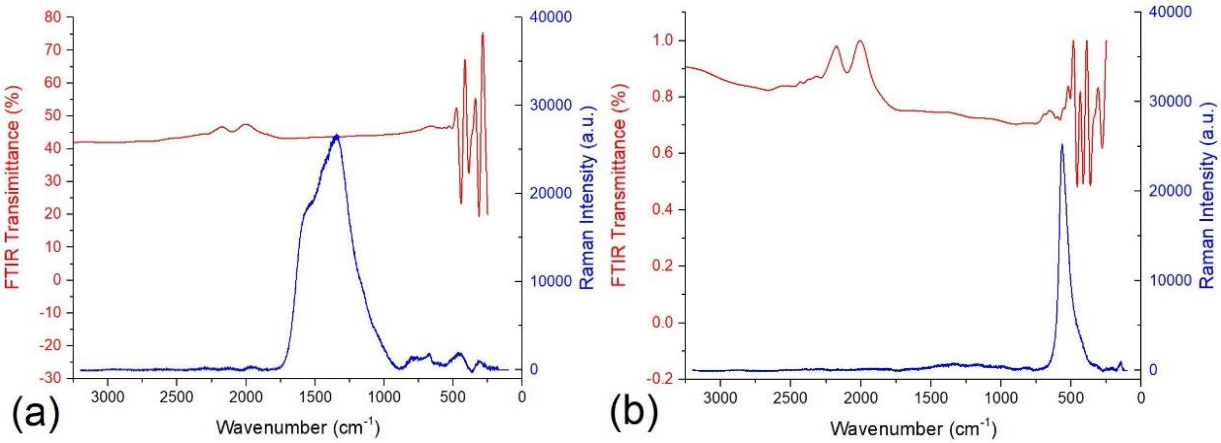


**Figure 3.14** FTIR and Raman spectra of (a) CuAg and (b) CuZn.

CuAg had two overlapping board Raman bands at 1,351.1 and 1,567.4 $cm^{-1}$ and CuZn had one sharp shift at 567.8 $cm^{-1}$.

To sum up, FTIR and Raman spectroscopy are complementary techniques that are commonly used for identification and characterization of functional groups in materials.

Raman spectra resulting from an inelastic Raman scattering process that occurs when light interacts with molecules whereas IR spectra result from light absorption by vibrating molecules [73]. Therefore, bands that are strong either in FTIR or Raman measurement tend to be weak in the other measurement. As both techniques are non-destructive and real-time analytical methods, the analysed samples could be further analysed with ICP-OES.

### 3.4.4 Elemental analysis using ICP-OES.

ICP-OES is an analytical technique widely used for the detection of chemical elements and the exact ionic concentrations of a material. This technique is based on producing excited atoms and detecting their specific wavelengths, which is known as emission spectrum.

In this study, nanomaterials were completely dissolved in concentrated nitric acid (70 v/v% $HNO_3$) prior to submission for ICP-OES analysis. For experimental details, please refer to Section 3.3.5.

There are two ways to determine presence of trace metals and their concentration for ICP-OES samples:

(1) Semi-quantitative approach: This method functions by correlating the count rates from a calibration curve and uses count rate/ppb calibration to determine concentrations for all elements in a sample, based upon their count rates. The aim of this approach is to trace and identify metal impurities.

(2) Fully quantitative approach: Different elemental standard solutions (Ag, Cu and Zn) in serial dilutions were prepared to generate the corresponding calibration curves resulting the best-of-fit straight-line formula (as shown below), which was used to calculate the relative ion concentrations detected from each analyte:

$$y = mx + c$$

This method provides ion concentrations of metallic elements within an order of magnitude to allow the desired metal ion type to be precisely quantified.

#### *3.4.4.1 Elemental analysis*

As shown in **Figure 3.15**, fully quantitative approach was applied to quantify Ag (red), Cu (blue) and Zn (black) in digested nanomaterial samples based on calibration standards. The

digested NF Cu10 had the highest $Cu^{+}$ or $Cu^{2+}$ ion concentrations, followed by NF CuO rods, QNA Cu, AMNP3, CuZn, AMNP2 and lastly by CuAg. The engineered QNA Ag accumulated higher $Ag^{+}$ or $Ag^{2+}$ ions than that of CuAg and AMNP2, while CuZn and AMNP3 were found to consist of $Zn^{2+}$ions concentrations as expected.

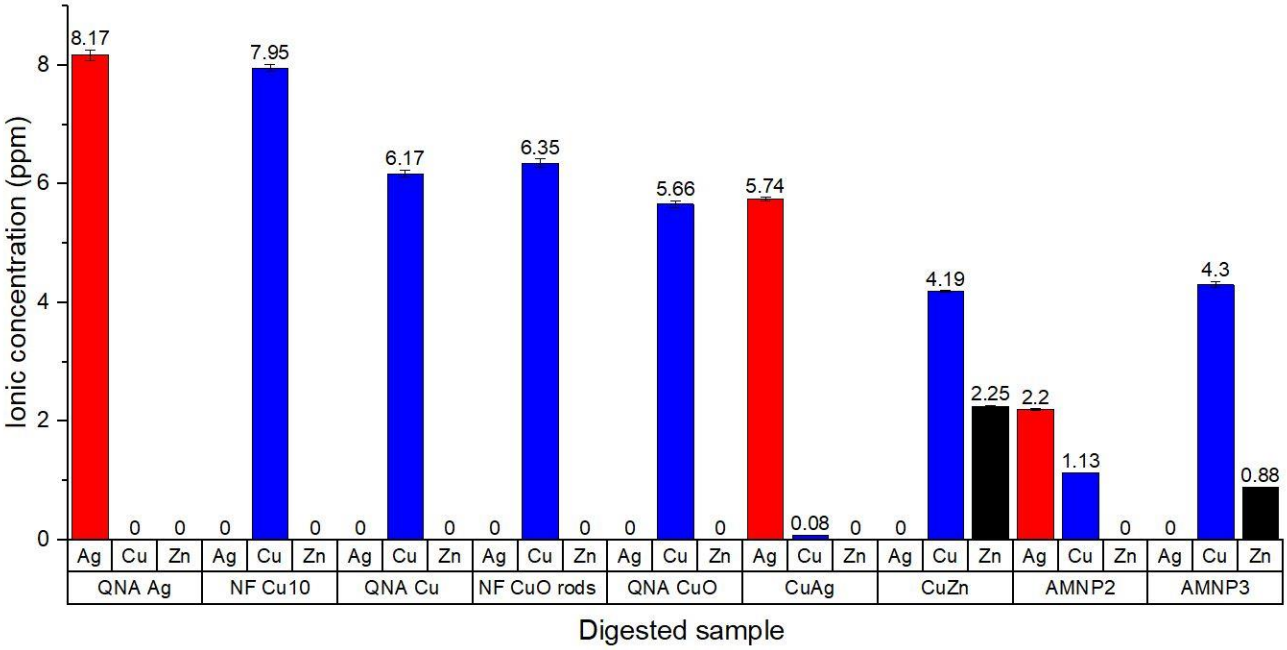


**Figure 3.15** Relative Ag, Cu and Zn ion concentrations (ppm) measured in different digested samples.

The order of $Cu^{+}$ or $Cu^{2+}$ ion concentrations found to be NF Cu10 > NF CuO rods > QNA Cu > AMNP3 > CuZn > AMNP2 > CuAg. The engineered QNA Ag had higher $Ag^{+}$ or $Ag^{2+}$ ions than that of CuAg and AMNP2. CuZn and AMNP3 both contained $Zn^{2+}$ions.

Other metallic elements were detected using semi-quantitative approach and the result of emission intensities from all samples is shown in **Table 3.4**. As can be seen, red values in the table are relative apparent emission intensities of minor metallic elements higher than that of blank ($HNO_3$), which may imply impurities from each sample. Particularly, a significant intensity of Al emission was found in QNA Ag. QNA Cu and CuAg were found extremely higher intensities of Fe and Mn, respectively. It is worth mentioning that element Al and Fe were proved to inhibit bacteria, which may suggest that the QNA materials had less purity, but some of minor elements may assist in killing bacteria [146, 175]. For element W, it was

found in CuZn, AMNP2, AMNP3. This is simply because AMNP3 was prepared from NF CuO rods and CuZn and WC was identified in AMNP2 in previous research [162].

**Table 3.4** Emission intensities of minor elements detected in different nanomaterials using ICP-OES.

Red values are relative apparent emission intensities of minor metallic elements higher than that of 2 v/v% $HNO_3$ blank.

| Emissions | Blank | QNA Ag | NF Cu10 | QNA Cu | NF CuO | QNA CuO | CuAg | CuZn | AMNP2 | AMNP3 |
|---|---|---|---|---|---|---|---|---|---|---|
| **Mo 202.032** | 9.3887 | 6.4669 | 6.69405 | 7.82629 | 6.81895 | 6.4595 | 8.6078 | 4.7898 | 6.6498 | 9.5393 |
| **Ni 231.604** | 19.485 | 19.0859 | 8.90448 | 15.7614 | 10.3632 | 20.0602 | 12.438 | 24.794 | 12.112 | 20.7285 |
| **Pb 220.353** | 8.4545 | 14.963 | 6.12876 | 12.9175 | 16.2924 | 24.6948 | 9.4807 | 14.562 | 14.463 | 10.1695 |
| **Mn 257.610** | 11.629 | 28.4004 | 18.129 | 15.675 | 14.8849 | 22.9168 | **114.29** | 20.801 | 34.752 | 27.6858 |
| **Cr 267.716** | 16.341 | 7.2839 | 16.776 | 22.9002 | 0.046997 | 10.356 | 22.64 | 9.4905 | 32.355 | 24.9204 |
| **Fe 238.204** | 84.45 | 114.873 | 66.6111 | **236.166** | 54.2125 | 82.5634 | 53.233 | 111.87 | 43.999 | 63.6879 |
| **K 766.491** | 2102.1 | 2645.12 | 2512.47 | 2468.73 | 2250.53 | 2680.66 | 2179.1 | 2209.5 | 2258.1 | 2269.83 |
| **Pd 340.458** | 38.878 | 29.329 | 22.8908 | 34.1883 | 29.2616 | 21.1519 | 21.417 | 46.901 | 23.644 | 36.6785 |
| **Ti 336.122** | 32.326 | 30.6169 | 18.0931 | 20.3711 | 45.0908 | 35.3024 | 18.552 | 26.001 | 39.612 | 24.2505 |
| **W 207.912** | 5.8183 | 8.91565 | 12.6726 | 9.19569 | 9.42575 | 8.89172 | 7.3034 | **35.896** | **37.043** | **19.2617** |
| **Ta 268.517** | 18.223 | 23.7138 | 24.186 | 20.6175 | 7.98385 | 19.4965 | 18.903 | 13.96 | 8.3515 | 14.8199 |
| **Pt 214.424** | 9.8209 | 10.9542 | 9.71245 | 5.33773 | 6.03434 | 11.0134 | 7.9179 | 7.0448 | 7.3935 | 15.7802 |
| **Sn 189.925** | 3.4677 | 2.70792 | 3.4493 | 3.39181 | 3.70747 | 2.86845 | 2.8405 | 6.118 | 4.2693 | 5.30681 |
| **Al 396.152** | 80.453 | **574.146** | 130.357 | 163.413 | 111.264 | 156.81 | 141.11 | 144.05 | 149.54 | 181.54 |
| **Ca 396.847** | 62137 | 61713 | 60066.6 | 70953.1 | 81708.9 | 56676.9 | 56016 | 55913 | 59247 | 64537.4 |
| **Au 242.794** | 13.957 | 17.5037 | 18.0914 | 4.59939 | 22.0007 | 19.2341 | 12.596 | 15.038 | 17.517 | 23.4824 |
| **Ba 455.403** | 236.42 | 322.169 | 294.812 | 451.801 | 282.854 | 245.589 | 229.96 | 259.27 | 258.25 | 277.881 |
| **Mg 279.553** | 2450.2 | 2526.91 | 2562.99 | 2784.97 | 3909.99 | 2486.92 | 2474.6 | 2494.7 | 2489.9 | 3080.48 |

### *3.4.4.2 Determining chemical formula of alloy nanoparticles.*

The microwave assist method was established to allow metal impurities completely traceable in without loss of the analyte during digestion process. As if such antimicrobial nanoparticle is to be used in healthcare or medical applications, it is important to investigate ion release effects produced by these potentially toxic materials. In other words, high level of metal ion release can inhibit the growth of bacterial but would also have a potential toxicity to mammals and living environments.

There were different chemical reactions and experimental phenomena happened to determine their reaction products when samples dissolve in $HNO_3$. During sample preparations, we observed productions of brown gas. As shown in equations below, $HNO_3$ reacted with certain metals and was reduced to give poisonous $NO_2$ whose gas is brown with an irritating odor. Alternatively, it may also produce NO as it is a colorless gas. In the case of Cu samples, such black nanoparticle had become a green solution after addition of concentrated $HNO_3$. This indicated that Cu(0) had been oxidized to give $Cu(NO_3)_2$ as $Cu^{2+}$ ions produce green colour.

Both Cu and CuO metals produced $Cu(NO_3)_2$ after reaction of $HNO_3$ digestion process as following:

$$For\ Cu\ NP \qquad 4\,HNO_3 + Cu \rightarrow Cu(NO_3)_2 + 2\,NO_2 + 2\,H_2O$$
$$For\ CuO\ NP \qquad CuO + 2\,HNO_3 \rightarrow Cu(NO_3)_2 + H_2O$$

Moreover, the reaction of Ag with $HNO_3$ produces $AgNO_3$, $NO_2$/NO and water. $Ag^+$ in $HNO_3$ may be electrolyzed to unstable $Ag^{2+}$. All reactions are as follows:

$$3Ag + 4\,HNO_3(cold\ and\ diluted) \rightarrow 3AgNO_3 + NO + 2H_2O$$
$$Ag + 2\,HNO_3(hot\ and\ concentrated) \rightarrow AgNO_3 + NO_2 + H_2O$$
$$2AgNO_3 + 3HNO_3 \rightarrow 2Ag(NO_3)_2 + HNO_2 + H_2O$$
$$Ag^{2+} + e^- \rightarrow Ag^+$$

For the reaction of Zn with $HNO_3$, the resulting product varies depending on acid concentrations – $NH_4NO_3$ is formed in concentrated $HNO_3$ as following:

$$Zn + 4HNO_3(60\%) \rightarrow Zn(NO_3)_2 + 2NO_2 + 2H_2O$$
$$3Zn + 8HNO_3(30\%) \rightarrow 3Zn(NO_3)_2 + 2NO + 4H_2O$$
$$4Zn + 10HNO_3(20\%) \rightarrow 4Zn(NO_3)_2 + 2N_2O + 5H_2O$$
$$5Zn + 12HNO_3(10\%) \rightarrow 5Zn(NO_3)_2 + N_2 + 6H_2O$$
$$4Zn + 10\,HNO_3(3\%) \rightarrow 4Zn(NO_3)_2 + NH_4NO_3 + 3\,H_2O$$

Ideally, samples with the same composition should contain equal number of elements such as NF Cu10 and QNA Cu as well as NF CuO rods and QNA CuO, but there were impurities from each sample and therefore digested samples performed differently. Theoretically, given 50 mg samples completely dissolving in 50 mL $HNO_3$ and further diluted 100 folds prior

analysis, the concentration of all digested samples is supposed to be 10 ppm. However, NF Cu10, QNA Cu, NF CuO rods and QNA CuO were found to be 7.95, 6.17, 6.35 and 5.66 ppm, respectively. Thus, this suggested that commercial NF Cu10 and NF CuO rods have higher purities than engineered QNA Cu and CuO, respectively.

Based on the result, it can be calculated that the elemental ratio of Cu and Ag for CuAg was 0.08:5.74. The weight percentage for Cu and Ag then can be computed as 1.4% and 98.6% as well as the molar ratio of Cu to Ag was 2:9.1. Similarly, the elemental ratio of Cu and Zn for CuZn was 4.19:2.33, the weight percentage of Cu and Zn were 65% and 35%, and the molar ratio of Cu to Zn was 1.23:0.54. Eventually, the formula for both nanoparticles then can be obtained - CuAg should be written as $Cu_1Ag_{42}$, and CuZn should be written as $Cu_{2.3}Zn_1$.

## 3.5 Summary

This chapter presented the characterization results of engineered and commercial nanoparticles using various instrumentation analytical technique. The features of this study include: (1) Two hexagonal WC NPs were both uniformly distributed; however, they were agglomerated. The corresponding FTIR and Raman spectra indicated the presence of monoclinic $WO_3$. (2) QNA Ag NPs were around 100 nm with irregular shapes that was observed *via* SEM. This was supported by corresponding XRD diffractogram showing multiple-crystal phases that contained elemental Ag, $AgNO_2$ and $AgNO_3$. (3) NF Cu10 NPs had a mixed shape of rod and rectangular, and QNA Cu NPs were mainly cubic in shape with a small amount of micron-sized spherical particles. The particle size of NF Cu10 NPs was very fine (10 - 30 nm) and was much smaller than engineered QNA Cu. (4) NF CuO rods NPs had long-rod crystalline with a particle size of approximately 40 - 50 nm, QNA CuO NPs were fluff-like with a particle size of approximately 10 nm. (5) Both CuAg and CuZn alloy NPs were spherical and have aggregation. It was confirmed that the particle size of CuAg was 90 - 95 nm, and the particle size of CuZn was 135 - 150 nm. XRD analysis found that CuAg alloy contained $Cu(OH)_2$ and $Cu_2O$ and CuZn as intermetallic compound contained $Cn_2Zn$ and ZnO. ICP experiments were carried out to successfully determine the purities of main elements (Ag, Cu and Zn) and the emission intensities of minor elements of samples after they were digested using microwave assist method. The formula for both alloy nanoparticles were therefore determined ($Cu_1Ag_{42}$ and $Cu_{2.3}Zn_1$).

## CHAPTER 4 PHYSIOCHEMICAL INVESTIGATION OF NANOPARTICLE SUSPENSIONS

### 4.1 Introduction

In order to learn the physiochemical behaviour of each nanomaterial and understand how these properties may attribute to antimicrobial effects, engineered and commercial nanomaterials (QNA Ag, QNA Cu, NF Cu10, NF CuO rods, QNA CuO, CuAg, CuZn, AMNP2 and AMNP3) were fully or partially investigated by nanoparticles tracking analysis (NTA), leaching study using ICP-OES, pH meter and Zetasizer, as summarized in **Table 4.1**. The details of nanomaterials are described in next section.

**Table 4.1** Investigation of physiochemical properties of nanoparticles by different techniques.

The row in the white indicates commercial nanoparticles: “SA” stands for nanomaterials from Sigma-Aldrich; and “NF” stands for nanomaterials from Suzhou Canfuo Nano Technology. The row in grey show engineering nanoparticle: “QNA” stands for nanomaterials from Intrinsiq Materials® (formally Qinetiq Nanomaterials).

| Sample | NTA | Leaching study | Zeta potential | pH |
|---|---|---|---|---|
| 1.SA WC | | | ● | ● |
| 2.QNA WC | | | ● | ● |
| 3.QNA Ag | ● | ● | ● | ● |
| 4.NF Cu10 | ● | ● | ● | ● |
| 5.QNA Cu | ● | ● | ● | ● |
| 6.NF CuO | ● | ● | ● | ● |
| 7.QNA CuO | ● | ● | ● | ● |
| 8.CuAg | ● | ● | ● | ● |
| 9.CuZn | ● | ● | ● | ● |
| 10.AMNP2 | ● | ● | ● | ● |
| 11.AMNP3 | ● | ● | ● | ● |

To study the physiochemical behaviour of these nanoparticles, each material was dispersed into aqueous suspensions, nanoparticle tracking analysis (NTA) was used to measure not only particle concentrations, but also their hydrodynamic sizes and distributions within the range between 10 to 545 nm. This can also reveal the difference between nanoparticle

suspensions and their powder forms. All nanoparticle suspensions were measured at three different concentrations (10, 50 and 100 ppm) and results were obtained in triplicates (please see Section 4.3.2 for experimental details). In order to effectively perform the antimicrobial activity, small hydrodynamic sizes and high particle concentration of the nanoparticle suspension are desired.

In addition to elemental analysis, ICP-OES in this chapter was employed to investigate the leaching properties of each nanomaterial. After nano-powders in either water or saline was dispersed and stood for 24 hours, the supernatants of nanoparticle suspensions were then subjected to ICP-OES for leaching analysis using fully quantitative method. Since metallic ion release is one of the main antibacterial effects, higher ion concentrations are expected to interact more readily with membrane proteins and nucleic acids in bacteria cells [143].

To further understand the stability of a dispersion, pH measurements were used to give a measure of the acidity or basicity of nanoparticle suspensions and zeta potential measurements were used to determine their surface charges [176]. The zeta potential exists when the nanoparticles is in contact with liquid and measuring the zeta potential can reflect the ability of electrostatic repulsion between adjacent nanoparticles. If two adjacent nanoparticles have a sufficiently high repulsive electrostatic force, they will not agglomerate. Therefore, zeta potential is considered as an indicator of the stability of nanoparticle suspensions, and pH is one of the most important factors that affects zeta potential value.

In conclusion, these physiochemical properties may explain the chance of nanoparticles exposure to the microbes during their treatment since they have direct effect on their antimicrobial abilities.

## 4.2 Nanomaterials

### 4.2.0 General

All engineered and commercial nanoparticles were used as received and stored in a dark and well-ventilated cupboard. For nanoparticle suspension and dispersion studies, nanoparticle samples were dispersed in either pure particle-free water (Acros, Belgium) or saline (0.9 wt/v% NaCl solution) at different concentrations. Ammonium hydroxide ($NH_4OH$) (Fisher Scientific®, UK) was diluted in pure particle-free water by 10 folds before it was used to treat Ag and CuAg NPs. For ICP-OES analysis, the 2 v/v% $HNO_3$ was prepared using 70

v/v% $HNO_3$ (Sigma-Aldrich, Merck, UK) diluted in pure particle-free water (Acros, Belgium). Different ICP analytical standards (Ag, Cu and Zn) at a concentration of 10,000 ppm were purchased from (Sigma-Aldrich, Merck, UK) and were diluted into serial concentrations for calibration purpose (see Section 4.3.4 for more details).

### 4.2.1 Tungsten carbide

SA WC with particle sizes of 150 - 200 nm was purchased from Sigma-Aldrich (US). The tungsten carbide samples appeared as dark grey powder.

QNA WC was engineered by Intrinsiq Materials® (formally Qinetiq Nanomaterials) using the Tesima™ thermal plasma technology [161]. Please see Section 3.2.1 for more details.

### 4.2.2 Silver

QNA Ag was engineered via the Tesima™ thermal plasma technology [158] provided by Intrinsiq Materials® (formally Qinetiq Nanomaterials). $NH_4OH$ (Fisher Scientific®, UK) was added to treat QNA Ag NPs prior to sonication. The details of this nanomaterials are identical to chapter previously reported, please refer to Section 3.2.2.

### 4.2.3 Copper and copper oxide

Two Cu NPs (QNA Cu and NF Cu10) with various particle shapes and sizes from different manufacturers were used in this study. QNA Cu was engineered by Intrinsiq Materials® (formally Qinetiq Nanomaterials) using patented technology called Tesima™ thermal plasma technology [161]. Commercial powder NF Cu10 was purchased from Suzhou Canfuo Nano Technology. The details of both nanomaterials are identical to chapter previously reported, please refer to Section 3.2.3.

QNA CuO was engineered by Intrinsiq Materials® (formally Qinetiq Nanomaterials) using patented technology called Tesima™ thermal plasma technology [161]. Commercial powder NF CuO rods was purchased from Suzhou Canfuo Nano Technology. The details of both nanomaterials are identical to chapter previously reported, please refer to Section 3.2.3.

### 4.2.4 CuAg and CuZn alloys

The alloy nanoparticles CuZn and CuAg were purchased from Sigma-Aldrich (Dorset, UK). $NH_4OH$ (Fisher Scientific®, UK) was added to treat CuAg NPs prior to the sonication process.

The details of both materials are identical to chapter previously reported, please refer to Section 3.2.4.

4.2.5 Antimicrobial nanoparticle formulations (AMNPs)

AMNP2 was previously engineered by Intrinsiq Materials® (formally Qinetiq Nanomaterials) using the Tesima™ thermal plasma technology [161]. A previous published report concluded that the atomic ratio of AMNP2 was 77.7% C, 5.5% O, 6.7% W, 4.7% Ag and 5.4% Cu [165].

AMNP3 consists of 55:45 ratio of NF CuO rods and CuZn which was developed during the collaborative project[1]. The details of both materials are identical to chapter previously reported, please refer to Section 3.2.5.

4.3 Instrumentation and methodology

4.3.1 Preparations of nanoparticle dispersions

All nanoparticles were weighed using a microbalance (*Shimadzu, Japan*). A titanium alloy Ti-Al-V liquid processor (Sonics & Materials®, USA, VC-750, Ø 13 mm, 750 W output power, 20 kHz) was used to disperse nanoparticle suspensions prior to their physiochemical analyses. Either pure particle-free water or saline was added into nanoparticles and the mixtures were dispersed at 40% working power with a pulse sequence (20 seconds ON, 5 seconds OFF) for 2 minutes. In a latter study, this method was compared with prolong dispersion time, and the results suggested the debris formed from the probe tipwas were less introduced into nanoparticle suspension, please see Section 7.4.2.3.

4.3.2 Nanoparticles tracking analysis (NTA)

Concentrations of 100 ppm samples were prepared using 2 mg of each nanoparticle of which were dispersed in 20 mL of Acros pure particle-free water using probe sonication prior NTA analysis. The hydrodynamic particle sizes and distributions of nano-suspensions were detected using a NanoSight LM14 Nanoparticles tracking analyser (Malvern Panalytical, UK). All nanoparticles were tracked using a 532 nm green laser source. Laser power, gain and focus were adjusted to optimum before data acquisitions. Images (640 X 480 pixels) captured and videos were recorded at real-time with a frame rate of 25 frames/s for 30 seconds. At least three successful analyses were obtained from multiple measurements. The build-in software (NTA 3.2) was used for particle detection and data acquisition, whilst real images were analysed by ImageJ software, MS Excel (Microsoft, USA) and OriginLab 2020 Pro (USA) were used for data processing.

Polystyrene latex standards (100 and 200 nm) purchased from Malvern Panalytical (UK) were used as standard for calibration. They were diluted into 100, 50 and 10 ppm and measured in triplicates. The results were shown in Appendix A.

### 4.3.3 The D-value and span value

A D-value can be presented as the cumulative undersize distribution showing the relative amount at/below a certain size. Usually, D10, D50 and D90 are used to investigate a particle size distribution curve. For instance, if the D10 is 126.8 nm, this represents 10% of the total volume of the sample has a size smaller than 126.8 nm, and if the D90 is 324.8 nm, this represents 90% of the total volume of the sample has a size smaller than 324.8 nm. The D10-to-D90 range focuses on main particle size range of the nanoparticles and is convenient to compare these nanoparticles. This value ignores 10% of the largest and smallest nanoparticles in the size distribution.

A relative fractional measure of width is obtained by dividing (D90–D10) by the measure of midpoint D50 as follows:

$$span = \frac{D90-D10}{D50} \times 100\% \quad (4\text{-}1)$$

which is referred as the span value and gives an indication of how far the D10-to-D90 range of particles is normalized with the midpoint (D50). In other word, this single value expresses the broadness of size distribution of nanoparticle– the higher span value the broader size range. This dimensionless measure of width shows size distribution in volume-based.

### 4.3.4 Interpretative method for size and types of distribution of nanoparticle suspension.

The nanoparticle size distributions were interpreted using the “vertical view” as shown in **Figure 4.1**, where the size distribution graphs were presented side by side. Each nanoparticle suspensions on the x-axis consists of five different symbols in a collinear line with different representative symbols. D10 and D90 are, respectively, represented by two triangle symbols (▼ and ▲), thus distance between D10 and D90 (D10-to-D90) expresses the main width of distribution of each material. In addition, the value of mode size, median size (D50) and mean size are, respectively, represented by star (★), square (■) and round

(●) The advantage of this method is to directly visualize different results in the same rectangular coordinate plane.

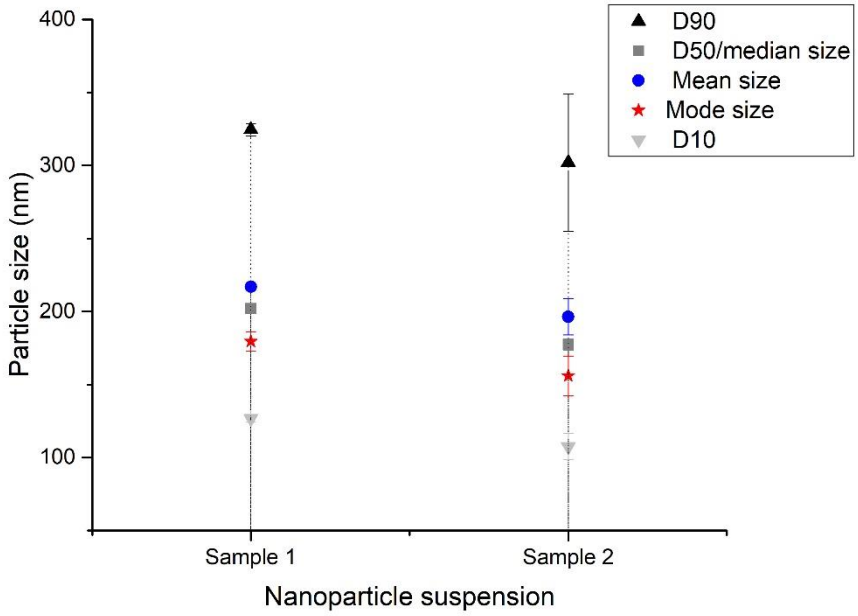


**Figure 4.1** A schematic graph of analysing size distribution.
Each nanoparticle suspension on x-axis consist of five different symbols in a collinear line with different representative symbols.

The relationship among mode size, D50 and mean size also reflect on the particle distributions in the mean of skewed distribution or normal distribution. As shown in **Figure 4.2**, if mode size is smaller than D50 whilst D50 is smaller than mean size (mode ★ < D50 ■ < mean ●), it can be considered as positively skewed distribution. Conversely, it is called negatively skew distribution. A normal distribution is the one when mode size, D50 and mean size are all equal. Overall, a positively skewed distribution is more desirable figure since this distribution contains more tiny particles over larger particles in comparison to the negatively skew distribution.

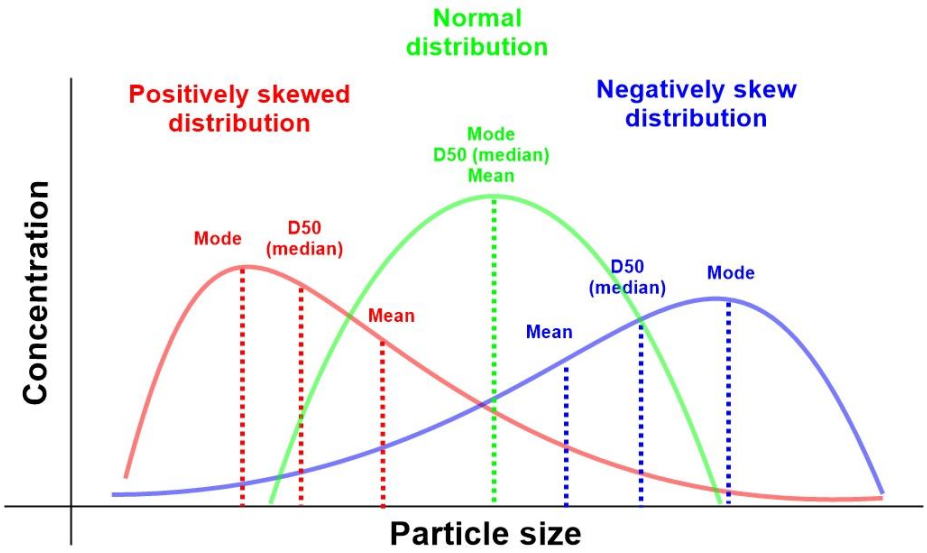


**Figure 4.2** A schematic diagram shows positively skewed distribution, normal distribution and negatively skew distribution depending on the relationship among mode, D50 (median) and mean size.

4.3.5 ICP-OES sample preparations: Leaching study

20 mg of each nanoparticle sample was dispersed in 20 mL either pure particle-free water or saline using probe sonication, all samples were left standing overnight for settlement. Supernatant from each sample was collected and then filtered using 0.1 µm syringe filter (Millipore) prior to ICP-OES acquisition. Fully quantitative approach was applied to quantify $Cu^{+}$ or $Cu^{2+}$, $Ag^{+}$ or $Ag^{2+}$ and $Zn^{2+}$ ion concentration in supernatant samples and emission intensities of wavelengths from all samples were obtained in triplicates.

4.3.6 Inductively coupled plasma optical emission spectrometry (ICP-OES)

The amount of saturated metallic ions in the nanoparticle supernatant sample ($Cu^{+}$ or $Cu^{2+}$, $Ag^{+}$ or $Ag^{2+}$ and $Zn^{2+}$ ions) were detected and quantified using inductively coupled plasma optical emission spectrometry Varian 710 (Germany) fitted with a Seaspray nebuliser. The details of this method were previously described, please refer to Section 3.3.4.

4.3.7 pH and zeta potential measurement

2 mg of each nanoparticle was dispersed in 20 mL of Acros pure particle-free water using probe sonication, these were then serial diluted into concentrations 50 and 10 ppm. All pH values were measured using a pH meter (Jenway Model 570 pH Meter, UK) and obtained in three successful measurements. Zeta potentials (mV) were measured using a Zetasizer

Nano ZS (Malvern Panalytical, UK). All samples were measured in triplicates at 25 °C with electrophoretic light scattering method. A dip cell (DTS1070, Malvern Instruments) was used to provide electrical trigger on charged particles. The data were analyzed using Malvern Zetasizer Software.

## 4.4 Results and discussion

### 4.4.1 NTA analysis of nanoparticles

The particle concentration and size distribution of these nanomaterials are important factors that directly influence to the material's rheology, suspension stability and antimicrobial properties. Nanoparticle tracking analysis (NTA) is an innovative system combining laser light scattering microscopy with a charge-coupled device camera which enables measurement of diffusion coefficient by taking continuous images of illuminated particles in suspension. By doing so, the NTA software then can determine not only particle concentrations, but also their hydrodynamic sizes and distributions within the nanoscale.

#### 4.4.1.1 Particle concentration and real-time analysis

In this study, 100 ppm (0.01 wt/v%) of each nanomaterial was dispersed in pure water using high frequency sonication probe. All NTA measurements were then collected for 30 seconds and repeated three times for each sample. Histograms show the concentration and size distributions of each nanoparticle suspensions with standard errors. The image in black background showed its visualized image captured at real-time using NTA.

Histograms in **Figure 4.3a** shows QNA Ag had a mode size at 185 nm with a concentration of $1.32 \times 10^7$ particles/ml, and the total concentration was $2.18 \times 10^9 \pm 1.14 \times 10^7$ particles/ml. In **Figure 4.3b**, the real-time image using NTA observed bright and tiny point scatters suggesting QNA Ag dispersed well. The scale bar was analysed by ImageJ.

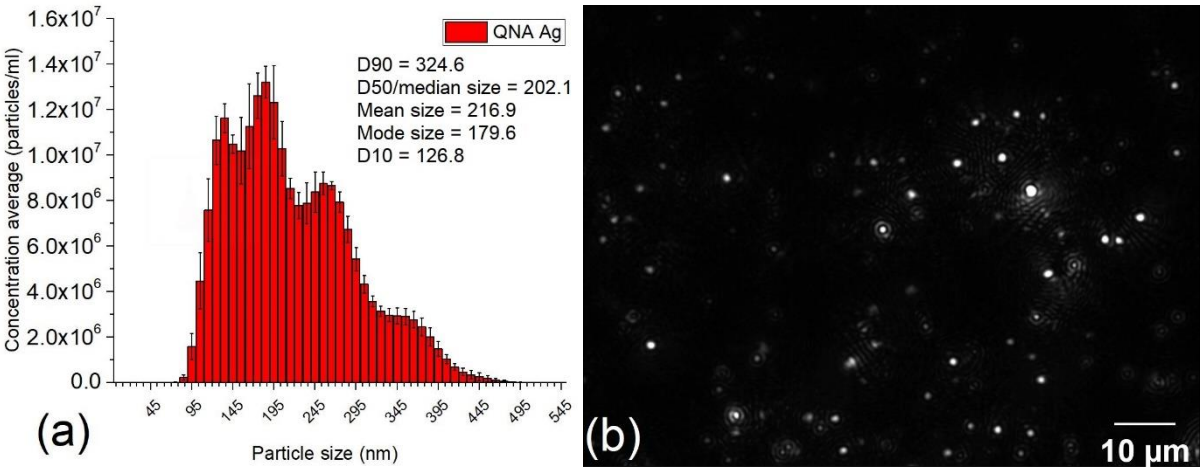


**Figure 4.3** (a) Particle size and distribution of engineered QNA Ag and (b) visualized image at real-time using NTA.

The mode size was 185 nm with a concentration of 1.32 x $10^7$ particles/ml, and the total concentration was 2.18 x $10^9$ ± 1.14 x $10^7$ particles/ml. The real-time image showed QNA Ag was small and bright scattering points.

As presented in **Figure 4.4**, two Cu NPs had quite opposite histograms with huge deviations. Specifically, NF Cu10 powder was supposed to have a size between10 to 30 nm with high purity. However, the NTA results showed that the mode size of NF Cu10 around 165 nm had a concentration of 2.58 x $10^6$ particles/ml. In contrast, QNA Cu had multiple peaks with concentrations between 2 x $10^6$ to 2.5 x $10^6$ particles/ml. The total concentrations of these two were, respectively, 2.63 x $10^8$ ± 2.32 x $10^6$ (NF Cu10) and 7.1 x $10^8$ ± 3.29 x $10^7$ particles/ml (QNA Cu). As a result, a better dispersibility of QNA Cu was determined than NF Cu10, which can also be directly seen from visualized images in **Figures 4.5**.

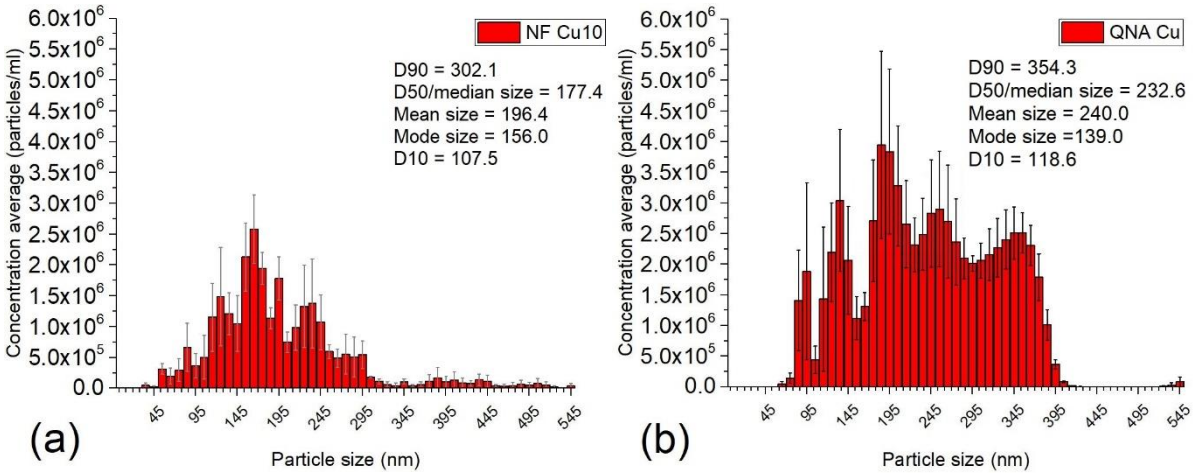


**Figure 4.4** Particle size and distribution of (a) commercial NF Cu10 and (b) engineered QNA Cu.

Two Cu NPs had quite opposite characterizations. QNA Cu suspension had a much higher total concentration than NF Cu10.

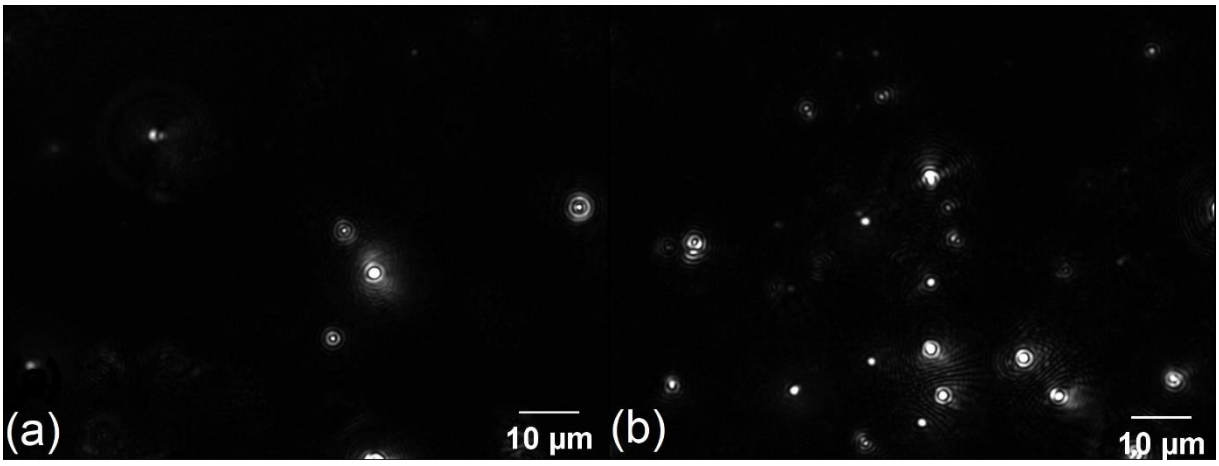


**Figure 4.5** Visualized images at real-time of (a) commercial NF Cu10 and (b) engineered QNA Cu.

QNA Cu had slightly more scattering points than NF Cu10, both of them showed low hydrodynamic concentration.

The NTA results of NF CuO rods and QNA CuO suspensions are shown in **Figure 4.6** and **4.7**. Both CuO suspensions had single peak (mode size) around 155 nm with a particle concentration of 1.42 x $10^7$ (NF CuO) and around 145 nm with a concentration of 5.34 x $10^7$ (QNA CuO) particles/ml. The total concentration of these two were 1.63 x $10^9$ ± 7.01 x $10^7$ (NF CuO) and 5.13 x $10^9$ ± 2.15 x $10^8$ particles/ml (QNA CuO), respectively. Therefore, QNA CuO had a higher particle concentration, while that of NF CuO rods had a lower

hydrodynamic concentration and the corresponding real-time NTA images are shown in **Figure 4.7**.

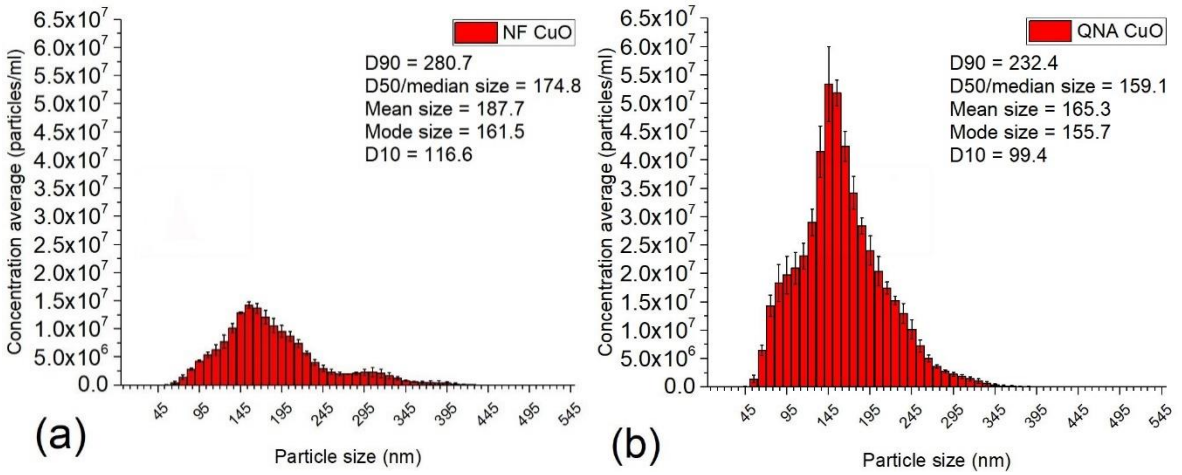


**Figure 4.6** Particle size and distribution of (a) commercial NF CuO rods and (b) engineered QNA CuO.

QNA CuO had a much higher total concentration than NF CuO. Besides, they had mode sizes around 155 nm.

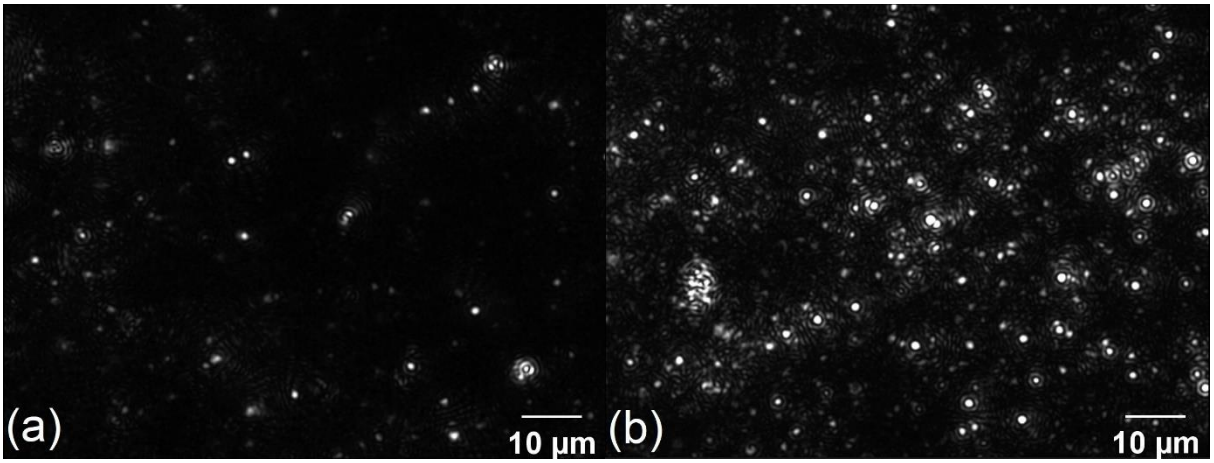


**Figure 4.7** Visualized images at real-time of (a) NF CuO and (b) QNA CuO.

The real-time image of QNA CuO showed more nanoparticles than NF CuO.

The hydrodynamic particle concentrations and size distributions of commercial CuAg and CuZn are shown in **Figure 4.8**. For the CuAg suspension, the concentration of mode size around 125 nm was 6.91 x $10^6$ particles/ml and the total concentration was 7.6 x $10^8$ ± 2.74 x $10^7$ particles/ml. However, the particle distribution for CuZn suspension was better dispersed in comparison of the CuAg suspension even though it had not been surface treated with any reagent. The mode size of CuZn suspension was found to be around 155 nm. At

this size, the concentration of CuZn was 1.57 x $10^7$ particles/ml. The total concentration of CuZn was 2.14 x $10^9$ ± 7.18 x $10^7$ particles/ml. The real-time images of NTA in **Figure 4.9** revealed the difference of point scatters of CuAg and CuZn as they have dissimilar optical properties.

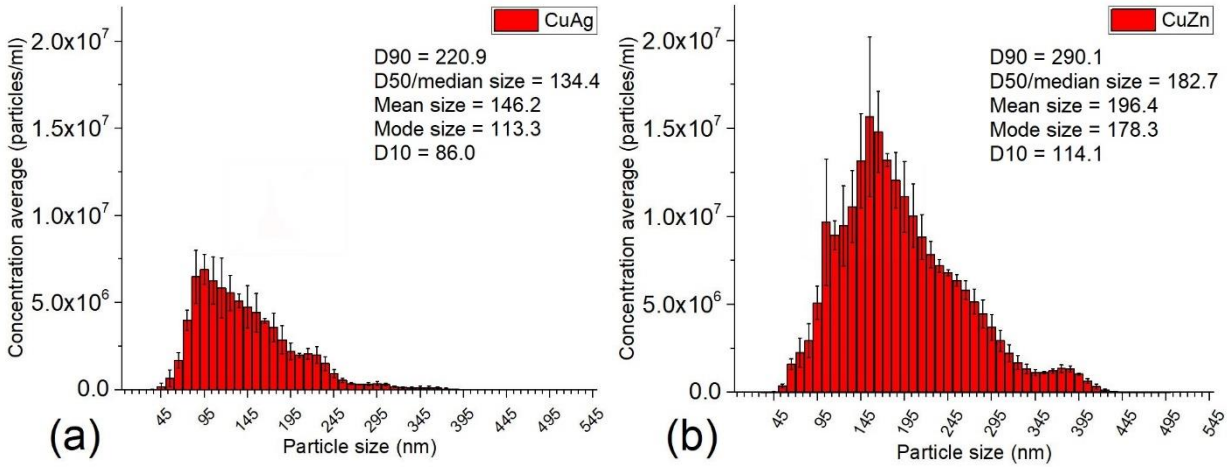


**Figure 4.8** Particle size and distribution of commercial CuAg and (b) CuZn. The CuZn suspension had higher total concentration than CuAg. And CuAg had a smaller mode size (125 nm) than CuZn suspension (15 nm).

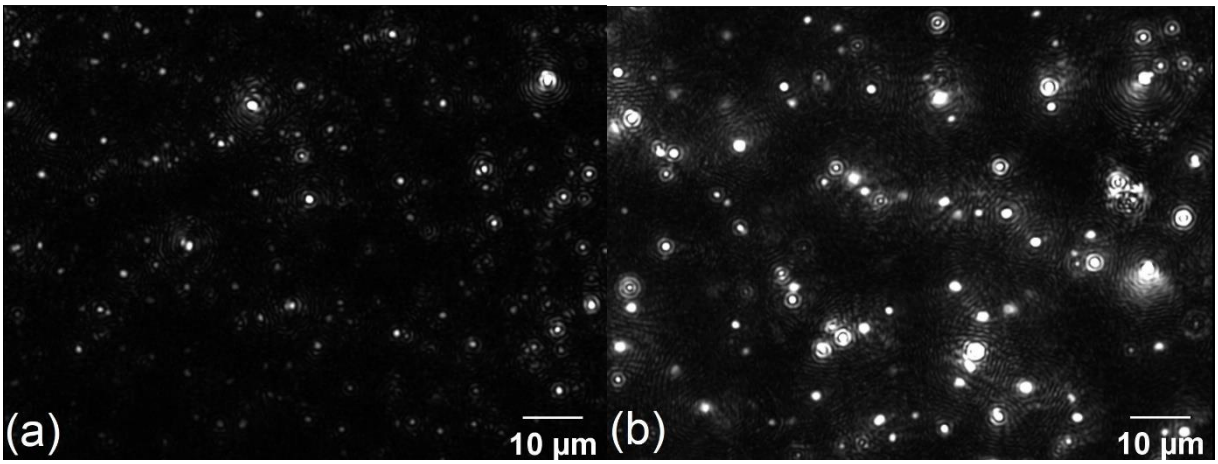


**Figure 4.9** Visualized images at real-time of (a) commercial CuAg and (b) CuZn. CuZn had brighter scattering points than CuAg due to refractive index.

As multi-elemental phases, AMNP2 and AMNP3 were poly-dispersed in suspension, as presented in **Figure 4.10**. The AMNP2 suspension had a wide range of particle size and the mode size of AMNP2 was approximately 35 nm with a concentration of 6.72 x $10^6$ particles/ml. Multiple peaks were detected from the AMNP3 suspension as well. One main peak around 175 nm with a concentration of 7.66 x $10^6$ particles/ml was observed, because the precursor

materials of AMNP3 includes NF CuO rods and CuZn, both of which had mode sizes around 175 nm. Additionally, other peaks of the AMNP3 suspension were evenly around 3 x $10^6$ particles/ml. The total concentration of AMNP2 and AMNP3 were, respectively, 8.62 x $10^8$ ± 1.89 x $10^8$ and 1.08 x $10^9$ ± 4.79 x $10^7$ particles/ml. Similarly, the real-time images from **Figure 4.11** observed AMNP2 had larger white rings than AMNP3.

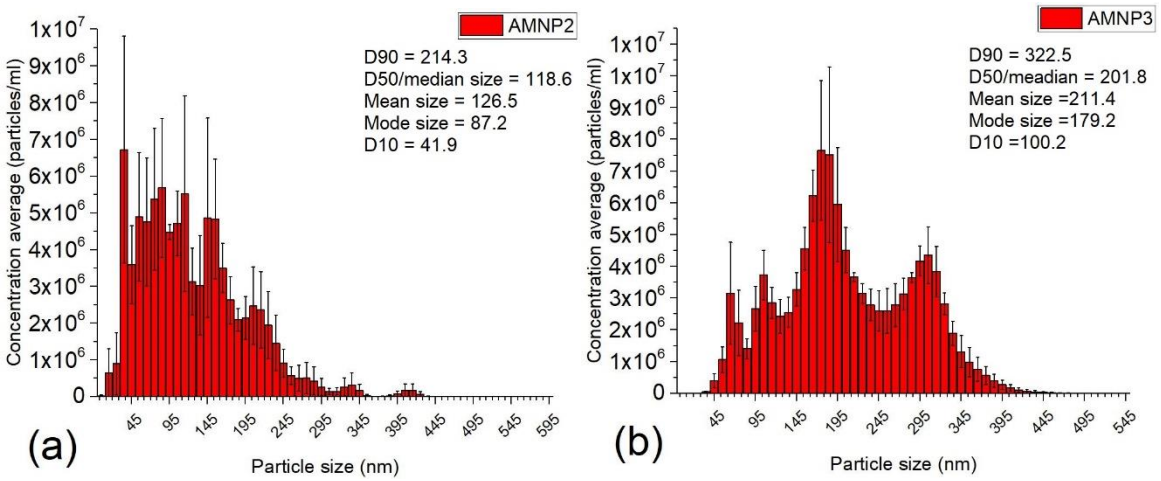


**Figure 4.10** Particle size and distribution of AMNP2 and (b) AMNP3.
The mode size of AMNP2 was approximately 35 nm, and that of AMNP3 was 175 nm. Both of them had multiple peaks due to containing different elements.

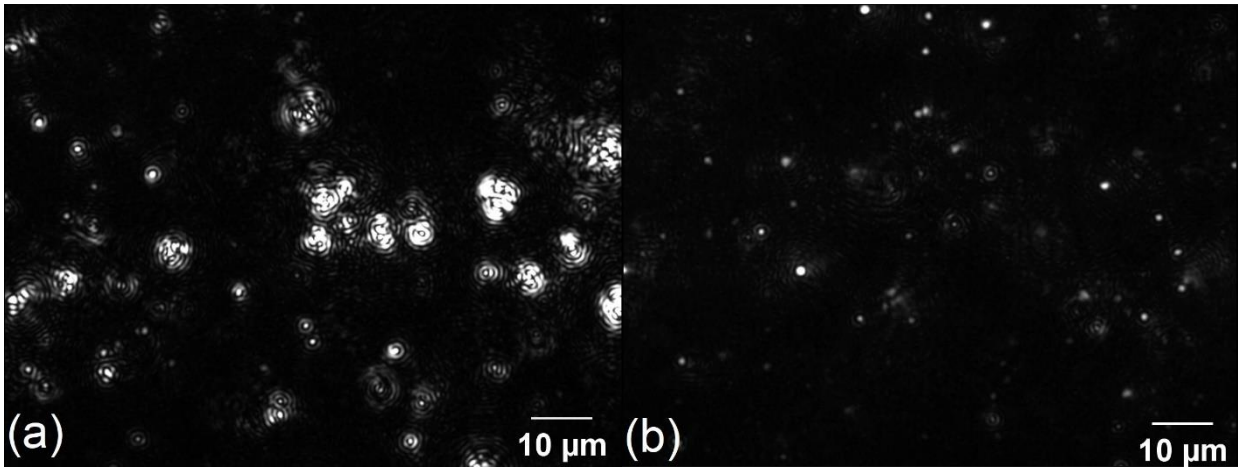


**Figure 4.11** Visualized images at real-time of (a) AMNP2 and (b) AMNP3.
It hardly saw scattering points in AMNP3, while AMNP2 had large white rings surrounding scattering points.

It is worth mentioning that, due to the differences of scattering properties, the setting of capture for different samples was changed accordingly, as displayed in **Table 4.2**. Camera level determines the brightness of the image which uses combination of shutter slider and

gain slider [177]. Particularly, shutter slider controls the duration of captured light and gain slider determines the sensitivity of the camera. Generally, longer shutter times and higher gain settings are required to capture dim or small particles. Therefore, in order to optimise capture, it is suggested to choose long enough capture duration and an appropriate concentration (between $10^7$ to $10^9$ particles/ml) to be reproducible on repeat analyse.

Detection threshold is another setting that adjusts the brightness of the image displayed on screen after capture so that particles are capable of being identified and tracked. As can be seen, although all samples were under the same gain slider (15), the difference in refractive index result in different shutter sliders and detection thresholds. Cu-based samples overall showed higher shutter sliders and detection threshold than QNA Ag because of a higher refractive index.

**Table 4.2** Capture settings of NTA for different nanoparticle suspension samples.

| Sample | Camera level | Shutter slider | Gain slider | Detection threshold |
|---|---|---|---|---|
| QNA Ag | 5 | 45 | 15 | 8 |
| NF Cu10 | 7 | 165 | 15 | 5 |
| QNA Cu | 6 | 86 | 15 | 8 |
| NF CuO rods | 6 | 86 | 15 | 11 |
| QNA CuO | 6 | 86 | 15 | 16 |
| CuAg | 6 | 86 | 15 | 14 |
| CuZn | 8 | 317 | 15 | 10 |
| AMNP2 | 6 | 86 | 15 | 16 |
| AMNP3 | 7 | 165 | 15 | 13 |

#### 4.4.1.2 Size distribution

As mentioned in Section 4.3.4, mean, median and mode size are typical values to present particle size distribution data - mean size is a calculated value of the average diameter of particle; median size (D50) is equal to the value splits the distribution with half above and half below this diameter; and mode size is the peak of the frequency distribution, which can be easily seen in the distribution as it is the highest peak seen . All these values were calculated and displayed in **Table 4.3**. To visualize more intuitively, the "vertical view " of size

distribution graphs were presented side by side. Finally, it was converted into one graph displayed in **Figure 4.12**.

**Table 4.3** Summary of mean, mode size and D-values of all samples.

| Sample | Mean size (nm) | Mode size (nm) | D10 (nm) | D50 (nm) | D90 (nm) |
|---|---|---|---|---|---|
| QNA Ag | 216.9(±2) | 179.6(±6.6) | 126.8(±2.6) | 202.1(±1.7) | 324.6(±4.2) |
| NF Cu10 | 196.4(±12.4) | 156(±13.6) | 107.5(±9.1) | 177.4(±4.1) | 302.1(±47) |
| QNA Cu | 240(±1.6) | 139(±28.5) | 118.6(±10.2) | 232.6(±10.2) | 354.3(±4.9) |
| NF CuO | 187.7(±1.1) | 161.5(±2.3) | 116.6(±1.1) | 174.8(±1) | 280.7(±9.9) |
| QNA CuO | 165.3(±2.2) | 155.7(±2.8) | 99.4(±1.5) | 159.1(±2.7) | 232.4(±4.5) |
| CuAg | 146.2(±0.7) | 113.3(±11.1) | 86(±2.8) | 134.4(±2.3) | 220.9(±4.8) |
| CuZn | 196.4(±2.8) | 178.3(±10.5) | 114.1(±3.2) | 182.7(±4.8) | 290.1(±6.1) |
| AMNP2 | 126.5(±9) | 87.2(±24.4) | 41.9(±7.6) | 118.6(±9.2) | 214.3(±15.2) |
| AMNP3 | 211.4(±5.7) | 179.2(±4.7) | 100.2(±4.6) | 201.8(±5.9) | 322.5(±6) |

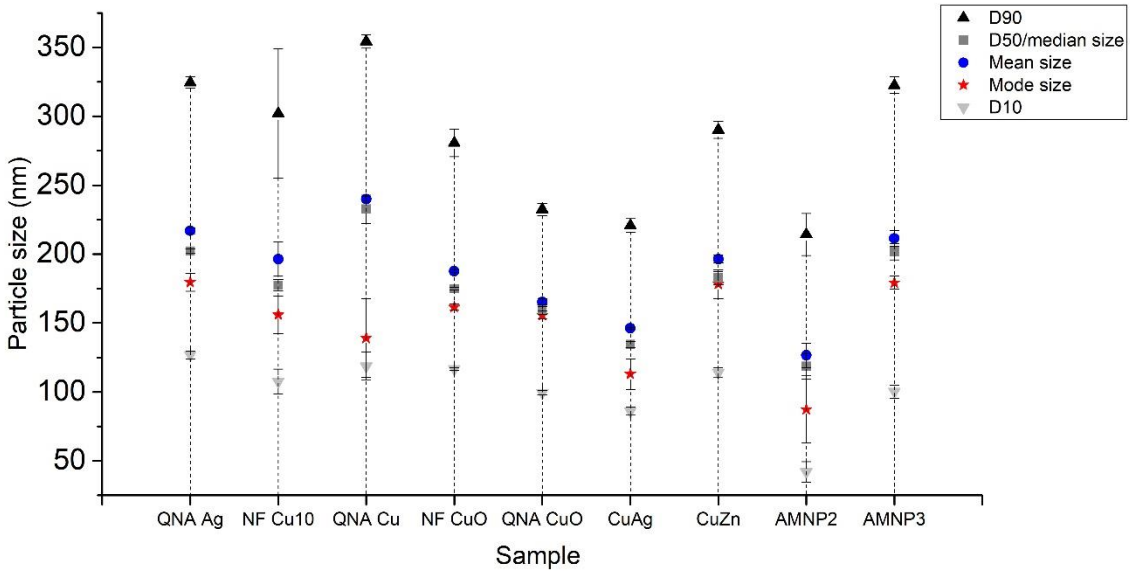


**Figure 4.12** A size distribution graph of all nanoparticles converted from Table 4.3. The "vertical view " of size distribution graphs were presented side by side. y-axis shows mean, mode size and D-values with different symbols.

As can be clearly seen in **Figure 4.12**, the two narrowest distributions (D10-to-D90) were QNA CuO and CuAg around 130 nm, lastly by QNA Cu and AMNP3 around 230 nm. The smallest value of D10 was AMNP2, while the largest D10 was QNA Ag. A very large error

bar was observed in the D90 of NF Cu10 suspension demonstrating it had the poorest dispersion at large size. The aggregation of nanoparticles was found due to high surface area, therefore its particle size in water was usually larger than powder. Regarding types of distribution in this experiment, all sample except QNA CuO can be considered as positively skewed distributions suggesting that they had high portion of tiny particle, while QNA CuO was closer to be a normal distribution.

The result of span value of all nanoparticle suspensions calculated using **Equation (4-1)** are shown in **Figure 4.13**, QNA Ag, NF CuO rods, QNA CuO and CuZn had span values under the dotted line, which indicates they had desirable narrow particle size distributions. On the contrary, the span of QNA Cu, AMNP2 and AMNP3 were over 100%, which inferred particle size widely distributed. It is worth mentioning that AMNP2 was the largest span value as it consist of multiple elements such as W, C, Cu and Ag [165].

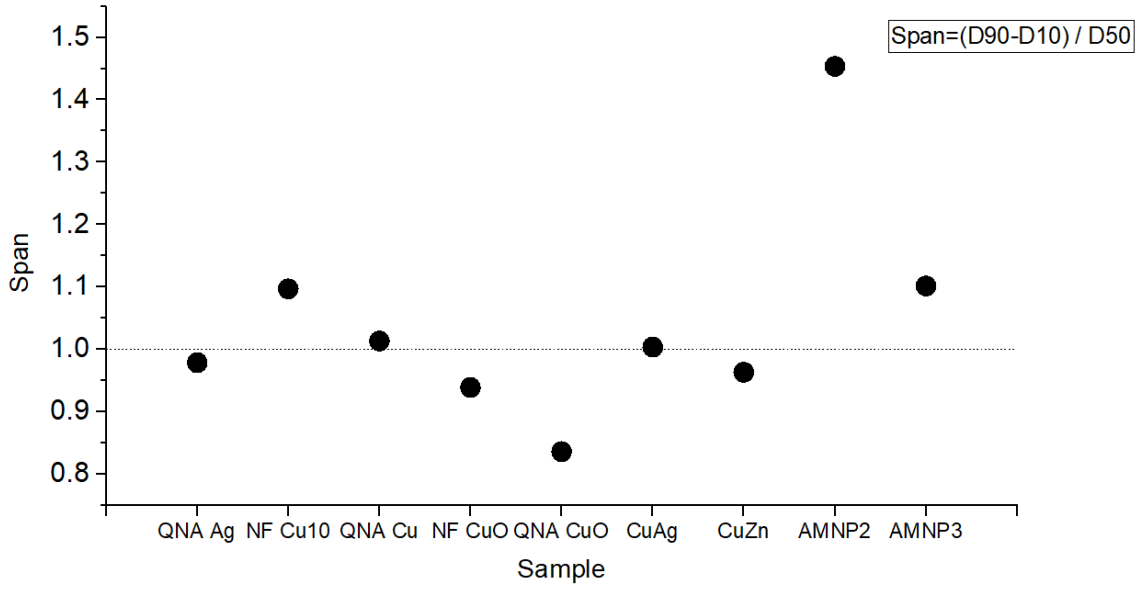


**Figure 4.13** The span value of nanoparticle suspensions.
It gives an indication of how far the D10-to-D90 range of particles is normalized with the midpoint (D50).

4.4.2 Leaching study using ICP-OES.

*4.4.4.1 Ion release study*

1000 ppm (0.1 wt/v%) of different nanomaterials were dispersed in pure water and saline using high frequency sonication probe, saturated $Cu^{+}$ or $Cu^{2+}$, $Ag^{+}$ or $Ag^{2+}$ and $Zn^{2+}$ ions of the supernatant of each sample were measured by ICP-OES using fully quantitative approach.

**Figure 4.14** showed the result of different nanoparticles released ions in water. It was found that two Cu and CuO NPs released different concentrations of Cu ions, but this cannot be determined to be related to the difference in purity. Specially, it was found that NF Cu10 had higher $Cu^{2+}$ ion release, because of the purity of NF Cu10 slightly higher than that of QNA Cu. However, QNA CuO with less purity than NF CuO released six times higher than the latter (please see Section 3.4.4.1).

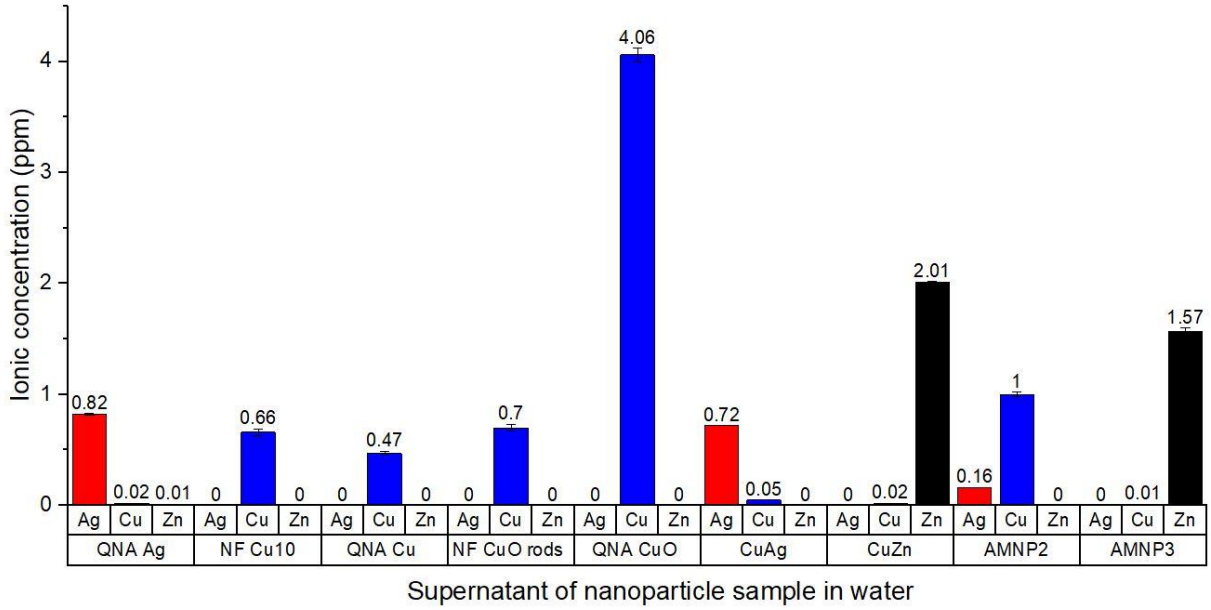


**Figure 4.14** Ag, Cu and Zn ion release of nanoparticles in water.
QNA CuO released much higher Cu ion than others, while the lowest ion release was from QNA Cu. QNA Ag and CuZn had similar Ag ion release values.

Moreover, the huge difference was observed when AMNP3 was compared with its precursor materials: CuZn and NF CuO rods. The mixture AMNP3 had only 0.01 ppm of Cu ion concentration in water. In contrast, the total of $Cu^{2+}$ ion concentrations from CuZn and NF CuO was 0.72 ppm. Nevertheless, all of our samples were safe to human body - none of Cu-contained nanoparticles released ions higher than dangerous level (5 ppm) after being dispersed and suspended in aqueous solutions.

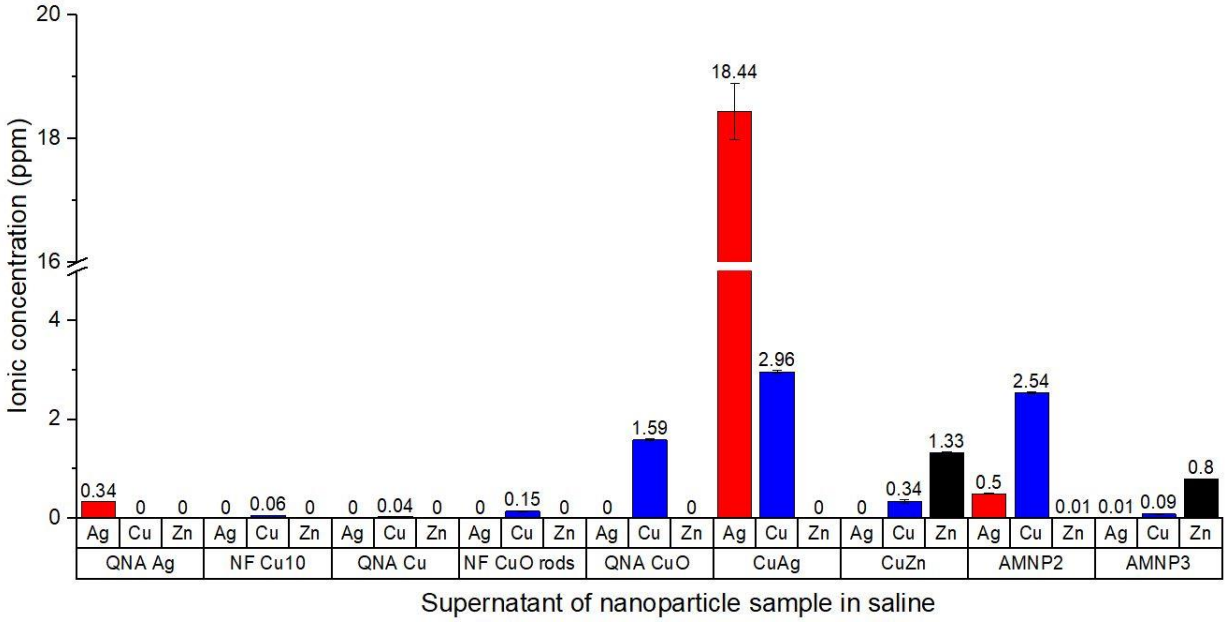


**Figure 4.15** Ag, Cu and Zn ion release of nanoparticles in saline.
All samples in saline generated more or less ion than their water solution. CuAg released much higher Ag ion than any other ions.

On the other hand, ion leaching from different nanoparticles in saline is displayed in **Figure 4.15**. For leaching $Cu^{+}$ or $Cu^{2+}$ ions in saline, NF Cu10, QNA Cu, NF CuO and QNA CuO were 0.06, 0.04, 0.15 and 1.59 ppm, respectively, while counterparts in water were 0.66, 0.47, 0.7, and 4.06 ppm, respectively. The leaching $Cu^{+}$ or $Cu^{2+}$ ions of CuAg, CuZn, AMNP3 and AMNP2 in saline were 2.96, 0.34, 0.09, and 2.54 ppm, respectively, while counterparts in water were 0.05, 0.02, 0.01, and 1 ppm, respectively. This comparison indicated that saline may suppress $Cu^{+}$ or $Cu^{2+}$ ion leaching from simple substance (e.g., Cu and CuO) than pure water, but it promoted $Cu^{+}$ or $Cu^{2+}$ ion leaching in multi-elemental materials. It is worth noting that, CuAg samples in saline released up to 18.44 ppm of $Ag^{+}$ or $Ag^{2+}$ ions, which may be an indication of a reaction between CuAg and saline (NaCl) resulting in the participation of AgCl [178]. This reaction may also occur to AMNP2 and QNA Ag as the $Ag^{+}$ or $Ag^{2+}$ ions of AMNP2 in saline and water were, respectively, 0.5 and 0.16 ppm, and QNA Ag in water and saline released 0.82 and 0.34 ppm of $Ag^{+}$ or $Ag^{2+}$ ions, respectively.

**Table 4.4** Comparison of released Cu ions of nanomaterials in water and saline.

Cu or CuO NPs released lower Cu ions in saline than water, while alloys (CuAg and CuZn) and antimicrobial nanoparticle formulations (AMNP2 and AMNP3) were the opposite.

| Nanomaterial | Cu ions in saline (ppm) | Cu ions in water (ppm) |
|---|---|---|
| NF Cu10 | 0.06 | 0.66 |
| QNA Cu | 0.04 | 0.47 |
| NF CuO | 0.15 | 0.7 |
| QNA CuO | 1.59 | 4.06 |
| CuAg | 2.96 | 0.05 |
| CuZn | 0.34 | 0.02 |
| AMNP2 | 2.45 | 1 |
| AMNP3 | 0.09 | 0.01 |

*4.4.4.2 The effect of pH level on ion release*

Ion release effects were carried out to assess leaching behaviour in different nanoparticles suspended in various aqueous media (pure water vs. saline). As mentioned earlier, the difference of pH levels in water and saline suspensions may influence the solubility of ions. To exclude other potential factors, ICP standards of $Cu^{+}$ or $Cu^{2+}$, $Ag^{+}$ or $Ag^{2+}$, and $Zn^{2+}$ ions were diluted into 0.1, 0.5 and 1 v/v% in water, saline and 2 v/v% $HNO_3$, respectively, and were measured by ICP-OES, plotted in **Figure 4.16**.

Accordingly, the pH of saline and pure water is supposed to be 5.5 and 7, respectively, and the pH of 2 v/v% of $HNO_3$ is normally 0.5. It is visible that the concentrations of all metal ions in $HNO_3$ were much higher than that in saline and water, especially for $Ag^{+}$ or $Ag^{2+}$ ions. For $Cu^{+}$ or $Cu^{2+}$ ions, the concentration in $HNO_3$ were higher than that of $Ag^{+}$ or $Ag^{2+}$ ions, while the concentrations in saline and water were lower. This may because $Cu^{+}$ or $Cu^{2+}$ ions bind to $OH^{-}$ more strongly than $Ag^{+}$ or $Ag^{2+}$ ions and yields more stable precipitation $Cu(OH)_2$.

Besides, the solubility of ions was not linear with pH, as ICP standards in water had slightly higher ion concentrations for all metals than saline samples, but the pH of saline sample was lower than water. In summary, water solvent is more suitable than saline for ion release, which is directly related to antimicrobial properties.

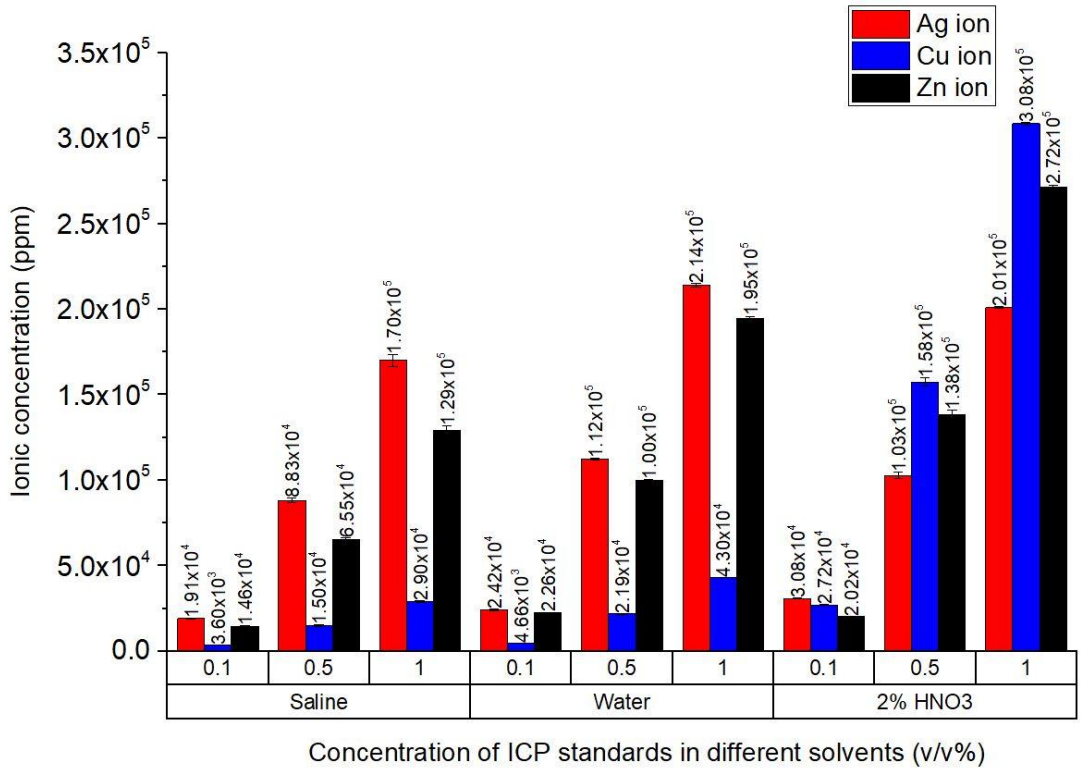


**Figure 4.16** The concentrations of ICP standards of Cu, Ag and Zn ions in saline, pure water and 2 v/v% $HNO_3$, respectively.

In general, the concentrations of all ions in pure water were higher than counterpart in saline but lower than counterpart in $HNO_3$, due to the difference of pH level.

In conclusion, the solubility of ions varies with solvents, this may have caused by the difference of pH levels and salt effect in the aqueous media. More investigations are being carried out to understand ion release properties of these antimicrobial nanoparticles.

*4.4.4.3 The difference between oxide and alloy on ion release*

In our study, ion release properties may not only be influenced by the pH levels in the medium, but also the difference between alloy and compound. Thus, concentrations of $Cu^{+}$ or $Cu^{2+}$ ions from both CuO NPs (oxide) and CuAg and CuZn (alloy) is discussed. To put all samples under the same conditions, the digested $Cu^{2+}$ ion concentrations from **Figure 3.15** were multiplied by 100 times and equal to 1000 ppm, which was as the same as their leaching ion concentrations. As can be seen in **Table 4.5**, NF CuO rods digested the highest $Cu^{+}$ or $Cu^{2+}$ ion concentration (the highest purity) among four samples, but it was not the highest leaching ion concentration neither in water nor in saline – the $Cu^{+}$ or $Cu^{2+}$ ions of NF CuO rods in saline were even the lowest concentration. Digested QNA CuO sample had the second

highest $Cu^{+}$or $Cu^{2+}$ ion concentration and it released much higher ions in water than others. The highest leaching concentration of $Cu^{+}$ or $Cu^{2+}$ ions in saline were obtained from CuAg, while its digested ion concentration was only 8 ppm.

It is also worth noting that, this ion release study may also be used to explain antimicrobial activities of different nanoparticles (please see Chapter 5), especially when the biological mechanism of microbial inhibition involves manipulation of protein ion channels.

**Table 4.5** 100 times of relative digested $Cu^{+}$ or $Cu^{2+}$ ion concentrations of different types of forms were compared with their ion release in water and saline, which were all at 1000 ppm.

| Sample | Relative digested ion concentration (ppm) | Relative leaching ion concentration in water (ppm) | Relative leaching ion concentration in saline (ppm) |
|---|---|---|---|
| NF CuO rods | 635 | 0.7 (0.11%) | 0.15 (0.024%) |
| QNA CuO | 566 | 4.06 (0.72%) | 1.59 (0.28%) |
| CuAg | 8 | 0.05 (0.625%) | 2.96 (37%) |
| CuZn | 419 | 0.02 (0.005%) | 0.34 (0.08%) |

**Table 4.6** shows the comparison between AMNP3 and NF CuO, CuZn due to the fact that AMNP3 consists of NF CuO rods and CuZn (55:45). Again, the digested ion concentrations are multiplied by 100 times to be compared with their leaching ion concentrations. The theoretical value of digested AMNP3 sample depends on the formula ratio of NF CuO and CuZn sample, which were 538 ppm for $Cu^{+}$ or $Cu^{2+}$ ions and 101 ppm for $Zn^{2+}$ ions. These values were close to the practical result of digestion concentrations (430 ppm for $Cu^{+}$ or $Cu^{2+}$ ions and 88 ppm for $Zn^{2+}$ ions). However, the results of ion release concentration between the theoretical values and the practical values were quite different. The theoretical release value of $Cu^{+}$ or $Cu^{2+}$ ion concentration of AMNP3 was up to 0.39 ppm, while its practical concentration was only 0.01 ppm. Additionally, the practical $Zn^{2+}$ ion concentration of SAF1,1 was observed to be 1.57 ppm which was higher than its theoretical value of $Zn^{2+}$ ions (0.9 ppm). The difference in theoretical and practical values may suggest that chemical reaction occurred during sonication process, i.e., the present of ZnO in the alloy materials may have reacted with CuO to yield more intermetallic compounds or alloy. This may reduce $Cu^{+}$ or

$Cu^{2+}$ ion release due to the formation of more stable ionic interaction in Cu and Zn. Likewise, the present of CuZn may undergo oxidation to yield ZnO, which would subsequently raise $Zn^{2+}$ ion release in AMNP3 sample.

**Table 4.6** Ion concentrations of NF CuO rods and CuZn in comparison of AMNP3. The difference in theoretical and practical values may suggest chemical reaction occurred during sonication process.

| Sample | NF CuO rods | CuZn | AMNP3 Theoretical release CuO:CuZn (55:45) | AMNP3 Practical release |
|---|---|---|---|---|
| Digestion ion concentrations (ppm) | Cu 635 | Cu 419<br>Zn 225 | Cu 538<br>Zn 101 | Cu 430<br>Zn 88 |
| Leaching ion concentration (ppm) | Cu 0.7 | Cu 0.02<br>Zn 2.01 | Cu 0.39<br>Zn 0.9 | Cu 0.01<br>Zn 1.57 |

### 4.4.3 pH and zeta potential measurement

The results of pH measurements are shown in **Figure 4.17**, where raw data is tabulated in Appendix B. The equilibrium of the solid nanoparticle and its ions in pure water and the acidity or basicity of sample is directly influenced by nanoparticle concentration. The pH levels of all samples were generally in the range between 6 and 7, and the highest pH was found in QNA Cu at 10 ppm. Both WC, QNA Cu and CuAg suspensions declined pH with increasing nanoparticle concentrations, while the pH of QNA Ag and QNA CuO suspensions were the opposite. The pH of the rest of them fluctuated with increased concentrations. The reason of this may be explained by disturbance from the physical particles presence in suspensions as they are not homogeneous solution.

The pH value of solvent has a significant effect on surface charge of nanoparticles, these positive or negative charges in the solvent will generate electrostatic forces to either maintain or destabilize the colloidal system. Under appropriate acidic conditions (usually), the nanoparticles in the suspension can be positively charged and generate a strong repulsive force that repels each other to obtain well-dispersed system. As pH changes, there is an isoelectric point where the surface of nanoparticles is neutral and the colloidal system is the

least stable [42]. Thus, the pH affects the stability of suspensions, the effectiveness of which further can be described as zeta potential.

The pH level may also affect the antibacterial activity of nanoparticles. Briefly, acidic conditions may assist metal ions in inhibiting bacteria since most of them are soluble in acid and then decrease pH [179], however metal ions are possibly removed or adsorbed by hydroxide ions at higher pH values. For instance, Hsueh *et. al.* (2017) presented that CuO NPs at pH=5 were more toxic to four different *S. aureus* strains than pH = 6 and 7, because the higher release of $Cu^{+}$ or $Cu^{2+}$ ion raises the production of ROS [180] (Please see Section 5.4.3). However, there is an opposite conclusion from Guldiren *et. al.* claiming that pH values are rarely relevant to antimicrobial activities as they obtained different results with similar pH levels [134]. Further investigation is still required to fully understand mechanism.

As an indicator of the stability of nanoparticle suspensions, zeta potential values varied depending on types of nanoparticles (in **Figure. 4.17**). Both WC and AMNP2 suspensions showed an increased absolute zeta potential values with increased concentrations. Suspensions of QNA CuO, CuZn and AMNP3 at a concentration of 10 to 100 ppm crossed the zero bridge and switched from a negative charged potential to a negative potential. For most cases, zero zeta potential, also called the point of zero charge, is equivalent to the iso electric point, which contains as much positively charged as negatively charged surface functions resulting in the least stable. NF Cu10, NF CuO and CuAg were found stable at all concentrations. QNA Ag suspensions at 10 and 100 ppm had zeta potential values more than -30 mV and it was considered as the most stable material perhaps with the aid of $NH_4OH$, followed by CuAg and AMNP2 suspensions. According to DLVO electrostatic theory, the stability of nanoparticle suspensions depends on the combination effect of van der Waals attraction and electrostatic repulsion. A high zeta potential (either positive or negative) prevents aggregation of nanoparticles in solution due to larger repulsive forces among particles. Conversely, absolute zeta potential values below this certain level stand the possibility for collisions of nanoparticles with subsequent aggregating [42]. As a rule of thumb, in general when a zeta potential value greater than 30 mV or less than -30 mV imply a stable suspension; the zeta potential of approximately ±20 mV can only maintain short-term stability; the zeta potential value in the range from -5 mV to +5 mV suffers from fast aggregation [181].

Likewise, the zeta potential value is influenced by the particle size. A signal of zeta potential from larger particles tends to dominate the zeta potential, which can also be caused by the agglomeration of nanoparticles with increasing their concentrations. This may explain why

each nanoparticle suspensions had fluctuating zeta potential values at different concentrations. In this study, the largest size distributions were QNA Cu and AMNP3, whose zeta potential values experienced fluctuation, while AMNP2 suspensions with favorable dispersibility had linear changes.

Apart from the effect of zeta potential on the stability of nanoparticles suspensions, zeta potential also affects the attachment of nanoparticles to cell membrane leading to subsequent antimicrobial activity *via* cellular uptake [182]. For positive-charged nanoparticles, a high affinity to cellular membrane has been found to contribute on electrostatic interactions because both bacteria cell walls are dominated by negative charges [183, 184]. On the other hand, negatively charged particles are likely to form clusters to bind at the positively charged sites of cells resulting in localized neutralization and a subsequent membrane bending, which in turn facilitates endocytosis for cellular uptake [185]

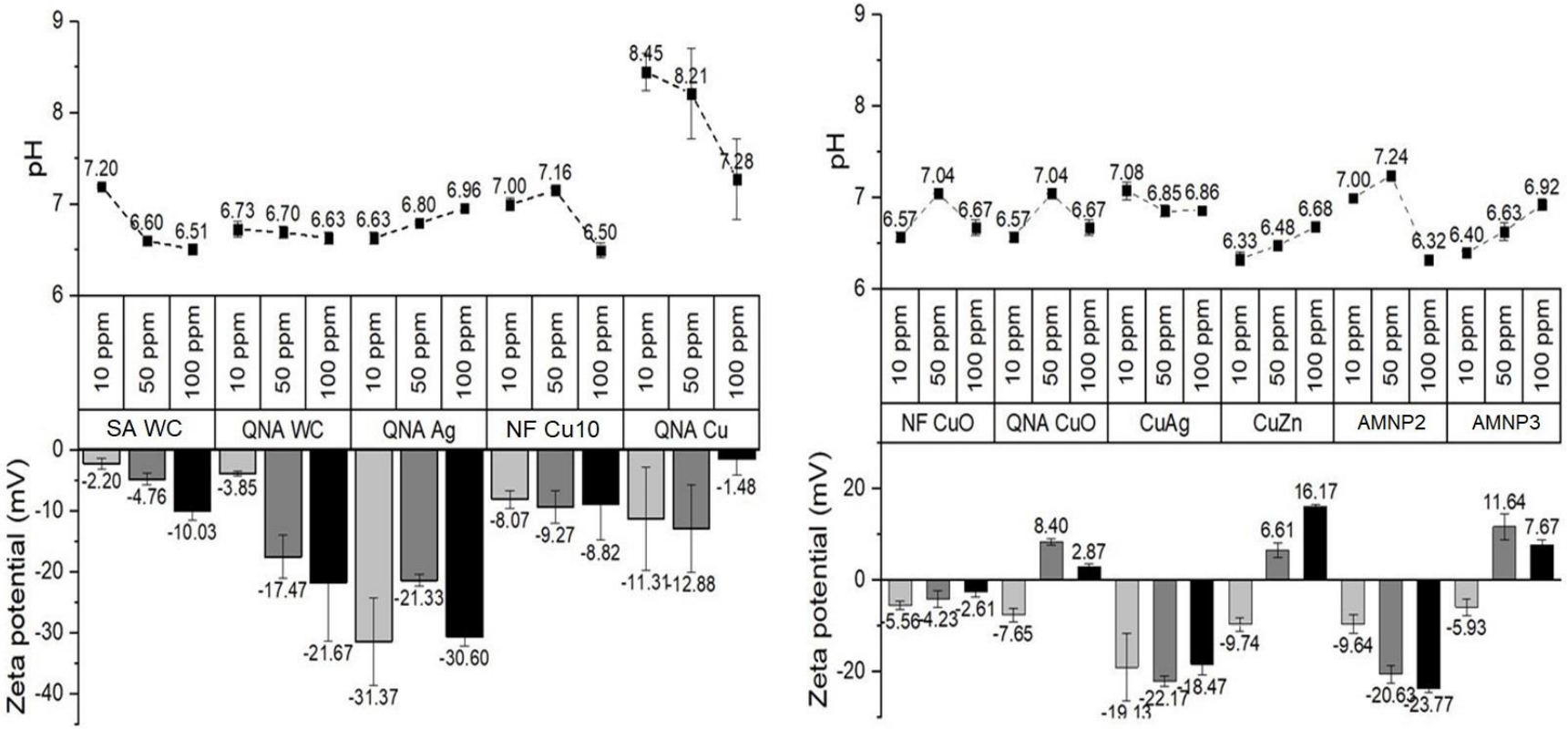


**Figure 4.17** pH and zeta potential measurements of all nanoparticles at 10, 50 and 100ppm.

## 4.5 Summary

The physiochemical properties of both commercial and engineered nanoparticle were measured, the results obtained were analysed and reported in this chapter. All nanoparticle suspensions were well dispersed, the NTA technique was applied to detect the presence of nanoparticle in suspensions at real-time and they showed particle concentrations between $10^8$ to $10^9$ particles/ml and mode size distributions approximately 150 nm which was larger than their powder. In addition, the visualized image generated by NTA can give us direct-viewing information that how each particle moves, and these scattering particles depends on their refractive index. The highest total hydrodynamic concentration was observed from QNA CuO suspension. CuAg suspension had the narrowest distributions. The largest size distributions were QNA Cu and AMNP3 suspensions.

Metal ion leaching from each type of nanoparticles supernatant using ICP-OES were measured. In all nanoparticle suspensions, low concentration of saturated Cu, Ag and Zn ions were found ranging from 0.16 to 1 ppm. The leaching properties of commercial and engineered nanoparticles performed differently in ion release effect and were not related to their purity. The highest ion release in water was $Cu^+$ or $Cu^{2+}$ from QNA CuO, and the highest ion release in saline was $Ag^+$ or $Ag^{2+}$ from CuAg. Additionally, the ion release study among two CuO NPs, alloys and AMNP3 also suggested ion release may depend not only on the type of forms, but also on the pH levels and salt effect in the aqueous media.

The measurement of pH and zeta potential of all samples were also investigated. Samples at different concentrations carried a various impact on pH level as well as zeta potential. This was because the surface charges and particle size of the nanoparticle in the solution not only affects the pH level, but also zeta potential value that reflects the stability of the solution. The pH of all samples was generally in the range between 6 and 7, the highest pH was from QNA CuO. The zeta potential of all samples was mostly negative, QNA Ag, CuAg and AMNP2 suspensions were considered the most stable suspensions.

# CHAPTER 5 ANTIMICROBIAL ACTIVITIES OF NANOPARTICLES AND LOADED FIBRE AGAINST GRAM BACTERIA

## 5.1 Introduction

In this chapter, an attempt to explain how these engineered and commercial nanoparticles may attribute to the interactions or deactivations of specific microbes is carried out. This can give a better understanding of mechanisms of action of nanoparticle behind the antimicrobial activity and assist us in developing more effective antimicrobial agents. The antimicrobial results were carried out using the plate count method generated through collaborative research with University College London. After selecting the highest kill efficiency among all nanoparticle, the incorporation of AMNP2 in PMMA fibre mats were successfully confirmed and tested.

## 5.2 Nanomaterials

### 5.2.0 General

All engineered and commercial nanoparticle samples were used as received and stored a in dark and well-ventilated cupboard. For antimicrobial studies, nanoparticle samples were dispersed either in pure particle-free water (Acros, Belgium) or chloroform from Sigma-Aldrich (Gillingham, UK) at different concentrations. $NH_4OH$ (Fisher Scientific®, UK) was diluted in pure particle-free water by 10 folds before it was used to treat Ag and CuAg NPs.

### 5.2.1 Tungsten carbide

SA WC with particle sizes of 150 - 200 nm was purchased from Sigma-Aldrich (US). The tungsten carbide samples appeared as dark grey powder.

QNA WC was engineered by Intrinsiq Materials® (formally Qinetiq Nanomaterials) using the Tesima™ thermal plasma technology [161]. Please see Section 3.2.1 for more details.

### 5.2.2 Silver

QNA Ag was engineered via the Tesima™ thermal plasma technology [158] provided by Intrinsiq Materials® (formally Qinetiq Nanomaterials). $NH_4OH$ (Fisher Scientific®, UK) was added to treat QNA Ag NPs prior to the sonication process. The details of this nanomaterials are identical to chapter previously reported, please see Section 3.2.2.

### 5.2.3 Copper and copper oxide

Two Cu NPs (QNA Cu and NF Cu10) with various particle shapes and sizes from different manufacturers were used in this study. QNA Cu was engineered by Intrinsiq Materials® (formally Qinetiq Nanomaterials) using patented technology called Tesima™ thermal plasma technology [161]. Commercial powder NF Cu10 was purchased from Suzhou Canfuo Nano Technology. The details of both nanomaterials are identical to chapter previously reported, please refer to Section 3.2.3.

QNA CuO was engineered by Intrinsiq Materials® (formally Qinetiq Nanomaterials) using patented technology called Tesima™ thermal plasma technology [161]. Commercial powder NF CuO rods was purchased from Suzhou Canfuo Nano Technology. The details of both nanomaterials are identical to chapter previously reported, please refer to Section 3.2.3.

### 5.2.4 CuAg and CuZn alloys

The alloy nanoparticles CuZn and CuAg were purchased from Sigma-Aldrich (Dorset, UK). $NH_4OH$ (Fisher Scientific®, UK) was added to treat CuAg NPs prior to the sonication process. The details of both nanomaterials are identical to chapter previously reported, please refer to Section 3.2.4.

### 5.2.5 AMNP2 formulation

AMNP2 was previously engineered by Intrinsiq Materials® (formally Qinetiq Nanomaterials) using the Tesima™ thermal plasma technology [161]. The details of this materials are identical to chapter previously reported, please refer to Section 3.2.5.

## 5.3 Instrumentation and methodology

### 5.3.1 Preparations of nanoparticle dispersions

For antimicrobial test, nanoparticles were weighed using a microbalance (*Shimadzu, Japan*). A titanium alloy Ti-Al-V liquid processor (Sonics & Materials®, USA, VC-750, Ø 13 mm, 750 W output power, 20 kHz) was used to disperse nanoparticle suspensions in water saline prior their physiochemical analyses. Please refer to Section 4.3.1 for the specification of sonication. For PMMA fibre mats incorporation, the procedure was the same at the mention, AMNP2 dispersed in chloroform instead of aqueous medium.

5.3.2 AMNP2 embedded PMMA fibre mats using pressurized gyration.

PMMA ($M_w$ 120,000 g/mol) and chloroform were obtained from Sigma-Aldrich (Gillingham, UK). 20 w/w% PMMA solution was prepared by dissolving PMMA in chloroform. The polymer solution was magnetically stirred for 24 hours to obtain a homogeneous solution. The AMNP2-loaded PMMA fibre mats were prepared by adding 0.5 w/w% of AMNP2 to the PMMA solution. The solutions were stirred for 30 minutes before spinning in order to ensure homogenous distribution of AMNP2. The details of the pressurized gyration apparatus and the preparation of the fibre mats are reported elsewhere [149].

5.3.3 Growth of bacterial strains

For the antimicrobial activities of nanoparticle, bacteria stock cultures of *P. aeruginosa* (NCTC 12903) and *S. aureus* (ATTC 6538P) were obtained from -80 ˚C freezer stocks containing 30% glycerol. Each stock solution was streaked onto Tryptic Soya Agar using a sterile loop and incubated at 37˚C for 24 hours. After incubation, a single colony of each strain was grown in Luria broth and placed on a shaker (150 rpm) for a further 24 hours at 37˚C. A 1:100 dilution of the overnight culture of each pathogen and inoculated into metallic nanoparticle samples at 0.05, 0.1 and 0.25 wt/v% concentrations using high power sonication for 2 min, in triplicate with Luria broth and incubated at 37˚C, shaken (150 rpm) for 24 hours.

For the antibacterial activity of loaded polymer fibres, the cells were cultured in nutrient broth (Oxoid, UK) for 16 hours at 30 °C and agitation at 150 rpm. The culture was then centrifuged at 4000 rpm for 15 min, the supernatant discarded and the cells resuspended in 100 mL phosphate buffered saline (PBS, Sigma-Aldrich).

5.3.4 Antimicrobial testing using the plate count.

For the antimicrobial activities of nanoparticles, viable bacterial cell concentrations were estimated by counting CFU's before and after exposure to the nanoparticle compounds. This was performed by serial dilution in Luria broth and then removing 10 µL of the serially diluted culture and spreading with sterile glass beads (5mm, Sigma-Aldrich, UK) onto an agar plate (Tryptic Soya Agar) in triplicate. The plates were then incubated at 37˚C for 24 hours and CFUs were counted. The results were expressed in terms of colony forming units (CFU) and the equation was applied [186]:

$$log(CFU/ml) = log(\frac{the\ number\ of\ colonies\ counted \cdot the\ dilution\ factor}{volume\ of\ culture\ plate}) \quad (5\text{-}1)$$

For the antibacterial activity of loaded polymer fibres, 0.5 w/w% AMNP-loaded fibre mats were assessed using Gram-negative *P. aeruginosa*. The cell suspension in PBS was then passed through the fibre mats deposited on discs at a flow rate of 1.67 ml/min. A sample of the bacterial suspension was taken before and after filtration through the mat. 10-fold serial dilutions were performed on all samples and these were then plated onto nutrient agar (Oxoid, UK) and incubated at 30 °C for 24 h, after which the number of viable colony-forming units of bacteria was obtained and a reduction due to filtration in viable number was calculated.

5.3.5 Result conversion (from log reduction to percentage reduction)

The antimicrobial results are presented either in percent reduction or log reduction. To convert log reduction to percent reduction, the following equation was applied:

$$P = (1 - 10^{-L}) \times 100\% \quad (5\text{-}2)$$

Where $P$ is percent reduction and $L$ is log reduction, respectively.

5.4 Results and discussion

Bacterial cell quantification after exposure to antimicrobial compounds was carried out to determine antimicrobial properties of engineered and commercial nanoparticles. The antimicrobial results were calculated using **Equation (5-1 )** and the log reduction were converted to percent reduction using **Equation (5-2)**. We hoped to link the antimicrobial effects to the physiochemical properties of nanoparticles we investigated throughout this research.

Overall, the size of nanoparticle may one of factors that directly or indirectly affected antimicrobial effects. For instance, smaller hydrodynamic particle sizes of nanoparticles have better antimicrobial effects [19, 122, 160, 187]. The reason of this can be explained as (1) smaller particles have greater quantity of particles at the same weight and relatively higher ratio of surface area to volume as compared to larger individual particles, thereby increasing the rate of reactive oxygen species (ROS) production and ions to kill bacteria, or (2) nanoparticles of tiny size can penetrate the cell wall of bacteria and/or uptake into cells to consequently cause cellular dysfunction [144, 145].

Shapes may also influence the antimicrobial effect of nanomaterials. A previous assumption from us was that rod-shaped *P. aeruginosa* and spherical *S. aureus* are easily killed by similar shapes of antimicrobial nanoparticles based on SEM images (shown in **Figure 5.1**). However, this assumption was found to only apply to some cases of this study. A study from Wang *et. al.* (2014) considered that nanocubes and rod shapes were more effective to kill bacteria due to the exposed planes and to the oxidation levels of the metals, whereas another study reported that hexagonal plate-like ZnO nanocrystals displayed significantly higher activity than rod-shaped crystals [188, 189].

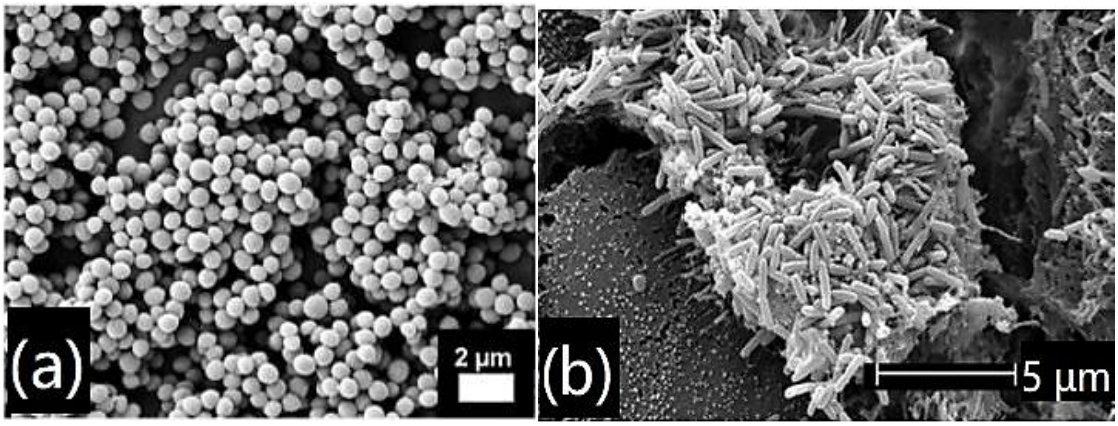


**Figure 5.1** SEM images of (a) *S. aureus and (b) P. aeruginosa* as representative of Gram-positive and Gram-negative bacteria, respectively [190, 191].

### 5.4.1 Antimicrobial effects of all engineered QNA nanoparticles

The engineered QNA nanoparticles (QNA WC, QNA Ag, QNA Cu and QNA CuO) were produced using thermal plasma Tesima™ process in which the precursor was evaporated at a sufficiently high temperature and atomized in a furnace, followed by decomposed into nanoparticles.

As shown in **Figure 5.2**, two WC NPs at all concentration showed no inhibitory effect on both bacteria, therefore they are determined to be exclusive of antimicrobial agents. The engineered QNA Ag, QNA Cu and QNA CuO were found to perform specific inhibitions against one type of the bacterium more than the other which agreed with studies that were previous reported by Ren *et. al.*[37]. In this report, engineered QNA Ag, QNA Cu and QNA CuO also showed antimicrobial effects against Epidemic methicillin-resistant *Staphylococcus aureus* (EMRSA), *S. epidermidis* and *E. coli*. Each element will be discussed in the following sections.

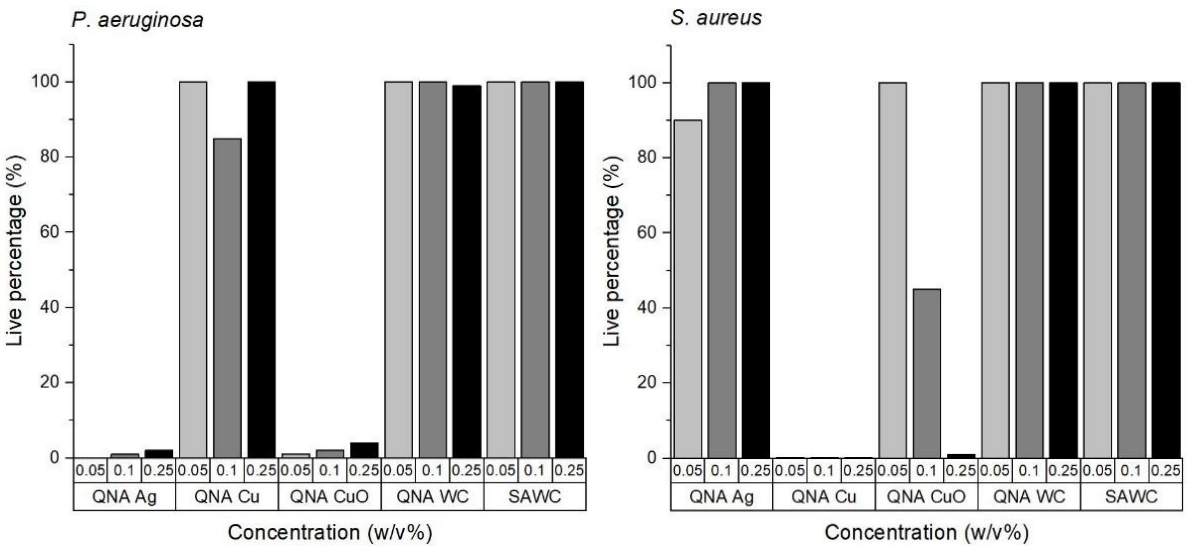


**Figure 5.2** Antimicrobial results of SA WC and QNA nanomaterials standards against *P. aeruginosa* and *S. aureus*[2] using the plate count method.
QNA materials were found to perform specific inhibitions against at least one type of the bacterium, except QNA WC.

### 5.4.2 Antimicrobial activities of Ag NPs

Studies have shown that the element that have antimicrobial properties is usually a transition metal such as Au, Ag, Cu and Zn, of which have incompletely filled d orbitals, so the redox activity is higher [144]. Recall that some certain essential transition metal ions present in biomolecules act as catalytic cofactors under normal conditions, excess quantities of them can be very toxic to bacteria [192]. Ag has a long history of being used as antimicrobial agents, thus various ways of cell disruptions have been studied more extensively [193].

In **Figure 5.2**, engineered QNA Ag showed to counter extremely well against *P. aeruginosa* at the minimum concentration at 0.05 wt/v%. Unexpectedly, this engineered QNA Ag showed almost no effect against the Gram-positive strain *S. aureus* and the lowest live bacteria population was observed from the lowest concentration of QNA Ag. According to previous studies, the release of $Ag^{+}$ or $Ag^{2+}$ ions is one of main antimicrobial mechanisms to inhibit bacteria, particularly the Gram-negative strain *P. aeruginosa*, because Gram-negative bacteria cell walls have lower resistance and negative-charged lipopolysaccharide electrostatically attracts $Ag^{+}$ or $Ag^{2+}$ ions into the bacteria cell (**Figure 5.3**) [144, 159]. Besides, $Ag^{+}$ or $Ag^{2+}$ ions may penetrate the bacterial cell wall as well [194]. Remember that the XRD

[2] Antimicrobial results were provided by research partner at UCL.

results showed QNA Ag contained $AgNO_2$ and $AgNO_3$ except elemental Ag, and $AgNO_3$ consists of an ionic bond between $Ag^+$ and $NO_3^-$, which easily dissolves in water and release $Ag^+$ or $Ag^{2+}$ ions to enhance antimicrobial properties. Consequently, $Ag^+$ or $Ag^{2+}$ ions can cause cellular dysfunction by (1) interacting with thiol groups (-SH) in enzymes and proteins resulting in protein deactivation; (2) forming complex with nucleic acids (such as DNA and RNA) to prevent cell division and reproduction; and (3) binding other biomolecules [5, 194, 195].

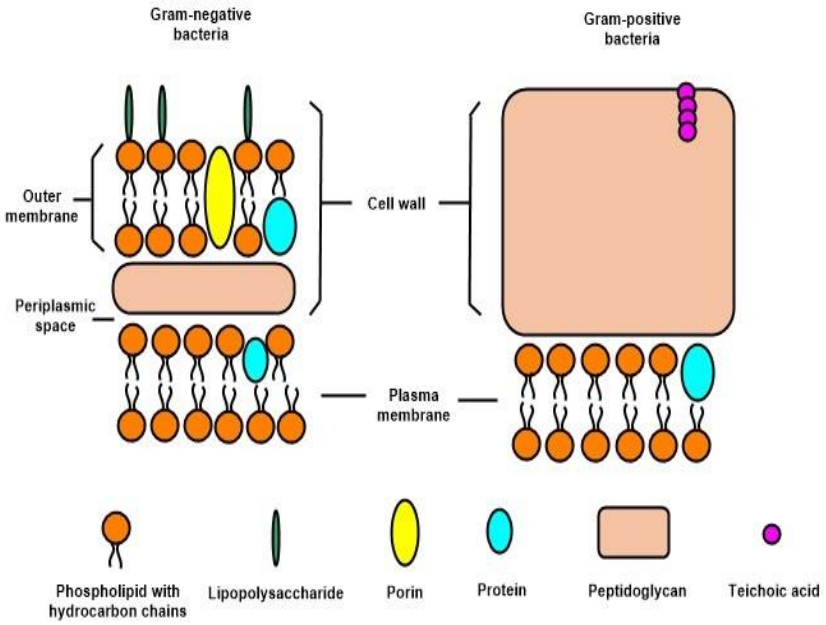


**Figure 5.3** Structure difference of Gram-negative and Gram-positive bacteria [144]. Gram-positive bacterial cell walls are thicker than Gram-negative as it has a thick and multi-layered peptidoglycan which acts as a protective layer.

Additionally, Ag NPs have also been found to inhibit bacteria by themselves. It has observed that Ag NPs can anchor to the bacterial cell wall, which physically damaged bacterial membrane and lead to cellular leakage and bacterial death [106, 196]. Alternatively, Ag NPs can also penetrate the membrane and enter the bacteria, followed by interacting with cellular structures and biomolecules such as proteins, lipids, and DNA [194]. The previous literature showed that *P. aeruginosa* cells treated with Ag NPs were elongated possibly due to stress conditions arresting cell division [144]. However, this activity may greatly vary with the size of Ag NPs [111]. Choi *et. al.* (2008) demonstrated that Ag NPs were difficult to move into the bacteria when their particle size is greater than 20 nm. At a particles size of around 5 nm, Ag NPs showed significantly more efficiency than 10 - 20 nm [187]. Looking through our NTA result (see Section 4.4.3.2), the particle size of QNA Ag was far from 20 nm, which in turn

demonstrated that the ROS production (see later) and/or $Ag^{+}$ or $Ag^{2+}$ ions dominated the effective antimicrobial activities in this case.

Last but not least, capping agents may have an effect on the toxicity of the nanoparticles, except increasing their dispersibility. Cavassin *et. al.* (2015) determined that Ag NPs stabilized with citrate and chitosan were more effective in killing bacteria than with polyvinyl alcohol and Ag NP alone because of an accelerated generation of $Ag^{+}$ or $Ag^{2+}$ ions [197]. In our case, although tiny amount of $NH_4OH$ was added into QNA Ag and CuAg suspensions, it may also help inhibit bacteria since it is alkalis.

### 5.4.3 Antimicrobial activities of Cu and CuO NPs

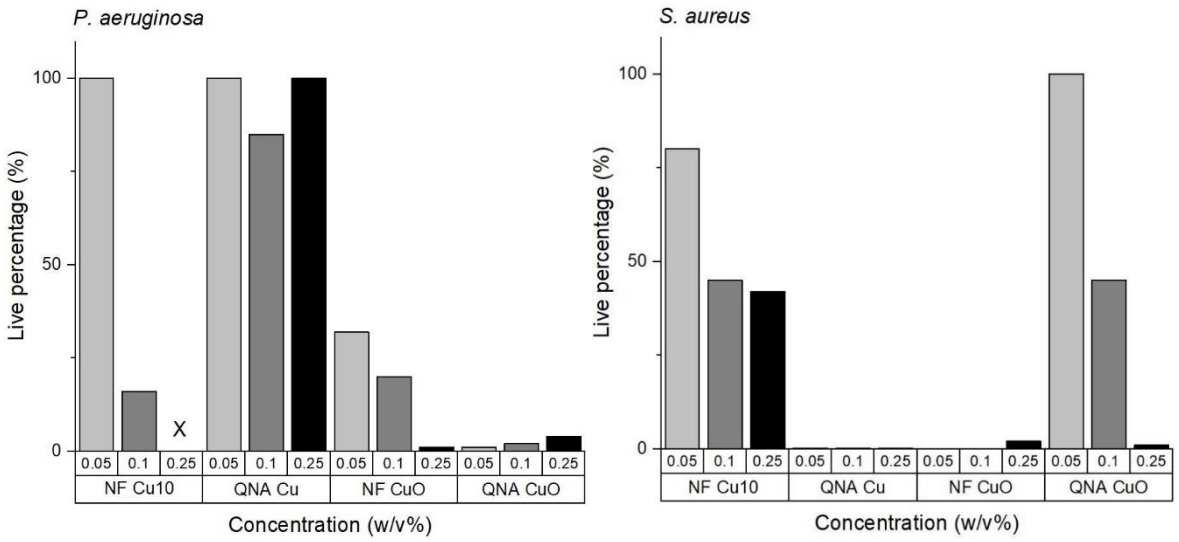


**Figure 5.4** Antimicrobial results of Cu and CuO nanomaterials standards against *P. aeruginosa* and *S. aureus*[2] using the plate count method.
NF Cu10 killed less bacteria than QNA Cu, and two CuO NPs were more effective to one type of the bacterium than the other.

Comparing with the engineered QNA Cu, commercial NF Cu10 made in China was overall found to have weaker antibacterial effects on *P. aeruginosa* and *S. aureus* (**Figure 5.4**). Apart from the antimicrobial result against *P. aeruginosa* of NF Cu10 at a concentration of 0.25 wt% was not available, NF Cu10 NPs killed more *P. aeruginosa* than *S. aureus* at 0.1 wt% of concentration, while the lowest concentration had the opposite result. By contrast, engineered QNA Cu NPs killed nearly all *S. aureus* even at the lowest concentration (0.05 wt%), while the three concentrations almost had no effect on *P. aeruginosa*. Engineered QNA CuO and commercial NF CuO NPs were found to perform slightly better antimicrobial effects

over the two Cu NPs, but the opposite activity of inhibiting bacterial strains was found. The commercial NF CuO rods NPs completely inhibited *S. aureus* except at the highest concentration (0.25 wt/v%) and the inhibition activity against *P. aeruginosa* was more than 70%. By contrast, QNA CuO showed to have better antimicrobial activities against both bacteria, the live populations of *P. aeruginosa* after exposure to QNA CuO at the three concentrations were no more than 5% and the antibacterial ability against *S. aureus* increased with the nanoparticle concentration until the concentration of 0.25 wt/v% killed 99% of bacteria. This antimicrobial effect of CuO correlated with the susceptibility of various microorganisms. Based on previous studies, *S. aureus* (Gram-positive) was more sensitive to CuO NPs comparing with *P. aeruginosa* (Gram-negative) because It has more -NH and -COOH groups on the cell surface and these groups are more sensitive to Cu. The antimicrobial result in this study may need further investigate [122]

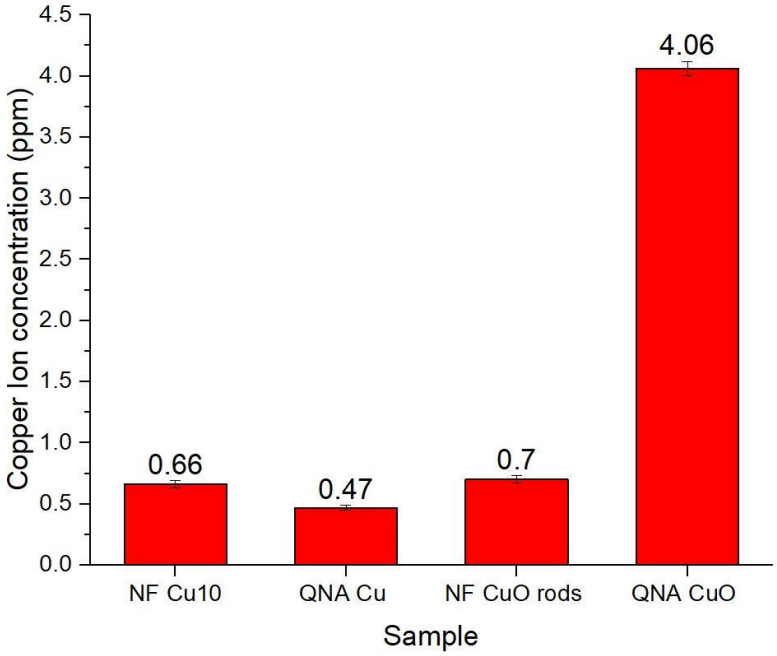


**Figure 5.5** Ion release of Cu and CuO NPs in water at concentration of 0.1 wt/v%. QNA CuO released much more ions than others but did not show the highest antimicrobial efficiency, especially for *S. aureus*.

According to reports, Cu NPs are found to be less efficient in killing bacteria in comparison to Ag NPs, even though Cu is expected to have a higher rate of ion release [198]. It may be explained by the fact that $Cu^{+}$ or $Cu^{2+}$ ions are a necessary co-factor (essential element) for different enzymatic systems and that cells possess mechanisms to maintain its homeostasis by avoiding its intracellular toxicity, whereas $Ag^{+}$ or $Ag^{2+}$ ions can irreversibly binding biomolecules [144]. In our case, engineered QNA CuO released over four times more $Cu^{+}$ or

$Cu^{2+}$ ions than other Cu-based samples (**Figure 5.5**) and overall QNA CuO exhibited the best inhibitory effect against both bacteria (**Figure 5.4**), while the ion release of QNA Ag was only 0.82 ppm.

As another major antimicrobial mechanism, reactive oxygen species (ROS), that includes superoxide anion radicals ($O_2^-$), hydroxyl radicals ($OH^*$), singlet oxygen ($^1O_2$) and hydrogen peroxide ($H_2O_2$), are supposed to be formed as natural by-products of cellular oxidative metabolism due to incompletely reduced O [199]. However, in the case of excessive $Cu^+$ or $Cu^{2+}$ ions, Haber-Weiss and Fenton reaction take place to overproduce ROS. The overproduction of ROS can induce oxidative stress, which damages cellular protein, lipid, DNA strand, nucleic acids, *etc.*, leading to cell death and genotoxic effects [200, 201]. In particular, $^1O_2$ is considered the most toxic species to bacteria cells, widely reacting with amine acids, vitamins, unsaturated fatty acids, proteins, and steroids. And $OH^*$ is also a strong oxidant oxidizing macromolecule such as carbohydrates, nucleic acids, lipids, and amino acids. $H_2O_2$ is generated by $O_2^-$, which can transform into $OH^*$ and $O_2$ [202]. Moreover, it also has been observed that $H_2O_2$ may penetrate the cell membrane [203]. Eventually, the ROS may have a collective effect on killing bacteria. It is important to highlight that other metals such as Zn, Fe can also trigger this mechanism [187, 204]. In previous elemental analysis, the intensity of Fe238.204 emission (236.166) detected in QNA Cu was much higher than blank (84.4505) and NF Cu10 (66.6111) (Please see Table 3.4), which may imply that the presence of Fe from QNA Cu also assist in killing bacteria as well.

Similarly, the antimicrobial effect of Cu and CuO NPs have been found to be size distribution dependent [122, 205], which potentially trigger the differences of $Cu^+$ or $Cu^{2+}$ ions and ROS level. Providing the NTA results presented in **Figure 5.6a**, although the mode size of NF Cu10 (200 nm) was slightly smaller than that of QNA Cu (250 nm), the total particle concentration of NF Cu10 was very low, suggesting that NF Cu10 NPs had heavy agglomeration and poor stability. This may be the reason why NF Cu10 had the opposite result at different concentrations. In **Figure 5.6b**, a similar NTA result also happened to both CuO NPs; the total particle concentration of NF CuO was much lower than that of QNA CuO. The NTA result indicated that the stability of NF materials in water was lower than that of QNA materials, and because of its hydrophilicity, CuO was more dispersed than hydrophobic Cu. All the above events can jointly explain the complex reasons for the antimicrobial results of CuO and Cu NPs.

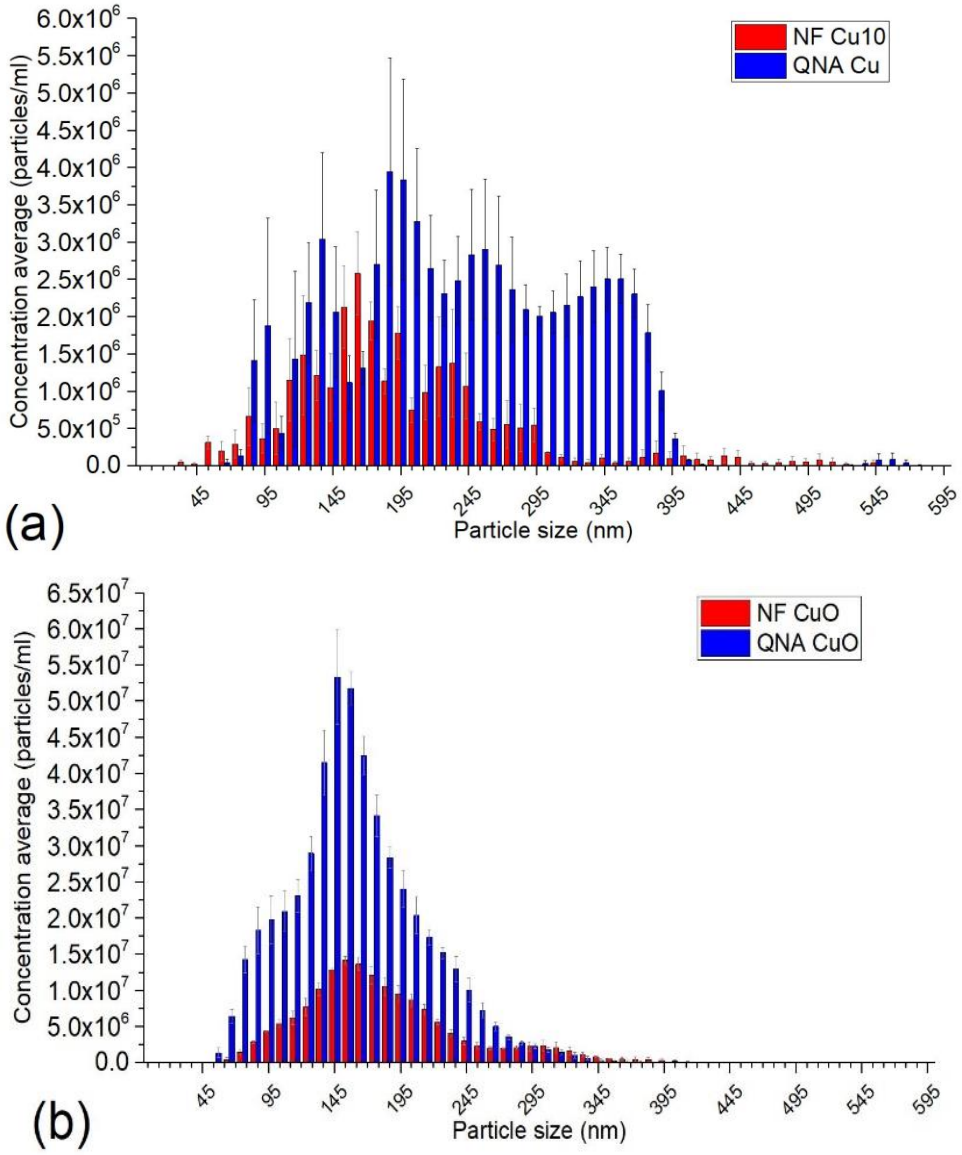


**Figure 5.6** Comparison of particle concentrations of (a) NF Cu10 and QNA Cu; and (b) NF CuO and QNA CuO using NTA.

NF materials in water was lower than that of QNA materials, and the size distributions among them were very different triggering the differences of $Cu^{+}$ or $Cu^{2+}$ ions and ROS level.

### 5.4.4 Antimicrobial activities of CuAg and CuZn NPs

As illustrated in **Figure 5.7**, it was found that commercial CuAg and CuZn NPs performed favourable antimicrobial activities against both bacterial strains. The antimicrobial result of CuAg alloy showed increasing inhibition with the higher concentration of the nanoparticle until at concentration 0.25 wt/v% almost completely inhibited *P. aeruginosa*, while that of *S. aureus* was the opposite. On the other hand, CuZn alloy observed more than 90% reduction

in both bacteria and the antimicrobial results at concentrations higher than 0.05 wt% were increased compared with that of 0.05 wt%. At concentrations of 0.25 and 0.1 wt/v%, CuZn can completely inhibit *P. aeruginosa* and *S. aureus*, respectively. Overall, both alloy nanoparticles showed more desirable antimicrobial properties in comparison of previous nanoparticles.

This antimicrobial activities of dual-element nanoparticles indicated that each element from these compounds may not only play respective roles in inhibiting each bacterium such as ion release, generation of ROS and binding intercellular, but also exerted a synergetic effect [134, 206]. Specially, CuAg NPs released $Ag^{+}$ or $Ag^{2+}$ ions, that was slightly lower than QNA Ag, as well as a tiny amount of $Cu^{+}$ or $Cu^{2+}$ ion, but the antimicrobial effect against *S. aureus* was massively enhanced comparing with QNA Ag. Besides, Zn from CuZn has been proved to effectively act in a similar way to antimicrobial mechanisms of Cu [134].

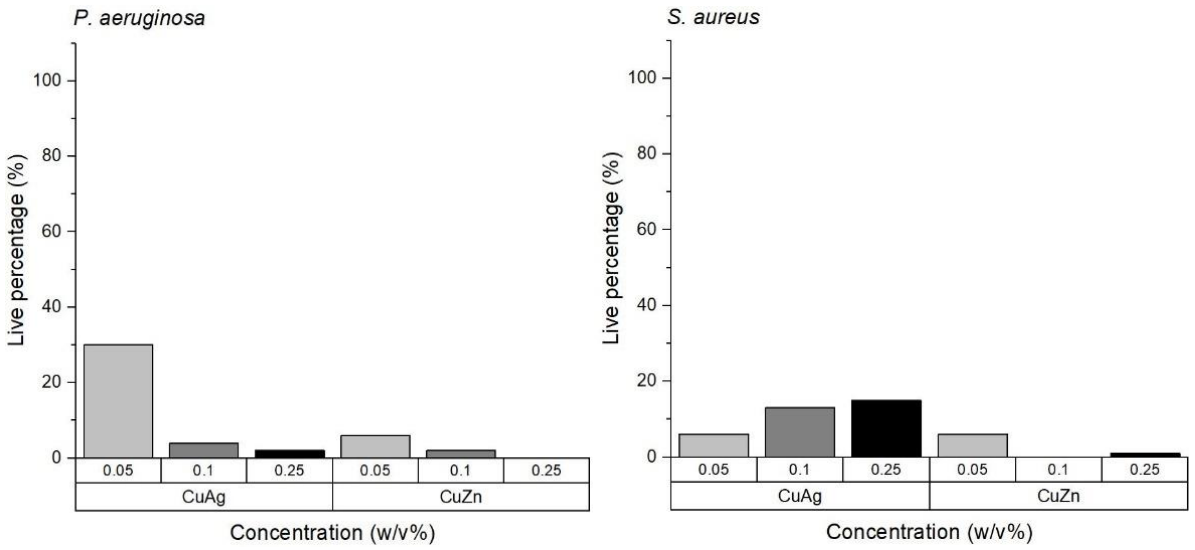


**Figure 5.7** Antimicrobial results of CuAg and CuZn nanomaterials standards against *P. aeruginosa* and *S. aureus*[2] using the plate count method.
The populations of live bacteria exposure to CuAg were less than 30%, while CuZn had even lower live bacteria.

5.4.5 Antimicrobial activities of AMNP2 formulation

In **Figure 5.8**, engineered AMNP2 performed very favourable antimicrobial inhibitions against both bacteria, only up to 0.1% bacterial survived after exposure to AMNP2. As the most complex nanomaterial, AMNP2 have many factors of destroying bacterial. Firstly, with elements more than Cu and Ag, AMNP2 may exert a stronger synergetic effect more than

CuAg and CuZn [165]. Besides, there are many researches indicating carbon-based materials can possess or enhance antimicrobial effects [139]. Particularly, carbon-based materials prepared by sonication are uniformly dispersed, which played a great role in binding metals to reinforce dispersibility and prevent their agglomeration[207, 208]. In another study, the author suggested that AMNP2 was not only effective for tumor-related inflammation, but also shows enlightenment for further research on cancer solutions [209].

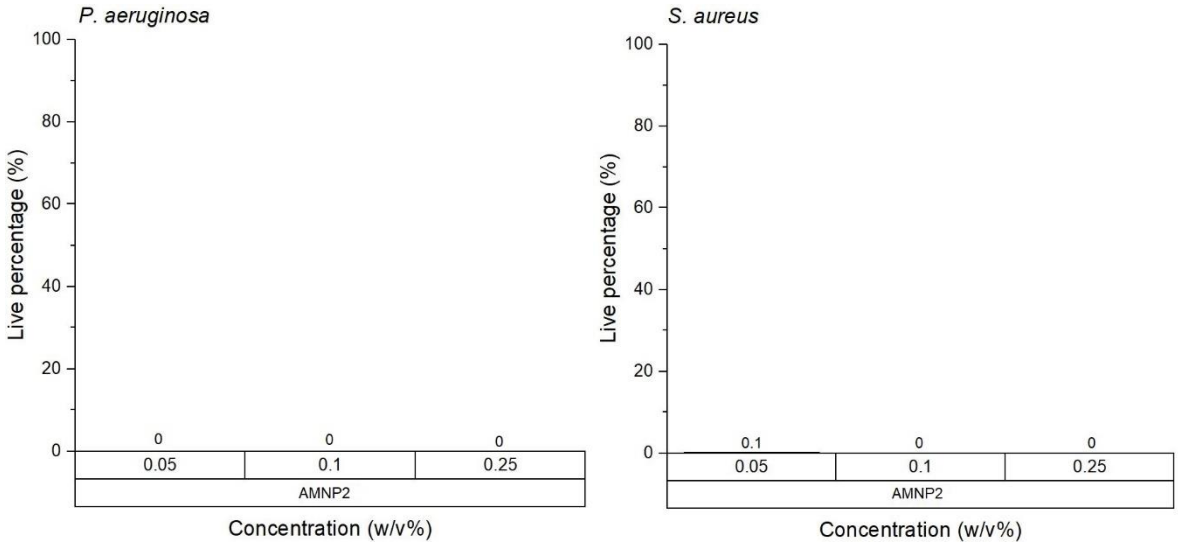


**Figure 5.8** Antimicrobial results of AMNP2 nanomaterials standards against *P. aeruginosa* and *S. aureus*[2] using the plate count method. AMNP2 killed both bacteria even the lowest concentration.

### 5.4.6 Antimicrobial activities of AMNP2-loaded fibre mats

According to the results of our collaborator University College London, the PMMA fibres loaded with AMNP2 was spun at a speed of 36,000 rpm and a working pressure of 0.3 MPa, which was confirmed by energy dispersive x-ray analysis [149]. As shown in **Figure 5.9**, the antimicrobial activity of the pure PMMA fibres was reduced *P. aeruginosa* cells by about 35%, while the antimicrobial activity of fibres loaded with 0.5 w/w% AMNP2 was reduced the bacteria cells by about 72%. PMMA is considered to be an ideal polymeric biocide since they have positively charged molecular chains in the fibres which attract negatively charged bacteria such as *P. aeruginosa* [210]. Additionally, the reduction of bacteria may be simply due to entrapment in the polymer fibres. Compared with the pure PMMA fibres as control, the reduction of bacteria was higher indicating that the incorporated AMNP2 can more effectively kill the bacteria, which was analysed in the last section. Nevertheless, AMNP2-

loaded PMMA fibres still killed less bacteria than AMNP2 formulation and it may need further research on incorporation of more nanoparticles into PMMA fibres.

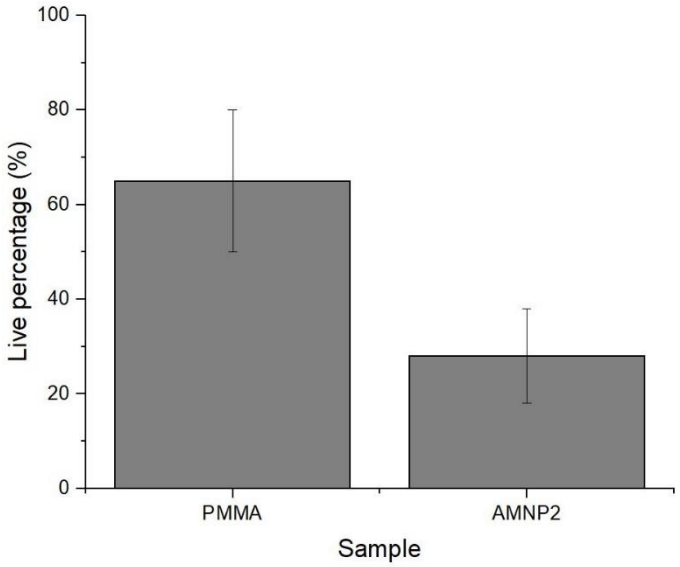


**Figure 5.9** Antimicrobial results of pure PMMA fibres and 0.5 w/w% of AMNP2-loaded PMMA fibres against *P. aeruginosa*[1,2].
the pure PMMA fibres reduced *P. aeruginosa* cells by about 35%, while that of 0.5 w/w% AMNP2 was about 72%.

## 5.5 Summary

In conclusion, this chapter intended to explain antimicrobial effect from perspective of nanoparticle properties. Apart from two WC NPs showing no inhibitory effect, Ag, Cu and Zn elements performed in complex and combined ways to kill bacteria. The excess formation of reactive oxygen species (ROS) overwhelmed the cellular antioxidant defence system and oxidative stress occurs causing damage to DNA, RNA, and proteins. The release of ions interacted with the functional groups of proteins and nucleic acids to cause cellular dysfunction. Physical contact damaged bacterial membrane leading to cellular leakage and bacterial death. In this study, Ag was the most effective elements among Cu and Zn, two of the three above metals showed a synergetic effect which was much more effective than single one.

After the formulation AMNP2-loaded PMMA fibre mats successfully showed more than double reduction of *P. aeruginosa* cells compared to the pure PMMA fibers, CuAg and CuZn are considered to be another two potential candidates for antimicrobial applications in biomedical engineering. Nevertheless, it is still essential to further investigate their stability to incorporate of more nanoparticles into PMMA fibers.

# CHAPTER 6 INVESTIGATION OF NANOPARTICLE SUPERNATANTS AND DISPERSANTS

## 6.1 Introduction

The antimicrobial activities showed QNA Ag, CuAg, CuZn and AMNP2 were favourable antimicrobial nanoparticles, while NF Cu10 was not. The reason may be explained that these metallic nanoparticles suspended in liquids are prone to form aggregates and settled fast due to gravity and other factors, thereby reducing chance of nanoparticles exposure to the microbes. The aim of this chapter is to analyse the stability of nanoparticle suspensions varying with time so that it would allow these favourable antimicrobial nanoparticles to be optimally incorporated into PMMA fibres.

This chapter first initially studied the ratio of gravity to Brownian force to predict the tendency of nanoparticle settling [211]. This was based on the density and hydrodynamic particle size of each nanoparticle (NF Cu10, QNA Ag, CuAg and AMNP2), where the density of CuAg and AMNP2 were theoretically calculated and the weight percent of AMNP2 formulation was converted from atomic percentage. In order to study the nanoparticle supernatants and dispersants, two different NTA methods were performed to analyse their span values and mass concentrations. The span value describes with one single value whether the relative dispersion of nanoparticles is wide or narrow and how much it has. The mass concentration shows the concentration expressed by the mass of the solute in parts per million (ppm) of the mass of the total solution. Overall, they have opposite expectations – the lower span the sharper size distribution and the higher mass concentration the better the dispersion.

## 6.2 Nanomaterials

### 6.2.0 General

All engineered and commercial nanoparticle samples were used as received and stored a in dark and well-ventilated cupboard. Please see Section 5.2.0.

### 6.2.1 Silver

QNA Ag was engineered via the Tesima™ thermal plasma technology [158] provided by Intrinsiq Materials® (formally Qinetiq Nanomaterials). $NH_4OH$ (Fisher Scientific®, UK) was added to treat QNA Ag NPs prior to the sonication process. Please see Section 3.2.2.

### 6.2.2 Copper

Commercial NF Cu10 was purchased from Suzhou Canfuo Nano Technology, it was claimed to have 10 - 30 nm particle size range and a spherical shape. The details of this nanomaterials are identical to chapter previously reported, please refer to Section 3.2.3.

### 6.2.3 CuAg alloy

The commercial CuAg nanoparticles were purchased from Sigma-Aldrich (Dorset, UK). $NH_4OH$ (Fisher Scientific®, UK) was added to treat CuAg NPs prior to the sonication process. The details of this materials are identical to chapter previously reported, please refer to Section 3.2.4.

### 6.2.4 AMNP2 formulation

AMNP2 was previously engineered by Intrinsiq Materials® (formally Qinetiq Nanomaterials) using the Tesima™ thermal plasma technology [161]. The details of this materials are identical to chapter previously reported, please refer to Section 3.2.5.

## 6.3 Instrumentation and methodology

### 6.3.1 The ratio of gravitational force to Brownian force

A functional suspension is expected to keep the suspension stable for the lifetime and/or easily occur dispersed settling. To predict whether nanoparticle suspensions keep the suspension stable physically or not, the ratio of gravitational force to Brownian force can estimate likelihood for settling [212]:

$$Ratio\ of\ gravitational\ force\ to\ Brownian\ force = \frac{r^4 \Delta\rho g}{k_b T} \quad (6\text{-}1)$$

Where r is the particle radius; $\Delta\rho$ is the density difference between the dispersed and medium phase; the gravity of Earth is $g = 9.8\ m/s^2$; the Boltzmann constant $k_b = 1.38 \times 10^{-23}\ J/K$; and temperature $T = 298\ K$.

6.3.2 The theoretical density of the mixture by the weight percent

The density of a mixture follows the rule of mixtures, which is based on the constituents. To determine the density of the sample by weight, it is defined as [213, 214]:

$$\frac{1}{\rho_{total}} = \frac{x}{\rho_a} + \frac{y}{\rho_b} + \frac{z}{\rho_c} \quad (6\text{-}2)$$

Where $\rho_a$, $\rho_b$ and $\rho_c$ are, respectively, the density of different elements and $x, y$ and $z$ is the weight ratio of the sample. The calculation assumes perfect mixing and that the sum of the initial volumes of the metals equals the total final volume.

6.3.3 Preparations of nanoparticle dispersions

All nanoparticles were weighed using a microbalance (*Shimadzu, Japan*). A titanium alloy Ti-Al-V liquid processor (Sonics & Materials®, USA, VC-750, Ø 13 mm, 750 W output power, 20 kHz) was used to disperse nanoparticle suspensions prior their physiochemical analyses. Please refer to Section 4.3.1 for the specification of sonication.

6.3.4 Analysis of nanoparticle supernatants and dispersants

In nanoparticle supernatant study, concentrations of 1000 ppm samples were prepared using 2 mg of QNA Ag/QNA Cu NPs of which were dispersed in 20 mL of Acros pure particle-free water using high power sonication for 2 minutes. Each suspension was shaken and then stood for 30 minutes before measurement, 1 mL of supernatant of the suspension was collected daily and then filtered using 0.1 µm syringe filter (Millipore) to be submitted to NTA for 5 days.

In nanoparticle dispersant study, concentrations of 10, 50 and 100 ppm samples were prepared using 0.2/1/2 mg of the four selected nanomaterials (QNA Ag, NF Cu10, CuAg and AMNP2) of which were dispersed in 20 mL of Acros pure particle-free water using probe sonication for 2 minutes. All samples were directly loaded in syringes during NTA measurements. The sample in each syringe was collected in triplicate at beginning and every 10 up to 30 minutes, during which the syringe stays still. Please see Section 4.3.2 for the specification of NTA.

### 6.3.5 The D-value and span value

A D-value can be thought of the cumulative undersize distribution showing the relative amount at/below a certain size. Usually, D10, D50 and D90 are used to investigate a particle size distribution curve.

A relative fractional measure of width is obtained by dividing (D90 – D10) by the measure of midpoint D50 as follows:

$$span = \frac{D90-D10}{D50} \times 100\% \quad (4\text{-}1)$$

which is referred as the span value and gives an indication of how far the D10-to-D90 range of particles is normalized with the midpoint (D50). Please see Section 4.3.3 for more explanations.

### 6.3.6 Interpretative method for particle concentrations and distributions

The nanoparticle size distributions were interpreted using the “vertical view” as displayed in **Figure 6**, where the size distribution graphs were presented side by side. The results of each nanoparticle suspension at different times are displayed on the x-axis and consists of five different symbols in a collinear line with different representative symbols. D10 and D90 are, respectively, represented by two triangle symbols (▼ and ▲). The value of mode size, median size (D50) and mean size are, respectively, represented by star (★), square (■) and round (●).

In addition, right y-axis shows a total concentration of the nanoparticle represented by grey bars. The specific value of concentration is located at the bottom of the bar. Therefore, the hydrodynamic particle concentration and size distribution of a nanoparticle suspension can be showed together.

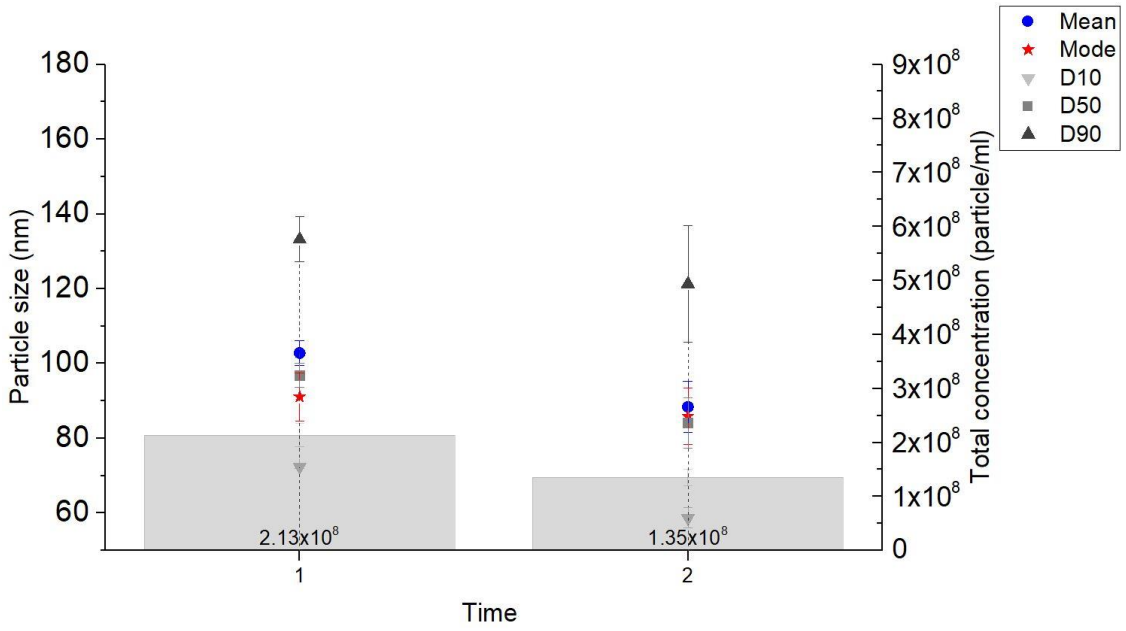


**Figure 6.1** A schematic graph of analysing particle concentration and size distribution. Left y-axis shows the results of the same suspension at different times, which consists of five different symbols of the collinear line. Right y-axis shows a total concentration of the nanoparticle represented by grey bars. The specific value of concentration is located at the bottom of the bar.

### 6.3.7 Unit conversion (from particles/ml to ppm)

To convert the number of particles per millilitre into the mass concentration, it requires to estimate the volume of each particle which is then multiplied by the density of the particle and the number of particles to obtain the concentration $c$ in ppm as following:

$$c = \text{number of particles/ml} \times \rho_p \times V_p \quad (6\text{-}3)$$

Where $c$ is the mass concentration of the particle, $\rho_p$ and $V_p$ are the density and volume of each particle, respectively.

## 6.4 Results and discussion

### 6.4.1 Theoretical calculation of the nanoparticle stability

The ratio of gravitational force to Brownian force of nanoparticles was calculated using **Equation (6-1)**. The particle size was determined by SEM images or reported elsewhere

[165]. The average particle size of QNA Ag, NF Cu10, CuAg and AMNP2 were, respectively, 100, 20, 92 and 15 nm. The density of Cu and Ag are, respectively, $8.96 \times 10^3 and\ 10.49 \times 10^3 kg/m^3$. CuAg and AVNP2 are simply considered as mixtures. Based on the weight percentage from Section 3.4.4.2, the theoretical density of CuAg alloy using **Equation (6-2)** was 10.46 $\times 10^3$ kg/m$^3$. The density of AMNP2 formulation using **Equation (6-2)** was 4.83 $\times 10^3$ kg/m$^3$ whose weight percentage was calculated from atomic percentage [165]. Specifically, the weight percentage of C, W, Ag, Cu and O were 30.07%, 39.69%, 16.34%,11.06% and 2.84%, respectively.

Brownian motion is the movement of particles suspended in liquid or gas in random directions at random speeds due to collisions with other particles[215]. The particles in medium tend to stably diffuse from regions of high concentration to regions of lower concentration with time and will disperse evenly throughout the medium. This process is called diffusion, and it can be considered a macroscopic example of Brownian motion. For nanoparticle suspensions, Brownian motion has a stronger effect to maintain the sub-micron particles in a dispersed phase before forming larger particles which are dominated by gravity. If the numerator is greater, nanoparticles in suspension are likely to become agglomerated and settling, while a greater denominator indicates a stable system. However, **Equation (6-1)** does not take in account potential particles interactions nor surface treatment [211]. For a concentration of electrically charged suspension, the stability of the suspension is also partially controlled by the electrostatic forces between particles, which is indicated by zeta potential [96]. As mentioned in the second part of Section 2.3.6, the DLVO theory stated when the repulsive forces overcome the attractive forces, adjacent particles repel each other and the value of absolute zeta potential is high (the suspension is stable). On the contrary, the particles tend to aggregate and the value of absolute zeta potential is low when the attractive forces is higher.

Therefore, to predict whether nanoparticle suspensions keep the suspension stable physically or not, the ratio of gravitational force to Brownian forces are tabulated below (Table 6.1), along with the results of zeta-potential in Figure 4.17. As can be seen, the value of QNA Ag, CuAg and AMNP2 were in the same order of magnitude and greater than that of NF Cu10. The suspensions of QNA Ag and CuAg were supposed to be fewer stable systems, so they were previously treated with $NH_4OH$ while NF Cu10 does not. Regarding zeta potential, QNA Ag had the highest absolute zeta potential values, followed by AMNP2 and CuAg, and lastly by NF Cu10.

**Table 6.1** The ratio of gravitational force to Brownian forces and Zeta-potential of samples calculated by **Equation (6-1)**.
The zeta potential values were obtained from Section 4.4.3.

| Sample | Concentration (ppm) | Zeta potential (mV) | The ratio of gravitational force to Brownian forces |
|---|---|---|---|
| QNA Ag | 10 | -31.37(±7.18) | $1.4 \times 10^{-4}$ |
| | 50 | -21.33(±0.91) | |
| | 100 | -30.6(±1.57) | |
| NF Cu10 | 10 | -8.07(±1.45) | $1.9 \times 10^{-7}$ |
| | 50 | -9.27(±2.68) | |
| | 100 | -8.82(±5.97) | |
| CuAg | 10 | -19.13(±7.33) | $10^{-4}$ |
| | 50 | -22.17(±1.21) | |
| | 100 | -18.47(±2.27) | |
| AMNP2 | 10 | -9.64(±1.98) | $2.9 \times 10^{-4}$ |
| | 50 | -20.63(±1.90) | |
| | 100 | -23.77(±0.87) | |

Unfortunately, the experimental works were limited and there is still a gap between predictive model and experimental result as the study of aggregation and settling dynamics of nanoparticles. One of these is Liyanage *et. al.* (2012) who developed an analytical method to predict the settling rates of micro-to-nanosized particle suspensions [216]. They assumed the nanoparticles aggregates of sufficient micro-sized size before starting noticeable settling. Afterwards, the Newtonian force takes over the intermolecular force, settling time therefore can be calculated. A feature of this work is that they did not only calculated spherical aggregates but accommodate non-spherical aggregates depend upon fractal dimension.

On the other hand, it is challenging to capture the movement of every single nanoparticle in medium and calculate the overall change of the solution, which requires other facilities took a lot of memory and calculation capacity. The most common measurement method is to mix nanoparticles into solution well and then regularly measure the descent of the solid-liquid interface, but this method highly depends on eye observation and subjective identification. For instance, Witharana *et. al.* (2012) studied the aggregation and settling behaviour of alumina nanoparticles near its isoelectric point using photography and small angle X-ray scattering [216]. Alternatively, Zheng *et. al.* (2019) investigated the sedimentation rate of

alumina nanoparticles by testing the absorbance of suspension using UV spectrophotometry, which relies on the determination of solution absorbance [217]. These experiments also focused on specific materials (mostly alumina) and usually had some limits of experimental conditions. Following two sections intend to analyse dispersibility of nanoparticle solution with NTA.

### 6.4.2 Supernatant study of engineered Ag and QNA Cu nanoparticles

The supernatants of QNA Ag suspension in total of 5 days were measured by NTA and the results is shown in **Figure 6.3**. The maximum total concentration from five days of QNA Ag achieved the highest value in the third day. The mode size and mean size of QNA Ag remained stable in the first four days and they dramatically increased to 124.8 and 127.8 nm on the last day, respectively. In addition, the D10-to-90 range of QNA Ag also reached the peak on the last day, which may be attributed to the formation of the agglomeration. Overall, this result showed stable systems due to a surface treatment and high zeta potential, although the theoretical ratio of gravitational force to Brownian force was relatively high.

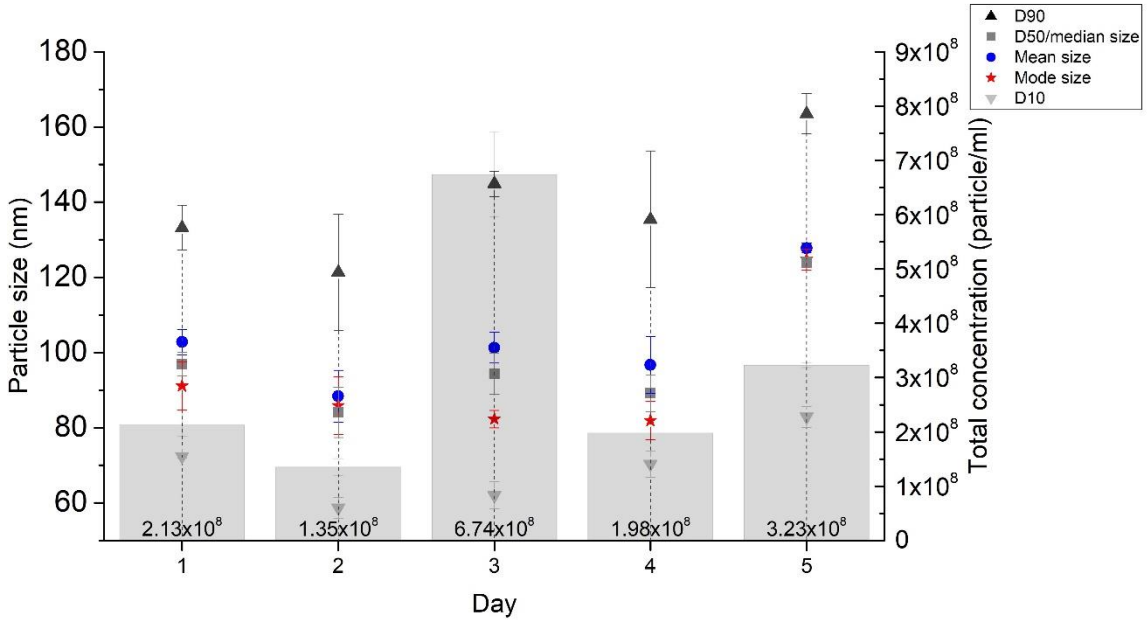


**Figure 6.2** The NTA results of QNA Ag supernatants.

The mode size and mean size of QNA Ag remained stable in the first four days and dramatically increased on the last day. The highest total concentration was observed in the third day.

**Figure 6.4** shows the result of QNA Cu supernatant in total of 5 days. The total concentrations from five days and D10-to-D90 range of QNA Cu were fluctuated. This is because every measurement was shaken and then stood for 30 minutes before capture. In the meantime, the experiment lost a tiny amount of volume due to measurement, theoretically the total concentration should increase slightly. The mode size of QNA Cu supernatant varied between 41.3 and 128.1 nm in five days. Compared with last theoretical section, the ratio of gravitational force to Brownian forces of NF Cu10 was lower than that of QNA Ag, but NF Cu10 had low zeta potential and finally the NTA results showed its suspension was unstable.

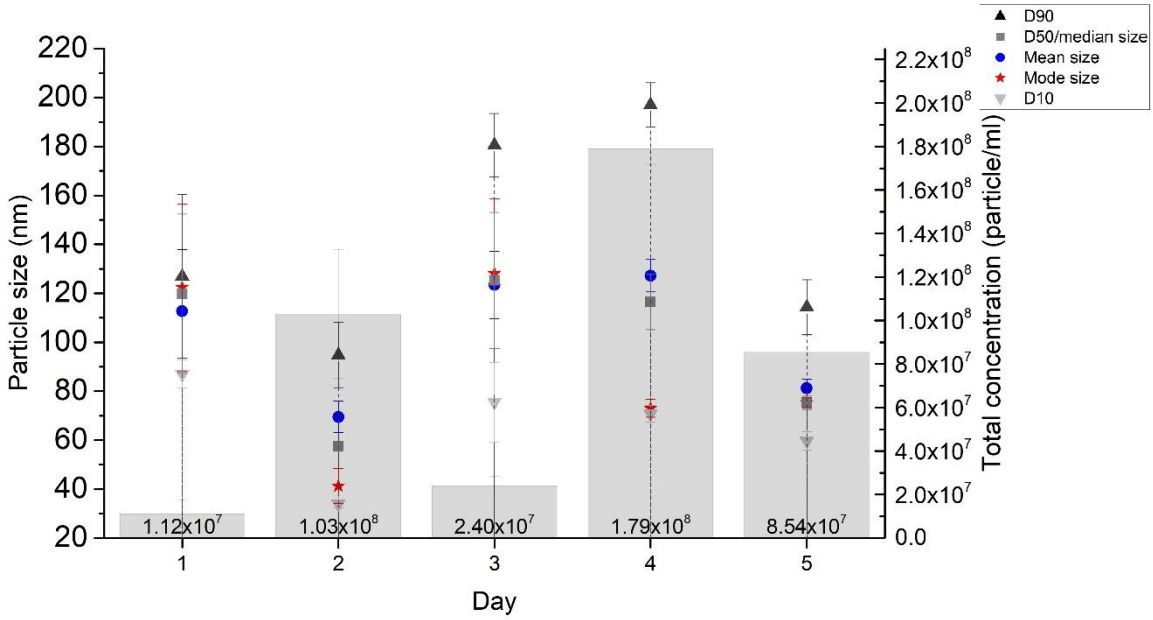


**Figure 6.3** The NTA results of QNA Cu supernatants**.**
The mode size of QNA Cu supernatant varied between 41.3 and 128.1 nm. The total concentration of QNA Cu was fluctuated.

In conclusion, this method measured QNA Ag and QNA Cu suspensions. The five-day results of size distributions of QNA Ag were slightly increased, while the hydrodynamic particle concentration and size distribution of QNA Cu were fluctuated, indicating a poorly dispersed suspension are highly random. This makes it difficult to fully describe NTA results. In addition, this experiment was used 0.1 μm syringe filters to expect remove larger aggregates and observe individual nanoparticles. However, the results were found to be larger than 100 nm, and the actual particle size should be larger as well as the widths of the distributions [218]. In next section, nanoparticle dispersant study was performed with another method.

### 6.4.3 Dispersant study of commercial and engineered nanoparticles

In this experiment, four suspensions changing over time were measured by NTA using nanoparticle dispersant study. It was found to only take up to 30 minutes to complete which also prevents contaminating facility. Please note that due to poor dispersibility, 100 ppm of NF Cu10 suspension was only measured three times and the last measurement was at 24 min.

#### *6.4.3.1 The dispersant measurements of engineered QNA Ag*

**Figure 6.4** to **6.6** show the NTA results of engineered QNA Ag at three different preparation concentrations (10, 50 and 100 ppm). They were collected at beginning and every 10 mins in total of half hour. The total concentration of QNA Ag at 10 ppm declined for 30 minutes and the size distribution was little changed. With increasing preparation concentration, the total concentration of QNA Ag at 50 ppm (grey bars) was decreased by first 10 minutes before increasing till the end of the period, while that of 100 ppm saw an opposite trend with an inflection point at 20 minutes. Recall that if mode size is smaller than D50 and meanwhile D50 is smaller than mean size (mode ★ < D50 ■ < mean ●), it is positively skewed distribution which represents the distributions contain more tiny particles otherwise it is called negatively skew distribution. All results of QNA Ag maintained positively skewed distributions during the measurement.

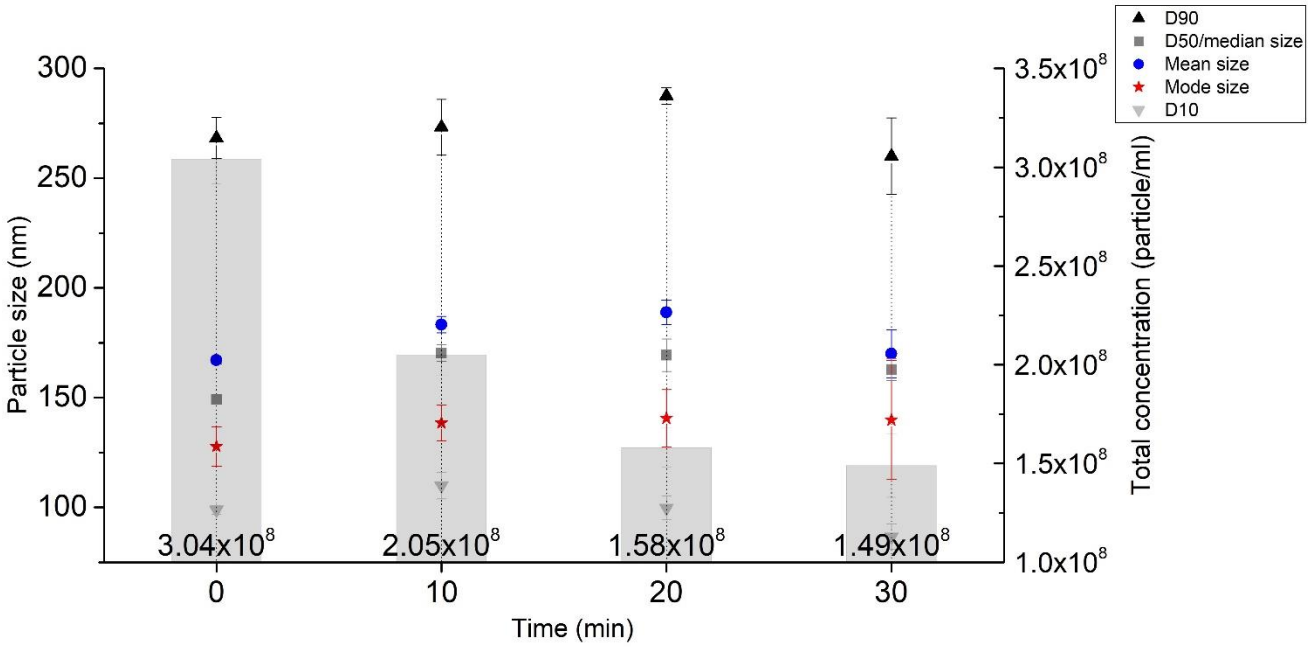


**Figure 6.4** Continuous NTA result of QNA Ag at 10 ppm.
The total concentration declined for 30 minutes and the size distribution was little changed.

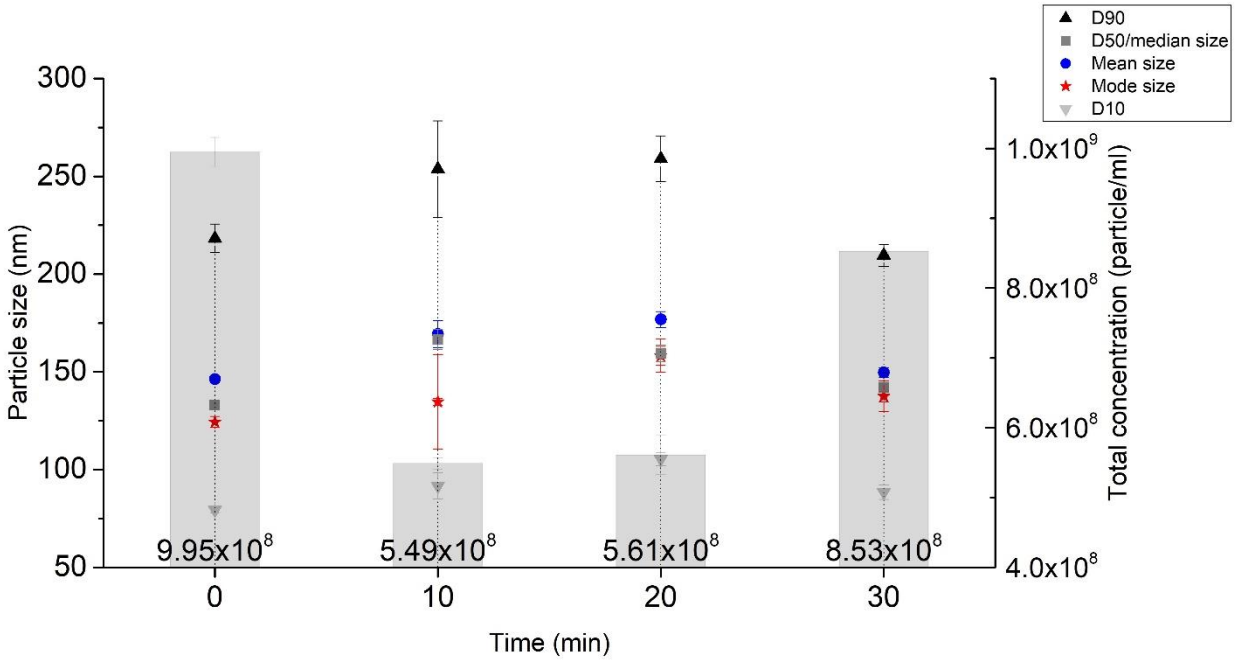


**Figure 6.5** Continuous NTA result of QNA Ag at 50 ppm. The size distribution
The highest size distribution was at 10 and 20 minutes, and the total concentration was at the beginning and end.

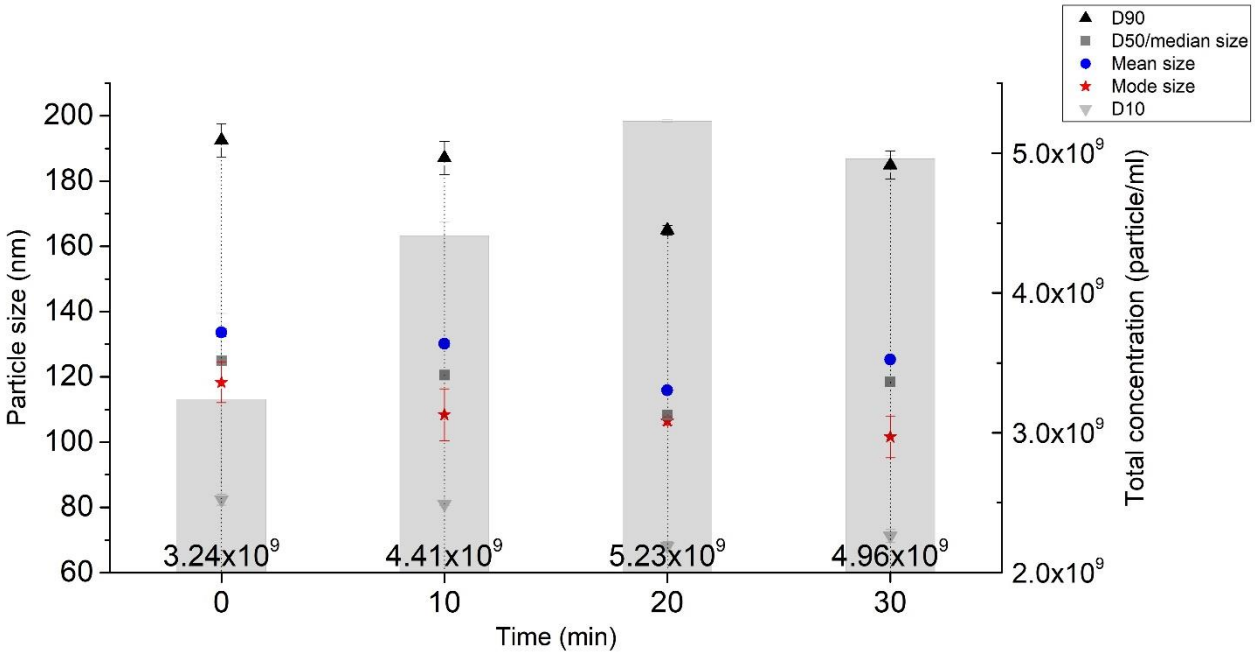


**Figure 6.6** Continuous NTA result of QNA Ag at 100 ppm.
The total concentration increased until 20 minutes, at which point it had the smallest size distribution.

Moreover, the span values and mass concentrations of QNA Ag were collected and plotted in **Figure 6.7** and **6.8**, respectively. The span value of QNA Ag was calculated using **Equation (4-1)**. During the measurement, it was varied from around 1.15 to 0.85. The calculation of mass concentration was determined using **Equation (6-3),** of which size of particle was based on the SEM images and the shape was considered as spherical. The mass concentration of QNA Ag sample at different preparation concentrations were stable, the 100-ppm QNA Ag sample increased mass concentration from 18 to 27 ppm after 30 min, suggesting the sample was treated well for dispersibility and high preparation concentration still showed satisfying dispersion performance. This can also be supported by **Table 6.1**, the zeta potential values of QNA Ag were closed to -30 mV and they had high ratio of gravitational to Brownian forces. Overall, the case of QNA Ag indicated that Brownian forces probably dominate over gravitational forces to provide electrostatic stability [145].

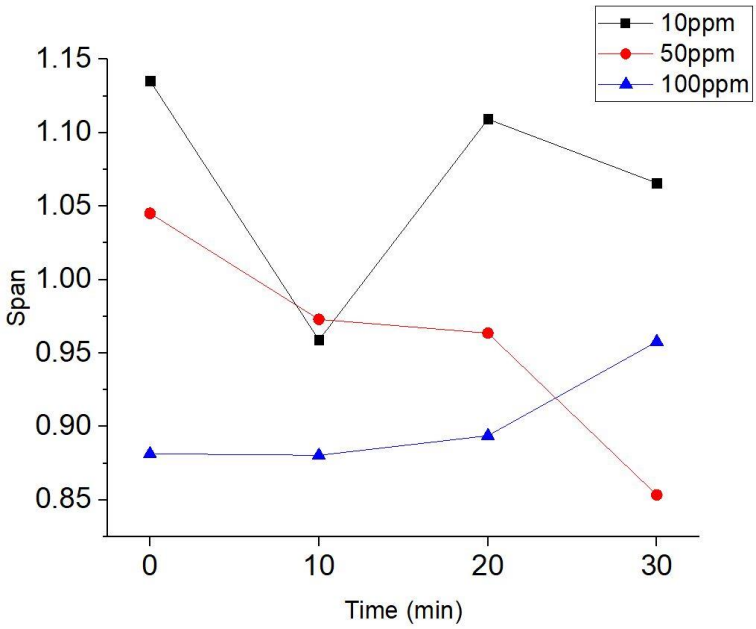


**Figure 6.7** The QNA Ag span value obtained by dividing (D90-D10) by D50 varied from 1.15 to 0.85.

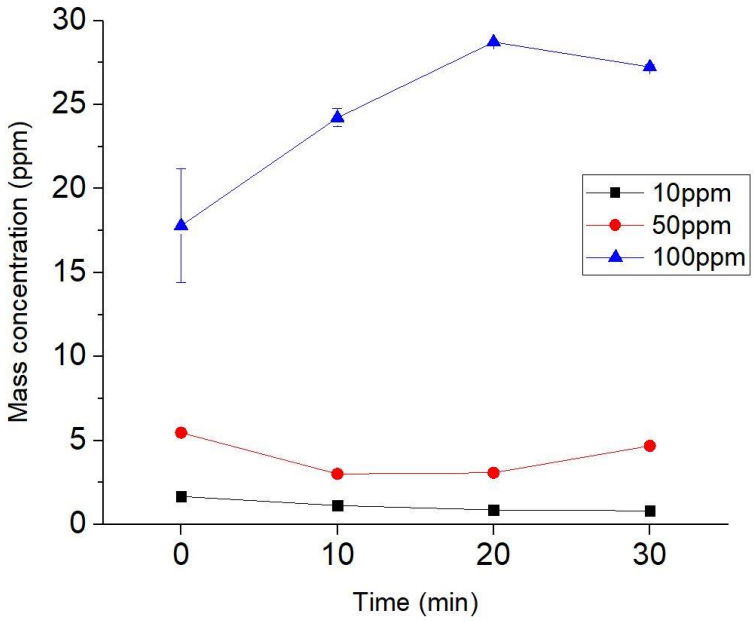


**Figure 6.8** The change of mass concentration of QNA Ag.

The mass concentration of QNA Ag sample at different preparation concentrations were stable, the mass concentration of QNA Ag at 100-ppm increased from 18 to 27 ppm after 30 min.

*6.4.3.2 The dispersant measurements of commercial NF Cu10*

Similarly, the NTA results of commercial NF Cu10 at different preparation concentrations (10, 50 and 100 ppm) were also monitored (**Figure 6.9** to **6.11**). It was observed that in most measurements the D50s of NF Cu10 were very closed to their mean sizes - even the 10 ppm of NF Cu10 suspensions was considered to be a normal distribution (mode ★ = D50 ■ = Mean ●) rather than positively skewed distribution. In other words, they had as many smaller particles as larger particles, with an average peak around 170 nm, while the particle size of the powder was only 10 - 30 nm.

The three different preparation concentrations of NF Cu10 suspensions showed the maximum total concentration from 30 minutes at different time points, which demonstrated that the total concentration of NF Cu10 suspensions varied greatly with time.

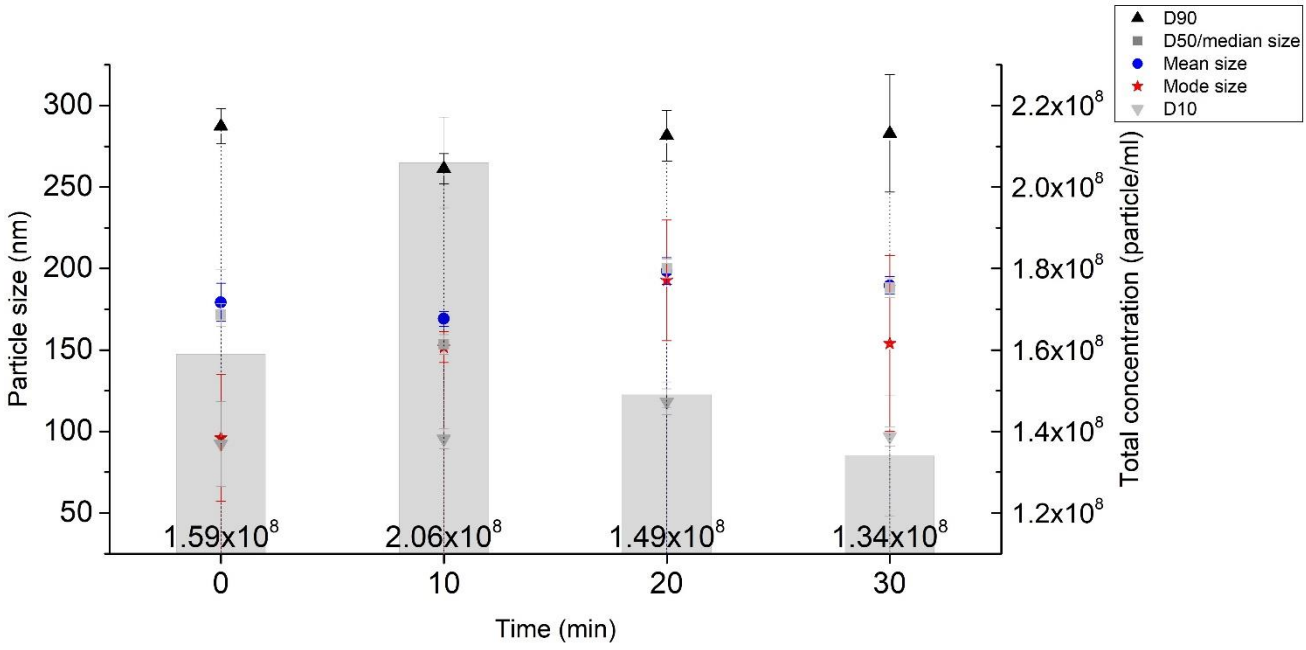


**Figure 6.9** Continuous NTA result of NF Cu10 at 10 ppm.
The total concentration increased until 10 minutes, at which point it had the smallest size distribution.

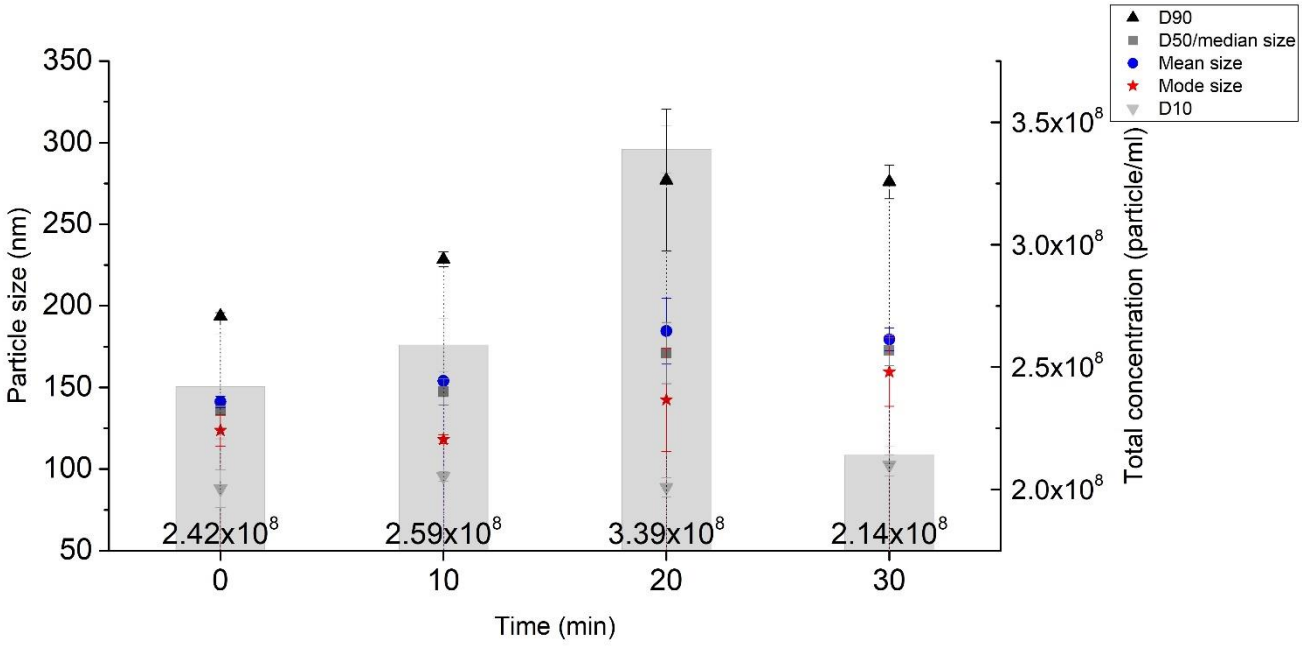


**Figure 6.10** Continuous NTA result of NF Cu10 at 50 ppm.
The total concentration and size distribution increased until 20 minutes, followed by declined.

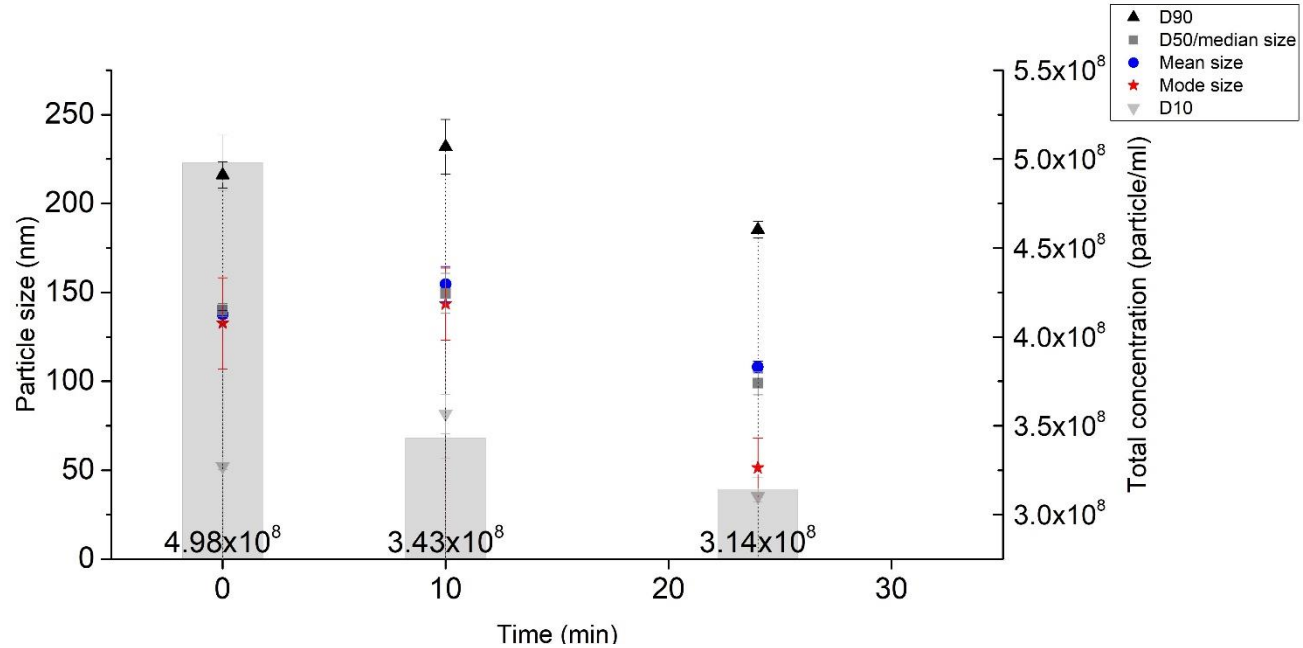


**Figure 6.11** Continuous NTA result of NF Cu10 at 100 ppm.
The total concentration decreased for 30 minutes, and the last measurement was at 24 minutes.

The span values and mass concentrations of NF Cu10 using **Equation (4-1)** and **(6-3)** are shown in **Figure 6.12** and **6.13**. Between 10 and 30 min, it was found the span value of NF

Cu10 varied with its preparation concentration. The span of NF Cu10 at 100 ppm increased to 1.5 after decreasing at first 10 min, and that of 50- and 10-ppm suspensions also showed inflection points. On the other hand, the mass concentrations of NF Cu10 suspensions at 10 and 50 ppm were observed to be fluctuated during 30 min, it was found that a 100-ppm Cu10 suspension was practically only about 0.01 ppm at 24 minutes. Theoretically, when the solid solution mass is equal, the preparation concentration of the particles is inversely proportional to the particle size and mass. However, in the case of NF Cu10 suspensions, it had much lower mass concentrations than QNA Ag, although its density and size are lower. These proved again that the NF Cu10 suspension was poorly dispersed, and this situation becomes worse at higher preparation concentrations, which is inconsistent with the ratio of gravitational force to Brownian forces. In conclusion, an increase in the preparation concentration of NF Cu10 resulted in larger size distributions (higher span value) and unstable mass concentrations.

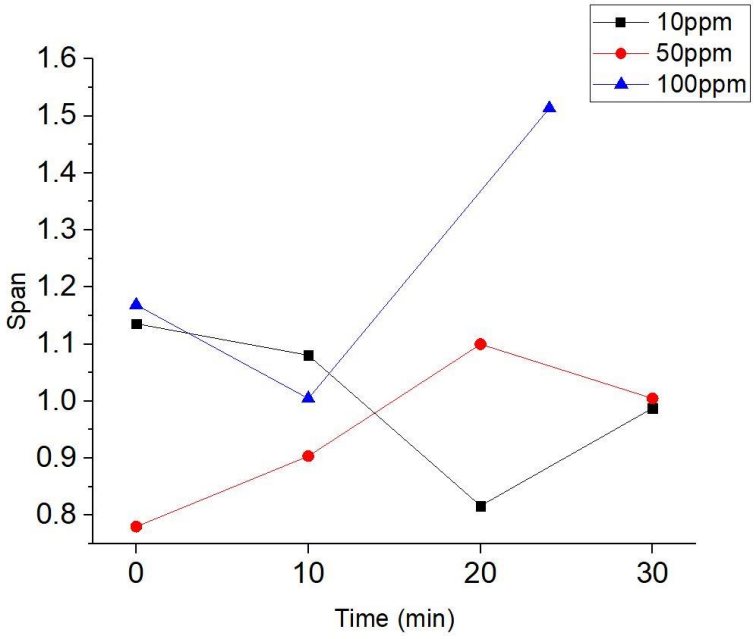


**Figure 6.12** The change of span value of NF Cu10.

The span value of NF Cu10 at 100 ppm increased to 1.5 after decreasing at first 10 minutes, and that of 50- and 10-ppm suspensions also showed inflection points.

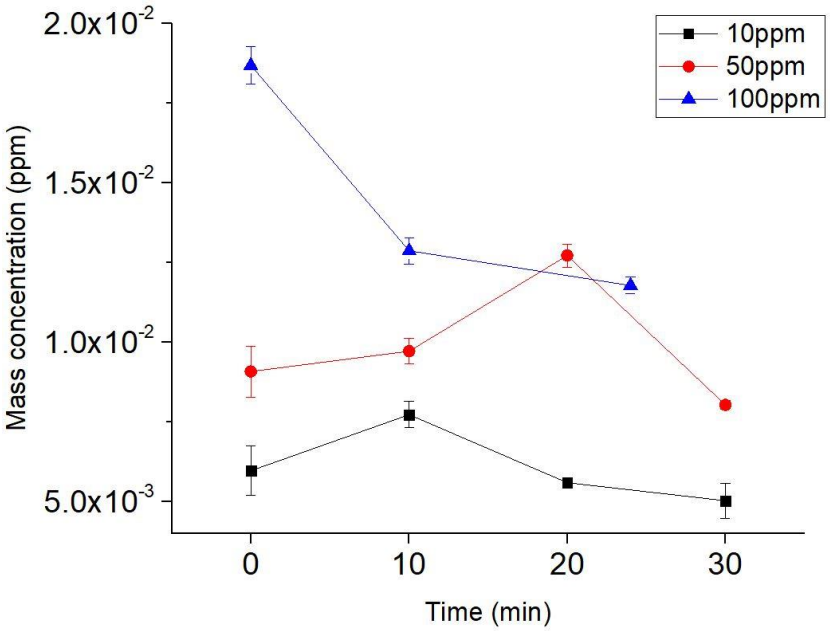


**Figure 6.13** The change of mass concentration of NF Cu10.

The 100 ppm of Cu10 suspension was practically about 0.01 ppm at 24 minutes and 10- and 50-ppm suspensions were even lower.

*6.4.3.3 The dispersant measurements of commercial CuAg*

**Figure 6.14** to **6.16** show the NTA results of commercial CuAg at three preparation concentrations (10, 50 and 100 ppm). With assistance of surfactant, CuAg suspensions generally gained well dispersibility. It was found that during this period, the D10-to-D90 range of CuAg suspensions below 50 ppm remained stable overall, while that of 100 ppm suspension gradually increased (moved up) but the size distribution was the opposite. This also caused an increase in the size distribution of the sample. In the first two measurements of CuAg at 100 ppm showed a positively skewed distribution (mode ★ < D50 ■ < mean ●), while the last two measurements were found to be negatively skewed (mean ● < D50 ■ < mode ★). At concentration of 10 and 100 ppm, the maximum total concentration from 39 minutes of CuAg was found at the beginning, while that of 50 ppm suspension was found at 10 min.

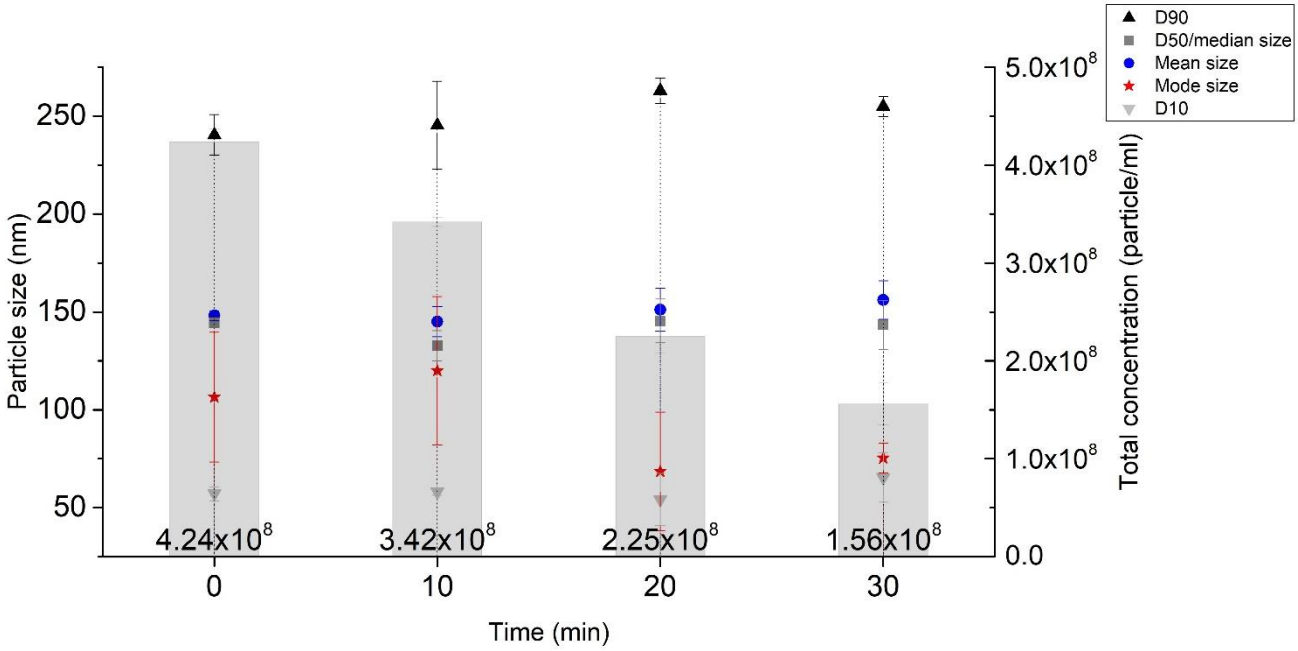


**Figure 6.14** Continuous NTA result of CuAg at 10 ppm.

During the measurement, the total concentration decreased and the size distribution was little increased.

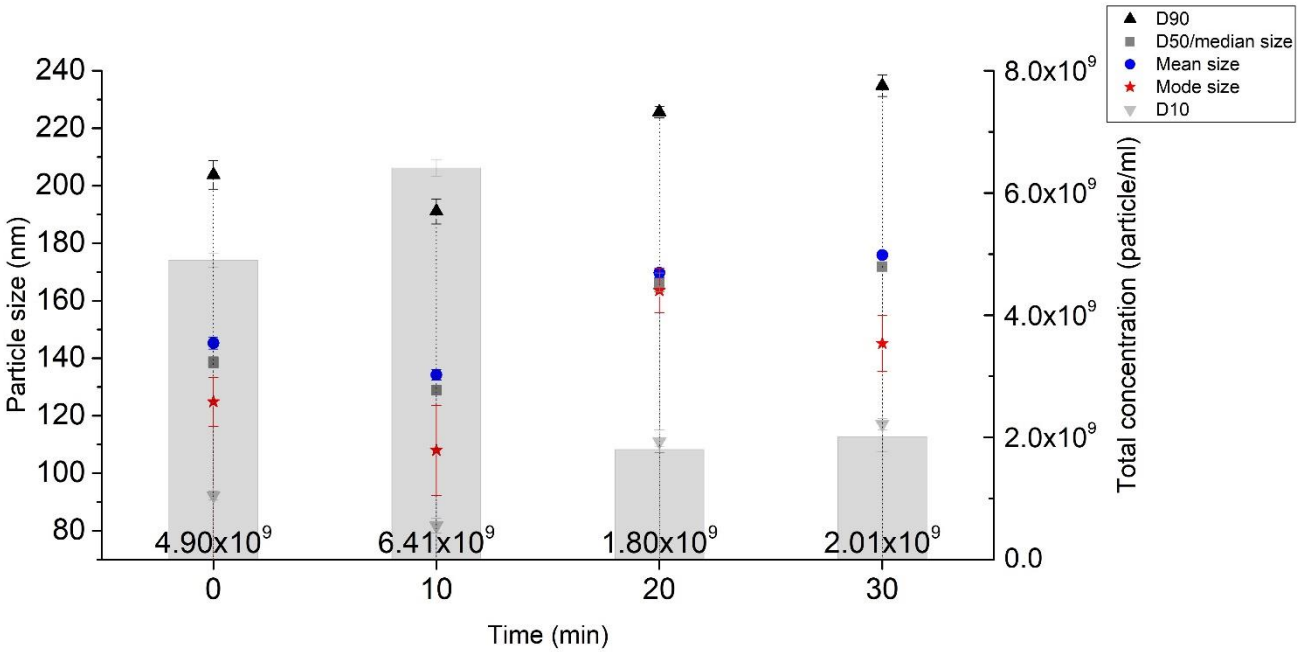


**Figure 6.15** Continuous NTA result of CuAg at 50 ppm.

The total concentration increased until 10 minutes, at which point it had the smallest size distribution.

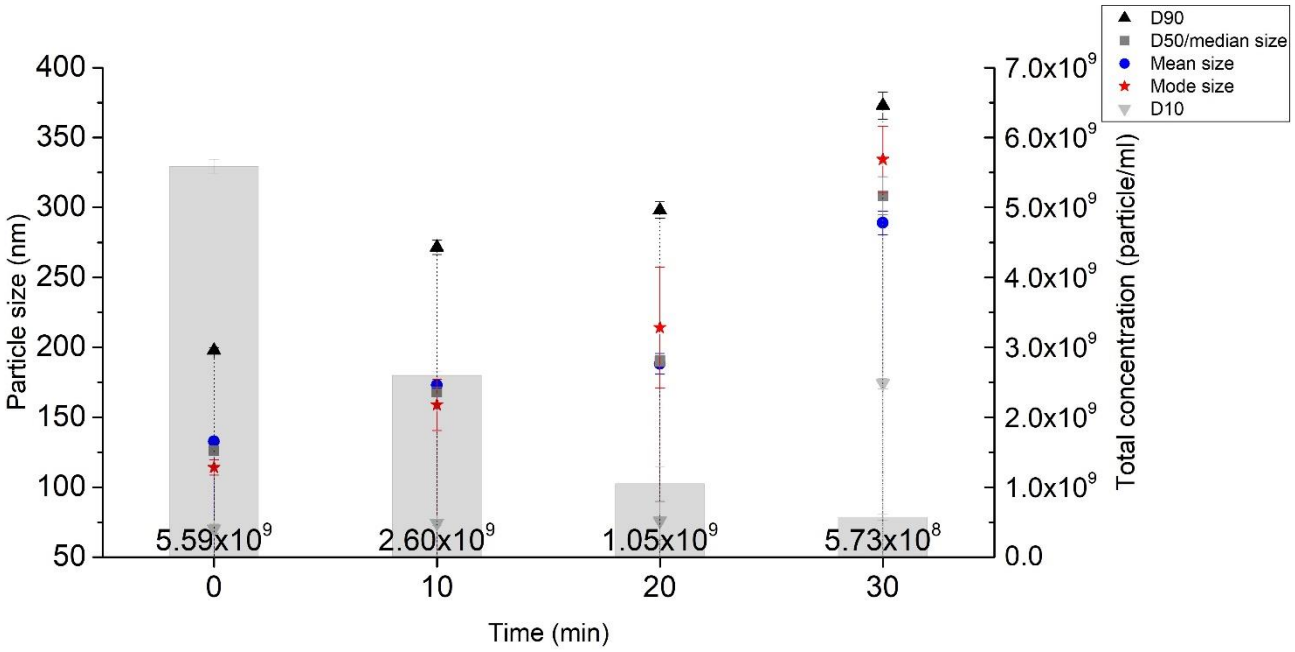


**Figure 6.16** Continuous NTA result of CuAg at 100 ppm.
During the measurement, the total concentration decreased, while the size distribution was the opposite.

Moreover, the span values and mass concentrations of CuAg using **Equation (4-1)** and **(6-3)** were, respectively, presented in **Figure 6.17** and **6.18**. Interestingly, it was observed that the span of CuAg at 100 ppm was between 10 and 50 ppm of the corresponding sample except that the last measurement of the 100-ppm sample dropped rapidly from 1.15 to 0.65. However, the mass concentration of CuAg at 100 ppm was basically at the same level of that of 50 ppm. During 30 minutes, the 50 ppm of CuAg suspension reached its maximum total concentration from 30 minutes at 10 min, at which point was even higher than all measurements of 100 ppm of CuAg, and then sharply declined. The reason for this very high concentration point is uncertain, it may be a status of complete distribution before aggregation and settlement, because it takes time for nanoparticles to diffuse. The total concentrations of CuAg at 10 ppm suspension did not change much and that of 100 ppm constantly dropped during 30 min. The general mass concentrations of CuAg suspensions were slightly lower than that of QNA Ag but higher than NF Cu10 suspensions, which had the same relationship as the ratio of gravitational force to Brownian forces and zeta-potential among three samples. All this suggested CuAg suspensions prepared with high concentrations may require more surfactant ($NH_4OH$) for the purpose of better dispersion. Nevertheless, it still provides high killing efficiency against Gram-negative bacteria (*P. aeruginosa*) and Gram-positive bacteria (*S. aureus*), which still can be further improved by simple modifications.

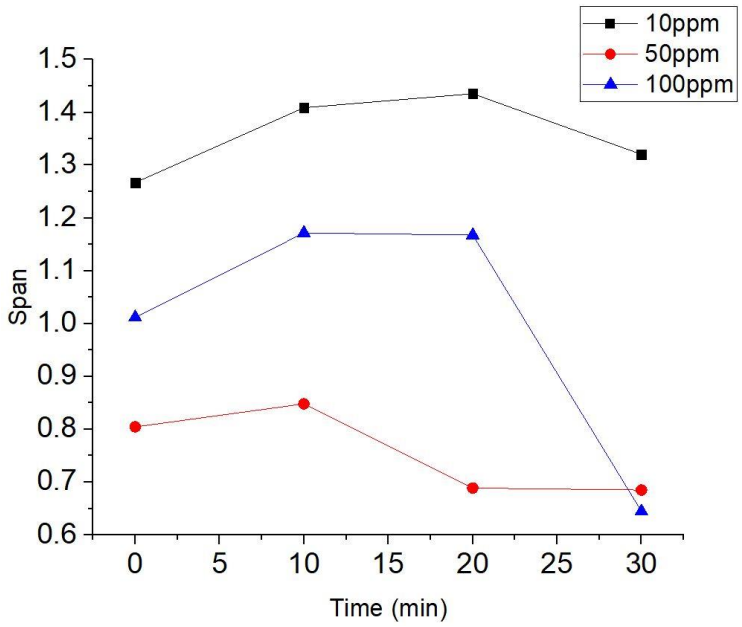


**Figure 6.17** The change of span value of CuAg.

It was observed that the span of CuAg at 100 ppm was between 10 and 50 ppm of the corresponding sample except that the last measurement of the 100-ppm sample dropped rapidly from 1.15 to 0.65.

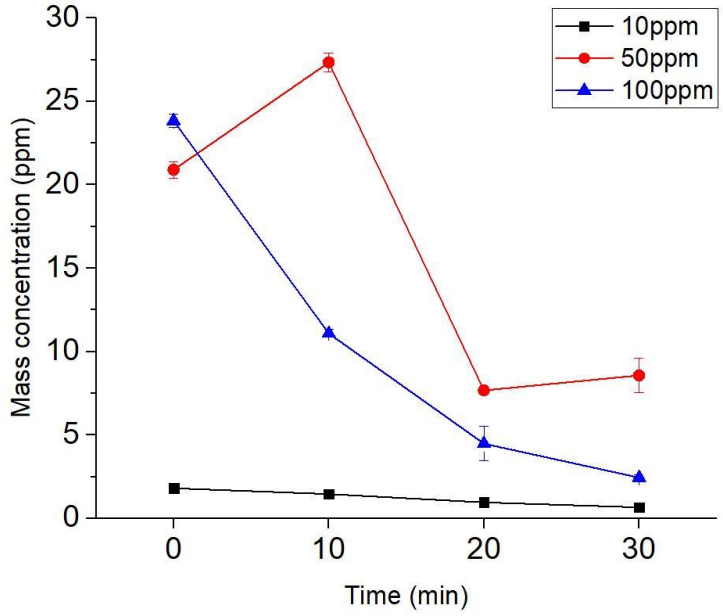


**Figure 6.18** The change of mass concentration of CuAg.

The total concentrations of CuAg at 10 ppm suspension did not change much and that of 100 ppm constantly dropped during 30 min. The overall mass concentrations of CuAg suspensions were slightly lower than that of QNA Ag but higher than NF Cu10 suspensions.

*6.4.3.4 The dispersant measurements of engineered AMNP2*

It can be seen from **Figure 6.19** to **6.21**, the D10-to-D90 range of AMNP2 suspensions at three preparation concentrations (10, 50 and 100 ppm), respectively, increased steadily. All size distributions of AMNP2 were considered as positively skewed distribution (mode ★ < D50 ■ < mean ●). To the opposite of CuAg suspensions, all the maximum total concentrations from 30 minutes of AMNP2 had an initial ascent before a decline trend. The maximum total concentration of AMNP2 at 100 ppm was found at 10 min, while that of other two preparation concentrations were found at 20 min. This may because increasing the preparation concentration intensifies particles colliding with each other resulting in earlier intense aggregation and settling.

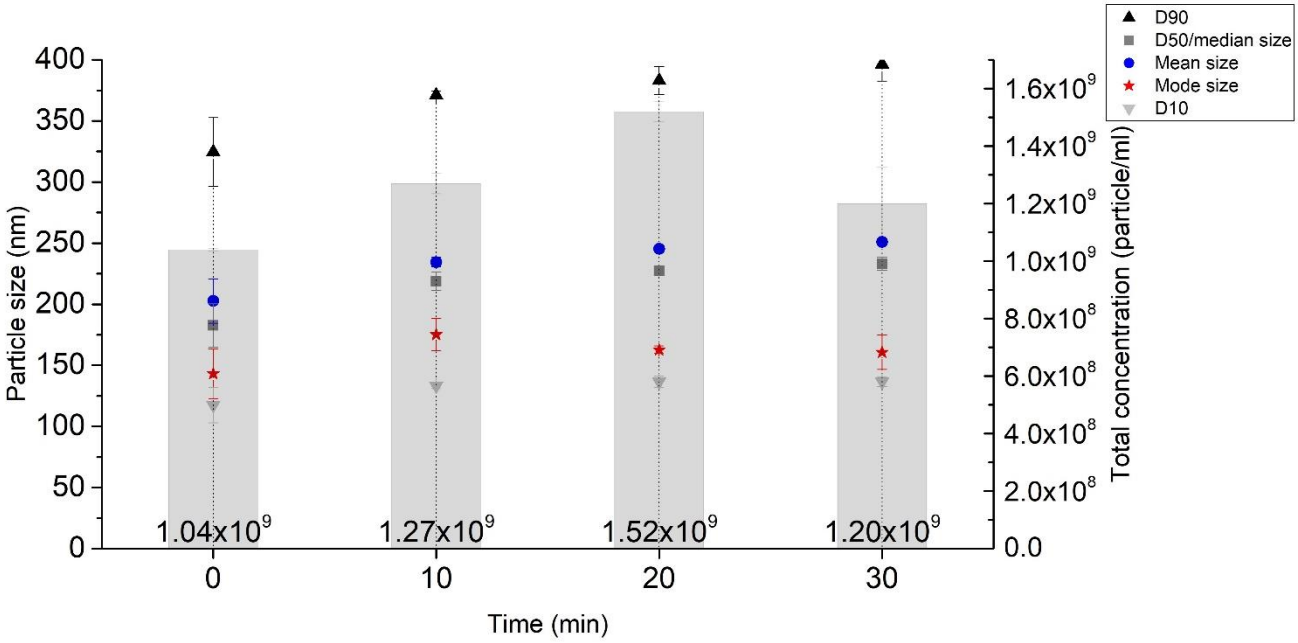


**Figure 6.19** Continuous NTA result of AMNP2 at 10 ppm.
The total concentration increased until 20 minutes, and the size distribution was slightly increased during the measurement.

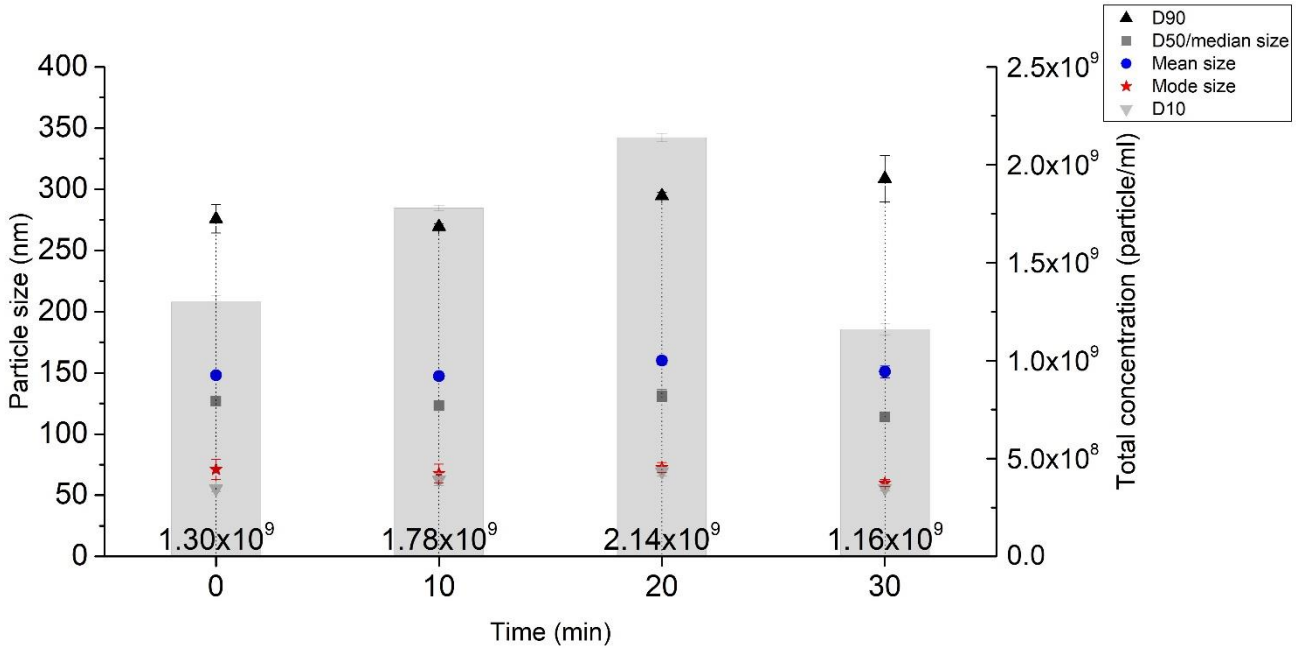


**Figure 6.20** Continuous NTA result of AMNP2 at 50 ppm.
The total concentration increased until 20 minutes, and the size distribution was increased after 10 minutes.

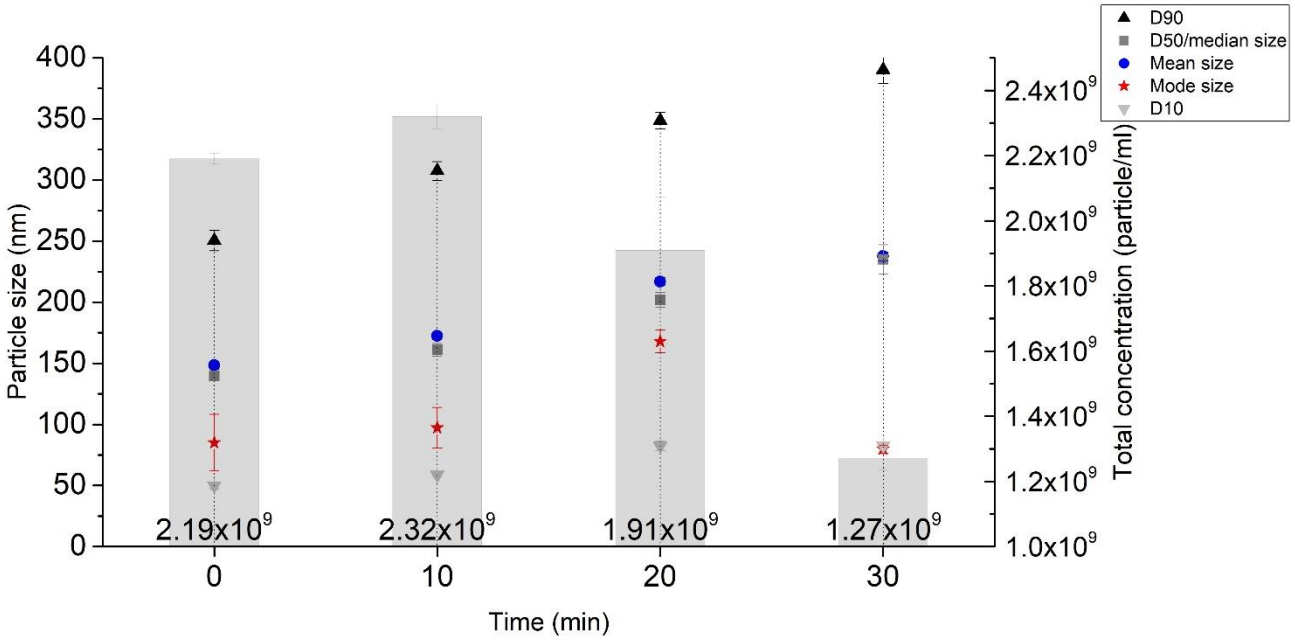


**Figure 6.21** Continuous NTA result of AMNP2 at 100 ppm.
The total concentration increased until 10 minutes, and the size distribution was increased. Increasing the preparation concentration intensified particles colliding resulting in earlier intense aggregation and settling.

In **Figure 6.22** and **6.23**, the obvious changes of span values and mass concentration using **Equation (4-1)** and **(6-3)** varied with increasing preparation concentrations. Similar to CuAg, the span of AMNP2 at 100 ppm was found between the other two preparation concentrations (10 and 50 ppm). In contrast, the mass concentration of AMNP2 at 100 ppm was approximately doubled as many as that of 50 ppm at the beginning. Similarly, all the mass concentrations of AMNP2 had an initial ascent before a decline trend, which may be a completely distributed state before aggregation and settlement. It is less likely to be a measurement error since the measurements were made in triplicate and this have been observed from different samples or concentrations many times. All three preparation concentrations of AMNP2 had approximately 10 ppm of mass concentration after 30 minutes. It can be seen that, although AMNP2 contains Ag element without surfactant treatments, it overall performed better stability in water than CuAg. This can also be seen in **Table 6.1**, the ratio of gravitational force to Brownian forces of AMNP2 was much lower than that of QNA Ag and CuAg. As a result, it had better killing efficiency of bacteria.

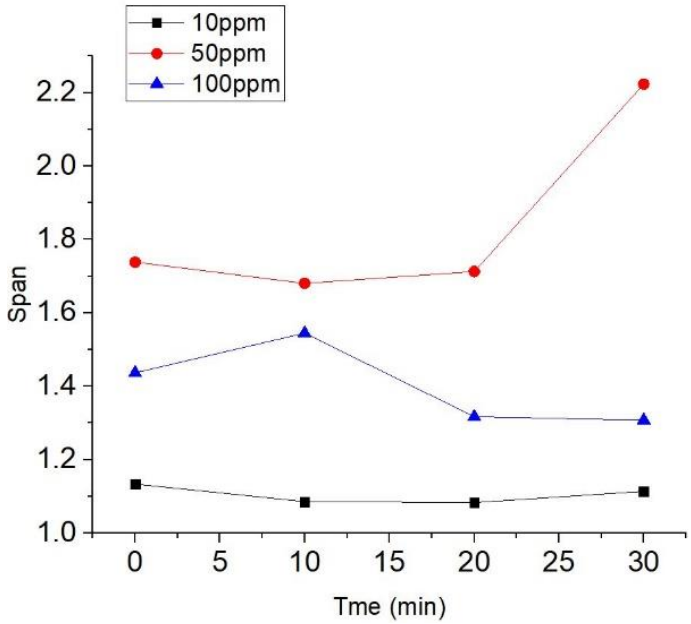


**Figure 6.22** The change of span value of AMNP2.
The span value of AMNP2 at 100 ppm was found between the other two preparation concentrations.

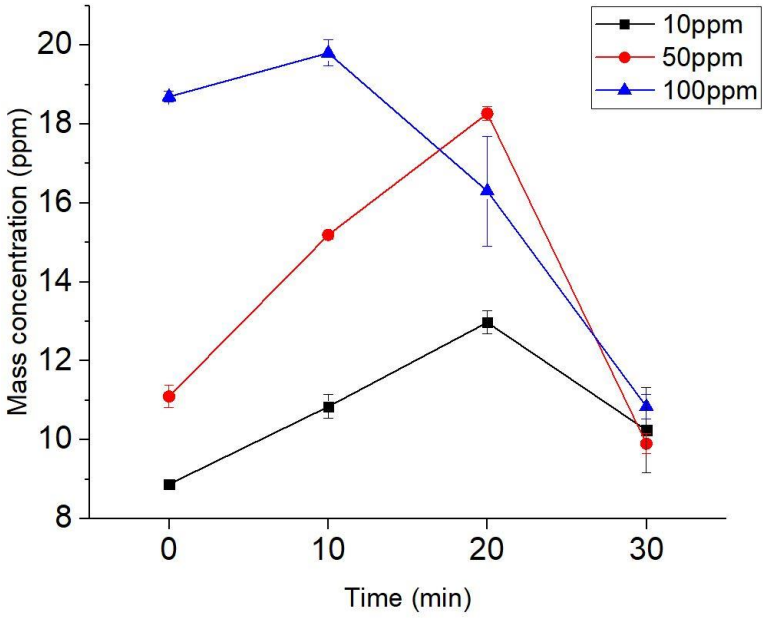


**Figure 6.23** The change of mass concentration of AMNP2.

The AMNP2 suspension at 100 ppm was approximately doubled as many as that of 50 ppm at the beginning. All three preparation concentrations of AMNP2 had approximately 10 ppm of mass concentration after 30 min.

## 6.5 Summary

The theoretical calculations were calculated at the beginning of this chapter. The difference between NFCu10 and the other three can only be seen in the order of magnitude, which was a bit far from the practical measurement today due to the combined effect of gravity, Brownian motion, pH, zeta potential, *etc*. Besides, this estimation does not take in account concentration or surface treatment.

The QNA Ag and QNA Cu nanoparticles were measured in the supernatant study in total of 5 days. The size distributions of QNA Ag were slightly increased, while the hydrodynamic particle concentration and size distribution of QNA Cu fluctuated. The dispersant results found that when the solutes of different nanoparticles were equal, increasing the preparation concentrations of QNA Ag brought a slight increase in size distribution but greater increase in mass concentration. All preparation concentrations of NF Cu 10 suspensions occurred great change of size distributions and mass concentrations. An appropriate processing is required to improve its stability. This situation also happened at higher preparation concentrations above 10 ppm of CuAg suspension, the mass concentration of CuAg at 100 ppm was lower than that of 50-ppm sample after 30 minutes, which was suggested to be

modified by adding more surfactant than QNA Ag. Although AMNP2 formulation contains element Ag without any surfactant treatment, it performed the best intrinsic stability among all nanoparticle so it had the best killing efficiency. In addition, the mass concentration reached the highest values between 20 and 30 minutes, during which time it is recommended to incorporate it into the PMMA polymer. Overall, the level of antimicrobial efficacy appeared to be highly dependent on their hydrodynamic sizes and stability.

On the other hand, this measurement method used NTA as only facility and consider nanoparticles as a collection of data instead of a group of single data point so that it can reflect on the overall characteristics and changes. This method can also reveal the difference of the same nanoparticle suspensions changing over time for the purpose of preparation selection and enhancement. In many measurements, the relationship between total hydrodynamic concentration and size distribution of the suspension was the opposite – when the particle concentration was lower, the size distribution was greater, and *vice versa* since the solutes of the nanoparticle were constant. This situation occurred more often at high concentrations, and this NTA processing method fully reflected that the agglomeration of nanoparticles caused the increase in size distribution and the decrease in the number of particles (particle concentration). Eventually, it is necessary to explore optimal parameters for processing nanoparticle suspensions, especially for the suspension with poor stability.

# CHAPTER 7 OPTIMISATION OF NANOPARTICLE DISPERSION PARAMETERS AND EXPLOITATION OF ALTERNATIVE PROCESSING METHOD

## 7.1 Introduction

This chapter separately explored two processing methods for the purpose of maximising the particle concentrations and obtaining monodispersed nanoparticle suspensions, which could create a stable hydrodynamic environment of nanoparticle in aqueous solution for microbial exposure and polymer incorporation.

According to previous chapters, two alloy nanoparticles (CuAg and CuZn) need to find optimal dispersing conditions for obtaining stable suspensions as they showed to have antimicrobial property. CuAg and CuZn suspensions were sonicated for 2 and 10 min, respectively, and their size distributions and zeta potential values were measured using NTA and Zetasizer in order to explore the differences in resulting physiochemical properties. A procedure operation of calibration of delivered power of sonication was performed to calculate the energy density of the preparation process. It describes the amount of energy transferred to a suspension per unit volume so that the preparation of nanoparticles can be described thermodynamically.

The alternative processing method is to use microwaves instead of sonication to prepare Cu NP suspensions for higher dispersion properties as their sonicated suspensions have poor dispersion. NTA was used to measure the size distribution of NF Cu10 NPs prepared at different temperatures, which is hoped to obtain a more uniform and monodispersed suspension than sonicated one.

## 7.2 Nanomaterials

### 7.2.0 General

All engineered and commercial nanoparticle samples were used as received and stored a in dark and well-ventilated cupboard. Please see Section 5.2.0.

### 7.2.1 Copper

Commercial powder NF Cu10 was purchased from Suzhou Canfuo Nano Technology, it was claimed to have 10 - 30 nm particle size range and a spherical shape. The details of this nanomaterials are identical to chapter previously reported, please refer to Section 3.2.3.

### 7.2.2 CuAg and CuZn alloys

The alloy nanoparticles CuZn and CuAg were purchased from Sigma-Aldrich (Dorset, UK). $NH_4OH$ (Fisher Scientific®, UK) was added to treat CuAg NPs prior to the sonication process. The details of both nanomaterials are identical to chapter previously reported, please refer to Section 3.2.4.

## 7.3 Instrumentation and methodology

### 7.3.1 Preparations of nanoparticle dispersions

All nanoparticles were weighed using a *microbalance (*Shimadzu, Japan*)*. A titanium alloy Ti-Al-V liquid processor (Sonics & Materials®, USA, VC-750, Ø 13 mm, 750 W output power, 20 kHz) was used to disperse nanoparticle suspensions prior their physiochemical analyses. Please refer to Section 4.3.1 for the specification of sonication.

### 7.3.2 Calculation of delivered power of sonication (energy density).

The calorimetric method of sonication can be employed for the direct measurement of the temperature increase during sonication, from which the effective delivered acoustic energy is calculated [219]. To determine the calorimetric curves, following **Equation (7-1)** is employed to calculate the power ($P$) that effective delivered into the suspension based on a temperature ($T$) vs. time ($t$) curve:

$$P = \frac{dT}{dt} m C_p \tag{7-1}$$

Where $\frac{dT}{dt}$, $C_p$ and $m$ are the slope of the regression curve, the specific heat of water and the mass, respectively. Probe sonication is as well operated either by continuous or pulsed mode. The pulsed mode refers to the device regularly generate vibrations, which has a better ability to maintain temperature steady. Specifically, the totally amount of energy ($E$) delivered to a suspension is measured as:

$$E = P * t \quad (7\text{-}2)$$

where $P$ is the applied power and $t$ is the total amount of on-pulse time. The duration of off-intervals can decelerate the rate of increase in temperature, which helps avoid agglomeration and subsequent settlement caused by particle collisions [220].

### 7.3.3 Analysis of the effects of sonication duration on alloy nanoparticles.

Concentrations of 100 ppm samples were prepared using 3 mg of CuAg and CuZn NPs of which were dispersed in 30 mL of Acros pure particle-free water using high power sonication for 2 and 10 min, respectively. After that, they were further diluted into 50 and 10 ppm. Three different concentrations of both sample suspension were collected in triplicate using NTA. Please see Section 4.3.2 for the specification of NTA.

### 7.3.4 The D-value

A D-value can be thought of the cumulative undersize distribution showing the relative amount at/below a certain size. Usually, D10, D50 and D90 are used to investigate a particle size distribution curve. Please see Section 4.3.3 for more explanations.

### 7.3.5 Interpretative method for particle concentrations and distributions

The nanoparticle size distributions were interpreted using the “vertical view”, where the size distribution graphs were presented side by side. The results of each suspension at different times are displayed on the x-axis and consists of five different symbols in a collinear line with different representative symbols. In addition, right y-axis shows a total concentration of the nanoparticle represented by grey bars. Please see Section 6.3.6 for more explanations.

### 7.3.6 DLS measurement of alloy nanoparticles

The hydrodynamic size and zeta potentials (mV) were measured using a Zetasizer Nano ZS (Malvern Panalytical, UK). All CuAg and CuZn samples were measured in triplicates at 25 °C with electrophoretic light scattering method. The most hydrodynamic sizes were acquired from each single replicate, the average sizes and zeta potentials with standard deviation

were calculated from all replicates. The details of this methods are identical to chapter previously reported, please see Section 4.3.6.

7.3.7 Analysis of the impurity concentration generated by sonication.

After sonication, the debris, that have generated by sonication probe, was found to be as an impurity in the prepared suspension. To determine the degree of contamination of the suspension, 20 ml of pure particle-free water without adding any nanoparticles was sonicated for 2 and 10 min. After each sonication, the concentration of the impurity was collected in triplicate using NTA. Please see Section 4.3.2 for the specification of NTA.

7.3.8 Analysis of microwave processing samples

Concentrations of 50/100 ppm samples were prepared using 1/2 mg NF Cu10 of which were dispersed in 20 mL of Acros pure particle-free water using microwave reactor (CEM discovery SP). A Teflon magnetic or glass stirrer was used to mix the samples. Each sample was, respectively, heated up to 50, 100 and 150 ℃ with high stirring level. They were held for 2 minutes and then cooled down to room temperature. The programs are shown in **Figure 7.1**. All samples were collected in triplicate using NTA. Please see Section 4.3.2 for the specification of NTA.

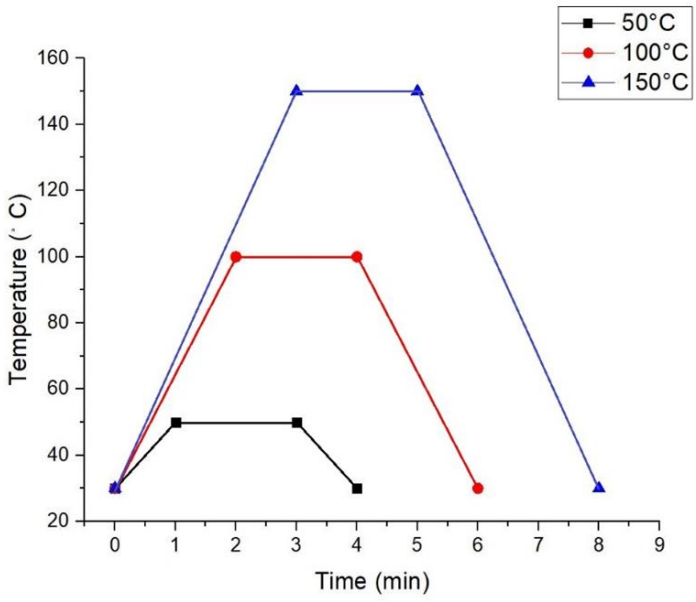


**Figure 7.1** Three programs of microwave heating of nanoparticles. Each sample was, respectively, heated up to 50, 100 and 150 ℃, followed by holding for 2 minutes and cooled down to room temperature.

## 7.4 Results and discussion

### 7.4.1 The calculation of delivered power of sonication (energy density).

In our lab, the operation of calculation of energy density was shown in **Figure 7.2**, which steps are further presented in Appendix C. Sonication powers at each amplitude were calculated using **Equation (7-1)** before it recorded as calorimetric curves at different device output settings in **Figure 7.3**.

**Figure 7.2** Setup for the measurement of probe sonication calorimetric curves. The sonication probe is immersed into a glass beaker with 500 mL of water and the probe immersion depth is 2.5 cm below the liquid surface. The temperature probe is fixed at a depth of 2.5 cm and 1 cm away from the sonication probe.

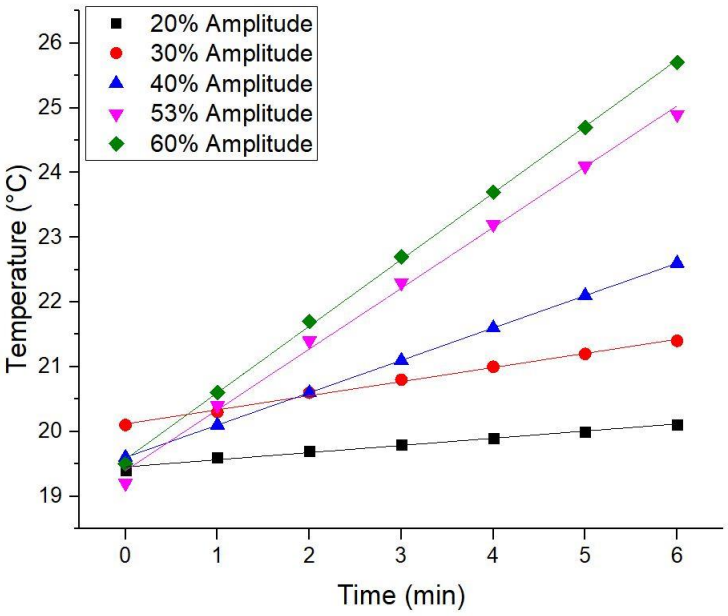


**Figure 7.3** Temperature increases as function of sonication time from 20% to 60% amplitude.

**Figure 7.4** showed the relationship between the calculated output power and the amplitude. Five different amplitude settings unexpectedly form a sigmoidal curve that may need a complex polynomial. It was considered that a linear fit has only been done from 30 to 53% amplitude, because exclusive amplitudes are relatively inappropriate to disperse suspensions. Eventually, an accurate linear ($R^2$-value > 0.99) was obtained to assist following study.

Thus, the suffered energy of suspension at 40% amplitude during sonication can be calculated using **Equation (7-2)**. As a result, the sonication power at 40% amplitude was $P_{40\%} = \frac{3K}{360\ s} \times 486.2\ g \times 4200\ J/(kg \cdot K) = 17\ W$. Moreover, the total energy of 2- and 10-minute sonication (cycles between 20 seconds on-pulse and 5 seconds off-pulse) were, respectively, 2,040 and 10,200 J. For the energy applied to a 30-ml suspension, the energy density (the amount of energy transferred per unit volume) of 2- and 10-minute sonication were, respectively, 68 and 340 J/ml. The effect of sonication duration on nanoparticle dispersions will be discussed in next section.

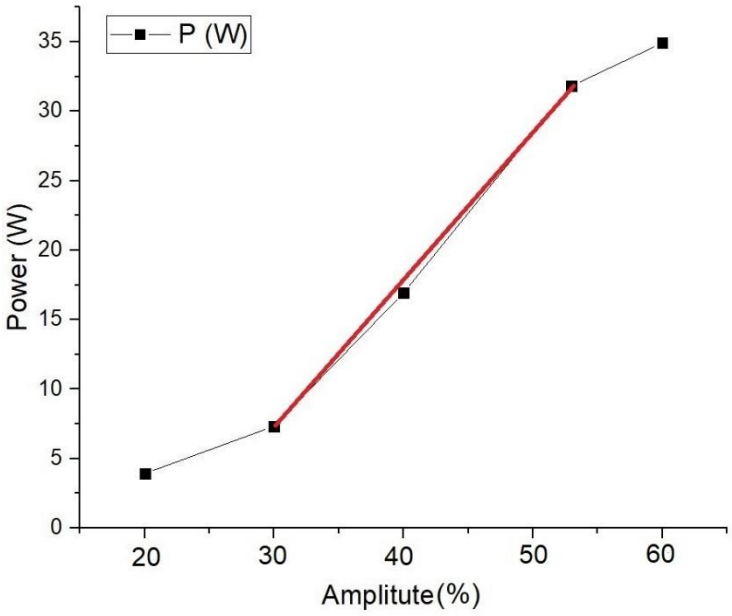


**Figure 7.4** Sonication power as function of probe amplitude. A linear fit was achieved from 30 to 53% amplitude.

7.4.2 The effects of delivered power on alloy nanoparticles.

*7.4.2.1 NTA analysis of CuAg and CuZn alloys*

The CuAg and CuZn suspensions at different concentrations (10, 50 and 100 ppm) were prepared using sonication for 2 and 10 min, respectively, and these two different sonication durations represented different energy density. The results were measured by NTA and shown in **Figure 7.5** and **7.6**. For two different sonication durations, the hydrodynamic size distributions (between D10 to D90) of CuAg suspensions for 10 minutes were smaller than that of 2 minutes indicating smaller size distribution. Their mode sizes measured by NTA were generally around 100 nm, but their mean size for 2- and 10-minute were, respectively, about 160 and 133 nm. The total concentrations (grey bars) of 10-minute sample of CuAg were slightly lower than that of 2-minute ones as well.

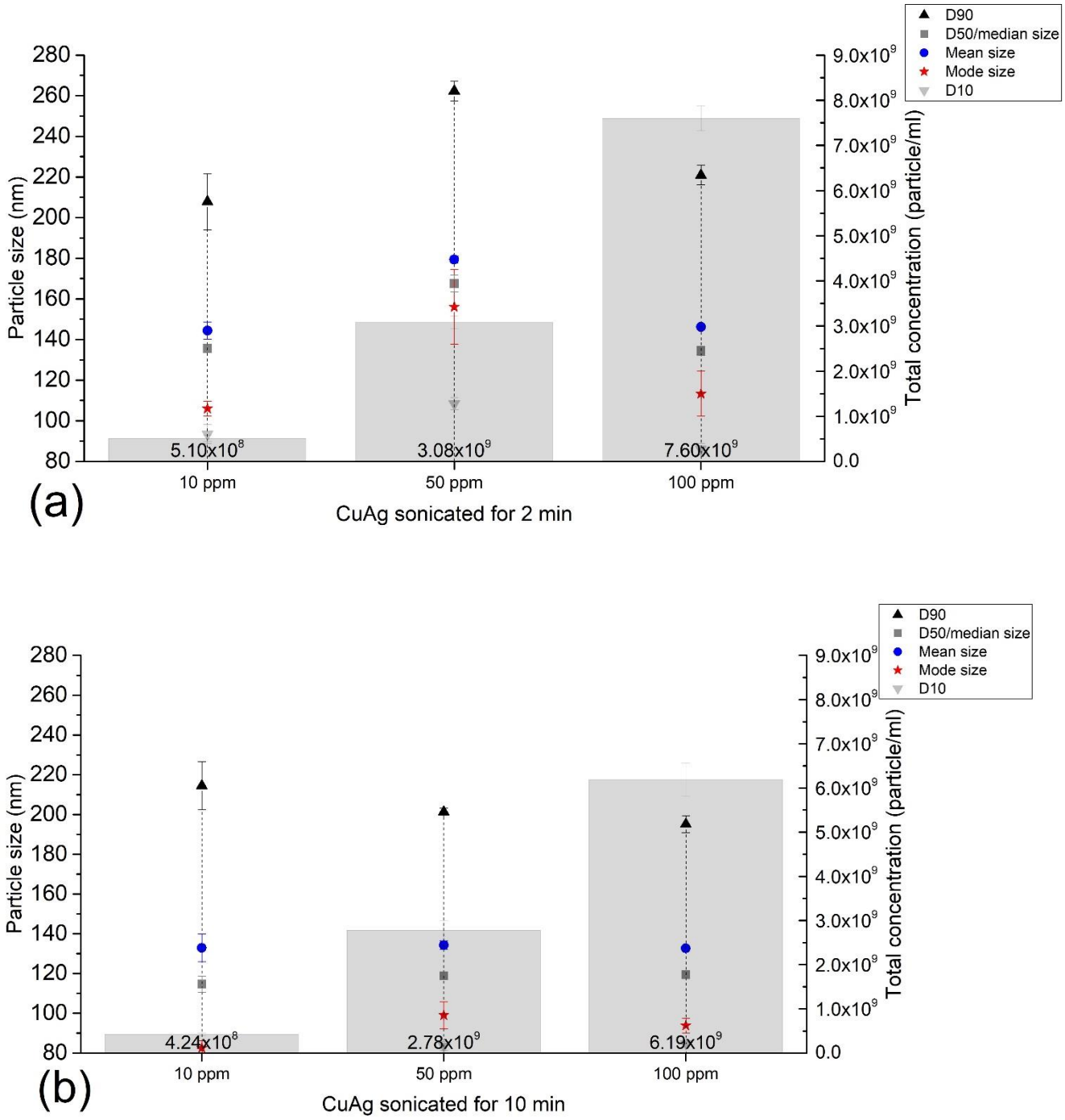


**Figure 7.5** The NTA results of CuAg sonicated for (a) 2-minute and (b) 10-minute duration at 10, 50 and 100 ppm.

The size distributions (D10 to D90) of CuAg suspensions for 10 minutes were smaller than that of 2 minutes and their mode sizes were generally around 100 nm.

To the opposite of CuAg suspensions, in **Figure 7.6**, CuZn suspensions subjected to sonication for 2 minutes and 10 minutes were quite different. The hydrodynamic size

distribution (D10 to D90) of 10-minute duration of CuZn at 10 ppm was in the range between 150 and 550 nm, which was much wider than that of 2-minute samples (between 97 to 275). This was also seen at 50 and 100 ppm of CuZn suspensions, the size distributions of CuZn suspensions for 2 minutes were both between 114 to 290 nm, while that of 10 minutes were between 100 to 330 nm.

Besides, at all three preparation concentrations (10, 50 and 100 ppm), 10-minute duration of CuZn suspensions had lower total concentrations than that of 2 minutes. According to last chapter, it was known that the agglomeration of nanoparticles caused the increase in size distribution and the decrease in hydrodynamic particle concentration. Apart from the nature that nanoparticles are prone to form aggregates and settled, longer sonication caused the excess energy not only cause overheating leading to the decrease of liquid cavitation strength, but also more energy to increase particle collisions [220].

And this can be reflected thermodynamically that the total energy delivered to solution in 10-minute sonication duration (10,200 J) was much more energy than that of 2-minute (2040 J), which was the same regarding energy density (equals to 340 and 68J/ml)

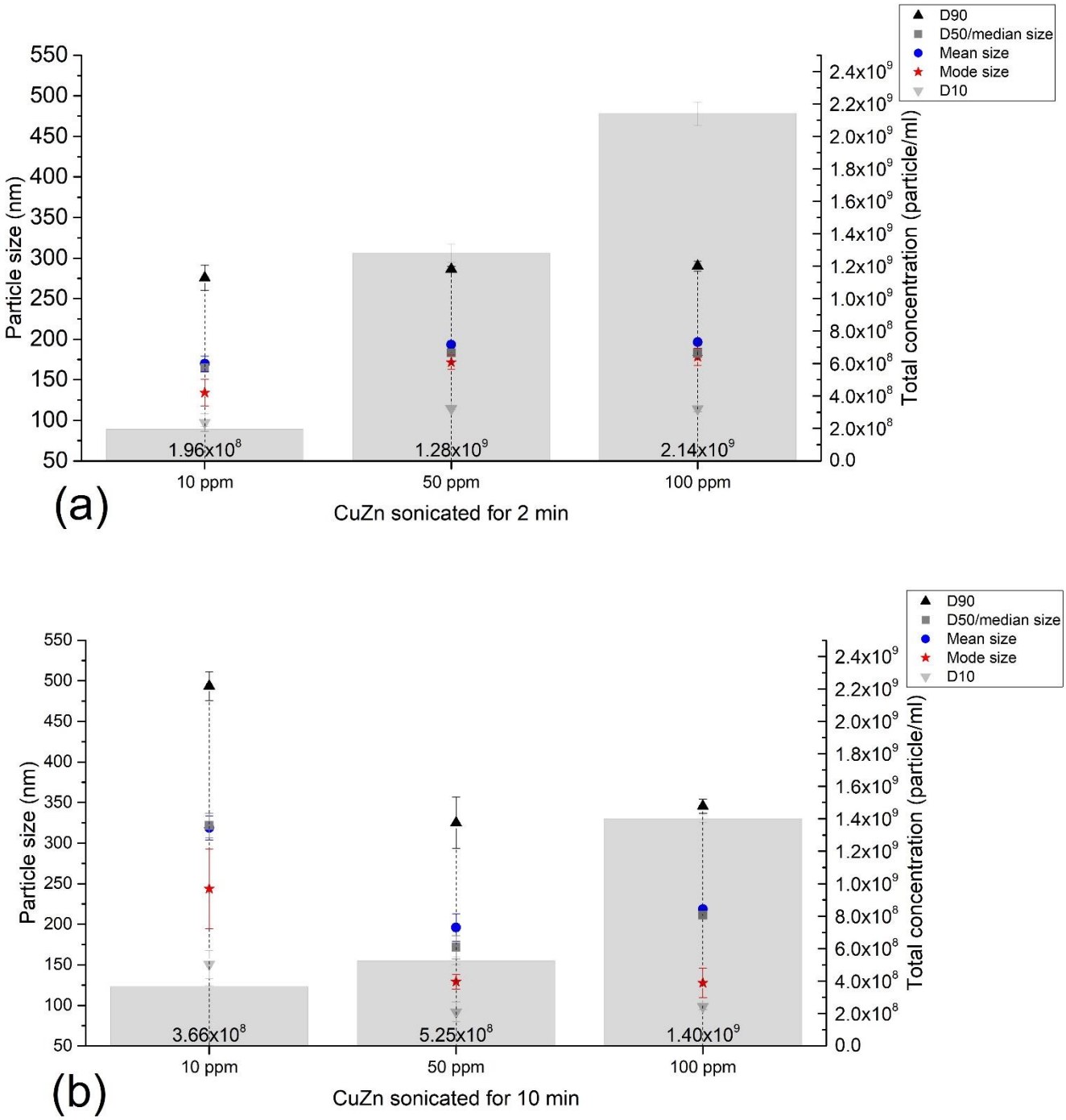


**Figure 7.6** The NTA results of CuZn sonicated for (a) 2-minute and (b) 10-minute duration at 10, 50 and 100 ppm.

10-minute duration of CuZn had wider size distributions (D10 to D90) and lower total concentrations than that of 2-minute samples.

*7.4.2.2 DLS analysis of CuAg and CuZn alloys*

After NTA measurement, 10, 50 and 100 ppm of CuAg and CuZn suspensions were then measured using Zetasizer in triplicate. As can be seen in **Table 7.2**, the suspensions of CuAg with 10-minute sonication duration showed less aggregation, it was the same when suspensions were diluted into low concentrations without further modified treatments. Meanwhile, the zeta potential values of CuAg suspensions for both sonication durations were on the same level closed to -30 mV, which inferred Brownian forces dominate over gravitational forces so that suspensions appear to be stable based on DLVO theory [211].

**Table 7.1** The results of 2-minute and 10-minute sonication duration of CuAg suspensions measured by Zetasizer.
The suspensions of CuAg with 10-minute sonication duration showed less aggregation, and no obvious changes of zeta potential were observed for CuAg suspensions.

| CuAg suspensions | | 2 min | 10 min |
|---|---|---|---|
| 10 ppm | Most hydrodynamic sizes (d.nm) | 243.4, 268.5, 321.7 | 243.4, 268.5, 321.7 |
| | Average size (d.nm) | 220±1.6 | 165±4.3 |
| | Zeta potential (mV) | -25.8±1.1 | -25.8±0.7 |
| 50 ppm | Most hydrodynamic sizes (d.nm) | 202, 218.1, 261.4 | 144.7, 155.6, 166.3 |
| | Average size (d.nm) | 176±2.8 | 126±1.9 |
| | Zeta potential (mV) | -39.5±0.8 | -37±0.7 |
| 100 ppm | Most hydrodynamic sizes (d.nm) | 186.2, 204.9, 233 | 140.4, 148.9, 155.6 |
| | Average size (d.nm) | 163±1.8 | 118±0.8 |
| | Zeta potential (mV) | -40.5±0.6 | -37.8±0.7 |

For 10-minute sonication duration of CuZn suspensions given in **Table 7.3**, they had huge average sizes with high deviation as well as lower absolute zeta potential values. A special attention was given to the 50-ppm CuZn suspension of 10-minute sonication duration, although it had a great zeta potential value (-23.2 mV), the average size (1593 nm) was more than 1.5 μm, which was huger than10 ppm and 100 ppm of CuZn for 10 min. Generally, CuZn

suspensions sonicated for 10 minutes were inferior to 2-minute duration, this may be due to increased collision frequency between the nanoparticles upon sonication. No obvious changes of zeta potential were observed for CuZn suspensions.

**Table 7.2** The results of 2-minute and 10-minute sonication of CuZn suspensions measured by Zetasizer.

10-minute sonication of CuZn had huge average sizes with high deviation. No obvious changes of zeta potential were observed for CuZn suspensions.

| CuZn suspensions | | 2 min | 10 min |
|---|---|---|---|
| 10 ppm | Most hydrodynamic sizes (d.nm) | 728.9, 819.8, 1115 | 220.3, 532.7, 532.9 |
| | Average size (d.nm) | 1089±164.2 | 538±111 |
| | Zeta potential (mV) | -8±1.6 | -17.8 ± 1.3 |
| 50 ppm | Most hydrodynamic sizes (d.nm) | 341, 374.9, 602.7 | 1351, 1399, 1449 |
| | Average size (d.nm) | 460±22.5 | 1593±76.4 |
| | Zeta potential (mV) | 24±0.6 | -23.2±0.9 |
| 100 ppm | Most hydrodynamic sizes (d.nm) | 679.8, 693.5, 729.4 | 1154, 1245, 1878 |
| | Average size (d.nm) | 583±18.3 | 1324±39.8 |
| | Zeta potential (mV) | 21.7±0.6 | 11.6±1.2 |

*7.4.2.3 Consideration of contaminations from sonication tip*

20 mL of pure water was sonicated for 2 and 10 min, respectively, i.e., they were suffered for, different energy density. As can be seen in **Figure 7.7**, the concentration of impurity increased with duration of sonication and the mode size of debris was around 80 nm. For usual preparation (2 min), the total concentration was around 1.18 x $10^8$ particle/ml, while 10-minute sonication duration generated up to 4.84 x $10^8$ particle/ml of total concentration. Thus, one should pay attention to the problem of ultrasonic treatment interfering with NTA results. Luckily, according to the reference mentioned in Section 4.3.1, the probe made of Ti-Al-V alloy shows no obvious antimicrobial effects.

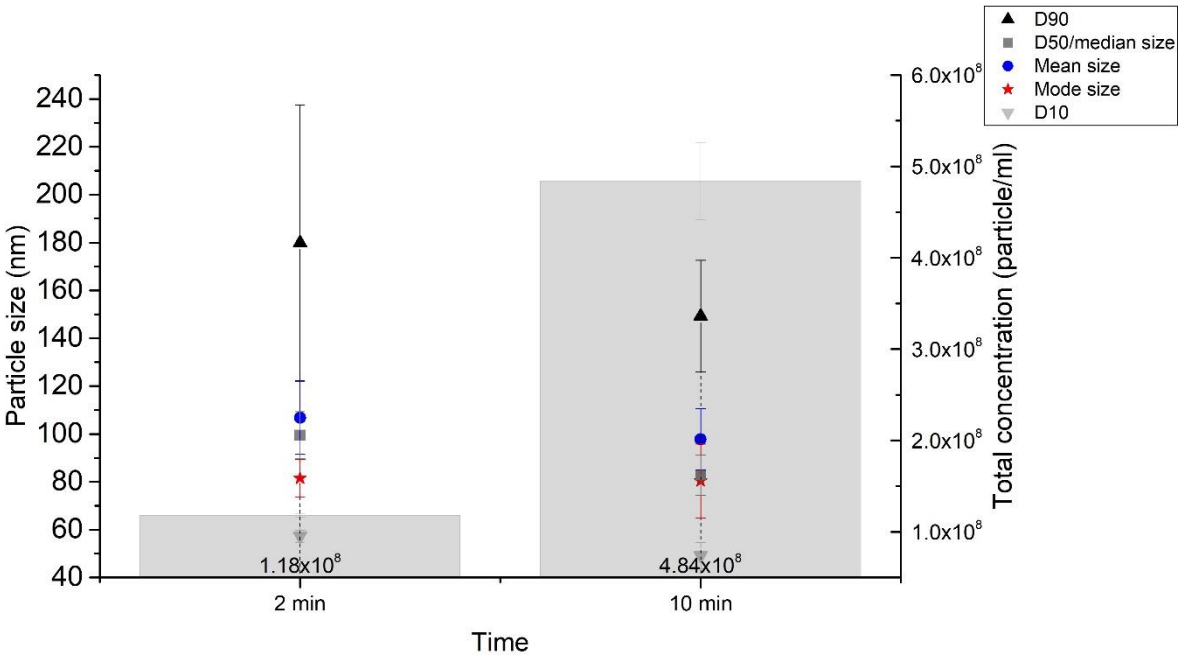


**Figure 7.7** The concentrations of accumulative impurity sonicated for 2 minutes and 10 minutes (equals to different energy density).

It can be clearly seen that under the same scale, the total concentration of impurity increased with duration of sonication and the mode size of debris was around 80 nm.

*7.4.2.4 Summary*

The sonication technique uses acoustic waves to break down the agglomeration of nanoparticles and disperse nanoparticles in a suspension. As two promising antimicrobial agents for the purpose of higher microbial exposure and polymer incorporation, CuAg and CuZn suspensions of various concentrations were, respectively, suffered from 2- and 10-minute sonication durations (equals to different energy density), and it can be concluded 2-minute sonication duration was more suitable for most nanoparticle preparations to obtain stable nanoparticle suspension which avoid overheating, particle collisions and contamination, especially for suspensions without surfactant treatments (only two of our samples were treated). Ion release was not measured since they were much lower than the limit of quantification. Neither there were not significant changes of zeta potential values on different sonication durations observed which was in agreement with the previous reference [42]. Therefore, it can be inferred that a long duration of sonication may not improve the stability and antimicrobial effects of nanoparticles.

### 7.4.3 Cu nanoparticle dispersion using microwave processing.

#### *7.4.3.1 NTA analysis of microwaved Cu suspensions*

According to the previous results, the sonicated NF Cu10 suspension showed poor dispersion and our study indicated that the contamination from sonication increased with duration of sonication, it is obvious that the concentration of tip debris could be too high, affecting the accuracy of NTA measurement. Therefore, an alternative method using microwave was developed to prepare Cu suspensions.

The NF Cu10 suspensions were prepared using microwave reactor with (a) Teflon or (b) glass stirrer and the results were measured by NTA. As can be seen in **Figure 7.8**, with increasing the limit of heating temperature, all samples were trend to narrow size distributions and raise concentrations of nanoparticle, suggesting an improvement of dispersion. By contrast, glass stirrer generated slightly wider size distributions (D10 to D90) than Teflon stirrer but higher total concentrations (grey bars) of nanoparticle. The mode sizes of nanoparticles for both stirrers were mostly observed near 100 nm, which were smaller than sonicated counterparts. Please refer to **Figure 4.6a**.

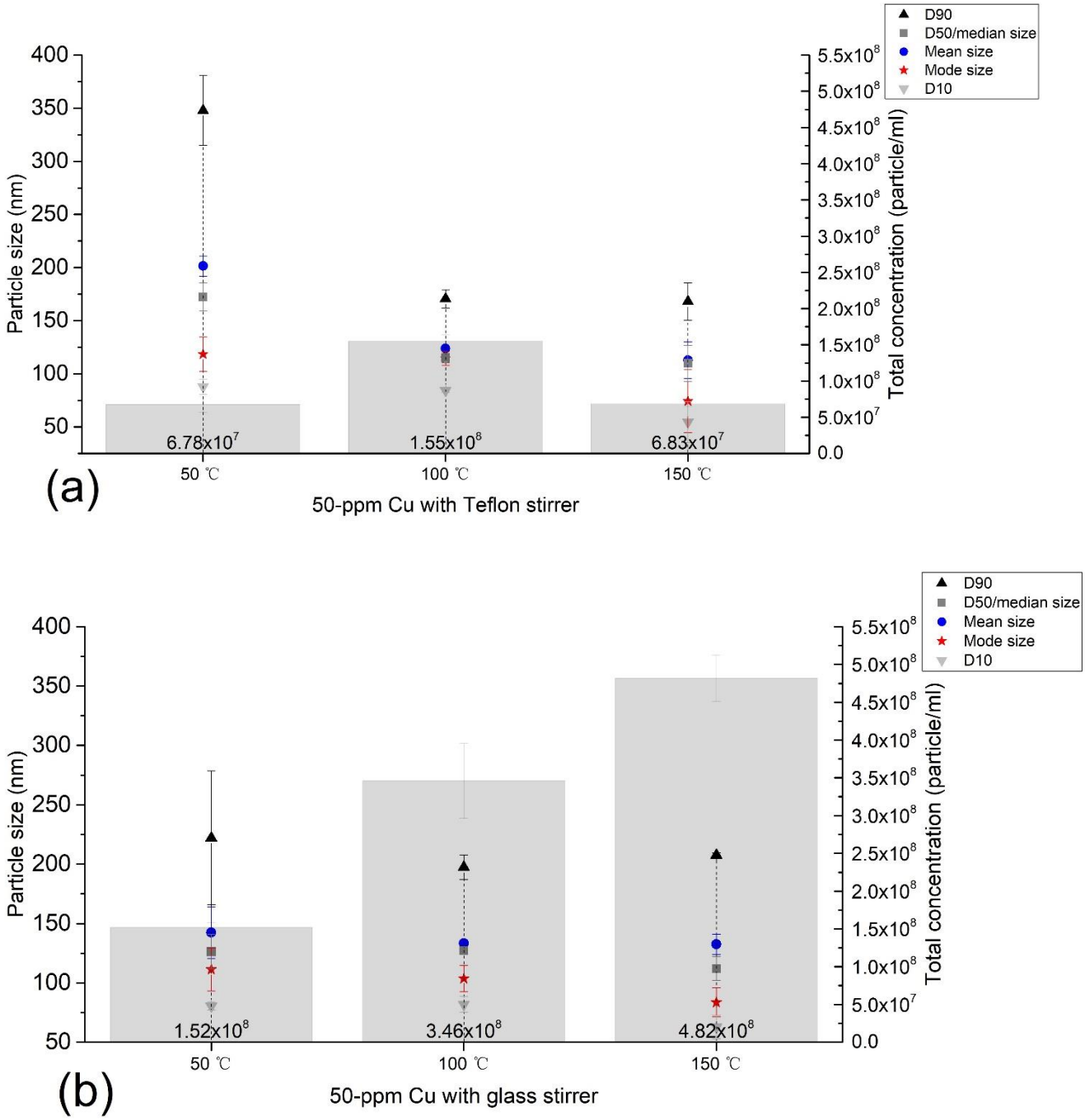


**Figure 7.8** The NTA results of NF Cu10 at 50 ppm when microwave reactor with (a) Teflon or (b) glass magnetic stirrer was heated up to 50, 100 and 150 ℃.

With increasing the limit of heating temperature more than 50 ℃, the size distributions were smaller and the total concentrations of nanoparticle raise. Glass stirrer generated wider size distributions than Teflon stirrer but higher total concentrations (grey bars) of nanoparticle.

**Figure 7.9** shows the hydrodynamic particle concentration and size distribution of NF Cu10 NP at 100 ppm when using (a) Teflon or (b) glass stirrer. At 10 and 50 ppm, glass stirrer generated larger size distributions (D10 to D90) and higher total concentrations (grey bars) then Teflon stirrer, but the mode sizes of samples for both stirrers were slightly far from 100 nm. NF Cu10 suspensions prepared below 100 ℃ of maximum heating temperature were less concentrated than sonicated counterparts, while samples heated at 150 ℃ displayed more desired distributions, especially the samples using Teflon stirrer.

Additionally, it is worth mentioning that microwave heating is able to avoid uncontrolled overheating as there is rapid cooling system by compressed air and heating temperature is controlled and recorded by microwave program, as displayed in **Figure 7.10**. Therefore, the energy density for processing a suspension can be controlled appropriately. A certain temperature higher than 150℃ could potentially generated a better suspension than sonication.

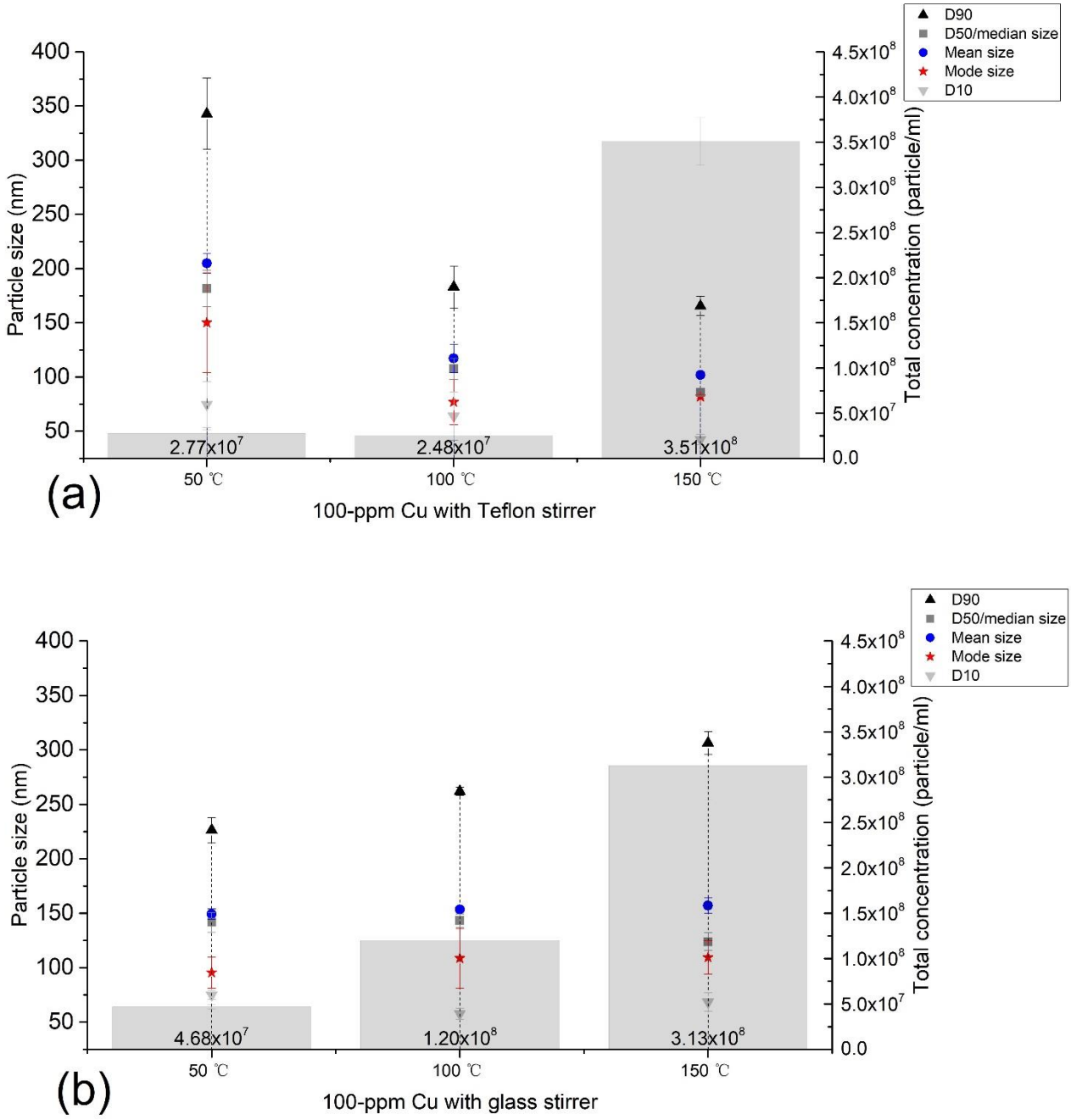


**Figure 7.9** The NTA results of NF Cu10 at 100 ppm when microwave reactor with (a) Teflon or (b) glass magnetic stirrer was heated up to 50, 100 and 150 ℃.
NF Cu10 suspensions prepared with Teflon stirrer and increasing temperature displayed more desired distributions.

.

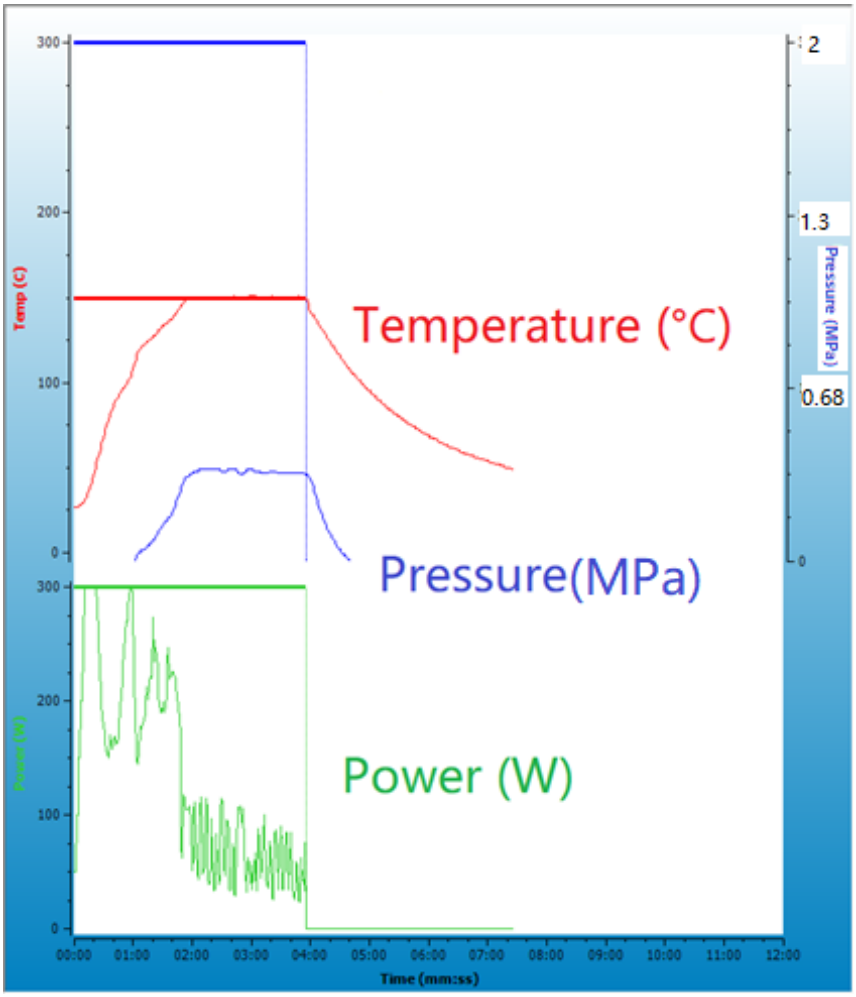


**Figure 7.10** A sample of NF Cu10 record at 100 ppm concentration using microwave reactor heated up to 150˚C.

*7.4.3.2 Summary and future perspectives*

In conclusion, the hydrodynamic concentrations and size distribution of nanoparticles varies with preparation conditions. The results demonstrated that nanoparticle suspensions at different concentrations exhibit better dispersion properties when the microwave reactor increases the limit of heating temperature. A certain temperature higher than 150℃ could potentially generate a better suspension than sonication. In the meantime, glass and Teflon stirrer showed different advantages – the glass stirrer provided higher particle concentrations while the Teflon stirrer displayed narrower size distributions.

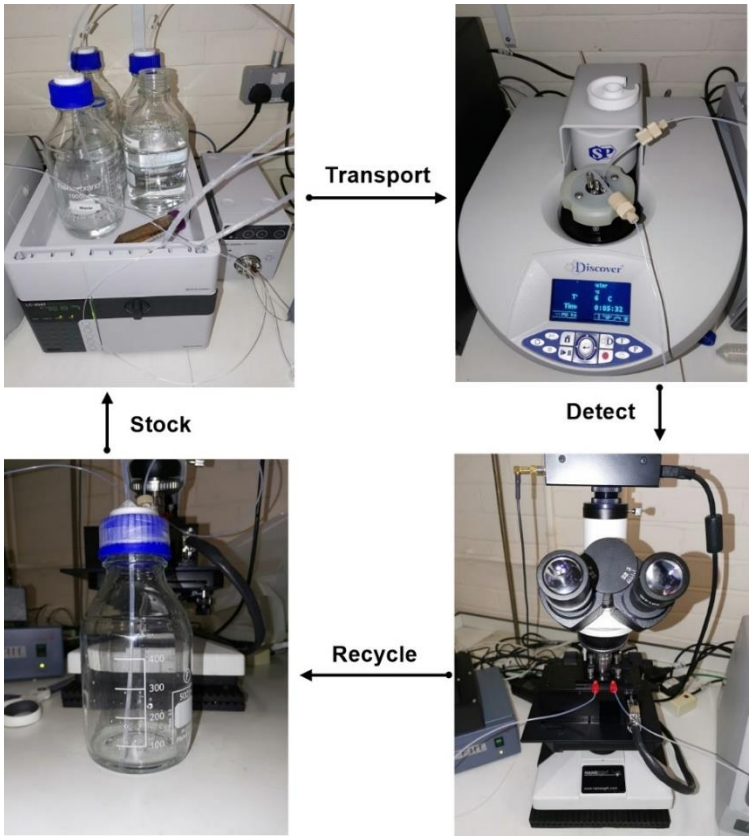


**Figure 7.11** Sustainable microwave heating and NTA detecting system. This system can continuously measure the size distribution of nanoparticle using NTA and effectively change preparation process of multiple conditions.

In **Figure 7.11**, a novel process method was developed allowing to measure samples using NTA during preparation process. Combined with our method of NTA measurement in last chapter, one enables to continuously measure the hydrodynamic size distribution of nanoparticle using NTA and effectively change preparation process of multiple conditions (such as temperature, flow rate and concentration) at the same time. The most important advantage of this system is the solution can avoid contamination from environment and overheating of nanoparticle during process. In the meantime, no transportation of sample requires which may also avoid contact with skin or eyes and inhalation of vapour or mist. The whole procedure is fully computer-controlled.

## CHARPTER 8 CONCLUSION AND FUTURE WORK

### 8.1 Summary of findings

Various sizes of Tungsten (W), Copper (Cu), Silver (Ag), Zinc (Zn) and their derivatives were investigated in this study. Several methods were developed to assist the study and numerous challenges have been addressed. The achievements and findings of this work are summarised as follows:

(1) Engineered and commercial nanoparticles were characterized *via* various facilities. SEM observed that the sizes of all particles were slightly larger than expectation. The shape of these particles including needle-like, sphere, cubic, *etc.* were also detected. XRD methods obtained the crystal structure and chemical compositions of certain materials, analysis from FTIR and Raman spectroscopy suggested the present of organic/inorganic components in some of these nanoparticles. ICP-OES analytical experiments successfully determined main elements purities of samples and emission intensities of minor elements which were fully digested using microwave assist method prior quantitative ICP-OES analysis. Based on the atomic ratio of elements from elemental analysis, formula for CuAg and CuZn nanoparticles were eventually calculated ($CuAg_{42}$ and $Cu_{2.3}Zn_1$).

(2) Nanoparticle suspensions were prepared from powder nanoparticles and treated well. NTA analysis measured the hydrodynamic particle concentration and size distribution of nanoparticle suspensions. The suspension properties were analysed by mean, median, mode size as well as span value. Additionally, metal ion leaching from the supernatant of each nanoparticle suspension was also carried out. It was noticed that the leaching properties of commercial and engineered nanoparticles performed differently in ion release effect, which were not directly related to their purity. The ion release study among CuO, alloy nanoparticles and AMNP3 also suggested ion release may not only depend on their types of forms but also pH levels and salt effect. The pH measurement and zeta potential of suspensions were also determined to understand their dispersibility. The pH of all samples was generally in the range between 6 and 7, the highest pH was from QNA CuO. The zeta potential of all samples was mostly negative, QNA Ag, CuAg and AMNP2 suspensions were considered the most stable suspensions.

(3) Given antimicrobial results of various nanoparticles against *P. aeruginosa* and *S. aureus*, it was proved that the antimicrobial effects can be attributed to many factors. First of all, only certain metals enable to inhibit bacteria, most of which are transition metals such as Cu, Ag, Zn, *etc.* Secondly, a solution of smaller particle size was more effectively to kill bacteria due to higher ratio of surface area to volume. Extreme tiny nanoparticles can even kill bacteria by penetrating the cell wall of bacteria and/or uptaking into cells. The shape of particle also influenced the antimicrobial effect. Thirdly, overproduction of ROS and ions can chemically inhibit bacteria by causing cellular dysfunction. It was found that the combination of multi-elements exerted a synergetic effect which allows less concentration but more effective in killing bacteria. Apart from elements themself, other factors such as pH, stability and modified treatment may also contribute on this effect. There may be an additional concern that the toxicity of solution should be under control of safety levels. Overall, alloy nanoparticle CuAg and CuZn showed the most promising physiochemical and antimicrobial characteristics, this is likely associated to their synergetic nature.

(4) To explore chances of nanoparticles exposure to the microbes and optimum incorporation into PMMA fibres, two different NTA methods were carried out. The QNA Ag and QNA Cu nanoparticles were measured in the supernatant study in total of 5 days. The size distributions of QNA Ag were slightly increased, while the hydrodynamic particle concentration and size distribution of QNA Cu were fluctuated. Later, the nanoparticle dispersant study was used to measure the stability of nanoparticle changing over time. QNA Ag and CuAg suspensions were surface-treated with $NH_4OH$ and were dispersed well, except CuAg suspension at 100 ppm had lower mass concentration than 50-ppm sample after 30 min, which was suggested to be modified by adding more surfactant than QNA Ag. The 100 ppm of Cu10 suspension was practically about 0.01 ppm at 24 minutes and 10- and 50-ppm suspensions were even lower. The mass concentration of AMMP2 formulation reached the highest values between 20 and 30 minutes, during which time it is recommended to incorporate it into the PMMA polymer. Overall, the level of antimicrobial efficacy appeared to be highly dependent on their hydrodynamic sizes and stability.

(5) A thermodynamics measurement for sonication duration, allowing the determination of the energy density delivered to a liquid medium, was calculated. Taking CuAg and CuZn as promising antimicrobial agents, it was found that the size of un-modified

CuZn suspension of nanoparticles increased with increasing sonication duration, while the $NH_4OH$-treated CuAg suspensions slightly lessened size with increasing sonication duration. For longer sonication duration, there was not significant change of zeta potential observed but impurity increased. In summary, 2-minute sonication duration was suitable for most processing preparation due to avoiding overheating, particle collisions and contamination. Therefore, a long duration of sonication may not improve the stability and antimicrobial effects of nanoparticles.

(6) Another process method based on microwave reactor was developed as an alternative method to process nanoparticle suspensions at different conditions including temperature, process time, concentration and type of stirrers. Increasing the limit of heating temperature using glass or Teflon stirrers enhanced the dispersion of nanoparticle, but both stirrers expressed different advantages in narrowing size distributions and raising particle concentrations. A certain temperature higher than 150℃ could potentially generated a better suspension than sonication. Combined with our previous processing method of NTA measurement in Chapter 6, this method could further turn into a part of continuously “microwave heating and NTA detecting” system to effectively process preparation, which avoids overheating of nanoparticles and contaminations at the same time during processing.

## 8.2 Future work

This research has shown various characterisations for antimicrobial nanoparticles. The study can further give an understanding regarding the stability of dispersion. The nanoparticle size could be further modified by milling to enhance ratio of surface area to volume. Further modification on nanoparticle solutions can be modified by changing pH (using buffer) to stabilize zeta potential of suspension. Avoiding adverse effects may also be taken in consideration when additional modifying agents are used.

Moreover, the dispersion property of nanoparticle solution can further be investigated using sustainable microwave heating and NTA detecting system which allows to optimize preparation conditions and observe particle distribution simultaneously. The advantage of this method is clean, safe, effective and full computer controlled. As the fact that the combination of multiply metals show synergy effects, a chemical synthesis of intermetallic compounds/alloy nanoparticle using microwave reactor can be carried out to properly customize process preparation and be finally incorporated into PMMA fibres.

Still, the antimicrobial activity of nanoparticle requires further understanding as well. NTA can be proposed to measure the number of nanoparticles in the suspension before and after exposure to bacteria in order to determine how many nanoparticles are attached to the bacteria cells. For example, if it is found that the concentration of nanoparticles is greatly decreased after an antibacterial activity, it may indicate that the nanoparticle tends to kill bacteria *via* attachment. Conversely, if the concentration of nanoparticles does not change, it may indicate that it kills bacteria *via* other mechanisms, such as ion release. A schematic figure of this assumption using NTA is displayed in **Figure 8.1.**

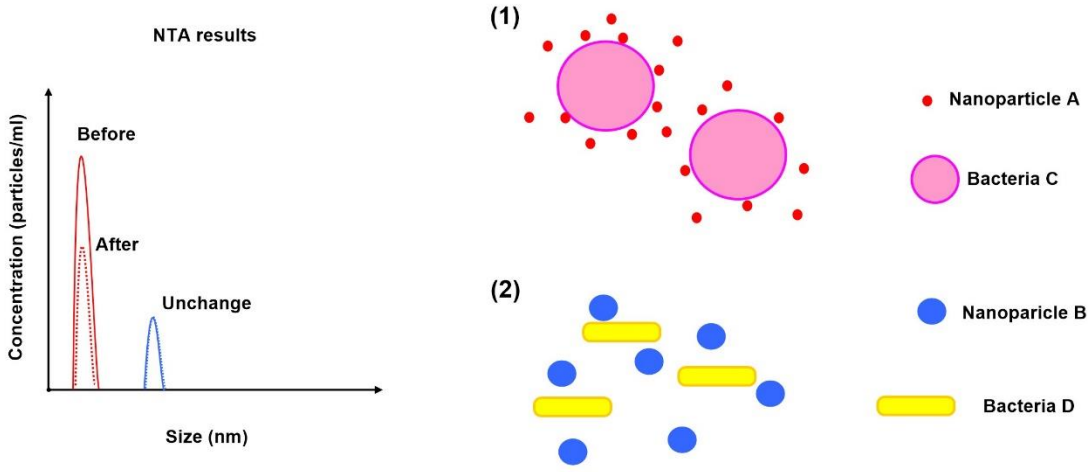


**Figure 8.1** A schematic figure of proposal to use NTA to detect whether the nanoparticles are attached to the bacteria cells.

There may be two possible situations: (1) the concentration of nanoparticles A is decreased after the antimicrobial activity against bacteria C; or (2) the concentration of nanoparticle B is remained the same after the antimicrobial activity against bacteria D.

## REFERENCE


1. Aminov, R.I., *A brief history of the antibiotic era: lessons learned and challenges for the future.* Frontiers in microbiology, 2010. **1**: p. 134.
2. Ippolito, G., S. Leone, F.N. Lauria, E. Nicastri, and R.P. Wenzel, *Methicillin-resistant Staphylococcus aureus: the superbug.* International journal of infectious diseases, 2010. **14**: p. S7-S11.
3. Atlanta, G., *CDC. Antibiotic Resistance Threats in the United States*, C.o.D. Control, Editor. 2019, U.S. Department of Health and Human Services.
4. Allaker, R.P. and G. Ren, *Potential impact of nanotechnology on the control of infectious diseases.* Transactions of the Royal Society of Tropical Medicine and Hygiene, 2008. **102**(1): p. 1-2.
5. Lemire, J.A., J.J. Harrison, and R.J. Turner, *Antimicrobial activity of metals: mechanisms, molecular targets and applications.* Nature Reviews Microbiology, 2013. **11**(6): p. 371-384.
6. De Berardis, B., G. Civitelli, M. Condello, P. Lista, R. Pozzi, G. Arancia, and S. Meschini, *Exposure to ZnO nanoparticles induces oxidative stress and cytotoxicity in human colon carcinoma cells.* Toxicology and applied pharmacology, 2010. **246**(3): p. 116-127.
7. Alagarasi, A., *Introduction to nanomaterials.* National Center for Environmental Research, 2011: p. 45-100.
8. Tolochko, N., *History of nanotechnology.* Nanoscience and nanotechnology. Encyclopaedia of life Support Systems (EOLSS), Developed under the auspices of the UNESCO, SEolss Published, oxford, 2009.
9. Thompson, D., *Michael Faraday's recognition of ruby gold: the birth of modern nanotechnology.* Gold Bulletin, 2007. **40**(4): p. 267-269.
10. Mody, V.V., R. Siwale, A. Singh, and H.R. Mody, *Introduction to metallic nanoparticles.* Journal of Pharmacy and Bioallied Sciences, 2010. **2**(4): p. 282.
11. Shen, W., J. Tang, R. Yang, H. Cong, X. Bao, Y. Wang, X. Wang, Z. Huang, J. Liu, and L. Huang, *Enhanced efficiency of polymer solar cells by incorporated Ag–SiO 2 core–shell nanoparticles in the active layer.* RSC Advances, 2014. **4**(9): p. 4379-4386.
12. Ghiaci, M., M. Tghizadeh, A.A. Ensafi, N. Zandi-Atashbar, and B. Rezaei, *Silver nanoparticles decorated anchored type ligands as new electrochemical sensors for glucose detection.* Journal of the Taiwan Institute of Chemical Engineers, 2016. **63**: p. 39-45.
13. Tamilvanan, A., K. Balamurugan, K. Ponappa, and B.M. Kumar, *Copper nanoparticles: synthetic strategies, properties and multifunctional application.* International Journal of Nanoscience, 2014. **13**(02): p. 1430001.
14. Rostami-Charati, F. and R. Akbari, *ZnO-nanoparticles as an Efficient Catalyst for the Synthesis of Functionalized Benzenes: Multicomponent Reactions of Sulfonoketenimides.* Combinatorial chemistry & high throughput screening, 2017. **20**(9): p. 781-786.
15. Kumar, B.V., H.S.B. Naik, D. Girija, and B.V. Kumar, *ZnO nanoparticle as catalyst for efficient green one-pot synthesis of coumarins through Knoevenagel condensation.* Journal of Chemical Sciences, 2011. **123**(5): p. 615-621.

16. Huynh, K.-H., X.-H. Pham, J. Kim, S.H. Lee, H. Chang, W.-Y. Rho, and B.-H. Jun, *Synthesis, Properties, and Biological Applications of Metallic Alloy Nanoparticles.* International Journal of Molecular Sciences, 2020. **21**(14): p. 5174.

17. Wang, C., L. Xu, X. Xu, H. Cheng, H. Sun, Q. Lin, and C. Zhang, *Near infrared Ag/Au alloy nanoclusters: tunable photoluminescence and cellular imaging.* Journal of colloid and interface science, 2014. **416**: p. 274-279.

18. An, C., Y. Kuang, C. Fu, F. Zeng, W. Wang, and H. Zhou, *Study on Ag–Pd bimetallic nanoparticles for electrocatalytic reduction of benzyl chloride.* Electrochemistry communications, 2011. **13**(12): p. 1413-1416.

19. Roduner, E., *Size matters: why nanomaterials are different.* Chemical Society Reviews, 2006. **35**(7): p. 583-592.

20. Ramalingam, G., P. Kathirgamanathan, G. Ravi, T. Elangovan, B. Arjunkumar, N. Manivannan, and K. Kasinathan, *Quantum Confinement*. 2020, IntechOpen. p. 1-11.

21. Kim, N.H., J.-Y. Kim, and K.J. Ihn, *Preparation of silver nanoparticles having low melting temperature through a new synthetic process without solvent.* Journal of nanoscience and nanotechnology, 2007. **7**(11): p. 3805-3809.

22. Loulijat, H., H. Zerradi, S. Mizani, E. mehdi Achhal, A. Dezairi, and S. Ouaskit, *The behavior of the thermal conductivity near the melting temperature of copper nanoparticle.* Journal of Molecular Liquids, 2015. **211**: p. 695-704.

23. Arole, V. and S. Munde, *FABRICATION OF NANOMATERIALS BY TOP-DOWN AND BOTTOM-UP APPROACHES–AN OVERVIEW.* 2014: p. 89-93.

24. Rogojan, R., E. Andronescu, C. Ghitulica, and B.S. Vasile, *Synthesis and characterization of alumina nano-powder obtained by sol-gel method.* UPB Buletin Stiintific, Series B: Chemistry and Materials Science, 2011. **73**(2): p. 67-76.

25. Teoh, G.L., K.Y. Liew, and W.A. Mahmood, *Synthesis and characterization of sol–gel alumina nanofibers.* Journal of Sol-Gel Science and Technology, 2007. **44**(3): p. 177-186.

26. Saleh, T.A. and V.K. Gupta, *Synthesis and characterization of alumina nano-particles polyamide membrane with enhanced flux rejection performance.* Separation and purification technology, 2012. **89**: p. 245-251.

27. Alwan, R.M., Q.A. Kadhim, K.M. Sahan, R.A. Ali, R.J. Mahdi, N.A. Kassim, and A.N. Jassim, *Synthesis of zinc oxide nanoparticles via sol–gel route and their characterization.* Nanoscience and Nanotechnology, 2015. **5**(1): p. 1-6.

28. Ramesh, S., *Sol-Gel Synthesis and Characterization of Ag3 (2+ x) AlxTi4-xO11+ δ (0.0 ⩽ x⩽ 1.0).* 2013: p. 1-8.

29. Zhou, R., S. Lin, H. Zong, T. Huang, F. Li, J. Pan, and J. Cui, *Continuous synthesis of Ag/TiO2 nanoparticles with enhanced photocatalytic activity by pulsed laser ablation.* Journal of Nanomaterials, 2017. **2017**: p. 1-9.

30. Verma, C., A. Janghel, S. Deo, P. Raut, D. Bhosle, S.S. Kumar, M. Agrawal, N. Amit, M. Sharma, and T. Giri, *A Comprehensive Advancement on Nanomedicines along with its various Biomedical Applications.* Research Journal of Pharmacy and Technology, 2015. **8**(7): p. 945-957.

31. Kumar, M. and Y. Ando, *Chemical vapor deposition of carbon nanotubes: a review on growth mechanism and mass production.* Journal of nanoscience and nanotechnology, 2010. **10**(6): p. 3739-3758.

32. Bhaviripudi, S., E. Mile, S.A. Steiner, A.T. Zare, M.S. Dresselhaus, A.M. Belcher, and J. Kong, *CVD synthesis of single-walled carbon nanotubes from gold nanoparticle catalysts.* Journal of the American Chemical Society, 2007. **129**(6): p. 1516-1517.

33. Adachi, M., S. Tsukui, and K. Okuyama, *Nanoparticle synthesis by ionizing source gas in chemical vapor deposition.* Japanese journal of applied physics, 2003. **42**(1A): p. L77.

34. Serio, M.A., D.M. Gruen, and R. Malhotra, *Synthesis and characterization of advanced materials*. 1998: American Chemical Society.

35. Kammler, H.K., L. Mädler, and S.E. Pratsinis, *Flame synthesis of nanoparticles.* Chemical Engineering & Technology: Industrial Chemistry - Plant Equipment - Process Engineering - Biotechnology, 2001. **24**(6): p. 583-596.

36. D'Amato, R., M. Falconieri, S. Gagliardi, E. Popovici, E. Serra, G. Terranova, and E. Borsella, *Synthesis of ceramic nanoparticles by laser pyrolysis: From research to applications.* Journal of analytical and applied pyrolysis, 2013. **104**: p. 461-469.

37. Ren, G., D. Hu, E.W. Cheng, M.A. Vargas-Reus, P. Reip, and R.P. Allaker, *Characterisation of copper oxide nanoparticles for antimicrobial applications*. International journal of antimicrobial agents, 2008. **33**(6): p. 587-590.

38. Ghaffarian, H.R., M. Saiedi, M.A. Sayyadnejad, and A.M. Rashidi, *Synthesis of ZnO nanoparticles by spray pyrolysis method.* 2011: p. 1-6.

39. Majid, I., G.A. Nayik, and V. Nanda, *Ultrasonication and food technology: A review.* Cogent Food & Agriculture, 2015. **1**(1): p. 1071022.

40. Taurozzi, J.S., V.A. Hackley, and M. Wiesner, *Preparation of nanoparticle dispersions from powdered material using ultrasonic disruption.* NIST special publication, 2012. **1200**(2): p. 1200-2.

41. Nickel, C., J. Angelstorf, R. Bienert, C. Burkart, S. Gabsch, S. Giebner, A. Haase, B. Hellack, H. Hollert, and K. Hund-Rinke, *Dynamic light-scattering measurement comparability of nanomaterial suspensions.* Journal of nanoparticle research, 2014. **16**(2): p. 2260.

42. Pradhan, S., J. Hedberg, E. Blomberg, S. Wold, and I.O. Wallinder, *Effect of sonication on particle dispersion, administered dose and metal release of non-functionalized, non-inert metal nanoparticles.* Journal of nanoparticle research, 2016. **18**(9): p. 285.

43. Cohen, J., G. DeLoid, G. Pyrgiotakis, and P. Demokritou, *Interactions of engineered nanomaterials in physiological media and implications for in vitro dosimetry.* Nanotoxicology, 2013. **7**(4): p. 417-431.

44. Yadav, T.P., R.M. Yadav, and D.P. Singh, *Mechanical milling: a top down approach for the synthesis of nanomaterials and nanocomposites.* Nanoscience and Nanotechnology, 2012. **2**(3): p. 22-48.

45. Mukhopadhyay, N., T. Yadav, and O. Srivastava, *An investigation on the transformation of the icosahedral phase in the Al-Fe-Cu system during mechanical milling and subsequent annealing.* Philosophical Magazine A, 2002. **82**(16): p. 2979-2993.

46. Kuppusamy, P., M.M. Yusoff, G.P. Maniam, and N. Govindan, *Biosynthesis of metallic nanoparticles using plant derivatives and their new avenues in pharmacological applications–An updated report.* Saudi Pharmaceutical Journal, 2016. **24**(4): p. 473-484.

47. Chandran, S.P., M. Chaudhary, R. Pasricha, A. Ahmad, and M. Sastry, *Synthesis of gold nanotriangles and silver nanoparticles using Aloevera plant extract.* Biotechnology progress, 2006. **22**(2): p. 577-583.

48. Lin, L., W. Wang, J. Huang, Q. Li, D. Sun, X. Yang, H. Wang, N. He, and Y. Wang, *Nature factory of silver nanowires: Plant-mediated synthesis using broth of Cassia fistula leaf.* Chemical Engineering Journal, 2010. **162**(2): p. 852-858.

49. Huang, K.-M., Z. Lin, and X. Yang, *Numerical simulation of microwave heating on chemical reaction in dilute solution.* Progress In Electromagnetics Research, 2004. **49**: p. 273-289.

50. Leonelli, C. and T.J. Mason, *Microwave and ultrasonic processing: now a realistic option for industry.* Chemical Engineering and Processing: Process Intensification, 2010. **49**(9): p. 885-900.

51. Estel, L., M. Poux, N. Benamara, and I. Polaert, *Continuous flow-microwave reactor: Where are we?* Chemical Engineering and Processing: Process Intensification, 2017. **113**: p. 56-64.

52. Hu, B., S.-B. Wang, K. Wang, M. Zhang, and S.-H. Yu, *Microwave-assisted rapid facile "green" synthesis of uniform silver nanoparticles: self-assembly into multilayered films and their optical properties.* The Journal of Physical Chemistry C, 2008. **112**(30): p. 11169-11174.

53. Blosi, M., S. Albonetti, M. Dondi, C. Martelli, and G. Baldi, *Microwave-assisted polyol synthesis of Cu nanoparticles.* Journal of Nanoparticle Research, 2011. **13**(1): p. 127-138.

54. Vernon-Parry, K., *Scanning electron microscopy: an introduction.* III-Vs Review, 2000. **13**(4): p. 40-44.

55. Puchalski, M., P. Dąbrowski, W. Olejniczak, P. Krukowski, P. Kowalczyk, and K. Polański, *The study of silver nanoparticles by scanning electron microscopy, energy dispersive X-ray analysis and scanning tunnelling microscopy.* Materials Science-Poland, 2007. **25**(2): p. 473-478.

56. Suleiman, M., M. Mousa, A. Hussein, B. Hammouti, T.B. Hadda, and I. Warad, *Copper (II)-oxide nanostructures: synthesis, characterizations and their applications-review.* Journal of Materials and Environmental Science, 2013. **4**(5): p. 792-797.

57. Suresh, Y., S. Annapurna, G. Bhikshamaiah, and A. Singh, *Copper Nanoparticles: Green Synthesis and Characterization.* International Journal of Scientific & Engineering Research, 2014. **5**(3,156-160).

58. Suzuki, S., *Physical and chemical properties of carbon nanotubes*. 2013: BoD–Books on Demand.

59. Wojtas, A. and M. Kalab, *A simple procedure for the preparation of stirred yoghurt for scanning electron microscopy.* Food microstructure, 1984: p. 197-198.

60. Golding, C.G., L.L. Lamboo, D.R. Beniac, and T.F. Booth, *The scanning electron microscope in microbiology and diagnosis of infectious disease.* Scientific reports, 2016. **6**: p. 26516.

61. Stadtländer, C., *Scanning electron microscopy and transmission electron microscopy of mollicutes: challenges and opportunities*. Modern research and educational topics in microscopy, 2007. **1**: p. 122-131.

62. V. Subha, S.K., S. Renganathan, *Green Synthesis of Silver Nanoparticles from a Novel Medicinal Plant Source Roots Extract of Mukia maderaspatana.* Colloid and Surface Science, 2016. **Vol. 1**(No. 1): p. 14-17.

63. Eaton, P., P. Quaresma, C. Soares, C. Neves, M. de Almeida, E. Pereira, and P. West, *A direct comparison of experimental methods to measure dimensions of synthetic nanoparticles.* Ultramicroscopy, 2017. **182**: p. 179-190.

64. Frigerio, C., J.L. Santos, J.A. Barbosa, P. Eaton, M.L.M. Saraiva, and M.L. Passos, *A soft strategy for covalent immobilization of glutathione and cysteine capped quantum dots onto amino functionalized surfaces.* Chemical Communications, 2013. **49**(25): p. 2518-2520.

65. Smith, M., K. Thompson, and F. Lennard, *A literature review of analytical techniques for materials characterisation of painted textiles—Part 2: spectroscopic and chromatographic analytical instrumentation.* Journal of the Institute of Conservation, 2017. **40**(3): p. 252-266.

66. Khan, S.A., S.B. Khan, L.U. Khan, A. Farooq, K. Akhtar, and A.M. Asiri, *Fourier transform infrared spectroscopy: fundamentals and application in functional groups and nanomaterials characterization*, in *Handbook of Materials Characterization*. 2018, Springer. p. 317-344.

67. Grdadolnik, J., *ATR-FTIR spectroscopy: Its advantage and limitations.* Acta Chimica Slovenica, 2002. **49**(3): p. 631-642.

68. Djomgoue, P. and D. Njopwouo, *FT-IR spectroscopy applied for surface clays characterization.* Journal of Surface Engineered Materials and Advanced Technology, 2013. **3**(04): p. 275.

69. Salam, M.A. and R. Burk, *Synthesis and characterization of multi-walled carbon nanotubes modified with octadecylamine and polyethylene glycol.* Arabian Journal of Chemistry, 2017. **10**: p. S921-S927.

70. Betancourt-Galindo, R., P. Reyes-Rodriguez, B. Puente-Urbina, C. Avila-Orta, O. Rodríguez-Fernández, G. Cadenas-Pliego, R. Lira-Saldivar, and L. García-Cerda, *Synthesis of copper nanoparticles by thermal decomposition and their antimicrobial properties.* Journal of Nanomaterials, 2014. **2014**: p. 10.

71. Belskaya, O.B., I.G. Danilova, M.O. Kazakov, R.M. Mironenko, A.V. Lavrenov, and V.A. Likholobov, *FTIR Spectroscopy of adsorbed probe molecules for analyzing the surface properties of supported Pt (Pd) catalysts*, in *Infrared Spectroscopy-Materials Science, Engineering and Technology*. 2012, InTech.

72. Saletnik, A., B. Saletnik, and C. Puchalski, *Overview of Popular Techniques of Raman Spectroscopy and Their Potential in the Study of Plant Tissues.* Molecules, 2021. **26**(6): p. 1537.

73. Exline, D., *Comparison of Raman and FTIR Spectroscopy: Advantages and Limitations.* Luettu, 2013. **27**: p. 2018.

74. Wartewig, S., *IR and Raman spectroscopy: fundamental processing*. 2006: John Wiley & Sons.

75. Spring, M., C. Ricci, D.A. Peggie, and S.G. Kazarian, *ATR-FTIR imaging for the analysis of organic materials in paint cross sections: case studies on paint samples from the National Gallery, London.* Analytical and bioanalytical chemistry, 2008. **392**(1-2): p. 37-45.

76. Costa, S., E. Borowiak-Palen, M. Kruszynska, A. Bachmatiuk, and R. Kalenczuk, *Characterization of carbon nanotubes by Raman spectroscopy.* Materials Science-Poland, 2008. **26**(2): p. 433-441.

77. Richter, H., Z. Wang, and L. Ley, *The one phonon Raman spectrum in microcrystalline silicon.* Solid State Communications, 1981. **39**(5): p. 625-629.

78. Ding, Q., L. Hang, and L. Ma, *Controlled synthesis of Cu nanoparticle arrays with surface enhanced Raman scattering effect performance.* RSC advances, 2018. **8**(4): p. 1753-1757.

79. Rivero, I.V. and C.O. Ruud, *Determination of the accuracy of phase analysis measurements on spherical surfaces through X-ray diffraction.* NDT & E International, 2008. **41**(6): p. 434-440.

80. Bunaciu, A.A., E.G. UdriŞTioiu, and H.Y. Aboul-Enein, *X-ray diffraction: instrumentation and applications.* Critical reviews in analytical chemistry, 2015. **45**(4): p. 289-299.

81. Kaliva, M. and M. Vamvakaki, *Chapter 17 - Nanomaterials characterization*, in *Polymer Science and Nanotechnology*, R. Narain, Editor. 2020, Elsevier. p. 401-433.

82. Valério, A. and S.L. Morelhao, *Usage of Scherrer's formula in X-ray diffraction analysis of size distribution in systems of monocrystalline nanoparticles.* arXiv preprint arXiv:1911.00701, 2019: p. 1-9.

83. Theivasanthi, T. and M. Alagar, *X-ray diffraction studies of copper nanopowder.* Archives of Physics Research, 2010: p. 112-117.

84. Zawrah, M., H.A. Zayed, R.A. Essawy, A.H. Nassar, and M.A. Taha, *Preparation by mechanical alloying, characterization and sintering of Cu–20 wt.% Al2O3 nanocomposites.* Materials & Design, 2013. **46**: p. 485-490.

85. Abbas, S.M., S.T. Hussain, S. Ali, F. Abbas, N. Ahmad, N. Ali, and Y. Khan, *One-pot synthesis of a composite of monodispersed CuO nanospheres on carbon nanotubes as anode material for lithium-ion batteries.* Journal of alloys and compounds, 2013. **574**: p. 221-226.

86. Hou, X. and B.T. Jones, *Inductively coupled plasma/optical emission spectrometry.* Encyclopedia of analytical chemistry, 2000. **11**: p. 9468-9485.

87. Francis, R. and R. Annick, *Chemical analysis modern instrumentation methods and techniques second edition.* John Willey and Sons France, 2007.

88. Santos, É.J.d., A.B. Herrmann, J.L. Olkuszewski, T.D. Saint'Pierre, and A.J. Curtius, *Determination of trace metals in electrolytic copper by ICP OES and ICP-MS.* Brazilian Archives of Biology and Technology, 2005. **48**(5): p. 681-687.

89. Du, B.D., D.V. Phu, L.A. Quoc, and N.Q. Hien, *Synthesis and investigation of antimicrobial activity of Cu2O nanoparticles/zeolite*. Journal of Nanoparticles, 2017. **2017**: p. 1-6.

90. Lin, Y., W. Qiqiang, Z. Xiaoming, W. Zhouping, X. Wenshui, and D. Yuming, *Synthesis of Ag/TiO 2 Core/Shell Nanoparticles with Antibacterial Properties.* Bulletin of the Korean Chemical Society, 2011. **32**(8): p. 2607-2610.

91. Filipe, V., A. Hawe, and W. Jiskoot, *Critical evaluation of Nanoparticle Tracking Analysis (NTA) by NanoSight for the measurement of nanoparticles and protein aggregates.* Pharmaceutical research, 2010. **27**(5): p. 796-810.

92. Malam, Y., E. J Lim, and A. M Seifalian, *Current trends in the application of nanoparticles in drug delivery.* Current medicinal chemistry, 2011. **18**(7): p. 1067-1078.

93. Wei, A., J.G. Mehtala, and A.K. Patri, *Challenges and opportunities in the advancement of nanomedicines.* Journal of controlled release, 2012. **164**(2): p. 236-246.

94. Bhise, N.S., R.B. Shmueli, J. Gonzalez, and J.J. Green, *A novel assay for quantifying the number of plasmids encapsulated by polymer nanoparticles.* Small, 2012. **8**(3): p. 367-373.

95. Carr, B. and M. Wright, *Nanoparticle Tracking Analysis: A Review of Applications and Usage 2010-2012 (Nanosight Ltd., 2013).* Google Scholar, 2013: p. 7.

96. Moore, J. and E. Cerasoli, *Particle light scattering methods and applications.* 2017.

97. Lu, G.W. and P. Gao, *Emulsions and microemulsions for topical and transdermal drug delivery*, in *Handbook of Non-Invasive Drug Delivery Systems*. 2010, Elsevier. p. 59-94.

98. Malarkodi, C., S. Rajeshkumar, K. Paulkumar, M. Vanaja, G. Gnanajobitha, and G. Annadurai, *Biosynthesis and antimicrobial activity of semiconductor nanoparticles against oral pathogens.* Bioinorganic chemistry and applications, 2014. **2014**: p. 1-10.

99. Bankier, C., Y. Cheong, S. Mahalingam, M. Edirisinghe, G. Ren, E. Cloutman-Green, and L. Ciric, *A comparison of methods to assess the antimicrobial activity of nanoparticle combinations on bacterial cells.* PloS one, 2018. **13**(2): p. e0192093.

100. Seil, J.T. and T.J. Webster, *Antimicrobial applications of nanotechnology: methods and literature.* International journal of nanomedicine, 2012. **7**: p. 2767.

101. Berney, M., F. Hammes, F. Bosshard, H.-U. Weilenmann, and T. Egli, *Assessment and interpretation of bacterial viability by using the LIVE/DEAD BacLight Kit in combination with flow cytometry.* Applied and environmental microbiology, 2007. **73**(10): p. 3283-3290.

102. Nocker, A., P. Sossa-Fernandez, M.D. Burr, and A.K. Camper, *Use of propidium monoazide for live/dead distinction in microbial ecology.* Applied and environmental microbiology, 2007. **73**(16): p. 5111-5117.

103. Dizaj, S.M., F. Lotfipour, M. Barzegar-Jalali, M.H. Zarrintan, and K. Adibkia, *Antimicrobial activity of the metals and metal oxide nanoparticles.* Materials Science and Engineering: C, 2014. **44**: p. 278-284.

104. Morones, J.R., J.L. Elechiguerra, A. Camacho, K. Holt, J.B. Kouri, J.T. Ramírez, and M.J. Yacaman, *The bactericidal effect of silver nanoparticles.* Nanotechnology, 2005. **16**(10): p. 2346.

105. Park, M.V., A.M. Neigh, J.P. Vermeulen, L.J. de la Fonteyne, H.W. Verharen, J.J. Briedé, H. van Loveren, and W.H. de Jong, *The effect of particle size on the cytotoxicity, inflammation, developmental toxicity and genotoxicity of silver nanoparticles.* Biomaterials, 2011. **32**(36): p. 9810-9817.

106. Sondi, I. and B. Salopek-Sondi, *Silver nanoparticles as antimicrobial agent: a case study on E. coli as a model for Gram-negative bacteria.* Journal of colloid and interface science, 2004. **275**(1): p. 177-182.

107. Jo, Y.-K., B.H. Kim, and G. Jung, *Antifungal activity of silver ions and nanoparticles on phytopathogenic fungi.* Plant Disease, 2009. **93**(10): p. 1037-1043.

108. Egger, S., R.P. Lehmann, M.J. Height, M.J. Loessner, and M. Schuppler, *Antimicrobial properties of a novel silver-silica nanocomposite material.* Applied and environmental microbiology, 2009. **75**(9): p. 2973-2976.

109. Kim, J.S., E. Kuk, K.N. Yu, J.-H. Kim, S.J. Park, H.J. Lee, S.H. Kim, Y.K. Park, Y.H. Park, and C.-Y. Hwang, *Antimicrobial effects of silver nanoparticles.* Nanomedicine: Nanotechnology, Biology and Medicine, 2007. **3**(1): p. 95-101.

110. Pal, S., Y.K. Tak, and J.M. Song, *Does the antibacterial activity of silver nanoparticles depend on the shape of the nanoparticle? A study of the gram-negative bacterium Escherichia coli.* Applied and environmental microbiology, 2007. **73**(6): p. 1712-1720.

111. Bera, R., S. Mandal, and C.R. Raj, *Antimicrobial activity of fluorescent Ag nanoparticles.* Letters in applied microbiology, 2014. **58**(6): p. 520-526.

112. Stevenson, J., A. Barwinska-Sendra, E. Tarrant, and K. Waldron, *Mechanism of action and applications of the antimicrobial properties of copper.* Microbial pathogens and strategies for combating them: Science, technology and education, 2013: p. 468-479.

113. Palza, H., *Antimicrobial polymers with metal nanoparticles.* International journal of molecular sciences, 2015. **16**(1): p. 2099-2116.

114. Blecher, K., A. Nasir, and A. Friedman, *The growing role of nanotechnology in combating infectious disease.* Virulence, 2011. **2**(5): p. 395-401.

115. Tkeshelashvili, L.K., T. McBride, K. Spence, and L.A. Loeb, *Mutation spectrum of copper-induced DNA damage.* Journal of Biological Chemistry, 1991. **266**(10): p. 6401-6406.

116. Macomber, L. and J.A. Imlay, *The iron-sulfur clusters of dehydratases are primary intracellular targets of copper toxicity.* Proceedings of the National Academy of Sciences, 2009. **106**(20): p. 8344-8349.

117. Yoon, K.-Y., J.H. Byeon, J.-H. Park, and J. Hwang, *Susceptibility constants of Escherichia coli and Bacillus subtilis to silver and copper nanoparticles.* Science of the Total Environment, 2007. **373**(2-3): p. 572-575.

118. DeAlba-Montero, I., J. Guajardo-Pacheco, E. Morales-Sánchez, R. Araujo-Martínez, G. Loredo-Becerra, G.-A. Martínez-Castañón, F. Ruiz, and M. Compeán Jasso, *Antimicrobial properties of copper nanoparticles and amino acid chelated copper nanoparticles produced by using a soya extract.* Bioinorganic chemistry and applications, 2017. **2017**: p. 1-6.

119. sani Usman, M., *Synthesis, characterization, and antimicrobial properties of copper nanoparticles.* International journal of nanomedicine, 2013. **8**: p. 4467-4479.

120. Mahapatra, O., M. Bhagat, C. Gopalakrishnan, and K.D. Arunachalam, *Ultrafine dispersed CuO nanoparticles and their antibacterial activity.* Journal of Experimental Nanoscience, 2008. **3**(3): p. 185-193.

121. Ahamed, M., H.A. Alhadlaq, M. Khan, P. Karuppiah, and N.A. Al-Dhabi, *Synthesis, characterization, and antimicrobial activity of copper oxide nanoparticles.* Journal of Nanomaterials, 2014. **2014**: p. 17.

122. Azam, A., A.S. Ahmed, M. Oves, M. Khan, and A. Memic, *Size-dependent antimicrobial properties of CuO nanoparticles against Gram-positive and-negative bacterial strains.* Int J Nanomedicine, 2012. **7**(9): p. 3527-3535.

123. Saraf, R., *Cost effective and monodispersed zinc oxide nanoparticles synthesis and their characterization.* International Journal of Advances in Applied Sciences, 2013. **2**(2): p. 85-88.

124. Jones, N., B. Ray, K.T. Ranjit, and A.C. Manna, *Antibacterial activity of ZnO nanoparticle suspensions on a broad spectrum of microorganisms.* FEMS microbiology letters, 2008. **279**(1): p. 71-76.

125. Azam, A., A.S. Ahmed, M. Oves, M.S. Khan, S.S. Habib, and A. Memic, *Antimicrobial activity of metal oxide nanoparticles against Gram-positive and Gram-negative bacteria: a comparative study.* International journal of nanomedicine, 2012. **7**: p. 6003.

126. Zhang, L., Y. Ding, M. Povey, and D. York, *ZnO nanofluids–A potential antibacterial agent.* Progress in Natural Science, 2008. **18**(8): p. 939-944.

127. Ravindranadh, M.R.K. and T.R. Mary, *Development of ZnO Nanoparticles for Clinical Applications.* Journal of Chemical, Biological and Physical Sciences (JCBPS), 2013. **4**(1): p. 469.

128. Jiang, W., H. Mashayekhi, and B. Xing, *Bacterial toxicity comparison between nano- and micro-scaled oxide particles.* Environmental pollution, 2009. **157**(5): p. 1619-1625.

129. Padmavathy, N. and R. Vijayaraghavan, *Enhanced bioactivity of ZnO nanoparticles—an antimicrobial study.* Science and technology of advanced materials, 2008. **9**(3): p. 035004.

130. Bahrami, K., P. Nazari, M. Nabavi, M. Golkar, A. Almasirad, and A.R. Shahverdi, *Hydroxyl capped silver-gold alloy nanoparticles: characterization and their combination effect with different antibiotics against Staphylococcus aureus*. Nanomedicine Journal, 2014. **1**(3): p. 155-161.

131. Li, H.F., K.J. Qiu, F.Y. Zhou, L. Li, and Y.F. Zheng, *Design and development of novel antibacterial Ti-Ni-Cu shape memory alloys for biomedical application.* Scientific Reports, 2016. **6**: p. 37475.

132. Cai, S., X. Jia, Q. Han, X. Yan, R. Yang, and C. Wang, *Porous Pt/Ag nanoparticles with excellent multifunctional enzyme mimic activities and antibacterial effects.* Nano Research, 2017: p. 1-14.

133. Vargas-Reus, M.A., K. Memarzadeh, J. Huang, G.G. Ren, and R.P. Allaker, *Antimicrobial activity of nanoparticulate metal oxides against peri-implantitis pathogens.* International journal of antimicrobial agents, 2012. **40**(2): p. 135-139.

134. Guldiren, D. and S. Aydın, *Antimicrobial property of silver, silver-zinc and silver-copper incorporated soda lime glass prepared by ion exchange.* Materials Science and Engineering: C, 2017. **78**: p. 826-832.

135. Dizaj, S.M., A. Mennati, S. Jafari, K. Khezri, and K. Adibkia, *Antimicrobial activity of carbon-based nanoparticles.* Advanced pharmaceutical bulletin, 2015. **5**(1): p. 19.

136. Kang, S., M. Herzberg, D.F. Rodrigues, and M. Elimelech, *Antibacterial effects of carbon nanotubes: size does matter!* Langmuir, 2008. **24**(13): p. 6409-6413.

137. Akhavan, O. and E. Ghaderi, *Toxicity of graphene and graphene oxide nanowalls against bacteria.* ACS nano, 2010. **4**(10): p. 5731-5736.

138. Arias, L.R. and L. Yang, *Inactivation of bacterial pathogens by carbon nanotubes in suspensions.* Langmuir, 2009. **25**(5): p. 3003-3012.

139. Yun, H., J.D. Kim, H.C. Choi, and C.W. Lee, *Antibacterial activity of CNT-Ag and GO-Ag nanocomposites against gram-negative and gram-positive bacteria.* Bulletin of the Korean Chemical Society, 2013. **34**(11): p. 3261-3264.

140. Ruparelia, J.P., A.K. Chatterjee, S.P. Duttagupta, and S. Mukherji, *Strain specificity in antimicrobial activity of silver and copper nanoparticles.* Acta biomaterialia, 2008. **4**(3): p. 707-716.

141. Volpe, C.M.O., P.H. Villar-Delfino, P.M.F. dos Anjos, and J.A. Nogueira-Machado, *Cellular death, reactive oxygen species (ROS) and diabetic complications.* Cell death & disease, 2018. **9**(2): p. 1-9.

142. Leuba, K.D., N.G. Durmus, E.N. Taylor, and T.J. Webster, *carboxylate functionalized superparamagnetic iron oxide nanoparticles (SPION) for the reduction of S. aureus growth post biofilm formation.* International journal of nanomedicine, 2013. **8**: p. 731.

143. Grass, G., C. Rensing, and M. Solioz, *Metallic copper as an antimicrobial surface.* Applied and environmental microbiology, 2011. **77**(5): p. 1541-1547.

144. Slavin, Y.N., J. Asnis, U.O. Häfeli, and H. Bach, *Metal nanoparticles: understanding the mechanisms behind antibacterial activity.* Journal of nanobiotechnology, 2017. **15**(1): p. 65.

145. Lai, H.-Z., W.-Y. Chen, C.-Y. Wu, and Y.-C. Chen, *Potent antibacterial nanoparticles for pathogenic bacteria.* ACS applied materials & interfaces, 2015. **7**(3): p. 2046-2054.

146. Ravishankar Rai, V. and A. Jamuna Bai, *Nanoparticles and their potential application as antimicrobials.* A Méndez-Vilas A, editor. Mysore: Formatex, 2011: p. 197-209.

147. Yeo, S.Y., H.J. Lee, and S.H. Jeong, *Preparation of nanocomposite fibers for permanent antibacterial effect.* Journal of Materials science, 2003. **38**(10): p. 2143-2147.

148. Farkas, J., H. Peter, P. Christian, J.A.G. Urrea, M. Hassellöv, J. Tuoriniemi, S. Gustafsson, E. Olsson, K. Hylland, and K.V. Thomas, *Characterization of the effluent from a nanosilver producing washing machine.* Environment international, 2011. **37**(6): p. 1057-1062.

149. Illangakoon, U.E., S. Mahalingam, K. Wang, Y.-K. Cheong, E. Canales, G. Ren, E. Cloutman-Green, M. Edirisinghe, and L. Ciric, *Gyrospun antimicrobial nanoparticle loaded fibrous polymeric filters.* Materials Science and Engineering: C, 2017. **74**: p. 315-324.

150. Pourmand, A. and M. Abdollahi, *Current opinion on nanotoxicology*. 2012, Springer. p. 1-3.

151. Vishwakarma, V., S.S. Samal, and N. Manoharan, *Safety and risk associated with nanoparticles-a review.* J. Miner. Mater. Charact. Eng, 2010. **9**(5): p. 455-459.

152. Zoroddu, M.A., S. Medici, A. Ledda, V.M. Nurchi, J.I. Lachowicz, and M. Peana, *Toxicity of nanoparticles.* Curr Med Chem, 2014. **21**(33): p. 3837-53.

153. Crisponi, G., V.M. Nurchi, J.I. Lachowicz, M. Peana, S. Medici, and M.A. Zoroddu, *Toxicity of nanoparticles: etiology and mechanisms*, in *Antimicrobial Nanoarchitectonics*. 2017, Elsevier. p. 511-546.

154. Trop, M., M. Novak, S. Rodl, B. Hellbom, W. Kroell, and W. Goessler, *Silver-coated dressing acticoat caused raised liver enzymes and argyria-like symptoms in burn patient.* Journal of Trauma and Acute Care Surgery, 2006. **60**(3): p. 648-652.

155. Chen, Z., H. Meng, G. Xing, C. Chen, Y. Zhao, G. Jia, T. Wang, H. Yuan, C. Ye, and F. Zhao, *Acute toxicological effects of copper nanoparticles in vivo.* Toxicology letters, 2006. **163**(2): p. 109-120.

156. De Jong, W.H., W.I. Hagens, P. Krystek, M.C. Burger, A.J. Sips, and R.E. Geertsma, *Particle size-dependent organ distribution of gold nanoparticles after intravenous administration.* Biomaterials, 2008. **29**(12): p. 1912-1919.

157. Xu, Z., C. Liu, J. Wei, and J. Sun, *Effects of four types of hydroxyapatite nanoparticles with different nanocrystal morphologies and sizes on apoptosis in rat osteoblasts.* Journal of Applied Toxicology, 2012. **32**(6): p. 429-435.

158. Brunner, T.J., P. Wick, P. Manser, P. Spohn, R.N. Grass, L.K. Limbach, A. Bruinink, and W.J. Stark, *In vitro cytotoxicity of oxide nanoparticles: comparison to asbestos, silica, and the effect of particle solubility.* Environmental science & technology, 2006. **40**(14): p. 4374-4381.

159. Wang, L., C. Hu, and L. Shao, *The antimicrobial activity of nanoparticles: present situation and prospects for the future.* International journal of nanomedicine, 2017. **12**: p. 1227.

160. Osonga, F.J., A. Akgul, I. Yazgan, A. Akgul, G.B. Eshun, L. Sakhaee, and O.A. Sadik, *Size and Shape-Dependent Antimicrobial Activities of Silver and Gold Nanoparticles: A Model Study as Potential Fungicides.* Molecules, 2020. **25**(11): p. 2682.

161. Ren, G., J.S. Oxford, P.W. Reip, and R. Lambkin-Williams, *Anti-Viral formulations Nanomaterials and Nanoparticles*. 2013: US 2013/0091611 A1, GB.

162. Cheong, Y.-K., J. Calvo-Castro, L. Ciric, M. Edirisinghe, E. Cloutman-Green, U.E. Illangakoon, Q. Kang, S. Mahalingam, R.K. Matharu, R.M. Wilson, and G. Ren, *Characterisation of the Chemical Composition and Structural Features of Novel Antimicrobial Nanoparticles.* Nanomaterials, 2017. **2017, 7, 152**.

163. Ren, G., J.S. Oxford, P.W. Reip, and L.-W. Robert, *Anti-viral formulations and nanomaterials and Nanoparticles*. 2010, Queen Mary & Westfield College, Intrinsiq Materials Limited, Retroscreen Virology Limited: GB.

164. Xu, L.J., J.X. Zhao, T. Zhang, G.G. Ren, and Z. Yang, *In vitro study on influence of nano particles of CuO on CA1 pyramidal neurons of rat hippocampus potassium currents.* Environmental Toxicology: An International Journal, 2009. **24**(3): p. 211-217.

165. Cheong, Y.-K., J. Calvo-Castro, L. Ciric, M. Edirisinghe, E. Cloutman-Green, U.E. Illangakoon, Q. Kang, S. Mahalingam, R.K. Matharu, and R.M. Wilson, *Characterisation of the chemical composition and structural features of novel antimicrobial nanoparticles.* Nanomaterials, 2017. **7**(7): p. 152.

166. Takenaka, S., E. Karg, C. Roth, H. Schulz, A. Ziesenis, U. Heinzmann, P. Schramel, and J. Heyder, *Pulmonary and systemic distribution of inhaled ultrafine silver particles in rats.* Environmental health perspectives, 2001. **109**(suppl 4): p. 547-551.

167. Kanwal, Z., M.A. Raza, S. Riaz, S. Manzoor, A. Tayyeb, I. Sajid, and S. Naseem, *Synthesis and characterization of silver nanoparticle-decorated cobalt nanocomposites (Co@ AgNPs) and their density-dependent antibacterial activity.* Royal Society open science, 2019. **6**(5): p. 182135.

168. Nandiyanto, A.B.D., R. Oktiani, and R. Ragadhita, *How to read and interpret FTIR spectroscope of organic material.* Indonesian Journal of Science and Technology, 2019. **4**(1): p. 97-118.

169. Khan, M.E., M.M. Khan, and M.H. Cho, *Fabrication of WO 3 nanorods on graphene nanosheets for improved visible light-induced photocapacitive and photocatalytic performance.* RSC Advances, 2016. **6**(25): p. 20824-20833.

170. Garcia-Sanchez, R.F., T. Ahmido, D. Casimir, S. Baliga, and P. Misra, *Thermal effects associated with the Raman spectroscopy of WO3 gas-sensor materials.* The Journal of Physical Chemistry A, 2013. **117**(50): p. 13825-13831.

171. Ravichandran, S., V. Paluri, G. Kumar, K. Loganathan, and B.R. Kokati Venkata, *A novel approach for the biosynthesis of silver oxide nanoparticles using aqueous leaf extract of Callistemon lanceolatus (Myrtaceae) and their therapeutic potential.* Journal of Experimental Nanoscience, 2016. **11**(6): p. 445-458.

172. Zhang, Y.C., J.Y. Tang, G.L. Wang, M. Zhang, and X.Y. Hu, *Facile synthesis of submicron Cu2O and CuO crystallites from a solid metallorganic molecular precursor.* Journal of crystal growth, 2006. **294**(2): p. 278-282.

173. Irwin, J., J. Chrzanowski, T. Wei, D. Lockwood, and A. Wold, *Raman scattering from single crystals of cupric oxide.* Physica C: Superconductivity, 1990. **166**(5-6): p. 456-464.

174. Shlimak, I., A. Butenko, E. Kogan, and M. Kaveh, *Irradiation-induced broadening of the Raman spectra in monolayer graphene.* Journal of Applied Physics, 2019. **126**(19): p. 194302.

175. Sultana, P., S. Das, A. Bhattacharya, R. Basu, and P. Nandy, *Development of iron oxide and titania treated fly ash based ceramic and its bioactivity.* Materials Science and Engineering: C, 2012. **32**(6): p. 1358-1365.

176. Berg, J.M., A. Romoser, N. Banerjee, R. Zebda, and C.M. Sayes, *The relationship between pH and zeta potential of~ 30 nm metal oxide nanoparticle suspensions relevant to in vitro toxicological evaluations.* Nanotoxicology, 2009. **3**(4): p. 276-283.

177. Carr, B. and M. Wright, *Nanoparticle tracking analysis.* Innovations in Pharmaceutical Technology, 2008. **26**: p. 38-40.

178. Ha, H. and J. Payer, *The effect of silver chloride formation on the kinetics of silver dissolution in chloride solution.* Electrochimica acta, 2011. **56**(7): p. 2781-2791.

179. Prasad, M., K.S. Sajwan, and R. Naidu, *Availability of Heavy Metals Applied to Soil through Sewage Sludge*, in *Trace Elements in the Environment*. 2005, CRC Press. p. 57-80.

180. Hsueh, Y.-H., P.-H. Tsai, and K.-S. Lin, *Ph-dependent antimicrobial properties of copper oxide nanoparticles in staphylococcus aureus.* International journal of molecular sciences, 2017. **18**(4): p. 793.

181. Bhattacharjee, S., *DLS and zeta potential–What they are and what they are not?* Journal of Controlled Release, 2016. **235**: p. 337-351.

182. Ciani, L., S. Ristori, C. Bonechi, C. Rossi, and G. Martini, *Effect of the preparation procedure on the structural properties of oligonucleotide/cationic liposome complexes (lipoplexes) studied by electron spin resonance and Zeta potential.* Biophysical chemistry, 2007. **131**(1-3): p. 80-87.

183. Bernfield, M., M. Götte, P.W. Park, O. Reizes, M.L. Fitzgerald, J. Lincecum, and M. Zako, *Functions of cell surface heparan sulfate proteoglycans.* Annual review of biochemistry, 1999. **68**(1): p. 729-777.

184. El Badawy, A.M., R.G. Silva, B. Morris, K.G. Scheckel, M.T. Suidan, and T.M. Tolaymat, *Surface charge-dependent toxicity of silver nanoparticles.* Environmental science & technology, 2010. **45**(1): p. 283-287.

185. Win, K.Y. and S.-S. Feng, *Effects of particle size and surface coating on cellular uptake of polymeric nanoparticles for oral delivery of anticancer drugs.* Biomaterials, 2005. **26**(15): p. 2713-2722.

186. Baron, F., M.-F. Cochet, W. Ablain, N. Grosset, M.-N. Madec, F. Gonnet, S. Jan, and M. Gautier, *Rapid and cost-effective method for micro-organism enumeration based on miniaturization of the conventional plate-counting technique.* Le Lait, 2006. **86**(3): p. 251-257.

187. Choi, O. and Z. Hu, *Size dependent and reactive oxygen species related nanosilver toxicity to nitrifying bacteria.* Environmental science & technology, 2008. **42**(12): p. 4583-4588.

188. Wang, L., H. He, Y. Yu, L. Sun, S. Liu, C. Zhang, and L. He, *Morphology-dependent bactericidal activities of Ag/CeO2 catalysts against Escherichia coli.* Journal of inorganic biochemistry, 2014. **135**: p. 45-53.

189. Mclaren, A., T. Valdes-Solis, G. Li, and S.C. Tsang, *Shape and size effects of ZnO nanocrystals on photocatalytic activity.* Journal of the American Chemical Society, 2009. **131**(35): p. 12540-12541.

190. Masters, E.A., A.T. Salminen, S. Begolo, E.N. Luke, S.C. Barrett, C.T. Overby, A.L. Gill, K.L. de Mesy Bentley, H.A. Awad, and S.R. Gill, *An in vitro platform for elucidating the molecular genetics of S. aureus invasion of the osteocyte lacuno-canalicular network during chronic osteomyelitis.* Nanomedicine: Nanotechnology, Biology and Medicine, 2019. **21**: p. 102039.

191. Woodworth, B.A., E. Tamashiro, G. Bhargave, N.A. Cohen, and J.N. Palmer, *An in vitro model of Pseudomonas aeruginosa biofilms on viable airway epithelial cell monolayers.* American journal of rhinology, 2008. **22**(3): p. 235-238.

192. Shleev, S., J. Tkac, A. Christenson, T. Ruzgas, A.I. Yaropolov, J.W. Whittaker, and L. Gorton, *Direct electron transfer between copper-containing proteins and electrodes.* Biosensors and Bioelectronics, 2005. **20**(12): p. 2517-2554.

193. Alexander, J.W., *History of the medical use of silver.* Surgical infections, 2009. **10**(3): p. 289-292.

194. Qing, Y.a., L. Cheng, R. Li, G. Liu, Y. Zhang, X. Tang, J. Wang, H. Liu, and Y. Qin, *Potential antibacterial mechanism of silver nanoparticles and the optimization of orthopedic implants by advanced modification technologies.* International journal of nanomedicine, 2018. **13**: p. 3311-3327.

195. Prabhu, S. and E.K. Poulose, *Silver nanoparticles: mechanism of antimicrobial action, synthesis, medical applications, and toxicity effects.* International Nano Letters, 2012. **2**(1): p. 32.

196. Khalandi, B., Asadi, N., Milani, M., Davaran, S., Abadi, A. J. N., Abasi, E. and Akbarzadeh, A., *A review on potential role of silver nanoparticles and possible mechanisms of their actions on bacteria.* Drug Res (Stuttg), 2017. **11**(2): p. 70–76.

197. Cavassin, E.D., L.F.P. de Figueiredo, J.P. Otoch, M.M. Seckler, R.A. de Oliveira, F.F. Franco, V.S. Marangoni, V. Zucolotto, A.S.S. Levin, and S.F. Costa, *Comparison of methods to detect the in vitro activity of silver nanoparticles (AgNP) against multidrug resistant bacteria.* Journal of nanobiotechnology, 2015. **13**(1): p. 64.

198. Yang, Y., J. Wang, Z. Xiu, and P.J. Alvarez, *Impacts of silver nanoparticles on cellular and transcriptional activity of nitrogen-cycling bacteria.* Environmental toxicology and chemistry, 2013. **32**(7): p. 1488-1494.

199. Yin, J.-J., J. Liu, M. Ehrenshaft, J.E. Roberts, P.P. Fu, R.P. Mason, and B. Zhao, *Phototoxicity of nano titanium dioxides in HaCaT keratinocytes—generation of reactive oxygen species and cell damage.* Toxicology and applied pharmacology, 2012. **263**(1): p. 81-88.

200. Fu, P.P., Q. Xia, H.-M. Hwang, P.C. Ray, and H. Yu, *Mechanisms of nanotoxicity: generation of reactive oxygen species.* Journal of food and drug analysis, 2014. **22**(1): p. 64-75.

201. Chiang, H.-m., Q. Xia, X. Zou, C. Wang, S. Wang, B.J. Miller, P.C. Howard, J.J. Yin, F.A. Beland, and H. Yu, *Nanoscale ZnO induces cytotoxicity and DNA damage in human cell lines and rat primary neuronal cells.* Journal of nanoscience and nanotechnology, 2012. **12**(3): p. 2126-2135.

202. Fridovich, I., *Biological effects of the superoxide radical.* Archives of biochemistry and biophysics, 1986. **247**(1): p. 1-11.

203. Fang, M., J.-H. Chen, X.-L. Xu, P.-H. Yang, and H.F. Hildebrand, *Antibacterial activities of inorganic agents on six bacteria associated with oral infections by two susceptibility tests.* International Journal of Antimicrobial Agents, 2006. **27**(6): p. 513-517.

204. Bishop, G.M., R. Dringen, and S.R. Robinson, *Zinc stimulates the production of toxic reactive oxygen species (ROS) and inhibits glutathione reductase in astrocytes.* Free Radical Biology and Medicine, 2007. **42**(8): p. 1222-1230.

205. Zakharova, O.V., A.Y. Godymchuk, A.A. Gusev, S.I. Gulchenko, I.A. Vasyukova, and D.V. Kuznetsov, *Considerable variation of antibacterial activity of Cu nanoparticles suspensions depending on the storage time, dispersive medium, and particle sizes.* BioMed research international, 2015. **2015**.

206. Nazeruddin, G., R. Prasad, Y. Shaikh, and A. Shaikh, *Synergetic effect of Ag-Cu bimetallic nanoparticles on antimicrobial activity.* Der Pharmacia Lettre, 2014. **3**: p. 129-136.

207. Liang, A., X. Jiang, X. Hong, Y. Jiang, Z. Shao, and D. Zhu, *Recent developments concerning the dispersion methods and mechanisms of graphene.* Coatings, 2018. **8**(1): p. 33.

208. Ovid'Ko, I., *Metal-graphene nanocomposites with enhanced mechanical properties: a review.* Reviews on Advanced Materials Science, 2014. **38**(2).

209. Li, J., M. Liu, J. Gao, Y. Jiang, L. Wu, Y.-K. Cheong, G. Ren, and Z. Yang, *AVNP2 protects against cognitive impairments induced by C6 glioma by suppressing tumour associated inflammation in rats.* Brain, behavior, and immunity, 2020. **87**: p. 645-659.

210. Muñoz-Bonilla, A. and M. Fernández-García, *Polymeric materials with antimicrobial activity.* Progress in Polymer Science, 2012. **37**(2): p. 281-339.

211. Larsson, M., A. Hill, and J. Duffy, *Suspension stability; why particle size, zeta potential and rheology are important.* Ann. Trans. Nordic Rheol. Soc, 2012. **20**: p. 209-214.

212. Larson, R.G., *The structure and rheology of complex fluids*. Vol. 150. 1999: Oxford university press New York.

213. Askeland, D.R., P.P. Phulé, W.J. Wright, and D. Bhattacharya, *The science and engineering of materials.* 2003.

214. Alger, M., *Polymer science dictionary*. 1996: Springer Science & Business Media.

215. Basu, K. and K. Baishya, *Brownian Motion: Theory and Experiment:: A simple Classroom Measurement of the Diffusion Coefficient*. arXiv preprint physics/0303064, 2003.

216. Witharana, S., C. Hodges, D. Xu, X. Lai, and Y. Ding, *Aggregation and settling in aqueous polydisperse alumina nanoparticle suspensions*. Journal of Nanoparticle Research, 2012. **14**(5): p. 851.

217. Zheng, X., Y. Li, D. Chen, A. Zheng, and Q. Que, *Study on Analysis and Sedimentation of Alumina Nanoparticles*. International journal of environmental research and public health, 2019. **16**(3): p. 510.

218. Cena, L.G., B.K. Ku, and T.M. Peters, *Particle collection efficiency for nylon mesh screens*. Aerosol Science and Technology, 2012. **46**(2): p. 214-221.

219. Kikuchi, T. and T. Uchida. *Calorimetric method for measuring high ultrasonic power using water as a heating material*. in *Journal of Physics: Conference Series*. 2011. IOP Publishing.

220. Liu, H., X. Hou, X. Li, H. Jiang, Z. Tian, and M.K.A. Ali, *Effect of Mixing Temperature, Ultrasonication Duration and Nanoparticles/Surfactant Concentration on the Dispersion Performance of Al2O3 Nanolubricants*. 2020: p. 1-18.

## APPENDIX A – RESULTS OF LATEX STANDARDS FOR NANOPARTICLE TRACKING ANALYSIS

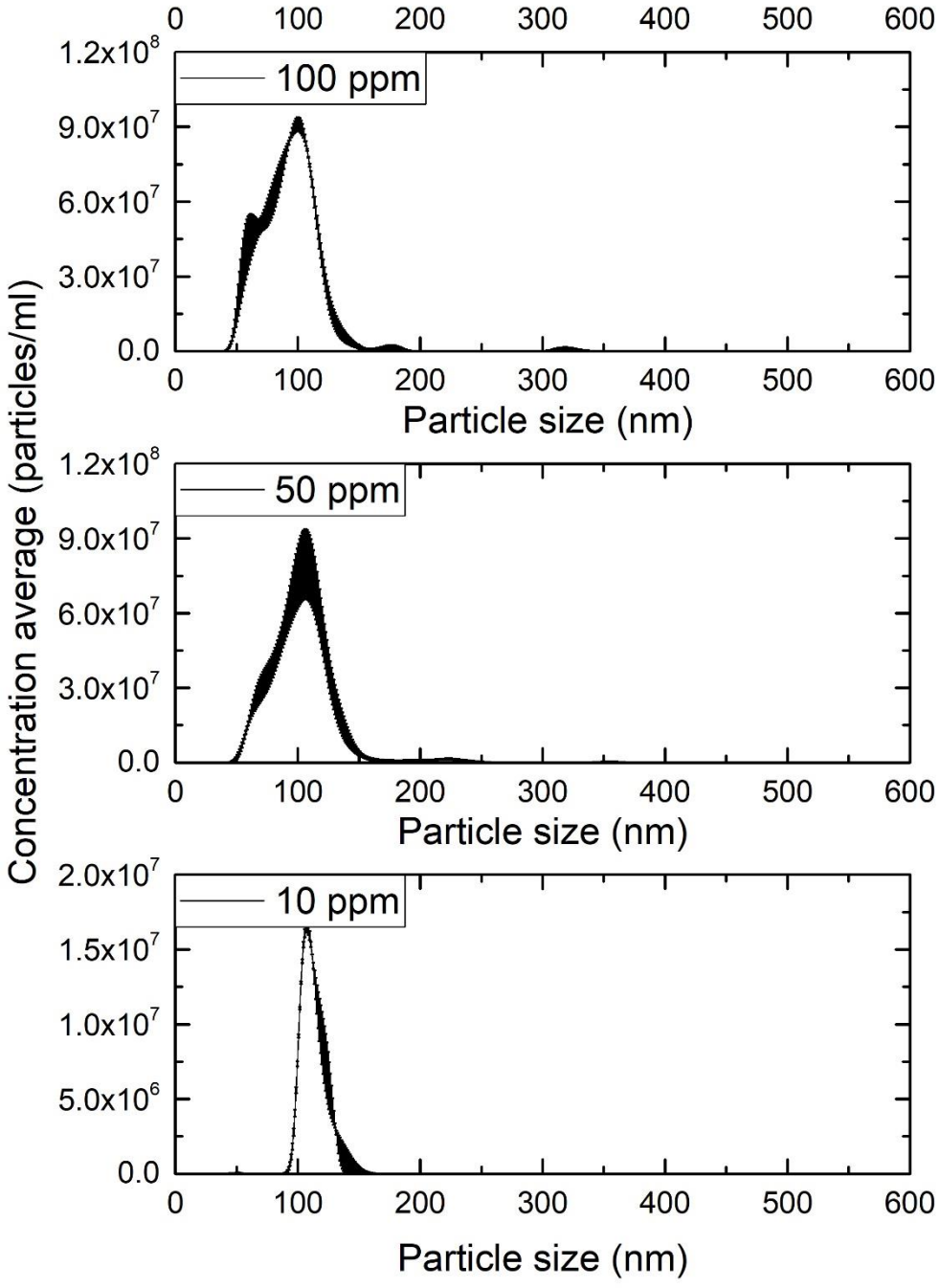


Figure 1 The size distributions of 100-nm PS latex standard at 100, 50 and 10 ppm

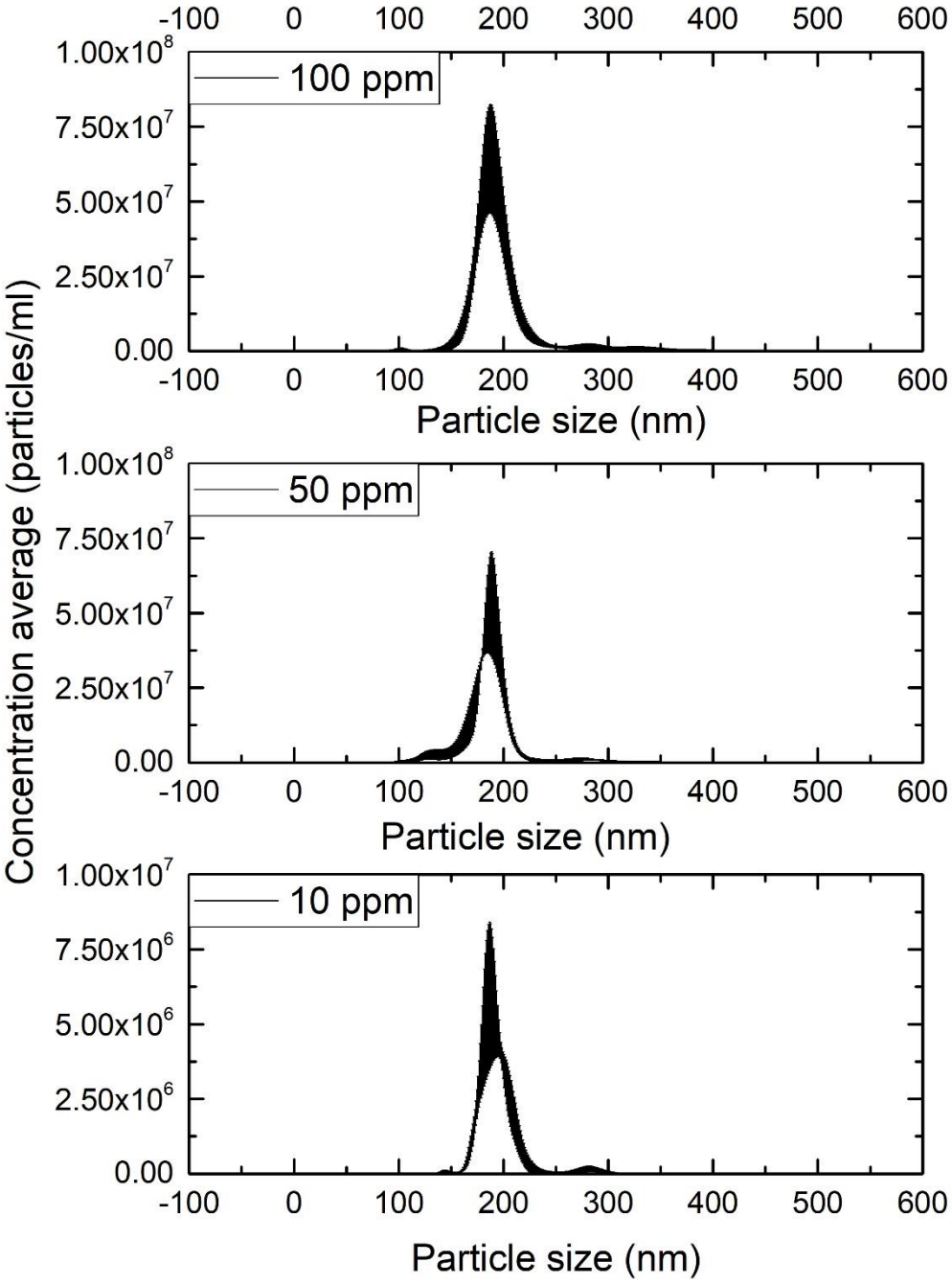


Figure 2 The size distributions of 200-nm PS latex standard at 100, 50 and 10 ppm

## APPENDIX B – RESULTS OF PH AND ZETA POTENTIAL FOR ALL SAMPLES

Table 1 The raw data of pH and zeta potential

| pH measurement | | | | |
|---|---|---|---|---|
| Suspensions | Concentration (ppm) | 1st Measurement | 2nd Measurement | 3rd Measurement |
| SAWC | 10 | 7.21 | 7.18 | 7.2 |
| | 50 | 6.62 | 6.61 | 6.58 |
| | 100 | 6.56 | 6.5 | 6.48 |
| QNA WC | 10 | 6.81 | 6.74 | 6.64 |
| | 50 | 6.73 | 6.74 | 6.62 |
| | 100 | 6.71 | 6.61 | 6.58 |
| QNA Ag | 10 | 6.71 | 6.59 | 6.6 |
| | 50 | 6.82 | 6.8 | 6.78 |
| | 100 | 6.98 | 6.96 | 6.93 |
| Cu10 | 10 | 6.92 | 7.04 | 7.04 |
| | 50 | 7.13 | 7.16 | 7.18 |
| | 100 | 6.59 | 6.47 | 6.44 |
| QNA Cu | 10 | 8.64 | 8.47 | 8.24 |
| | 50 | 8.04 | 8.77 | 7.82 |
| | 100 | 7.78 | 6.95 | 7.1 |
| NF CuO | 10 | 6.63 | 6.55 | 6.53 |
| | 50 | 7.04 | 7.05 | 7.04 |
| | 100 | 6.76 | 6.66 | 6.59 |
| QNA CuO | 10 | 6.63 | 6.55 | 6.53 |
| | 50 | 7.04 | 7.05 | 7.04 |
| | 100 | 6.76 | 6.66 | 6.59 |
| CuAg | 10 | 7.06 | 6.99 | 7.18 |
| | 50 | 6.92 | 6.84 | 6.8 |
| | 100 | 6.87 | 6.89 | 6.82 |
| CuZn | 10 | 6.42 | 6.29 | 6.28 |
| | 50 | 6.43 | 6.47 | 6.53 |
| | 100 | 6.62 | 6.7 | 6.72 |
| AVNP2 | 10 | 7.01 | 7 | 6.98 |
| | 50 | 7.29 | 7.22 | 7.22 |
| | 100 | 6.37 | 6.31 | 6.28 |
| SAF1.1 | 10 | 6.42 | 6.38 | 6.39 |
| | 50 | 6.52 | 6.66 | 6.71 |
| | 100 | 6.87 | 6.91 | 6.99 |

| Zeta potential | | | | |
|---|---|---|---|---|
| Suspensions | Concentration (ppm) | 1st Measurement | 2nd Measurement | 3rd Measurement |
| SAWC | 10 | -1.43 | -3.09 | -2.08 |
| | 50 | -4.99 | -5.57 | -3.73 |
| | 100 | -11.3 | -10.4 | -8.38 |
| QNA WC | 10 | -3.4 | -4.07 | -4.08 |
| | 50 | -17.9 | -13.7 | -20.8 |
| | 100 | -19.3 | -32.3 | -13.4 |
| QNA Ag | 10 | -30.1 | -39.1 | -24.9 |
| | 50 | -21.7 | -20.3 | -22 |
| | 100 | -30.9 | -28.9 | -32 |
| Cu10 | 10 | -6.53 | -8.28 | -9.41 |
| | 50 | -6.78 | -8.94 | -12.1 |
| | 100 | -2.16 | -13.7 | -10.6 |
| QNA Cu | 10 | -2.54 | -12 | -19.4 |
| | 50 | -11.4 | -20.7 | -6.53 |
| | 100 | -4.51 | 0.47 | 0.39 |
| NF CuO | 10 | -5.17 | -6.65 | -4.87 |
| | 50 | -2.32 | -4.46 | -5.91 |
| | 100 | -2.04 | -1.98 | -3.8 |
| QNA CuO | 10 | -5.96 | -8.53 | -8.46 |
| | 50 | 8.82 | 8.73 | 7.64 |
| | 100 | 3.59 | 2.64 | 2.37 |
| CuAg | 10 | -27.6 | -14.9 | -14.9 |
| | 50 | -20.8 | -23.1 | -22.6 |
| | 100 | -20.9 | -18.1 | -16.4 |
| CuZn | 10 | -8.02 | -10.7 | -10.5 |
| | 50 | 8.08 | 6.84 | 4.9 |
| | 100 | 16 | 16.7 | 15.8 |
| AVNP2 | 10 | -9.69 | -7.64 | -11.6 |
| | 50 | -22.6 | -20.5 | -18.8 |
| | 100 | -22.8 | -24 | -24.5 |
| SAF1.1 | 10 | -5.35 | -4.47 | -7.96 |
| | 50 | 13.6 | 12.8 | 8.51 |
| | 100 | 8.94 | 6.68 | 7.38 |

## APPENDIX C - STEPS FOR THE DETERMINATION OF DIRECT SONICATION CALORMIETRIC CURVES

1. Fill a 600 mL cylindrical borosilicate beaker with 500 mL of de-ionized water (resistivity $\geqslant$18 MΩ.cm)
2. Determine the mass of the liquid using a top loading balance (first tare the empty 600 mL beaker).
3. Immerse the sonicator probe (horn) approximately 2.5 cm (1") below the liquid surface.
4. Immerse a temperature probe connected to a temperature meter and data logger. The probe tip should be about 1 cm away from the sonicator probe (Figure 1).
5. Select a sonicator output power setting and, operating in continuous mode, record the water temperature increase for the initial 5 minutes. During sonication, ensure that the beaker does not shift position, especially when operating at high power settings; this can be accomplished, for instance, by using a clamp attached to a ring stand.
6. Using the recorded values, create a temperature vs. time curve and obtain the best linear fit for the curve using least squares regression.